

University of Mississippi

eGrove

---

Electronic Theses and Dissertations

Graduate School

---

2017

# Graphene Nano-Composites For Hypervelocity Impact Applications

Alharith Manasrah  
*University of Mississippi*

Follow this and additional works at: <https://egrove.olemiss.edu/etd>



Part of the [Engineering Commons](#)

---

## Recommended Citation

Manasrah, Alharith, "Graphene Nano-Composites For Hypervelocity Impact Applications" (2017).  
*Electronic Theses and Dissertations*. 432.  
<https://egrove.olemiss.edu/etd/432>

This Dissertation is brought to you for free and open access by the Graduate School at eGrove. It has been accepted for inclusion in Electronic Theses and Dissertations by an authorized administrator of eGrove. For more information, please contact [egrove@olemiss.edu](mailto:egrove@olemiss.edu).

# GRAPHENE NANO-COMPOSITES FOR HYPERVELOCITY IMPACT APPLICATIONS

A Dissertation

presented in partial fulfillment of requirements

for the degree of doctor of philosophy

in the Department of Civil Engineering

The University of Mississippi

by

ALHARITH MANASRAH

November 2016



Copyright Alharith Manasrah 2016

ALL RIGHTS RESERVED

## ABSTRACT

The Low Earth Orbit (LEO) is a harsh environment cluttered with natural meteoroids and man-made debris, which can travel at velocities approaching 15 km/s. Most space activities within the LEO will encounter this environment. Thus, the spacecraft and its hardware must be designed to survive debris impact. This research introduces new procedures to produce a nano-composite material with mortar-brick nano-structure inspired from nacre. Nacre-like composites were successfully manufactured, based on three host polymers, with a wide range of graphene concentrations. The manufactured exfoliated graphene nano-platelet, embedded in a host polymer, provided good potential for enhancement of the hypervelocity impact (HVI) shield resistance. The nano-composites are suggested for use as a coating. Moreover, explicit dynamic finite element studies were conducted for further investigation of the hypervelocity impact of the graphene-based coatings in order to understand the effect of the coating on the crater formation and the exit velocity. This dissertation presents the results of the characterization and numerical sensitivity study of the developed material parameters. The numerical simulations were performed by implementing Autodyn smooth particle hydrodynamics. This study provides innovative, low-weight shielding enhancements for spacecraft, as well as other promising applications for the manufactured nano-composites.

## DEDICATION

This dissertation is dedicated to my family and friends who helped me and guided me through my own times of stress and anxiety. In particular, my parents Mohammad Ali and Marwa Obaidat. To my lovely wife Dr. Bayan Alquran, who supported me during my study. To my brothers and sister: Obadah, Yaman, Almothana, and Shahid. This work would not have been possible without their support.

## LIST OF ABBREVIATIONS

NASA – National Aeronautics and Space Administration

LEO – low earth orbit

ISS – International space station

HVI – Hypervelocity impact

GEO – Geospatial earth orbit

LGG – Light-gas guns

JSC – Johnson space center

FCRP – Fiber carbon reinforced polymer

HC – Honeycomb

SPH – Smooth particles hydrodynamics

PEI – Polyetherimide

PU – Polyurea

xGnP – Exfoliated Graphene nano-Platelet

OxGnP – Oxidized exfoliated Graphene nano-Platelet

NIRL – Nano infrastructure research laboratory

XPS – X-ray photoelectron spectroscopy

AFM – Atomic force microscopy

SEM – Scan electron microscopy

SHPB – Split-Hopkinson pressure bar

TGA – Thermogravimetric analysis

EIS – Electrochemical impedance spectroscopy

DMA – Dynamic mechanical analysis

MTS – Material testing system

ANN – Artificial neural network

EoS – Equation of state

PTFE – Polytetrafluoroethylene

DMAc – Dimethylacetamide

PI – Polyimide

GO – Graphite oxide

AC – Alternating current

$E'$  – Storage modulus

$E''$  – Loss modulus

$T_g$  – Glass transition temperature

Tan ( $\delta$ ) – Tan delta

DSGZ – Duan-Saigal-Greif-Zimmerman

JC – Johnson-Cook

CNIP – Coating normalized isolated performance.

## ACKNOWLEDGMENTS

I would like to acknowledge the National Aeronautics and Space Administration for financial support received under subcontract grant # NNX13AD24A. Also, I would like to express my deepest appreciation to my advisor Dr. Ahmed Al-Ostaz and my committee members, Drs. Alexander Cheng, Ellen Lackey, and Hunain Alkhateb. Also, I acknowledge Dr. Yacoub Najjar for providing the his ANN program.

Lastly, I acknowledge Dr. Xiaobing Li and the collegial support from my fellow doctoral students. Khalil Qatu, Grace Rushing, Hatem Almasaeid, Damian Stoddard, and Hashem Almashaqbeh. You made this part of my life enjoyable and enriching.

## TABLE OF CONTENTS

ABSTRACT .....	i
DEDICATION .....	ii
LIST OF ABBREVIATIONS .....	iii
ACKNOWLEDGMENTS .....	vi
TABLE OF CONTENTS .....	vii
LIST OF TABLES .....	xii
LIST OF FIGURES .....	xiii
1. INTRODUCTION .....	1
1.1 Space environment .....	1
1.2 Hypervelocity Impact experimental testing .....	4
1.3 Literature review .....	4
1.4 Material Background .....	10
1.4.1 Polymers .....	10
1.4.1.1 Epoxy .....	10
1.4.1.2 Polyurea .....	11
1.4.1.3 Polyetherimide .....	12
1.4.2 Nano Materials .....	13
1.4.2.1 Exfoliated Graphene Nanoplatelet .....	13



1.5	Characterization Techniques .....	15
1.6	Finite Element Analysis .....	16
1.7	Objectives.....	17
2.	METHODOLOGY .....	18
2.1	Approach .....	19
2.2	Manufacturing processes.....	19
2.2.1	xGnP functionalization.....	19
2.2.2	Manufacturing the nano-composites .....	21
2.2.2.1	Epoxy based xGnP or OxGnP.....	21
2.2.2.1.1	xGnP or OxGnP roll milled epoxy nano-composite.....	22
2.2.2.1.2	xGnP or OxGnP based epoxy papers.....	23
2.2.2.1.3	Laminating Based Epoxy Papers .....	26
2.2.2.2	xGnP based PEI .....	27
2.2.2.2.1	Low concentration xGnP based PEI .....	27
2.2.2.2.2	High concentration xGnP based PEI.....	28
2.2.2.2.3	Laminating xGnP-PEI films .....	30
2.2.2.3	Polyuria based xGnP or OxGnP .....	30
2.2.2.3.1	Low concentration xGnP or OxGnP based PU nano-composite .....	31
2.3	Characterization .....	31

2.3.1	Chemical properties.....	31
2.3.1.1	X-ray Photoelectron Spectroscopy .....	32
2.3.1.2	Raman spectroscopy .....	35
2.3.2	Imaging.....	37
2.3.2.1	Atomic Force Microscope.....	37
2.3.2.2	Scanning Electron Microscope .....	42
2.3.3	Thermal Properties .....	44
2.3.3.1	Thermogravimetric analysis.....	45
2.3.4	Electrochemical properties .....	47
2.3.4.1	Electrochemical Impedance Spectroscopy .....	47
2.3.5	Mechanical properties.....	50
2.3.5.1	Dynamic Mechanical Analysis .....	50
2.3.5.1.1	Controlled Force Mode.....	51
2.3.5.1.2	Temperature sweep .....	53
2.3.5.1.3	Multi-Frequency Mode .....	59
2.3.5.2	Tensile Test.....	62
2.3.5.3	High strain rate utilizing SHPB .....	67
2.3.5.3.1	Compression test.....	67
2.4	Material modeling .....	77

2.4.1	Equation of state .....	78
2.4.2	Constitutive model.....	78
2.4.3	Artificial Neural Networks .....	84
2.4.3.1	Quasi static stress-strain.....	86
2.4.3.1.1	Stress-controlled model .....	87
2.4.3.1.2	Strain-controlled model .....	88
2.4.3.1.3	Stopping criterion model.....	89
2.4.3.1.4	Sensitivity analysis.....	90
2.4.3.2	High strain rate stress-strain.....	94
2.4.3.2.1	Strain-controlled model .....	95
2.4.3.2.2	Sensitivity analysis.....	97
2.5	Finite Element Analysis .....	99
2.5.1	ANSYS Autodyn introduction .....	99
2.5.2	Autodyn Hydrodynamic code.....	100
2.5.3	Smooth Particles Hydrodynamics .....	100
2.5.4	SPH parts models .....	100
2.5.4.1	Projectile .....	101
2.5.4.2	Substrate.....	101
2.5.4.3	Coating.....	102

2.5.5	Convergence study .....	102
2.5.6	Sensitivity analysis of material constants.....	103
2.5.6.1	Simulations Matrix.....	103
2.5.6.2	Numerical simulation results .....	104
2.5.7	Layer stacking effect .....	115
2.5.8	Varying coating thickness .....	117
3.	Conclusions and Recommendations .....	121
3.1	Conclusions .....	121
3.2	Recommendations .....	123
	REFERENCES .....	125
	APPENDIX A.....	136
	APPENDIX B .....	144
	APPENDIX C .....	158
	APPENDIX D .....	160
	APPENDIX E .....	187
	APPENDIX F .....	190
	VITA.....	217

## LIST OF TABLES

Table 1: Impact at low and high velocity.....	3
Table 2: Impact response of material.....	17
Table 3: Percentage of carbon atoms allocated to several functional groups.....	35
Table 4: Fitting parameters for Epoxy based nano-composites.....	83
Table 5: Fitting parameters for PU based nano-composites .....	83
Table 6: Fitting parameters for PEI based nano-composites .....	84
. Table 7: sample ANN Table results reporting .....	88
Table 8: ANN models structures and statistics .....	95
Table 9: EoS, material model, and failure model. ....	101
Table 10: Model constants for reference coating.....	102

## LIST OF FIGURES

Figure 1: Schematic of earth's orbits.....	1
Figure 2: LEO orbital population.....	2
Figure 3: GEO orbital population image .....	2
Figure 4: molecular structure of (a) VP1000 (b) ISONATE 143L System.....	12
Figure 5: Typical molecular structure of PEI .....	13
Figure 6: SEM image shows the morphology of xGnP .....	14
Figure 7: Research Program.....	18
Figure 8: Storage moduli for xGnP and OxGnP papers .....	21
Figure 9: Three-roll mill dispersing xGnP.....	23
Figure 10: Vacuum filtration system used to infuse epoxy between xGnP or OxGnP.....	24
Figure 11: Epoxy poured on xGnP cake.....	25
Figure 12: Carver hydraulic compression press.....	25
Figure 13: xGnP paper after curing .....	26
Figure 14: xGnP-PEI precipitation in distilled water .....	28
Figure 15: xGnP-PEI (a) precipitation before pressing; (b) paper after pressing.....	28
Figure 16: Filtration system used for manufacturing.....	30
Figure 17: Filtered xGnP-PEI cake.....	30
Figure 18: PU in Teflon mold after curing .....	31
Figure 19: Overall XPS for (a) xGnP (b) OxGnP.....	33
Figure 20: The C1s peaks in the XPS spectra of (a) xGnP (b) OxGnP .....	34
Figure 21: Raman results comparison (a) G-band peak (b) D-band peak .....	36
Figure 22: Typical Raman spectra for GO.....	37

Figure 23: AFM phase scan of xGnP (left) and OxGnP (right).....	38
Figure 24: Height scan of OxGnP (10*10 $\mu\text{m}$ ).....	39
Figure 25: 2D Height images of xGnP (left) and OxGnP (right) .....	40
Figure 26: Amplitude error scans of xGnP (left) and OxGnP (right).....	41
Figure 27: Phase scans of xGnP (left) and OxGnP (right).....	42
Figure 28: Alignment of xGnP in the papers during manufacturing (56 wt. %) .....	43
Figure 29: SEM images of xGnP-PEI fracture surface.....	44
Figure 30: Typical SEM image (a) 3% xGnP (b) 3% OxGnP nano-composites.....	44
Figure 31: TGA Q500 by TA Instruments.....	45
Figure 32: (a) Typical weight loss of xGnP or OxGnP papers due to decomposition (b) xGnP or OxGnP contents in the manufactured based epoxy papers.....	46
Figure 33: (a) Typical weight loss of xGnP, PEI, and xGnP-PEI papers due to decomposition; (b) xGnP loading in the xGnP-PEI paper with variation of PEI concentration in DMAc.....	47
Figure 34: xGnP-Epoxy sample clamped to the impedance tester .....	48
Figure 35: xGnP or OxGnP based epoxy nano-composite impedance with respect to frequency.....	49
Figure 36: Impedance of xGnP-PEI papers with various xGnP concentrations with respect to frequency.....	49
Figure 37: DMA Q800 by TA Instruments.....	51
Figure 38: Stress strain response for (a) xGnP-Epoxy paper (b) xGnP-PEI paper.....	51
Figure 39: Stress at break for epoxy-based papers .....	52
Figure 40: Stress-strain response of xGnP-PEI paper: (a) stress at break; (b) strain at break.	53
Figure 41: relation between $E^*$ , $E'$ , $E''$ , and $\text{Tan}(\delta)$ .....	53

Figure 42: Typical (a) Storage (b) Loss Moduli curves obtained from DMA for epoxy based nano-composites .....	54
Figure 43: Loss modulus for xGnP-Epoxy or OxGnP-Epoxy at 50 °C (a) roll milled nano-composites (b) Papers at 40 °C. ....	55
Figure 44: Storage modulus for xGnP-Epoxy or OxGnP-Epoxy (a) roll milled nano-composites (b) Papers at 40 °C. ....	55
Figure 45: Tg for xGnP-Epoxy or OxGnP-Epoxy (a) roll milled nano-composites (b) Papers .....	56
Figure 46: Max tan $\delta$ for xGnP-Epoxy or OxGnP-Epoxy (a) roll milled nano-composites (b) Papers.....	56
Figure 47: Comparison of (a) storage modulus (b) loss modulus of PEI, xGnP-PEI (59 wt. %), and pure xGnP papers .....	57
Figure 48: Effect of xGnP content on (a) the storage modulus (b) loss modulus of of xGnP-PEI paper at 40 °C.....	58
Figure 49: Effect of xGnP loading in xGnP-PEI on glass transition temperature. ....	58
Figure 50: Tan $\delta$ of xGnP-PEI papers (a) Typical response (b) tan $\delta$ at different xGnP loadings.....	59
Figure 51: Frequency sweep comparison between neat epoxy and xGnP-Epoxy paper like 57 wt. % (a) loss modulus (b) storage modulus.....	60
Figure 52: Storage Modulus for roll-milled nano-composite (a) xGnP-Epoxy (b) OxGnP-Epoxy .....	61
Figure 53: Storage Modulus for paper nano-composite (a) xGnP-Epoxy (b) OxGnP-Epoxy.....	61



Figure 54: Loss Modulus for roll-milled nano-composite (a) xGnP-Epoxy (b) OxGnP-Epoxy .....	62
Figure 55: Loss Modulus for paper nano-composite (a) xGnP-Epoxy (b) OxGnP-Epoxy .....	62
Figure 56: Dog bone shaped specimen (a) Roll-milled casted in silicon mold (b) Laminated tabbed with epoxy .....	63
Figure 57: MTS and extensometer for stress-strain and Poisson's Ratio measurement .....	64
Figure 58: Typical (a) stress-strain curve (b) axial-traverse strain curve for xGnP-epoxy nano-composite .....	65
Figure 59: Stress-strain response of xGnP-Epoxy roll-milled nano-composite (a) stress at break (b) strain at break. ....	65
Figure 60: Stress-strain response of xGnP-Epoxy laminated nano-composite (a) stress at break (b) strain at break. ....	66
Figure 61: Poisson's ratio of (a) Roll-milled (b) laminated xGnP-Epoxy nano-composite.....	67
Figure 62: SHPB setup used to conduct the experiments .....	68
Figure 63: SHPB data acquisition system.....	68
Figure 64: Camera and strobes configuration during SHPB test.....	69
Figure 65: Typical test results of epoxy specimen (a) Incident, reflected and transmitted pulses (b) Strain rate (c) Validation of the equilibrium stress state.....	70
Figure 66: Typical dynamic compressive true stress-strain curve of xGnP-Polymer .....	72
Figure 67: High-speed images associated with stress history during SHPB compression loading process of xGnP-Epoxy 0.5 wt. % specimen at strain-rate of 3290/s (a) E0 (b) E1 (c) E2 (d) E3 (e) Beyond failure.....	73

Figure 68: High-speed images associated with stress history during SHPB compression loading process of xGnP-PU 0.5 wt. % specimen at strain-rate of 3677/s (a) U0 (b) U1 (c) U2 (d) U3 (e) Sample out of SHPB .....	74
Figure 69: High-speed images associated with stress history during SHPB compression loading process of xGnP-PEI 0.5 wt. % specimen at strain-rate of 3176/s (a) P0 (b) P1 (c) P2 (d) P3 (e) Beyond failure .....	75
Figure 70: Toughness sensitivity to strain rate for (a) xGnP-Epoxy (b) OxGnP-Epoxy.....	76
Figure 71: Toughness sensitivity to strain rate for (a) xGnP-PU (b) OxGnP-PU .....	77
Figure 72: Toughness sensitivity to strain rate for xGnP-PEI.....	77
Figure 73: DSGZ Model fit model for (a) Epoxy (b) xGnP-Epoxy 0.5 wt. % (c) xGnP-Epoxy 1 wt. % (d) xGnP-Epoxy 57 wt. % (e) OxGnP-Epoxy 0.5 wt. % (f) OxGnP-Epoxy 1 wt. % (g) OxGnP-Epoxy 57 wt. %.....	81
Figure 74: DSGZ Model fit model for (a) PU (b) xGnP-PU 0.2 wt. % (c) xGnP-PU 0.5 wt. % (d) xGnP-PU 1 wt. % (e) OxGnP-PU 0.2 wt. % (f) OxGnP-PU 0.5 wt. % (g) OxGnP-PU 1 wt. % .....	82
Figure 75: DSGZ Model fit model for (a) PEI (b) xGnP-PEI 0.5 wt. % (c) xGnP-PEI 1 wt. % (d) xGnP-PEI 50 wt. % .....	83
Figure 76: Sample of ANN architecture for strain-controlled model.....	85
Figure 77: Visual representation of the simulation results. ....	88
Figure 78: ANN simulations compared with experimental stress-strain curves for (a) 0.5 wt. % (b) 25 wt. % (c) 40 wt. % (d) 85 wt. % .....	91
Figure 79: Sensitivity analysis simulation for the strain-controlled model.....	92
Figure 80: Sensitivity analysis simulation for the stress-controlled model.....	92

Figure 81: Mechanical properties calculated from the stress-strain responses (a) toughness (b) maximum tangent modulus (c) maximum strength (d) maximum strain .....	94
Figure 82: Epoxy-based nano-composite stress-strain response for (a) Pure Epoxy (b) 0.5% OxGnP-Epoxy (c) 1% xGnP-Epoxy .....	96
Figure 83: PU-based nano-composite stress-strain response for (a) 0.5 % xGnP-PU (b) 0.5% OxGnP-PU .....	96
Figure 84: PEI-based nano-composite stress-strain response for a) 0.5 % xGnP-PEI b) 1 % xGnP-PEI .....	97
Figure 85: xGnP-PEI strain rate sensitivity analysis for (a) PEI (b) 1% xGnP-PEI.....	98
Figure 86: Sensitivity analysis of OxGnP-Epoxy based nano-composite to OxGnP loading at stain rate of (a) 1000 S <sup>-1</sup> b) 4000 S <sup>-1</sup> .....	99
Figure 87: Average exit velocity for the different element size .....	103
Figure 88: Coatings Isolated performance illustration.....	105
Figure 89: Typical sphere particles velocity drop after impact of Aluminum substrate coated with reference coating.....	105
Figure 90: Average exit velocity of impactor after impact by substrate coated with reference xGnP-Epoxy 1 wt. % compared to blank substrate (a) Aluminum (b) Kevlar-Epoxy (c) Steel .....	106
Figure 91: CNIP deviation from reference coating on Aluminum substrate after impact velocity of (a) 1km/sec (b) 7km/sec (c) 10km/sec.....	108
Figure 92: CNIP deviation from reference coating on Kevlar-Epoxy substrate after impact velocity of (a) 1km/sec (b) 7km/sec (c) 10km/sec.....	109

Figure 93: CNIP deviation from reference coating on Steel substrate after impact velocity of (a) 1km/sec (b) 7km/sec (c) 10km/sec .....	110
Figure 94: Measurement of crater diameter from simulation .....	111
Figure 95: Crater diameter resulting from impact of substrate coated with reference xGnP-Epoxy 1 wt. % compared to blank substrate (a) Aluminum (b) Kevlar-Epoxy (c) Steel .....	112
Figure 96: Crater diameter deviation from Aluminum substrate with reference coating after impact velocity of (a) 1km/sec (b) 7km/sec (c) 10km/sec .....	113
Figure 97: Crater diameter deviation from Kevlar-Epoxy substrate with reference coating after impact velocity of (a) 1km/sec (b) 7km/sec (c) 10km/sec .....	114
Figure 98: Crater diameter deviation from Steel substrate with reference coating after impact velocity of (a) 1km/sec (b) 7km/sec (c) 10km/sec .....	115
Figure 99: CNIP variation with shield layering (a) Aluminum (b) Kevlar-Epoxy (c) Steel ..	116
Figure 100: Variation of crater diameter with shield layering (a) Aluminum (b) Kevlar-Epoxy (c) Steel .....	117
Figure 101: Normalized exit velocity variation by replacing certain substrate thickness by coating (a) Aluminum (b) Kevlar-Epoxy (c) Steel .....	119
Figure 102: Variation of crater diameter by replacing certain substrate thickness by coating (a) Aluminum (b) Kevlar-Epoxy (c) Steel .....	120

## 1. INTRODUCTION

Satellites and space shuttles face harsh environmental conditions at Low Earth Orbit (LEO). This includes man-made orbital debris that consist of everything from derelict spacecraft and launch vehicles to paint flakes and solid rocket motor effluent. Many methods and techniques were implemented to improve the shielding performance of space vehicles. Several materials used construct multilayer shields were aluminum, Kevlar, Nextel, etc.

Composites, containing the recently discovered nano-carbon material called graphene, showed superior improvement to mechanical, physical and other properties [1], [2]. Lighter weight material is required to minimize the cost of shipping to outer space. Graphene added to polymers will be used extensively in this application, due to its unique properties that include low density, high strength, toughness, and others. It is important to study and investigate the methods that can protect space shuttles against such an environment.

Different characterization techniques and pretesting were done to explore the surface or to determine mechanical and physical properties of the manufactured nano-composite under study. Also, computational simulations employing finite element modeling were used as a means of evaluating the performance of this nano-composite at several impact velocities.

### 1.1 Space environment

LEO is currently of great importance to the human race because of the fact that most scientific satellites, including NASA's Earth Observing System fleet and the International Space Station (ISS) are located in LEO orbit [3].

Due to its proximity to the earth, it is more efficient to place a satellite in LEO because it will minimize the required energy. This also provides low communication latency and high bandwidth. LEO can be defined as the orbit that ranges from 180-2000 km above the earth[4], as shown in Figure 1.



Figure 1: Schematic of Earth's orbits

Materials face many challenges in this environment as they are subjected to multiple aggressive effects like solar radiation, thermal cycling which can range from -50 °C to 150 °C, and bombardment by low and high-energy charged particles [5]. Another challenge is the hypervelocity impact (HVI) of spacecraft by meteoroids/debris. The last threat has increased significantly in recent years [6]. Figure 2 and Figure 3 provide an illustration of the escalating “space junk accumulation” in earth's orbit [7]. Thus, researchers are looking for ways to minimize the HVI damage or prevent it completely for spacecraft in LEO. This is a serious problem facing spacecraft. Thus, NASA satellite mission controllers track anything that may enter the path of their satellites. As of May 2009, earth-observing satellites had been moved three separate times to avoid the impact of orbital debris [3].

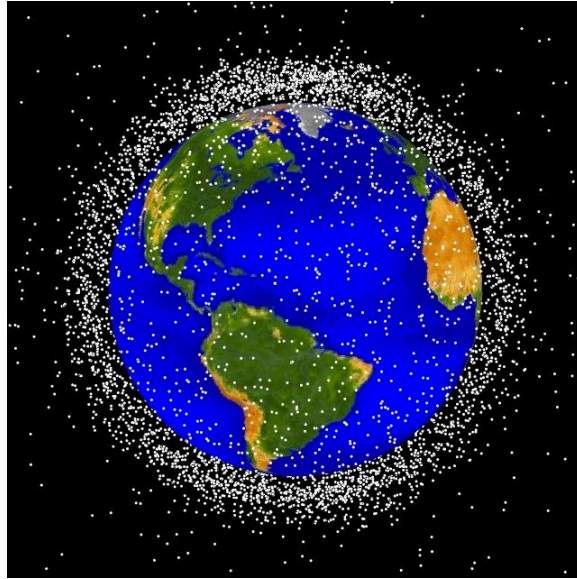


Figure 2: LEO orbital population

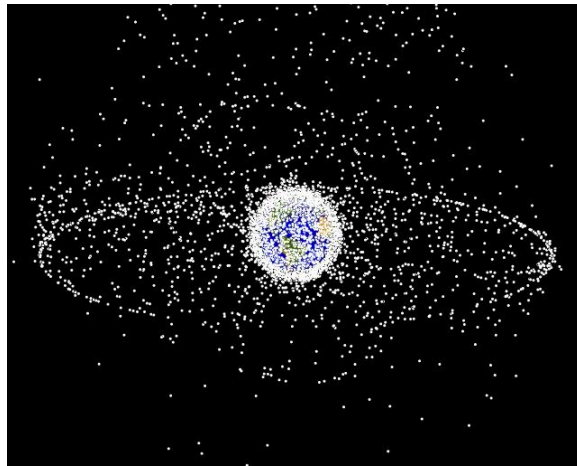


Figure 3: GEO orbital population image

Meteoroids are natural small rocky particles that orbit the sun. Debris are metallic man-made objects in orbit around the earth. Meteoroid velocities range from 11 km/s to 72 km/s, with an average for Earth-orbiting spacecraft of 19 km/s. Particle densities range from 2 g/cm<sup>3</sup> for particles less than one micro-gram; for particles 0.01 g and greater, the density is 0.5 g/cm<sup>3</sup> [1]. However, debris impact velocities range from 1 km/s to 15 km/s, with an average of 8 to 9 km/s. With most impactor debris composed of metallic fragments, we assume debris particle density to be 2.8 g/cm<sup>3</sup>, corresponding to aluminum metal [9].

The state of the debris cloud is a key factor governing the performance of space shields. The debris cloud may consist of solid, liquid, or vapors from the projectile and bumper materials, or a combination of the three states, depending on the impact pressure with the bumper. If the debris cloud contains solid fragments, there is a high possibility that they penetrate the rear wall at contact time. This possibility is lower if the fragments are in liquid or vapor states. The pressures generated in the projectile and bumper at initial impact, which controls the resulting state of the material after release from compression, is a function of multiple variables, including projectile velocity, projectile and shield material properties, and thickness. Loading from blast on the rear wall is a function of shield standoff distance. Table 1 shows a comparison of the low and high velocity impact response of material.

Table 1: Impact at low and high velocity

Velocity	Low	High
Deformation	Global	Local
Response Time	ms - s	$\mu$ s - ms
Strain	< 10%	> 50%
Strain Rate	< $10 \text{ s}^{-1}$	> $10000 \text{ s}^{-1}$
Pressure	< Yield Stress	10 - 100 x Yield Stress

At low impact velocities below 3km/s, Whipple shield performance is less effective because initial impact pressures are low. After impact with the bumper, the projectile deforms but remains intact. A substantially intact projectile will impact the shield's rear wall and perforate it. The projectile is more damaging as velocity increases in the low velocity range.

At intermediate velocities, which increase from 3 km/s to 7 km/s, the projectile will fragment upon impact on the bumper and will begin to melt above a velocity of 5.5 km/s. For aluminum- aluminum impacts, aluminum projectiles will melt when impact pressures reach 0.65 Mbar, which can be generated by normal impact at 5.5 km/s [10]. Rear wall damage decreases if the projectile is totally fragmented and partially melted. Thus, shield protection



capability in terms of the maximum particle size that can penetrate the shield increases as velocity increases in this velocity range.

At high velocities in excess of 7 km/s, the debris cloud reaching the rear wall will contain liquid, vapor, and various fractions of solids, from the projectile and bumper, depending on impact conditions. The critical maximum particle diameter that the shield can stop decreases with increasing velocity in the high velocity regime.

## 1.2 Hypervelocity Impact experimental testing

Hypervelocity impact tests are an important part of spacecraft shielding design. Dr. W.D. Crozier and his team who invented the light-gas gun (LGG) at the New Mexico School of Mines in 1946, which uses hydrogen gas as a propellant, accelerating impactors with velocity up to 4 km/s [1]. Two-stage LGGs are capable of launching projectiles up to 7 km/s. The LGGs are capable of covering a fraction of orbital debris velocities, only 40% of the orbital debris threat [11]. However, the 3-stage hypervelocity launcher developed at Sandia National Laboratories [12] provides useful information on shield capabilities in the range of 10-15 km/s.

## 1.3 Literature review

Christiansen et. al. [13] studied shields that consisted of 3-4 ceramic cloth (Nextel) spaced bumpers with a rear wall made of Kevlar, while low-density polyurethane foam was used between the bumper layers and the rear wall. The shields were tested at NASA Johnson Space Center (JSC) and Southwest Research institute for Hypervelocity impact, ballistic limit equations were derived from the test results for possible applications in the space station.

K. Thoma et. al. [14] developed a material model of Nextel and Kevlar-Epoxy, which was incorporated in a mesh free numerical model. Additionally, the influence of projectile shape protection performance of Whipple shields was studied. For these shapes, systematic

numerical simulation was used to overcome the experimental difficulties of accelerating these shapes. Finally, they outlined the systematic characterization approach of metallic foams in “sandwich bumper shields”, and they discussed the benefits of using these materials in the mentioned application.

E. Fahrenthold and Y.K. Park [15] implemented rate-dependent material models in numerical simulations of multi-layered Aluminum-Nextel-Kevlar shields at impact velocities of 7 and 11 km/s. The simulation results showed conservative estimation of the protection provided by the studied shields.

R. A. Clegg et. al. [16] and W. Riedel et. al. [17] developed two experimental techniques to simulate space debris impact; the first was optimized to evaluate damage, while the second experiment reproduce strain rates and stresses in plate impact. Additionally, a detailed material model was developed for shock wave loading, which simulates the correct thermodynamic response of orthotropic materials. The developed material model was implemented in Autodyn to study the extent of damage and residual strength of fiber composite materials after impact.

J. Eftis et. al.[18] simulated hypervelocity impact of glass projectiles with Aluminum 1100 plates at 6 km/h using a constitutive-micro-damage model. The numerical simulations were validated for three projectile diameters to target thickness ratios.

J. H. Kerr and E. P. Fahrenthold [19] studied the Whipple shield impact simulation method. The simulation accuracy was validated for impact velocities above 8 km/h at an oblique impact angle of  $30^\circ$  compared with experimental results. The results were also compared with previously established ballistic limit equations to further illustrate the accuracy of the simulations methodology.

S. Rayan et. al. [20] performed numerical simulations of carbon fiber reinforced plastic/aluminum honeycomb sandwich panels using Autodyn. A combination of existing theoretical methods was developed and compared with experimental results. The developed procedure showed accurate representation of the experimental data for a range of impact velocities and angles. However, the developed methodology started to deviate from the experimental results with increasing projectile size. This was found to be due to the under prediction of the inter-laminar tensile strength by the numerical model.

M. Katayama et. al.[21] studied hypervelocity impact of projectiles onto single-walled Whipple bumper shields for three impact velocities 2, 4 and 7 km/s. Experimental testing was performed using three different accelerators, namely; one-stage powder-gun, two-stage light-gas gun, and a rail gun. The experimental results were compared with numerical simulations using Eulerian and Lagrangian descriptions. A parametric study was performed in order to optimize the material properties of the bumper and the wall. Both numerical methodologies were in agreement with the experimental results.

N. Kawai et. al. [22] studied the behavior of an advanced ceramic thruster made of monolithic silicon nitride ceramics. The developed material plates were tested by impact of stainless steel spheres and other materials 0.2-0.8 mm in diameter with impact velocity up to 8 km/s using a two-stage gas gun. The penetration equations of the developed material were found. Moreover, three fracture patterns were found: cratering, cratering with spallation, and perforation.

G. Hussain et. al. [23] studied the impact of shaped charge onto Whipple shields in order to optimize the shield thickness to be used in protection in light armor. Both experimental and simulation results showed that a 0.75 mm shield thickness provided the optimum protection from the studied shaped charges.

Y.K. Park and E.P. Fahrenthold [24] developed an improved hybrid particle finite element method designed for hypervelocity impact. The method introduced internal energy variables as generalized coordinates in a new formulation of the thermo-dynamical Lagrangian equations. The developed method leads to reduction of computational demand of the numerical simulation. The problems simulated using the developed method were in excellent agreement with the exact equations in one-dimensional problems and the experimental results for three-dimensional problems.

J. Bonet et. al. [25] studied the formulation for smooth particle hydrodynamics simulation of fluid and solid problems. The resulting equations were found to treat the continuum as a Hamiltonian system where the particles are represented in internal energy terms. Each equation of motion was developed as a Lagrangian equation. The developed formulation preserved the physical constants of motion.

S. Katz et. al. [26] studied hypervelocity impact of debris with impact velocities up to 3 km/s onto thin film micro-composites with a thickness of  $\sim 10 \mu\text{m}$ . The films were made of Kevlar 29-epoxy and Spectra-epoxy composites. The damaged areas were examined. For the Spectra-epoxy composite, failure mechanism was found to be new surface creation; while for the Kevlar-epoxy fiber, pull out was the dominant mechanism.

S. Ryan et. al. [27] developed a model that is experimentally validated in order to study the impact-induced transient wave in the local structure of FCRP/Al HC. Impactor momentum was used to simplify some features of the transient wave expressed in a mathematical function. The characterization of the transient waveform was used to extrapolate the elastic wave form to the impact location, which was defined as time history force to be used in finite element structural simulations for local disturbance to vibration sensitive locations.

J. A. Zukas and D. R. Scheffler [28] performed numerical simulation for mono-block and multilayered plates using Lagrangian and Eulerian wave propagation codes. The Lagrangian simulation was found to best represent the experimental and analytical results, while the Eulerian simulations were not accurate in describing the multiple perforation.

G. R. Johnson et. al. [29] studied Smoothed Particle Hydrodynamics (SPH) and developed a normalized smoothing function to be used in the computational algorithm of SPH. They also discussed the problems with smoothing functions, smoothing distances, free boundaries, material interfaces, and artificial viscosity. Additionally, they developed a technique to allow SPH nodes to interact with standard finite element grids through sliding, attachment, and automatic generation of SPH nodes from distorted finite elements.

M. C. Price et. al. [30] studied the relationship between impact crater size and projectile diameter for micrometer scale and smaller sized impactors. They performed numerical simulations using ANSYS Autodyn. Preston-Tonks-Wallace constitutive model was used in the numerical simulations. The results were compared with experimental results for high purity tantalum, Aluminum alloy 1100 and copper. The results showed the parameters of Preston-Tonks-Wallace for the studied materials need to be refined to model micrometer scale hypervelocity impact events accurately.

E. P. Fahrenthold and R. J. Hernandez [31] performed numerical simulations using the hybrid-particle finite element method and an orthotropic elastic-plastic material model for reinforced carbon-carbon. The results from the simulations agreed with the experimental results. Projectile shape and orientation were found to have modest effects for flat plate projectiles at impact velocities above the ballistic limit.

J. Eftis et. al. [32] developed a set of constitutive-micro-damage equations to model shock compression and micro-damage and fracture resulting from hypervelocity impacts. The

developed equations were developed for polycrystalline materials. Numerical simulations were performed for Aluminum 1100 rectangular plates and spherical soda-lime glass projectiles. The results from the numerical simulations were found to accurately represent the experimental data.

G. Gongshun et. al. [33] studied hypervelocity impact on AL-Whipple shields by 2017-T4 Aluminum alloy sphere projectiles. Different modes of the crater distribution on the rear wall of the AL-Whipple shield were obtained and analyzed. The results showed that with the increase of the projectile diameter, impact velocity, and shielding spacing, the crater distribution increased.

R. Destefanis et. al. [34] conducted a study to improve manned spacecraft shields using different configurations of different materials. The testing results did not show improvement on the debris shields developed by Alenia Spazio for the International Space Station (ISS) manned elements.

M. J. Eller et. al. [35] conducted a study on the interaction of hypervelocity nano-particles with a two-dimensional material and ultra-thin targets, including single layer graphene, multi-layer graphene, and amorphous carbon foils. Projectiles were mass selected gold nano-particles produced from a liquid metal ion source. The ejected area was much larger than the molecular dynamic simulations.

H. Shang and W. Wang [36] studied hypervelocity impact on two graphene armor systems using molecular dynamic simulations: namely spaced armor, which consists of a number of graphene plates, spaced certain distances apart and laminated copper/graphene composites with the graphene layer inside copper, or on the impact or back surface. The first system showed that the penetration resistance increased with a decreased number of layers. The

second system had much higher penetration resistance that increased when the graphene layers were on both the impact and back surfaces.

#### 1.4 Material Background

The main concern for the development of nanotechnology is our ability to understand, model, and simulate the behavior of small structures and to bridge nanostructure's properties and full-scale functions. Material modeling and simulation helps to set the guidelines that could guide material manufacturing development and to control material properties, structures, and processes at physical implementation. In this research, experimental-theoretical approaches were coupled to study the response of nano-composite materials to hypervelocity impact.

In order to protect the space shuttles against the hazard of hypervelocity impact, proper shielding must be employed using the best available materials. When existing materials cannot deliver the desired performance, it is important to introduce a new material. Recent interest in the use of graphene-based nano-composite materials in infrastructure applications requires further investigation. In this research, wide ranges of nano-composites were used, which can be divided into three main categories: Epoxy based nano-composites, PEI based nano-composites, and Polyurea based nano-composites.

##### 1.4.1 Polymers

Three polymers are used in this study. They include:

###### 1.4.1.1 Epoxy

The epoxy used for the production of graphene papers and the roll milled nano-composite was Epoxy resin Baxxores ER 5300 (part A), and amine hardener BAXXODUR EC 5720 (part B) was used as the host polymer. These were purchased from BASF Corporation, NY, USA. The ratio of the epoxy resin (part A) over the epoxy hardener (part B) was 10:3 by weight. The resin has a relatively low viscosity at room temperature. Mixing the resin will

generate small sized bubbles. Thus, the resin is degased until all the small bubbles are removed. Leaving the polymer in the degassing chamber for longer time after the small bubbles are removed will actually generate larger bubbles within the polymer.

This phenomenon happens due to the boil off of the shorter molecular chain of the acid compound. This will cause premature vitrification and nucleation of the polymer. Thus, extra degassing time is not allowed to prevent this phenomenon from happening, as it will result in a weaker finished product.

The curing cycle of this epoxy started at room temperature, then ramped up to 70 °C and held that temperature for six hours. After the six hours, the temperature gradually decreased back to room temperature.

#### 1.4.1.2 Polyurea

PU is classified as an elastomeric material. The toughness and large strain capacity of elastomers can be exploited to absorb a considerable amount of energy during impact or blast events. Elastomers are composed of long polymer chains with some cross-linking or connection by chemical bonds. Cross-linking makes elastomers reversibly stretchable within a significant deformation range. In the un-stretched state, the polymer chains are in random directions. When load is applied, polymer chains elongated and oriented parallel to the loading direction. When load is released, the cross-link sites guide the elastomer back to its original shape as the chains once again randomize. Damping (energy dissipation) is generated during deformation due to the friction of molecules against each other. This behavior is strain-rate dependent. The elastomer used in this study was PU. PU is well known for its high elongation, strength at failure, and superior modulus of elasticity. The PU Part A used in this study is VP1000, which is Versalink P-1000 oligomeric diamine produced by Air Products and Chemicals, Inc., PA, USA, (see Figure 4 (a)). Polyurea Part B Isonate 143L modified



MDI is a polycarbodiimide-modified diphenylmethane diisocyanate, produced by Dow Chemical Company, MI, USA. Typical molecular structure of Isonate used in this study is shown in Figure 4 (b). The PU cures at 80 °C for four hours, with 4:1 mixing of part A to part B by weight.

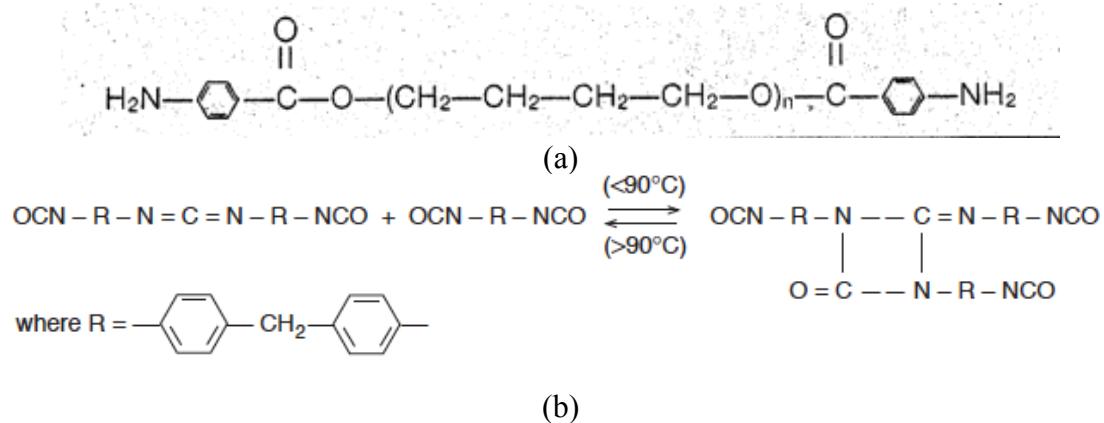


Figure 4: molecular structure of (a) VP1000 (b) ISONATE 143L System

PU monomer is a product of reaction between organic amine and organic isonate. The organic group along with urea linkage form a chain segment that has a high glass transition temperature (called hard segment), and the remaining organic amine group forms a chain segment with lower glass transition temperature (called soft segment).

Due to this complex microstructure, PU shows varying mechanical responses under different loading conditions. Most PU applications are based on its superior ability to harden under applied loading and absorb the kinetic energy associated with the waves generated by ballistic projectiles.

#### 1.4.1.3 Polyetherimide

PEI is a thermoplastic polymer containing cyclic amide. PEI is a polyimide condensation polymer derived from the bi-functional carboxylic anhydrides and primary diamines [42]. PEI has been used as matrix in the fabrication of various composites: PEI/glass fiber composites [43], Nanoparticles coated with PEI-polyurethane (SiO<sub>2</sub>/PEI- polyurethane)

nanofibrous composite membranes [44], Single walled nanotubes (SWNTs)/PEI nanocomposites [45]. Typical molecular structure of PEI is shown in Figure 5. The PEI used in this study was purchased from Sigma-Aldrich. This PEI has a weight-averaged molecular weight (Mw) of 47,000 g/mol.

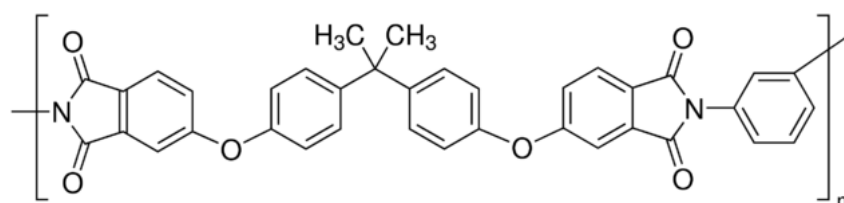


Figure 5: Typical molecular structure of PEI

#### 1.4.2 Nano Materials

In this study, graphene nanoplatelets are used as nano fillers.

##### 1.4.2.1 Exfoliated Graphene Nanoplatelet

The first decade of the 21<sup>st</sup> century has witnessed the development of unprecedented new material technology based on carbon nanotubes, nanowires, nanoparticles, electronic polymers, biopolymers, hybrid plastics, bio-inspired micro-structural composites, and nanoclays. Graphene draws researchers' attention because of its superior mechanical properties (Young's modulus  $\sim 1.0$  TPa [37]), thermal conductivity ( $\sim 5000$  Wm<sup>-1</sup> K<sup>-1</sup>) [38], and excellent electrical conductivity. Such properties can be highly cost effective. The estimate of the graphene nano-platelets cost is \$5/lb or even less [2]. Exfoliated graphene nano-platelet (xGnP) based composites and their fabrication process attracts scientists. Several methods were investigated at NISL in order to fabricate papers and nano-composites with these outstanding properties, trying to mimic the biomaterials unique layer-by-layer structures such as bone, teeth and nacre.

xGnP provides functionalization possibilities. One of the most famous examples is the graphite oxide, which offers potential for cost-effective, large-scale production of graphene-

based materials [39]. The oxidation process enhances the mechanical properties despite the presence of defect content. Oxidized graphene single sheets exhibit an extraordinary elastic modulus, approaching the pristine graphene value [40].

Recently, research has been reported that xGnP could also be used as nano-reinforcements in polymer systems. The xGnP are expected to be marketed at an approximately low price once high demand and full production is achieved. This cost will be significantly less than carbon nanotubes, yet the mechanical, electrical, and thermal properties of xGnP are comparable to those of carbon nanotubes. Thus, these xGnP could be an alternative, cost-effective material for carbon nanotubes. The use of xGnP opens up many new possible applications where electrical conductivity, electromagnetic shielding, gas barrier resistance, high thermal conductivity, high fracture toughness, or low flammability is required. The addition of xGnP to a polymer is expected to provide an enhancement of the properties of the polymer matrix by optimizing the adhesion of xGnP to the matrix. Figure 6 shows the morphology of xGnP.

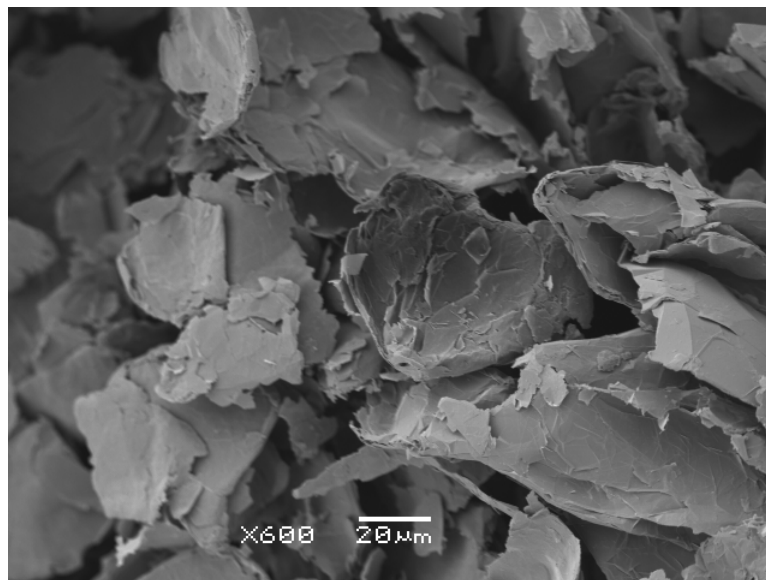


Figure 6: SEM image shows the morphology of xGnP

These nano platelets are typically less than 5 nm thick and can be synthesized with lateral dimensions ranging from less than 1  $\mu\text{m}$  to up to 100  $\mu\text{m}$ . xGnP reinforcements are expected to influence the performance of polymeric material.

The xGnPs used in this research have diameters of 50  $\mu\text{m}$ , and they were bought from XG Sciences Inc., Lansing, MI, USA. Pristine graphenes were heated in the oven at 500  $^{\circ}\text{C}$  for five hours before using, in order to remove any moisture and possible impurities prior to use.

The morphology of xGnP is hypothesized to have major benefits to hypervelocity particle capture and containment. Thus, the creation of a multilayered structure at the nano level by using suitable array of very thin layers nano-composite layers could have the potential to achieve the capture and confinement of cracks upon impact by combining the crack arresting capability and energy absorption properties of the xGnP through the mortar-brick arrangement of the nano particles.

This research proposes to manufacture graphene-based nano-composites that vary, xGnP loadings, host polymer, platelets orientation, and surface treatment of the platelets, in order to produce a nano-engineered structure for hypervelocity particle capture and confinement, an optimized material structure capable of achieving the confinement metrics, and desired capture with a low areal density is expected to be produced.

### 1.5 Characterization Techniques

Multiple characterization techniques were investigated. Chemical properties like the crystallinity and functional groups are of great importance; such properties could be determined using XPS and Raman spectroscopy. AFM and SEM imaging techniques can be beneficial to get an idea about the dispersion of the xGnP or OxGnP in the host resin and the alignment of the platelets.


The extraction of mechanical and physical properties of the materials that are manufactured could be very beneficial in understanding the way they behave. Properties like tensile strength and elongation are of great importance in determining the fundamental characteristics of a material. A universal testing machine can be employed to get these properties. The dynamic mechanical analysis could be used to provide stress/strain curves, storage modulus, loss modulus, and the glass transition temperature. SHPB can be used to get the strength, and elongation of the material at high strain rates. This research discusses new fabrication methods for xGnP nano-composites both pristine and oxidized, using several host polymers, and will determine the physical, chemical and mechanical properties, which will be discussed and compared to each other.

#### 1.6 Finite Element Analysis

Elastic -plastic constitutive laws can be developed based on the mechanical properties; these laws can be used inside finite element analysis code for analyzing the large deformation associated with hypervelocity impact. Autodyn software will be used for this study.

Explicit dynamics can be used to study a wide range of events at high strain rates involving impact and blast loadings. An explicit solution provides the most efficient and accurate method for computing material response at high strain rates (see Table 2).

Table 2: Impact response of material

Solution	Impact Velocity (m/s)	Strain Rate (1/s)	Effect
Implicit  Explicit	< 50	$< 10^{-5}$	Static / Creep
	50 - 1000	$10^{-5} - 10^{-1}$	Elastic
	1000 - 3000	$10^{-1} - 10^1$	Elastic-Plastic (Material strength significant)
	3000 - 12000	$10^5 - 10^6$	Primarily Plastic (Pressure equals or exceeds material strength)
	> 12000	$10^6 - 10^8$	Hydrodynamic (Pressure many times material strength)
		$> 10^8$	Vaporization of Colliding solids

### 1.7 Objectives

- Manufacture Nacre-like nano-composites from exfoliated graphene nano-platelets for hypervelocity impact protection.
- Explore the effect of oxidation on multi-functional properties of the manufactured xGnP paper/composite.
- Investigate the effect of xGnP loading on xGnP nano-composite properties, including chemical, thermal, mechanical, electrical and surface properties. Also, understand the effect host polymers have on these properties.
- Determine the shielding efficacy of the produced materials and systems numerically, using finite element hydrodynamic code.
- Develop constitutive models to represent material behavior at high strain rates.
- Conduct a sensitivity analysis of the constitutive models constants to determine relevant material parameters that affect shielding performance.

## 2. METHODOLOGY

The overall research program is summarized in the following figure.

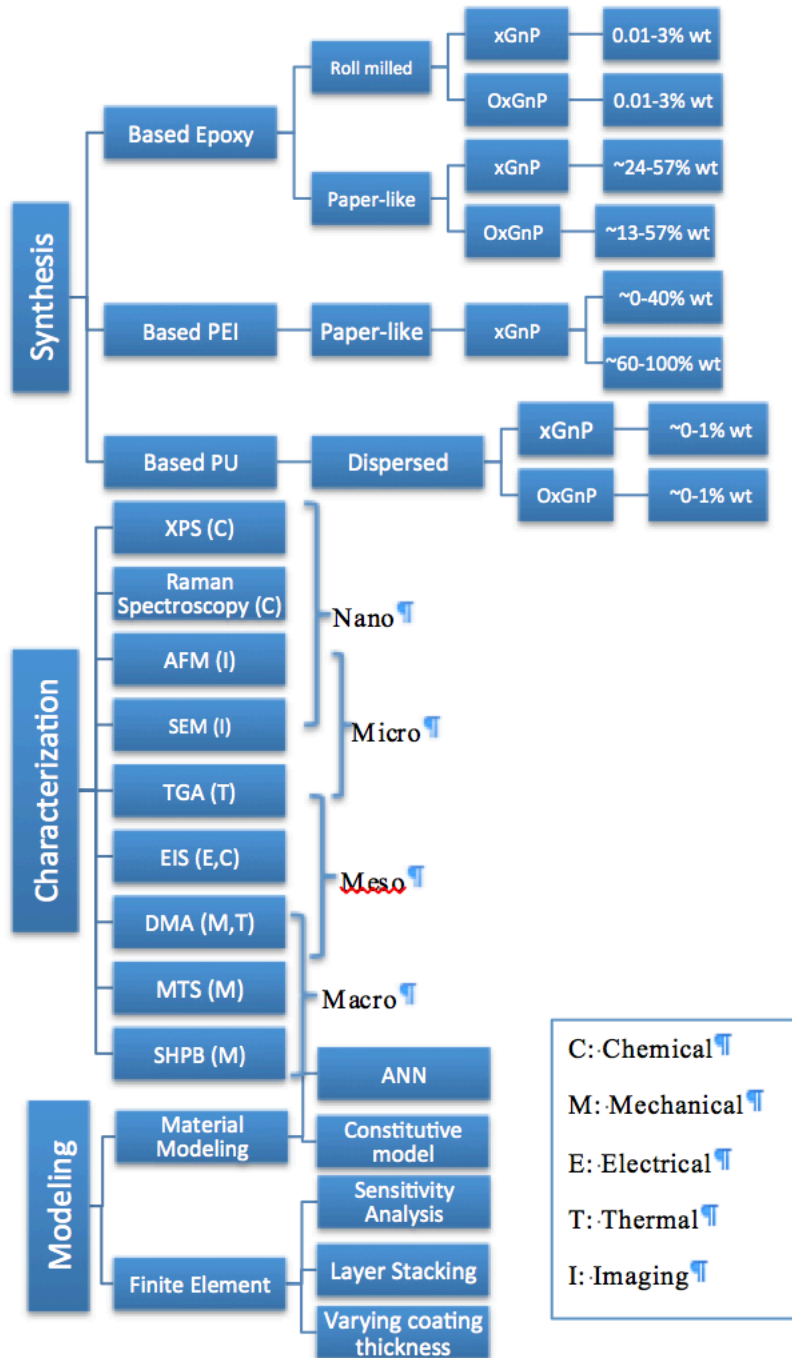


Figure 7: Research Program

## 2.1 Approach

This research starts with the pre-testing phase, to determine the parameters that will be used to develop material strength model and the EoS that will be used in the simulation. Characterization of tested materials includes multiple experimental techniques discussed in detail in the following sections.

This research introduced new methods used to manufacture paper-like graphene sheets and nano-composites at different concentrations. After determining the material parameters, finite element simulation will be conducted. Autodyn software was implemented in this study. SPH meshing technique was used in order to avoid problems with severe mesh tangles and distortions associated with the traditional Lagrangian meshing technique. The task of this study is to conduct a parametric study of the manufactured graphene based nano-composites.

## 2.2 Manufacturing processes

Several manufacturing processes are being considered for making the xGnP or OxGnP nano-composites. Some processes produce a paper-like composite with thickness below 0.2 mm. Other processes produce moldable thicker nano-composites. The mold dimensions can control the thickness and final shape of the produced nano-composite. Further details are in section 2.2.2.

### 2.2.1 xGnP functionalization

A paper published by Grayfer et al. referred to functionalization by oxidation [8]. A certain amount of xGnP was mixed with concentrated sulfuric acid (95% or higher) and nitric acid (70%). The volume ratio of sulfuric acid to nitric acid was 3:1. The whole mixture was magnetically stirred in a three-neck glass flask and heated to 70 to 90 °C for a period ~ 9hours. The acid vapor was condensed and refluxed by a water-condenser on the flask during the entire reaction process. The amount of xGnPs relative to acids was typically 1g xGnP of



to 100 ml of the acids mixture. A few trials were conducted to find out that this ratio of xGnP to total volume of acids is sufficient. XPS results in section 2.3.1.1 confirm that xGnP was effectively oxidized. After reaction, the resulting mixture was filtered through PTFE porous film, pulling acid with a water-jet vacuum. The collected xGnPs were re-dispersed in about 500ml-distilled water, stirred and sonicated for 1 minute, then filtered. After 5 cycles of water washing, sonication, and filtration, the filter paper was switched to Whatman quality filter paper for 5 additional cycles of water washing, sonication and vacuum filtration to complete the purification. However, one piece of porous PTFE needed to be placed on the Whatman filter paper for easy peel-off from the OxGnP after drying. The purified OxGnP were dried in the oven at 70 °C for 1 hour. Overheating is not recommended for OxGnP, as heat causes loss of the introduced oxygen groups.

The xGnP is hydrophobic by nature, while the grown oxygen groups changed the graphenes to be hydrophilic. Section 2.3.1.1 and section 2.3.1.2 discuss the effect of oxidation and the effect of heating over OxGnP. XPS results were analyzed for identification of the oxygen groups.

Preliminary DMA results in Figure 8 show that the modulus of oxidized graphene paper increases by over 800% from the pristine graphene paper (simply pressing the xGnP and OxGnP at 4 MPa for 5 minutes produced these papers). This increase should be attributed to the interaction from oxygen groups. If a binder polymer is properly infused between xGnP, the formed graphene/polymer nano-composite may exhibit enhanced properties. The manufacturing processes of these composites are discussed in section 2.2.2

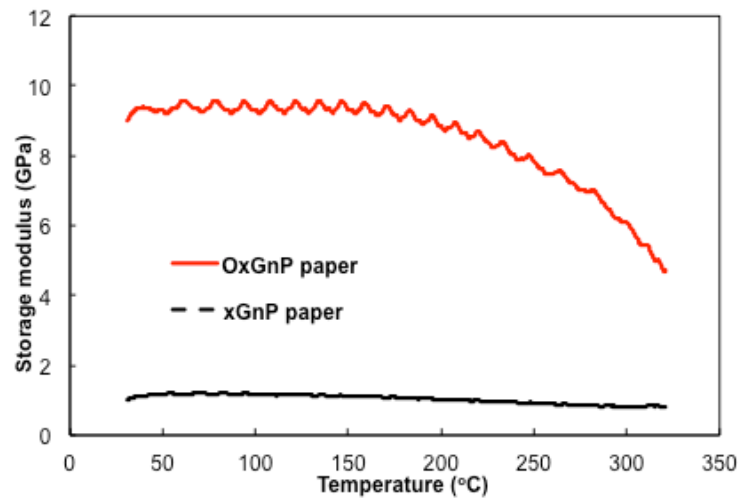


Figure 8: Storage moduli for xGnP and OxGnP papers

## 2.2.2 Manufacturing the nano-composites

Nano-engineered composite materials offer the possibility of achieving the desired performance by introducing nanoparticles that are controlled in their concentration and orientation in the host polymers. An example of natural material that shows high toughness and low modulus is Nacre (Sea shell-Mother of Pearl). In this research, a bio-inspired material that utilizes graphene nano platelets nano composites has been used. However, adding nano particles to polymeric materials may not improve their strength, but it will show improvement in other properties.

The xGnP or OxGnP nano-composites were manufactured based on three hot polymers; each host polymer has different properties. The nano-composites production process optimized depending on the host polymer. Details are discussed in the following sections.

### 2.2.2.1 Epoxy based xGnP or OxGnP

Two different manufacturing processes are being considered for making the xGnP-based epoxy nano-composite. The first process produces a paper-like nano-composite based on pressing pressure; the resulting paper has a thickness of  $\sim 0.2$ mm with high graphene loading  $\sim 20$ -57%.

The second process is based on shear mixing by three-roll mill. This method produces a lower percentage of graphene up to 3% by weight, producing a moldable xGnP-Epoxy.

#### 2.2.2.1.1 xGnP or OxGnP roll milled epoxy nano-composite

A three-roll mill was used to disperse and exfoliate the xGnP or OxGnP nanoparticles in the epoxy (see Figure 9). First, epoxy part A (Baxxores ER 5300) and either xGnP or OxGnP were weighed and mixed together. The mixture was stirred for three minutes and then placed between the feed and the center rolls. Once the rolls started moving, the platelets were spread gradually in the resin. The shear forces generated between the adjacent rolls achieved the dispersion. Shear mixing was carried out at room temperature with a rotation speed of 700 rpm; 10 passes were applied to get good platelets dispersion in the epoxy. It was observed that the solution became viscous and opaque as the graphene dispersed with each pass. The final product from the milling was collected and mixed with the hardener (BAXXODUR EC 5720). After adding hardener and mixing for three minutes, the solution was left for 15 minutes in the vacuum chamber for degassing. After degassing, the solution was cast in silicon molds and cured in an oven at 70 °C for 6 hours, according to manufacturer's recommendations. Nano-composites were prepared with either xGnP or OxGnP with loadings from 0.01% to 3% by weight.



Figure 9: Three-roll mill dispersing xGnP

#### 2.2.2.1.2 xGnP or OxGnP based epoxy papers

Preparing graphene-based epoxy nano-composite by simple mixing can be achieved. However, it is hard to achieve high graphene content in epoxy because uncured epoxy resin is often viscous, and the graphene has a high surface area but very low bulk density. Mixing these two at high graphene loading is a real challenge. To get around this challenge, a pressure pressing technique was developed, as discussed below.

Six grams of either xGnP or OxGnP was exfoliated in 1000 ml distilled water, with ~1 g of PEI surfactant to enhance the exfoliation of the platelets. The mixture was stirred overnight in a one-neck glass flask and then subjected to a 5 minute sonication bath.

Afterward, the suspension was vacuum-filtered at vacuum pressure equal to -66 cm mercury through a porous Teflon glass fiber fabric, to obtain a graphene-PEI cake. The Teflon fabric was purchased from Northern Composites, Inc., Hampton, NH, USA. The cake was then dried in an oven at 340 °C for 1 hour to allow the water to evaporate and decompose the remaining PEI. However, the OxGnP was heated at 120 °C to prevent the loss of oxygen groups upon excessive heating. The heating effect on OxGnP is discussed in section 2.3.1.2.

The dried xGnP or OxGnP cake was placed between two porous Teflon papers and then placed on a filtration system (see Figure 10), which is connected to a vacuum pump.

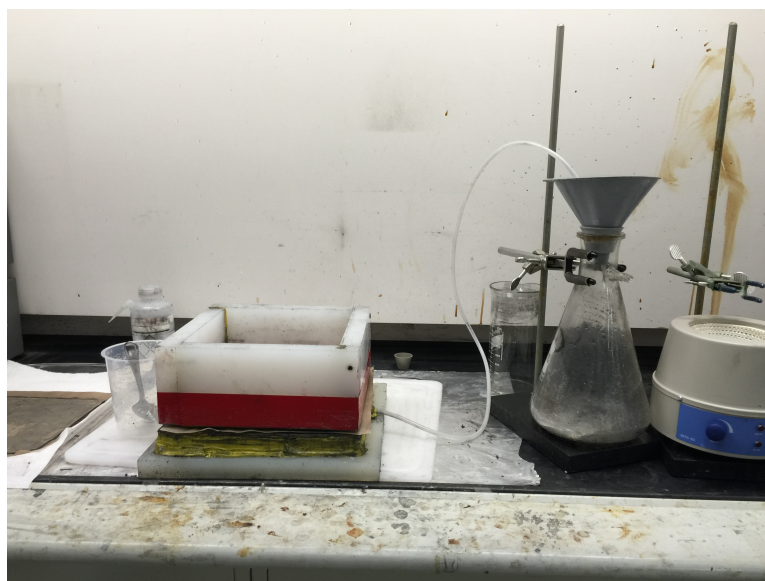


Figure 10: Vacuum filtration system used to infuse epoxy between xGnP or OxGnP

Then, a certain amount of epoxy is poured over the xGnP or OxGnP cake (Figure 11), and a vacuum was run to remove excessive epoxy and force it to infuse between the platelets. The epoxy infusion system used has a very low viscosity, which allows it to infuse smoothly between the platelets. After epoxy filtration, the graphene cake with the Teflon paper were sandwiched in two layers of absorbent papers and then clamped with two aluminum panels for pressing. The press equipment was a Carver hydraulic compression press (Model 5401, Carver, Inc., IN, USA). The press equipment has a maximum clamping force of 48 tons and can heat up to 350 °C (see Figure 12). The release agent for de-molding after pressing was 44-NC™ (Northern Composites, Inc., Hampton, NH, USA). By varying the applied force during the pressing time, we got different pressures based on the area of the sample. The pressure was applied for 5 minutes at room temperature. The pressures used were 0.25, 0.5, 1, 2, and 4 MPa for both xGnP and OxGnP.

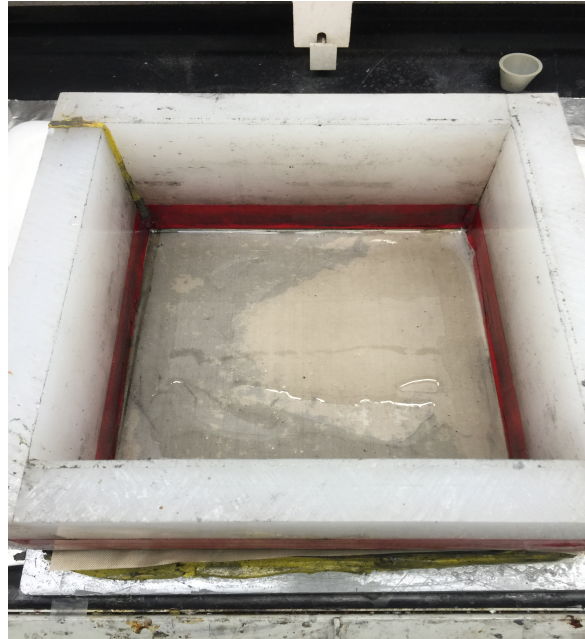


Figure 11: Epoxy poured on xGnP cake.



Figure 12: Carver hydraulic compression press

Varying the pressure can control the epoxy percentage, pore content, and alignment of the platelets in the manufactured papers. Following pressing, the papers were cured in an oven at 70 °C for 6 hours according to manufacturer recommendations. Both xGnP or OxGnP prepared papers have high percentages of graphene (see Figure 13). The percentages of graphene in the manufactured papers were obtained from TGA; further details are in section

2.3.3.1. The percentage of xGnP ranged ~24-57 wt. %. However, for OxGnP, the range was ~13-57 wt. %.

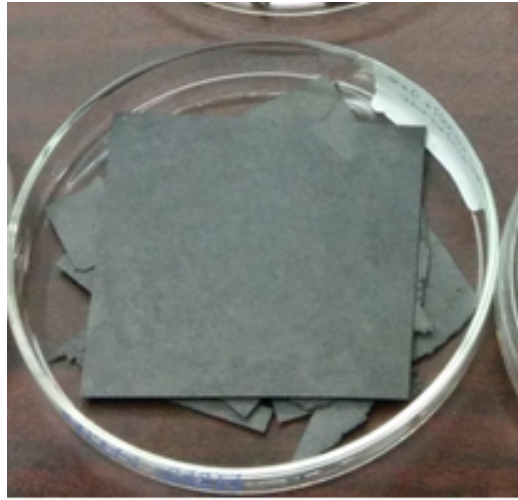


Figure 13: xGnP paper after curing

#### 2.2.2.1.3 Laminating Based Epoxy Papers

The xGnP papers were fabricated by following the procedure reported in the previous section. In order to achieve a thicker nano-composite, lamination is suggested. The lamination procedure is discussed below.

The fabricated papers were placed on top of each other ~10 papers, then placed in a container. Epoxy part A mixed with part B was poured onto them and placed into the degassing chamber for 10 minutes. Then the stack was removed and sandwiched between porous coated fabrics and a breather cloth, then placed in a vacuum bag. The vacuum bag was sealed carefully to make sure that there would be no leakage.

Once everything was ready the vacuum bag was connected to the vacuum pump, the vacuum pre-consolidated the excess resin. Thus pressure induced on the laminated composite will give us bubble free composite. The stack then cured at the proper curing time and temperature as recommended by the epoxy supplier. The temperature was ramped from room

temperature to 70 °C and remained at 70 °C for 6 hours. At the end of curing cycle, the stack was removed carefully and allowed to cool down.

#### 2.2.2.2 xGnP based PEI

PEI is a thermoset polymer with melting temperature around 350 °C. This temperature is above the temperature that cause loss of the introduced oxygen groups in OxGnP. Thus OxGnP-PEI cannot be manufactured, as the host polymer has to be heated up to 350 °C for molding.

The next two sections discuss two different manufacturing processes to produce xGnP based PEI nano-composite. The first process produces a paper-like nano-composite by utilizing solvent followed by precipitation in distilled water. The resulted paper has low graphene loading ~0-40%. The second process employs Filtration/hot press. This process is capable of producing a higher percentage of graphene up 100% by weight.

##### 2.2.2.2.1 Low concentration xGnP based PEI

Low concentration xGnP-PEI nano-composites in the range of 0-40 wt. % xGnP can be easily achieved by mixing xGnP with the PEI in the PEI/DMAc (DMAc was purchased from Fisher Scientific) solution followed by precipitation in distilled water (see Figure 14).



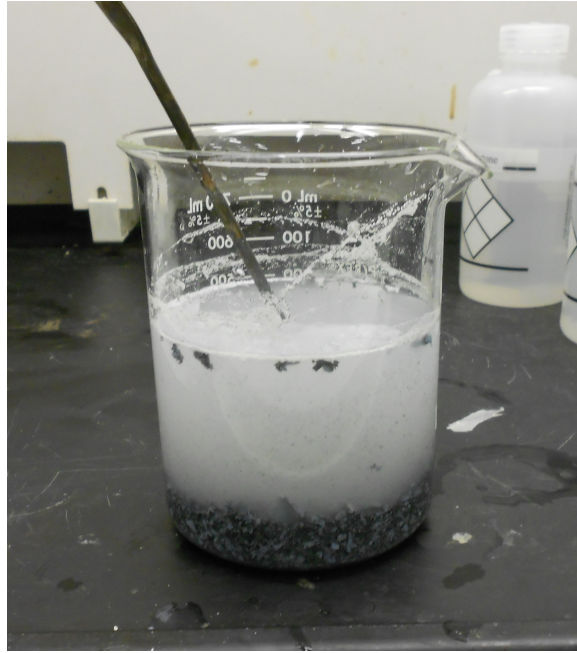
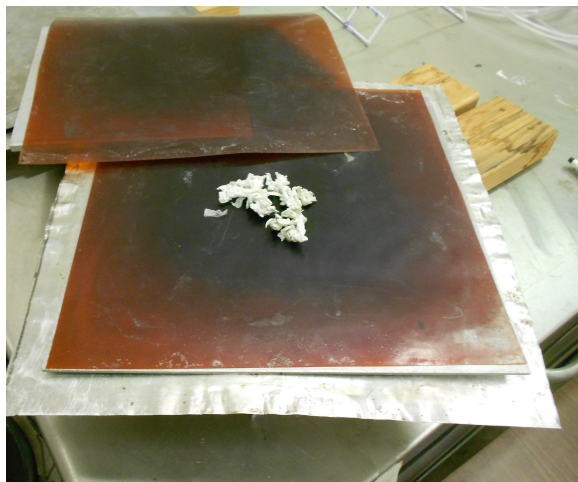
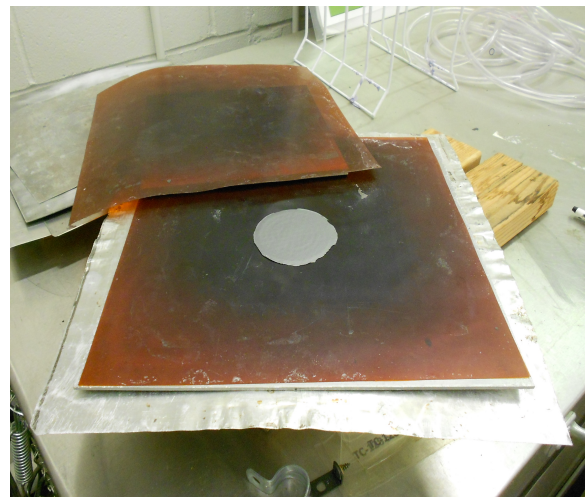


Figure 14: xGnP-PEI precipitation in distilled water

The precipitated mixture dried in an oven at 190 °C for 1 hour to remove the DMAc and was then hot-pressed at 350 °C to make composite films (see Figure 15). This process includes hot pressing at high temperature. Thus, OxGnP-PEI nano-composite cannot be manufactured as increasing the temperature of OxGnP above 120 °C will cause loss of the functional groups.



(a)



(b)

Figure 15: xGnP-PEI (a) precipitation before pressing; (b) paper after pressing

#### 2.2.2.2.2 High concentration xGnP based PEI

To achieve higher concentration of xGnP in the xGnP-PEI Papers (60-100 wt. %), a filtration/hot press procedure was followed. The mixture of 0.5 g xGnPs and 50 ml DMAc was stirred in a 250 ml one-neck glass flask for 5 minutes and then subjected to a 1 minute bath sonication. Certain amounts of PEI (1-5 g) were added. While being stirred and quenched with a condenser, the mixture of xGnPs, PEI and DMAc was refluxed for half an hour. After being cooled to room temperature, the suspension was vacuum-filtered using the filtration system shown in Figure 16, (vacuum pressure: -66 cm mercury) through a porous Teflon fabric to obtain a xGnP-PEI cake (see Figure 17), which was then heated in an oven at 190 °C for 1 hour to allow the DMAc to evaporate. The dried xGnP-PEI cake was placed between two ultra-high temperature Kapton polyimide (PI) films (thickness: 0.127 mm; upper use temperature of 399 °C, bought from McMaster-Carr, Atlanta, GA) that were used as the inner liner in the mold. These PI films were sprayed with the release agent and then clamped with two aluminum panels for hot pressing. Hot pressing pressure of 10 MPa was controlled based on the applied load and the area of the sample. The pressure was applied for 4 minutes duration at 340 °C. The pressed paper was then lightly pressed a second time (about 3 MPa, 1 min and 340 °C) in order to smooth the final xGnP-PEI paper. In addition, neat PEI paper or pure xGnP paper was produced by the same hot pressing method described for xGnP-PEI paper.

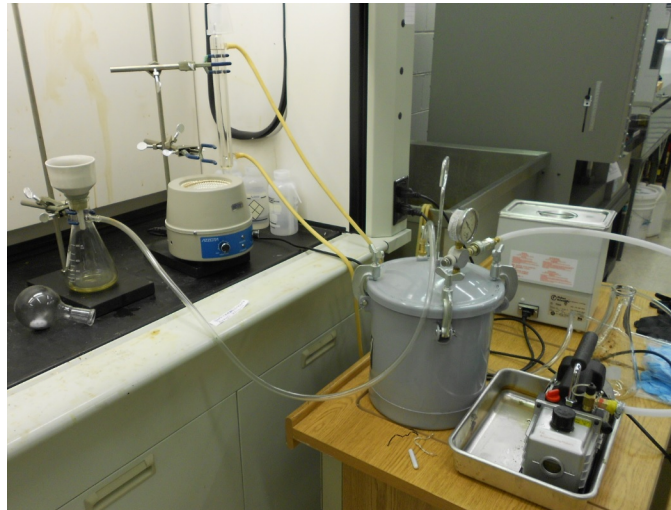


Figure 16: Filtration system used for manufacturing

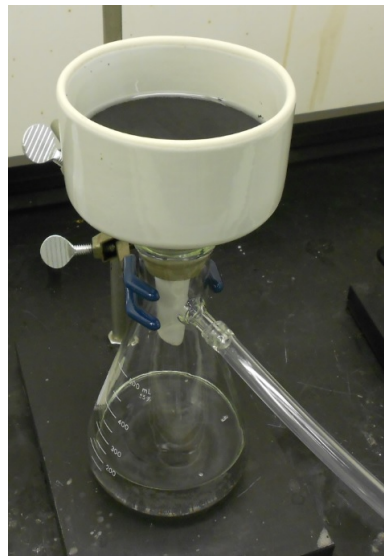


Figure 17: Filtered xGnP-PEI cake

#### 2.2.2.2.3 Laminating xGnP-PEI films

The previous two sections describe the procedure to produce xGnP-PEI thin films (~0.1 mm) with various xGnP concentrations. In order to obtain thicker nano-composite, stacking, heating and pressing can be employed, as PEI is thermoplastic polymer. In this xGnP-PEI lamination process, enough xGnP-PEI films were stacked and pressed together under 2 MPa at 312 °C for about 1 minute. Thick aluminum bars were used as spacers to control and achieve the desired thickness.

#### 2.2.2.3 Polyuria based xGnP or OxGnP

Either xGnP or OxGnP based PU were manufactured successfully with graphene loading up to 1% by weight.

#### 2.2.2.3.1 Low concentration xGnP or OxGnP based PU nano-composite

The right amount of either xGnP or OxGnP was dispersed in 150 ml acetone in a beaker assisted by sonication to break possible graphene agglomerations. During sonication, the beaker was sealed. Then 80g VP1000 diamine was dissolved in acetone and added to the mixture with stirring and sonication (1-2 minutes). The whole mixture was then heated to about 70 °C to evaporate the acetone overnight in a hood. Then 20 g diisocyanate, 143 L isonate, was transferred to the mixture followed by quick mixing in about 1-2 minutes. The mixture was transferred into a Teflon mold with controlled spacing, and then cured in oven at 80 °C for 4 hours; the xGnP-PU nano-composite could be de-molded and cut into desired shape (see Figure 18). In this study, the dynamic properties of the PU based nano-composite were the only property investigated.

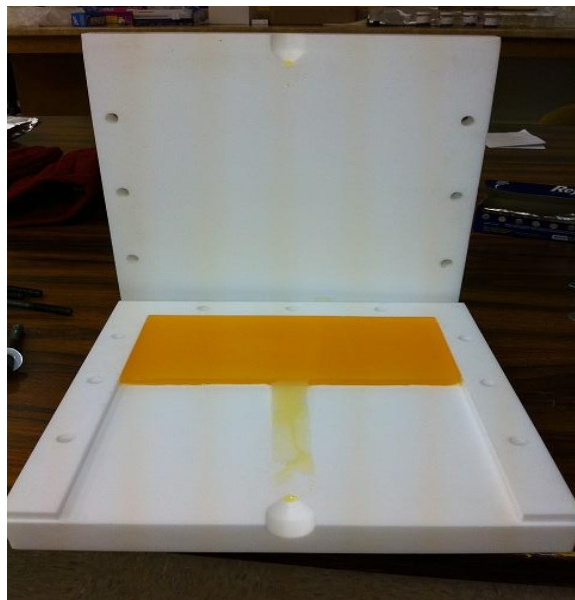


Figure 18: PU in Teflon mold after curing

## 2.3 Characterization

### 2.3.1 Chemical properties

Surface chemical properties of the manufactured nano-composites including crystallinity, functionalization, and details are discussed in the following two sections.

### 2.3.1.1 X-ray Photoelectron Spectroscopy

XPS is a surface-sensitive quantitative spectroscopic technique that measures elemental composition. XPS spectra are obtained by irradiating a material with a beam of X-rays while simultaneously measuring the kinetic energy and number of electrons that escape from the surface of the material being analyzed. XPS surface chemical analysis was used to analyze the surface chemistry of xGnP in its pristine state and after functionalization (OxGnP).

XPS spectrum is a plot of the number of electrons detected versus the binding energy of the electrons detected. Each element produces a characteristic set of XPS peaks at characteristic binding energy values that directly identify each element that exists on the surface of the material being tested. These characteristic spectral peaks correspond to the electron configuration of the electrons within the atoms. The number of detected electrons in each of the characteristic peaks is directly related to the amount of element within the sampling volume. To generate atomic percentage values, each raw XPS signal must be corrected by dividing the number of electrons detected by a relative sensitivity factor and normalized over all of the detected elements. Since hydrogen is not detected, these atomic percentages exclude hydrogen. The XPS analysis was carried out with a Phi 5400 ESCA system with a magnesium K  $\alpha$  X-ray source at pressure between  $1.33 \times 10^{-6}$  and  $1.33 \times 10^{-5}$  Pa with pass energy of 29.35 eV and a take-off angle of  $45^\circ$ .

OxGnP were analyzed using XPS to investigate the effect of oxidation on surface chemistry, compare xGnP and OxGnP, and then study the associated chemical bonds. An overall scan reveals specimen atoms, and a regional scan of an element will show the neighboring chemistry and chemical bonds linked. Figure 19 (a) and (b) compare the overall scans for

xGnP and OxGnP, which shows that the oxygen content in OxGnP's was increased by functionalization. The pristine graphenes value were around 3-4 % oxygen because of the presence of defect sites that are extremely active and instantly capture oxygen from air to form various oxygen groups [46].

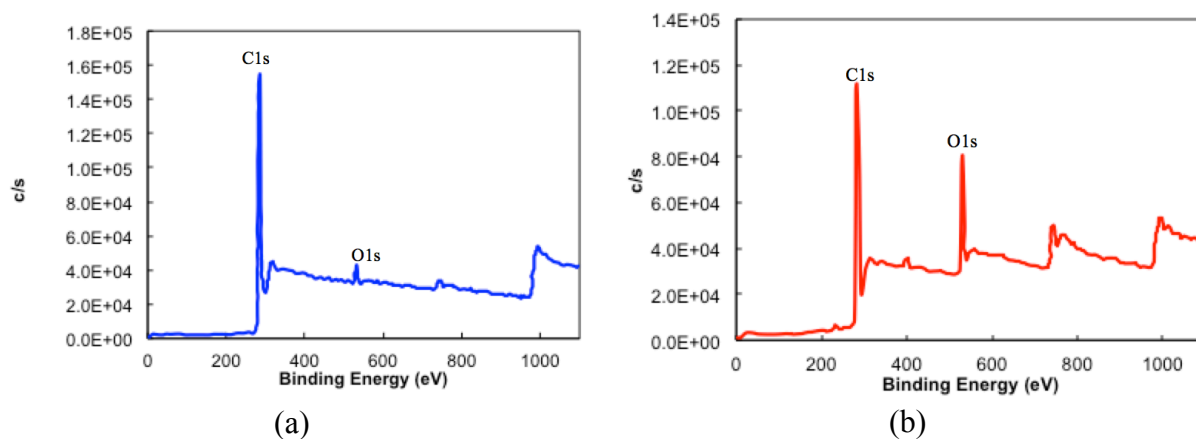


Figure 19: Overall XPS for (a) xGnP (b) OxGnP

In Figure 20 (a) and (b), the C 1s peaks in the XPS spectra are deconvoluted to analyze chemical bonds on the graphenes. The sub-peak 1 comes from  $sp^2$  carbon, which is graphitic. This type of carbon forms the basic hexagonal structure of graphenes. The others are hybridized carbons, one s orbital and three p orbitals are hybridized, that have four valences ready to form covalent bonds with another type of atom, which is oxygen in this research. The sub-peak 1 is at the lowest position because other carbons adjacent to oxygen are stronger in trapping electrons. Therefore, other sub-peaks appear at higher electron-binding energy locations.

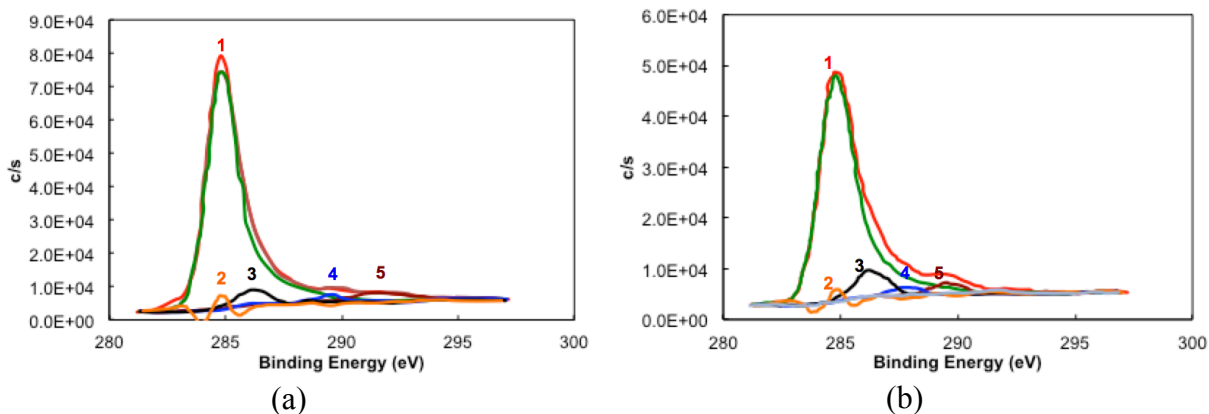


Figure 20: The C1s peaks in the XPS spectra of (a) xGnP (b) OxGnP

Upon close inspection, there is a small difference in position between oxygen groups that have different capabilities to trap electrons. This difference can be analyzed by the deconvolution of the main peak to identify specific chemical bonds. Figure 20 summarizes the chemical bonds for xGnP and OxGnP, were the C1s peak position and the percentage of carbon atoms, based on total carbons, allocated to various functional groups. Sub-peaks correspond to the deconvoluted peaks.

The decline of  $sp^2$  carbon atoms from xGnP to OxGnP was only 2%, which was very small. It confirmed that the oxidation did not convert xGnP to graphite oxide GO. From previously published research [47] [48], peak 2 arises from hydroxyl and epoxy groups (C-OH and C-O-C). Carbonyl groups (ketone C=O, acid anhydride O=C-O-C=O) contribute to peak 3. Peak 4 is assigned to carboxyl groups (-COOH and 2-pyrone). The  $\pi-\pi^*$  is called a satellite peak [49]. The results indicate that after oxidation by acids, more oxygen groups were introduced onto graphenes, which would allow for versatile further chemical treatment for various applications. The qualification and quantification of functional groups explain the weight loss from TGA test shown in section 2.3.3.1. At higher temperatures, the majority of these groups were removed/de-functionalized.



Table 3: Percentage of carbon atoms allocated to several functional groups.

Deconvoluted peak	C1s sub-peak binding energy (eV) (bond-allocated carbon concentration [atomic%])				
	1	2	3	4	5
Functional groups	C=C-C ( $sp^2$ )	C-O/ C-O-C	C=O	O-C=O	$\pi-\pi^*$
xGnP	284.78 (87.74)	286.28 (4.03)	287.78 (0.96)	289.58 (1.81)	291.49 (5.46)
OxGnP	284.74 (85.07)	286.24 (7.93)	287.74 (2.25)	289.58 (3.53)	291.49 (1.22)

### 2.3.1.2 Raman spectroscopy

Raman spectroscopy is a spectroscopic technique based on the scattering of monochromatic light from a laser source. The frequency of photons in monochromatic light changes upon interaction with a sample. Photons of the laser light are absorbed by the sample and then reemitted. Frequency of the reemitted photons is shifted up or down in comparison with original monochromatic frequency, which is called the Raman effect. This shift provides information about rotational vibrational and other low frequency transitions in molecules. A sample is normally illuminated with a laser beam. Scattered light is collected with a lens and is sent through spectrophotometer to obtain Raman spectrum of a sample. It is easy to understand the Raman spectrum of crystals with identical atoms all in the same configuration. In these cases, you often see just one dominant Raman band because there is just one molecular environment of the crystal. Thus Raman spectroscopy is particularly well suited to molecular morphology characterization of carbon materials. The Raman spectrum at every band corresponds directly to a specific vibrational frequency of a bond within the molecule. The vibrational frequency and hence the position of the Raman band is very sensitive to the orientation of the bands and weight of the atoms at either end of the bond. In this spectroscopy characterization, a Horiba Scientific LabRAM Aramis Raman was used with an Nd-YaG laser as the source illumination. A spectrometer with a 532.15 nm laser was used. The laser spot size used in our experiment was 2-3  $\mu\text{m}$ , confocal hole diameter 400  $\mu\text{m}$ ,



diffraction grating 1800 g/mm; the region scanned was 100 to 4000 nm; the exposure time was 15 s; and eight different locations were selected in the test.

xGnP has G' or what is called 2D-band from the disorder portion and G-band peak from the graphitic portion. xGnP and the OxGnP mixed with PEI surfactant and heated up to 350 °C both got a G-peak position at ~1576 which means the simple mixing of xGnP with PEI surfactant and heating at 350 °C did not change the chemistry or chemical bonds in graphene.

Comparing the peak of OxGnP with that of xGnP, the up-shift proves the impact of oxygen functional groups. Also, the split upper shoulder for OxGnP confirms that the oxidation functionalization succeeded. However, the disappearance of this shoulder for OxGnP/PEI indicates that the heating at 350 °C caused some loss of oxygen groups (see Figure 21(a)). Closer examination of the G-band peaks shows clear difference between OxGnP and xGnP, not only the shift but also the upper shoulder caused by the introduced functional groups.

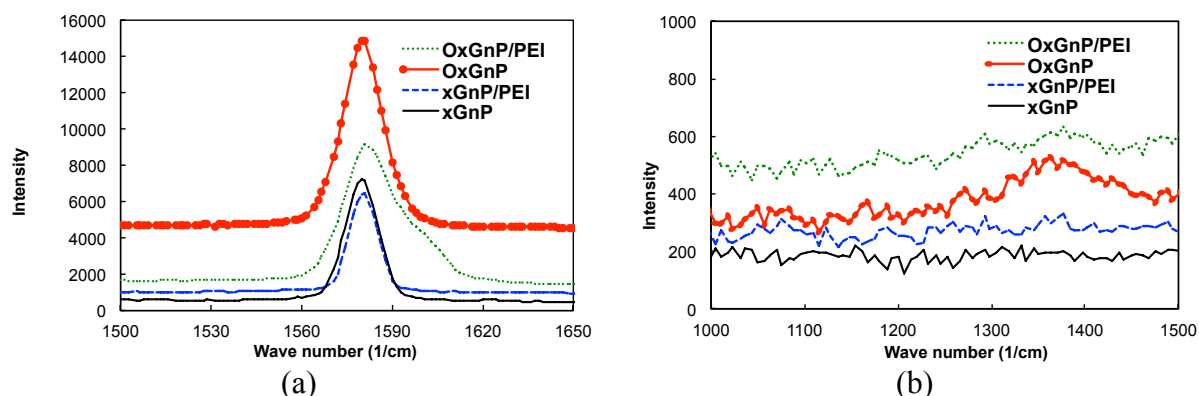


Figure 21: Raman results comparison (a) G-band peak (b) D-band peak

The rise of a 2D-band peak for OxGnP compared with xGnP around 1368 further confirms the functionalization success and introduction of oxygen groups (see Figure 21(b)). The lack of this peak for the xGnP and xGnP/PEI shows that both are highly crystalline.

Raman spectra for OxGnP look very different from GO from previously published research [50] [51] (Figure 22). The oxidation process using concentrated acids only attached some oxygen groups at the platelet's surface. However, the graphitic structure essentially remains

intact. Raman result is in agreement with XPS results shown in section 2.3.1.1, which shows very little loss in graphitic carbon atoms ( $sp^2$ ).

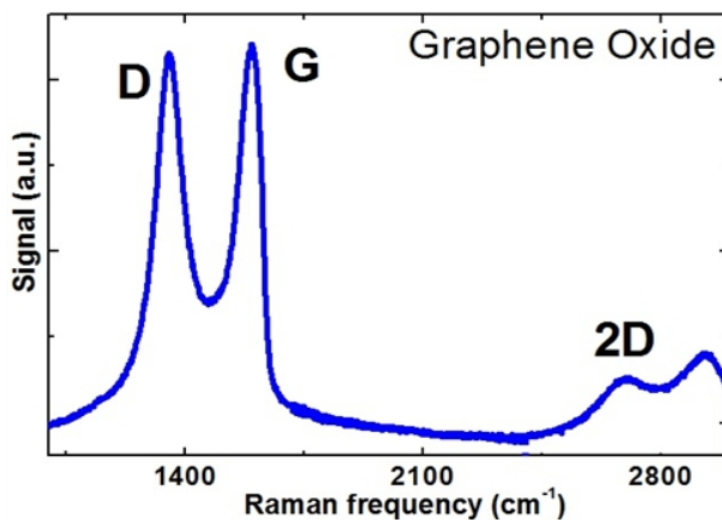


Figure 22: Typical Raman spectra for GO

## 2.3.2 Imaging

### 2.3.2.1 Atomic Force Microscope

The Atomic Force Microscope is a kind of high-resolution scanning probe microscope; the resolution is on the order of fractions of a nanometer. The AFM is able to measure local properties. The probe moves over a small area of the sample surface, measuring the property simultaneously. Scans were obtained with a Bruker MultiMode (MMAFM-2) AFM in tapping mode. The image resolution was 512 samples/line, and the scan rate was 0.8 Hz. The scan size was 5 x 5  $\mu\text{m}$ . The AFM scans shows that the OxGnP (Figure 23 right) has more conglomerations compared with xGnP (Figure 23 left), which shows a smoother surface.

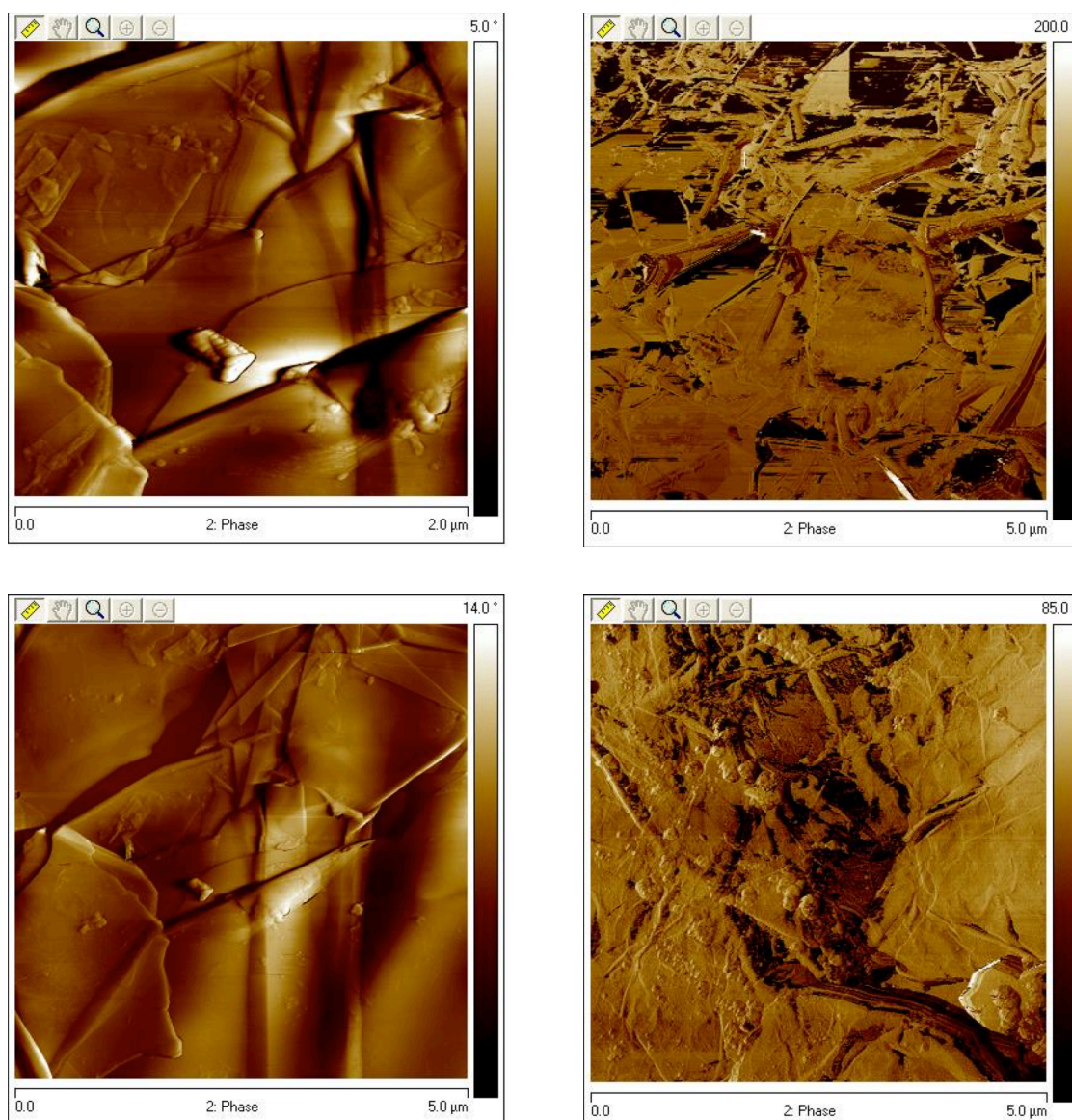


Figure 23: AFM phase scan of xGnP (left) and OxGnP (right)

Another AFM scanning technique was implemented using a DNISP nanoindentation probe (242.38 N/m average spring constant). Both xGnP and OxGnP were scanned. The platelets were pressed and attached with double-sided tape to a 12 mm diameter sample disk. The samples were scanned at a time where the ambient noise/vibrations were greatly reduced. Scanning parameters were varied for each image to get the best possible quality. In general, the AFM parameters were adjusted so that the best topographic image could be obtained.

In Figure 25, Figure 26 and Figure 27 the image sizes are, from top down, 80  $\mu\text{m}$ , 40  $\mu\text{m}$ , 20  $\mu\text{m}$ , and 10  $\mu\text{m}$ . A J scanner was used, and it is not necessarily suited for smaller scan sizes. The green squares represent the area that was in focus of the next smaller image. In some cases, these image insets are not perfectly square even though the smaller image is. This is most likely due to hysteresis of some sort.

Figure 25 shows the comparison between xGnP and OxGnP of the 2D height. Figure 26 compares the amplitude error, and Figure 27 compares the phase. By looking at Figure 25, it can be seen that the smaller scans show some possible indication of noise in the OxGnP images. This phenomenon is highlighted with green circles in Figure 24. It is unclear at this point if these dark spots are noise or part of the topography that is not picked up by larger scans.

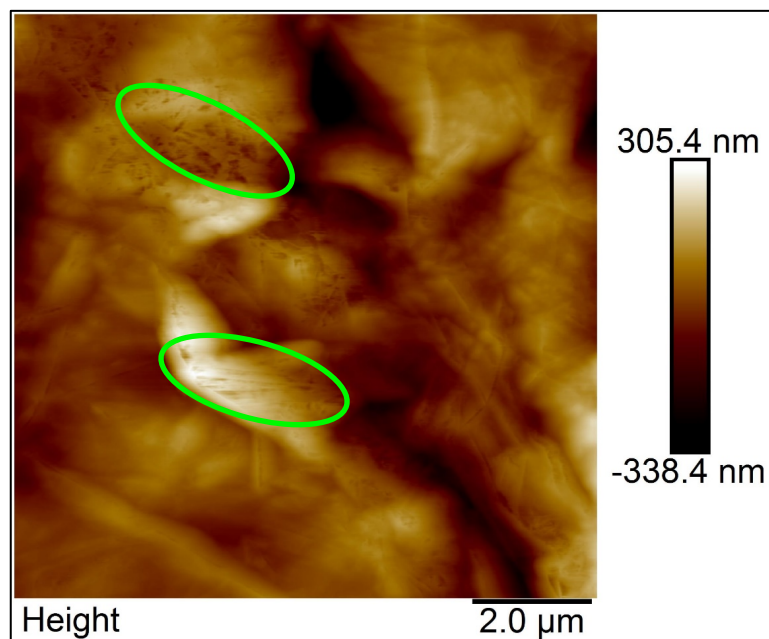


Figure 24: Height scan of OxGnP (10\*10  $\mu\text{m}$ )



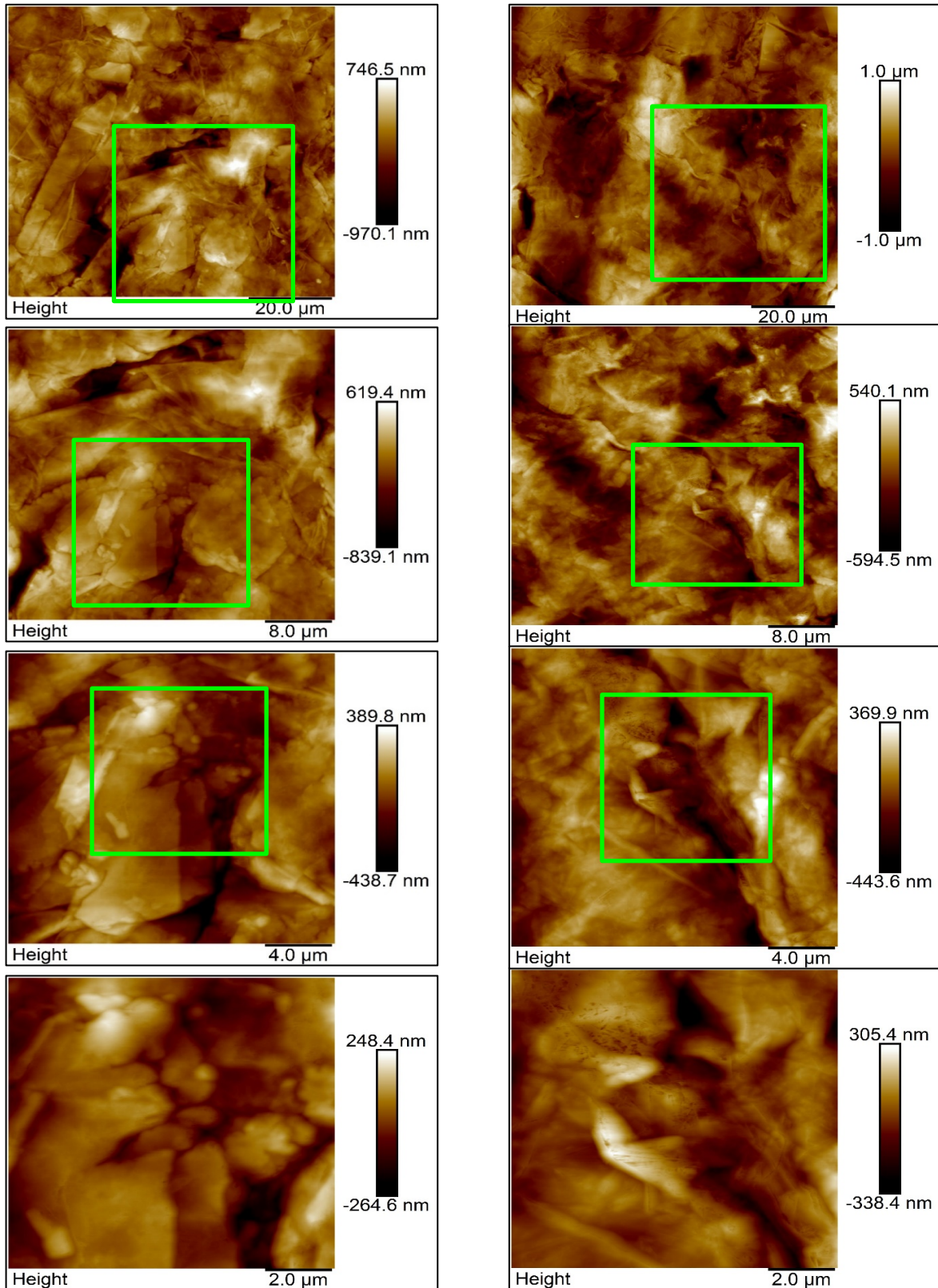


Figure 25: 2D Height images of xGnP (left) and OxGnP (right)



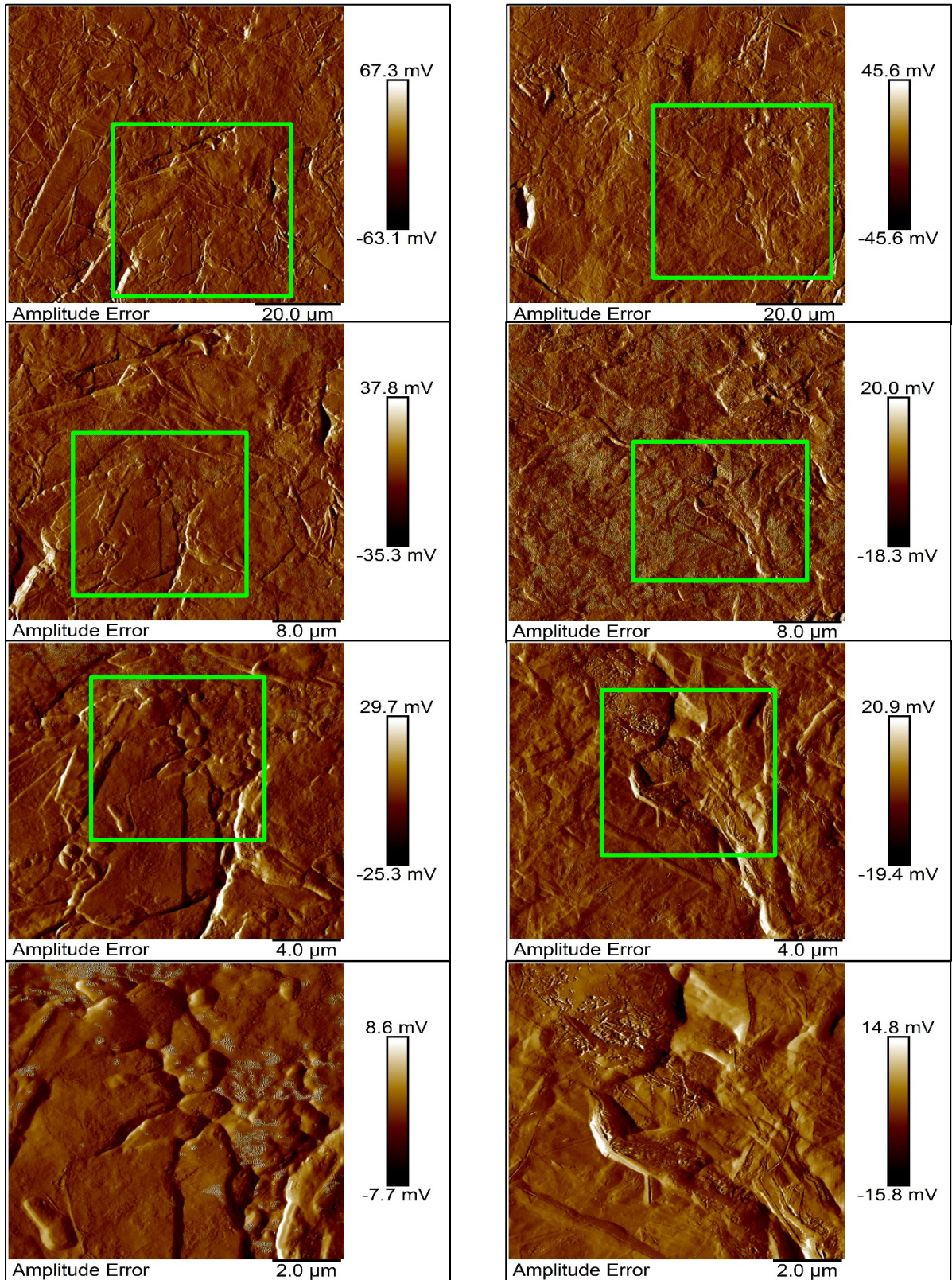


Figure 26: Amplitude error scans of xGnP (left) and OxGnP (right)



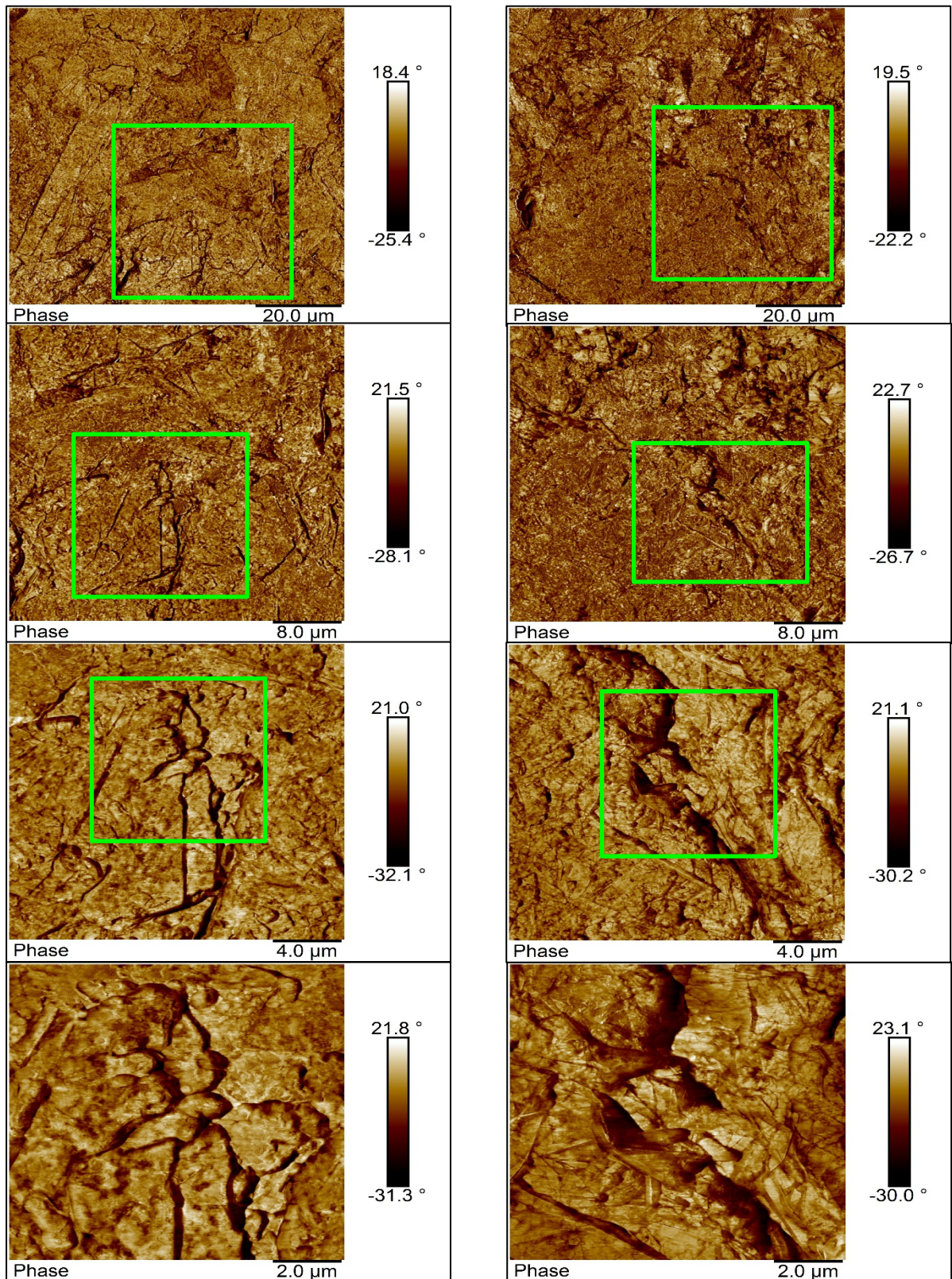


Figure 27: Phase scans of xGnP (left) and OxGnP (right)

### 2.3.2.2 Scanning Electron Microscope

SEM is an electron microscope that produces images of sample surface by scanning it with a focused electron beam. The electrons interact with atoms on sample surfaces, producing various detectable signals, which contain information about the sample's composition and topography. In this research, images were obtained by Jeol JSM 5600 (JEOL USA, Inc., Peabody, MA, USA). For thin film samples, the specimens were frozen at -20 °C then fractured in order to minimize the distortion of the platelets on the fractured surface. The fracture surfaces were scanned by the SEM. Figure 28 shows the alignment of xGnP in the manufactured xGnP-Epoxy paper. Some distortion appears at the fracture area, which might occur upon breakage.

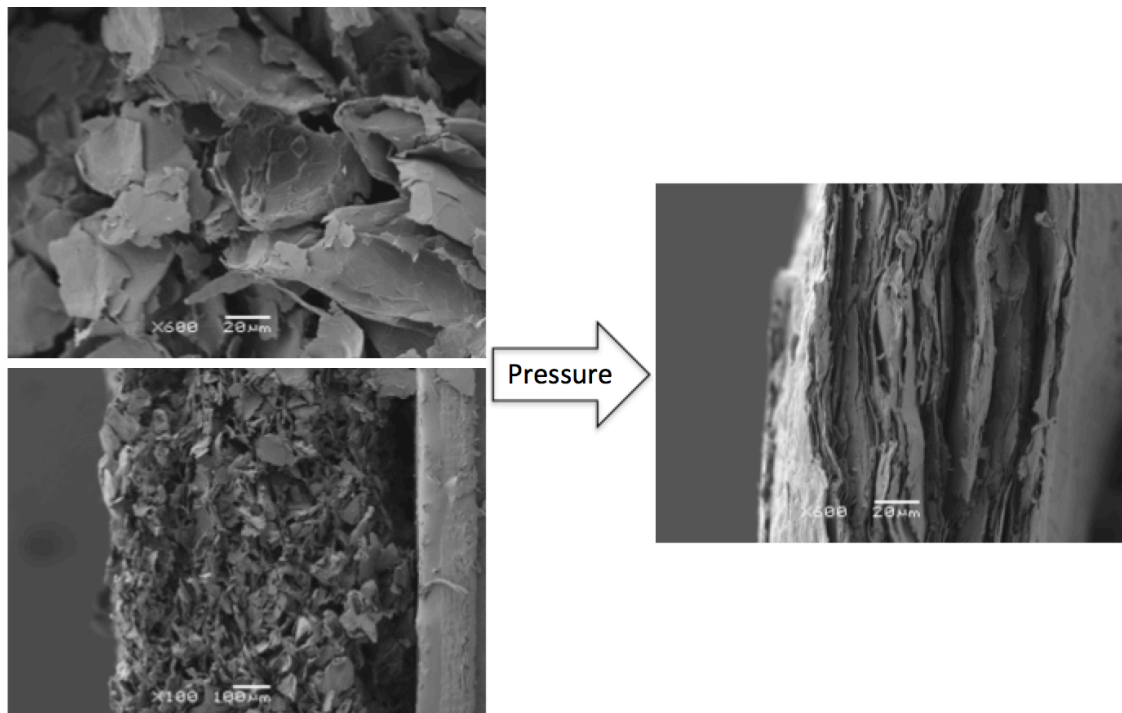


Figure 28: Alignment of xGnP in the papers during manufacturing (56 wt. %)

Similar alignment was observed in xGnP-PEI papers. Figure 29 shows the xGnP alignment in the xGnP-PEI paper. Similar distortion appears at the fracture area, which might occur upon breakage.



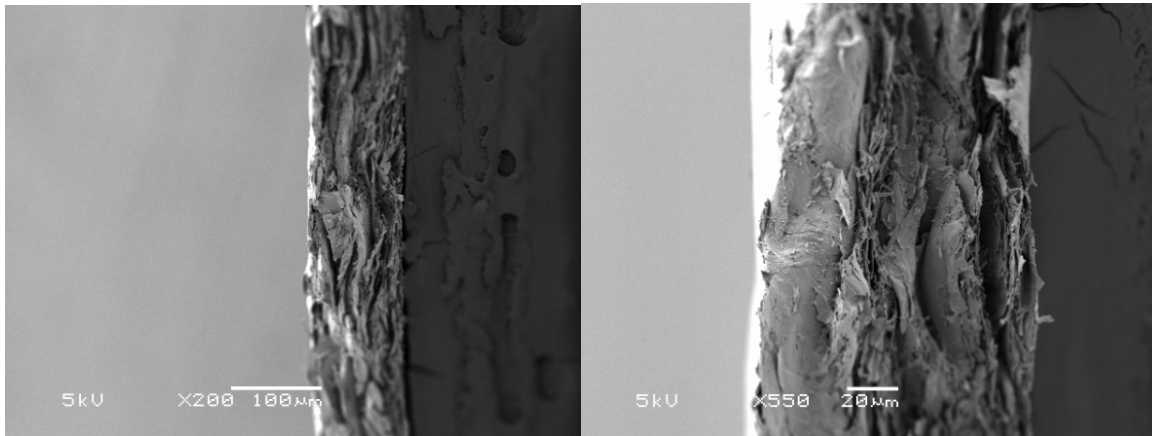


Figure 29: SEM images of xGnP-PEI fracture surface.

The thicker nano-composites with loading of xGnP or OxGnP were prepared for SEM by mechanical polishing, in which silicon carbide that has 1200 um grit size was used. It is clear in the SEM images of xGnP-Epoxy that the xGnP is dispersed better than the OxGnP. The oxygen groups introduced to the OxGnP seem to bond the platelets with each other rather than enhancing the bond between the platelets and the epoxy. This platelet-to-platelet bonding caused agglomeration. OxGnP-Epoxy SEM images contained more clusters (Figure 30 (b)) compared to xGnP-Epoxy (Figure 30 (a)).



Figure 30: Typical SEM image (a) 3% xGnP (b) 3% OxGnP nano-composites

### 2.3.3 Thermal Properties

The thermal properties were investigated mainly using TGA. Platelets loading, glass transition temperature, decomposition temperature, and other properties could be determined by employing thermal analysis.

### 2.3.3.1 Thermogravimetric analysis

TGA is a method of thermal analysis in which changes of a material's mass are measured as a function of ramping temperature. TGA can provide information about physical phenomena, such as phase transition and vaporization. Likewise, TGA can provide information about chemical phenomena like decomposition.

The main use for TGA in this study is to determine mass loss due to decomposition at different temperature levels. Since xGnP, OxGnP, and host polymers have different thermal stabilities, it is possible to use TGA to determine the xGnP or OxGnP concentration in the produced nano-composite.

TGA Q500 (TA Instruments Inc., New Castle DE, USA) was used to characterize the thermo stability of the composites (see Figure 31). The TGA furnace internal temperature gradually increased from room temperature to 650 °C at a constant rate of 20 °C/minute in nitrogen gas.



Figure 31: TGA Q500 by TA Instruments

For Epoxy nano-composites, typical weight loss curves of epoxy-based nano-composites are shown in Figure 32 (a). TGA results showed that changing the applied pressure in the

pressing machine could vary the final xGnP or OxGnP loading. The platelet content can be calculated to generate a manufacturing guiding curve to guide the process of making graphene based epoxy papers. The calculated xGnP, OxGnP percentages in the manufactured papers based on the applied pressure are shown in Figure 32 (b).

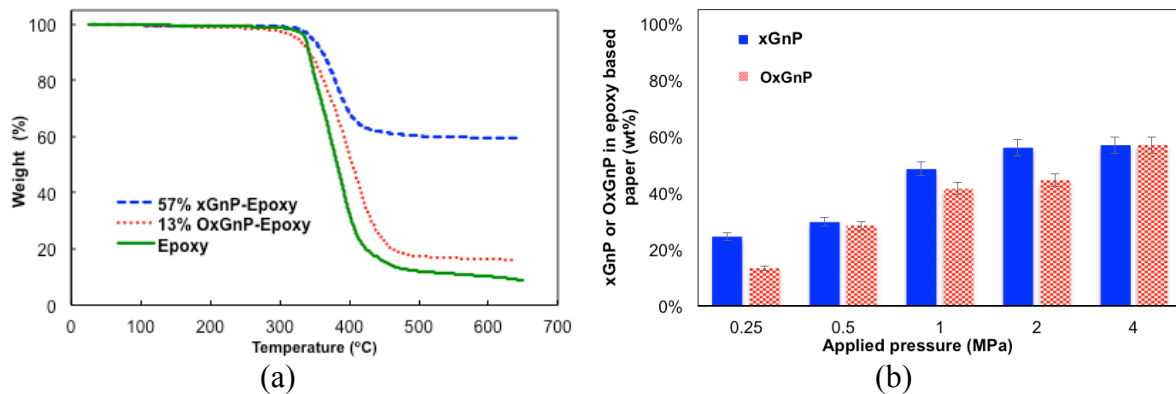


Figure 32: (a) Typical weight loss of xGnP or OxGnP papers due to decomposition (b) xGnP or OxGnP contents in the manufactured based epoxy papers

Similarly, the TGA was used to determine the xGnP concentration in the xGnP-PEI composite film. Changing the PEI concentration in the DMAc solution during the manufacturing can vary the xGnP loading. When the PEI concentration is higher, its solution becomes more viscous. As a result, more PEI will be retained with the xGnP after filtration. Based on the residue of xGnP, PEI and xGnP-PEI papers obtained from TGA results are shown in Figure 33 (a); the xGnP contents were calculated to generate a calibration curve to guide the preparation of xGnP-PEI papers (Figure 33 (b)).

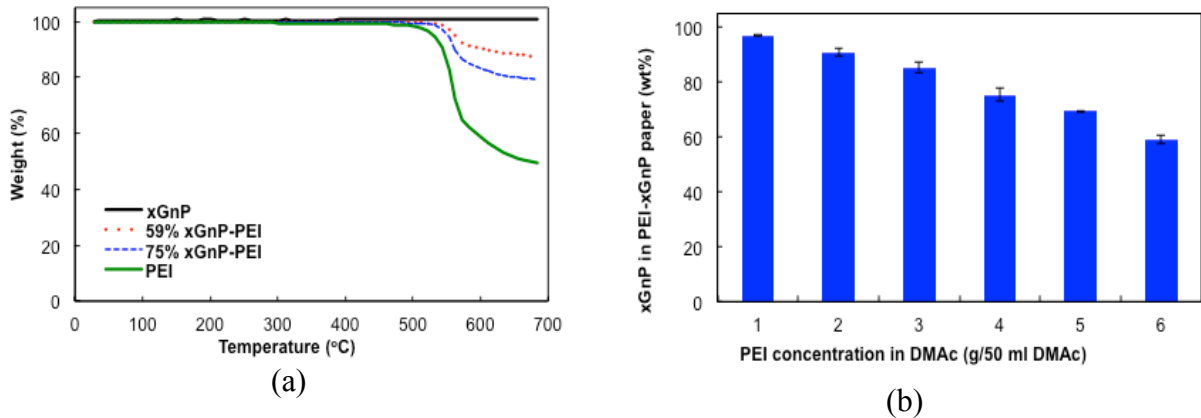


Figure 33: (a) Typical weight loss of xGnP, PEI, and xGnP-PEI papers due to decomposition; (b) xGnP loading in the xGnP-PEI paper with variation of PEI concentration in DMAc.

### 2.3.4 Electrochemical properties

Electrochemical properties of pure polymer and manufactured nano-composite were investigated. Also, the effect of platelets loading on these properties is reported.

#### 2.3.4.1 Electrochemical Impedance Spectroscopy

EIS was employed to investigate the Electrochemical properties. During an impedance measurement, a frequency response analyzer is used to impose a small amplitude AC signal to the material. The AC voltage and current response of the material are analyzed to determine the resistive, capacitive and inductive behavior, and the impedance of the material at that particular frequency.

A Gamry electrochemical impedance spectroscope was used to measure the impedance of the manufactured nano-composite at room temperature. Adhesive copper tapes of 6 mm wide were stuck to the surface of nano-composite. The sample is then clamped in the impedance tester as shown in Figure 34.

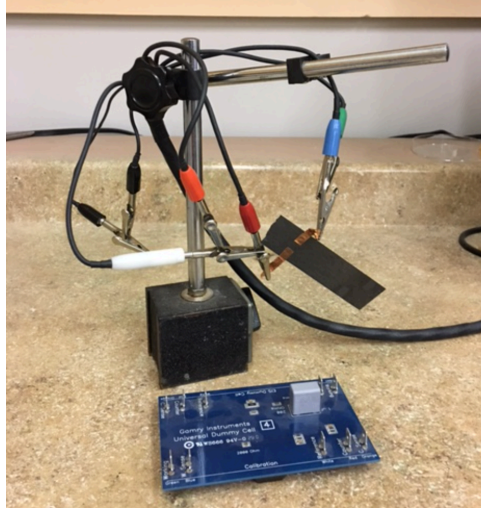


Figure 34: xGnP-Epoxy sample clamped to the impedance tester

The distance between the two copper tapes was 10 mm. The relation between impedance, capacitance, resistance, and phase angle can be seen in equation (1).

$$\text{Impedance } Z = Z_0 \cos \phi + jZ_0 \sin \phi \quad (1)$$

Where:

$Z_0 \cos \phi$  is resistance

$Z_0$ : is impedance magnitude

$jZ_0 \sin \phi$  is capacitance

$\phi$ : is phase angle

Equivalent circuit modeling of EIS data can be used to extract physically meaningful properties of the electrochemical system by modeling the impedance data in terms of an electrical circuit composed of ideal resistors, capacitors, and inductors.

For epoxy-based nano-composites, the impedance value at several frequencies for xGnP or OxGnP are displayed in Figure 35. The epoxy roll milled nano-composite with low percentage of xGnP or OxGnP exhibited exceptionally larger impedances compared with either xGnP-Epoxy or OxGnP-Epoxy paper with high loadings. Apparently, both xGnP-Epoxy and OxGnP-Epoxy papers made by filtration/pressing possessed low impedance in magnitude (high conductivity). On the other hand, the results show capacitive behavior at low platelet concentrations for both xGnP-Epoxy and OxGnP-Epoxy.

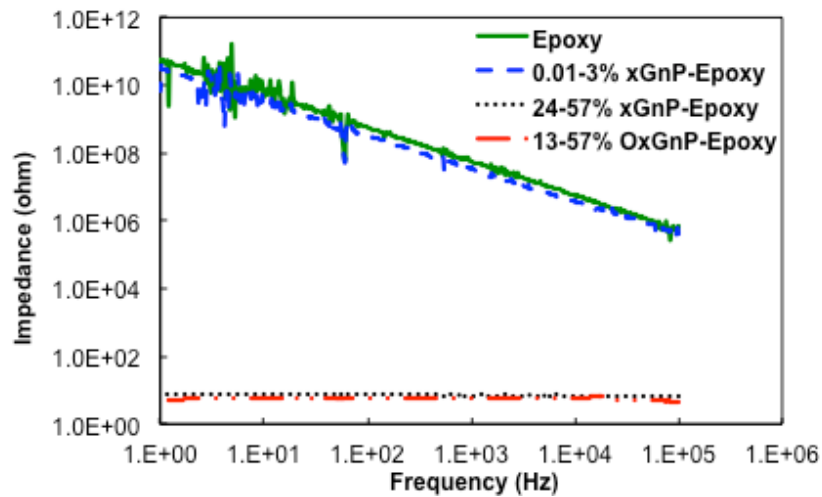


Figure 35: xGnP or OxGnP based epoxy nano-composite impedance with respect to frequency

Similarly, Figure 36 displays the impedance values for xGnP-PEI paper samples. xGnP-PEI with xGnP loading up to 10 wt. % nano-composite exhibited exceptionally larger impedances than the films with high xGnP loadings. This indicates that the xGnP papers with xGnP loadings above 60 wt. % made by filtration/hot-press possessed substantially lower impedance compared with the composite films with low xGnP concentrations ( $\leq 10$  wt. %). Therefore, the results indicate substantially high electrical conductivity for the papers of high xGnP loadings.

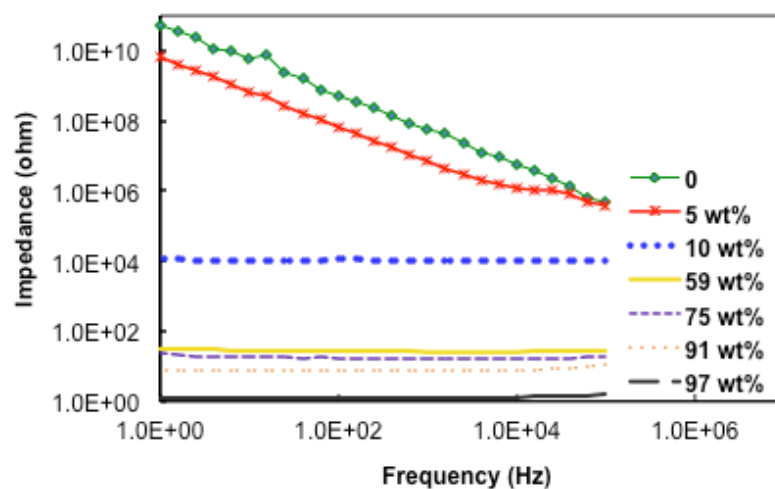


Figure 36: Impedance of xGnP-PEI papers with various xGnP concentrations with respect to frequency

Both epoxy and PEI based nano-composites showed significant improvement in electrical conductivity (lower impedance value). The impedance values for both PEI and Epoxy papers at high xGnP loadings indicate that these papers can be used for multifunctional applications, including dissipating an electrical charge from a lightning strike as well as other applications in electronic devices due to their superior electrical conductivity.

### 2.3.5 Mechanical properties

By obtaining the mechanical properties, we can comprehend the different variables that these materials possess, from different xGnP percentages to the functionalization effect.

The DMA method is used to test thin films of the materials to obtain stress-strain curves, elastic and loss modulus, glass transition temperature, and other properties. However, for thicker nano-composites, including laminated nano-composites, an MTS machine with attached two-dimensional extensometer was used to get the stress strain curve and Poisson's ratio.

#### 2.3.5.1 Dynamic Mechanical Analysis

DMA is an analysis method that is used to characterize and measure the mechanical properties of materials, especially polymers and viscoelastic materials. DMA Q800 (TA Instruments Inc., New Castle DE, USA) was used to characterize the thermo-mechanical properties of the manufactured nano-composite (see Figure 37). DMA was used in several modes to obtain different properties that would help in further investigations of the materials.



Figure 37: DMA Q800 by TA Instruments

Samples were tested using the thin film clamp, which is best suited for thin films and fibers. The samples were clamped from both ends; the upper clamp is stationary while the lower is movable. The specimen was cut into rectangular strips (width: 4-5 mm, thickness:  $\sim 0.2$  mm).

#### 2.3.5.1.1 Controlled Force Mode

A stress-strain tensile test was conducted on six specimens of the same material to ensure that there is consistency to a certain limit within the results. Preload force of 0.01N was used. All samples were tested at controlled temperature ( $35^{\circ}\text{C}$ ). The samples loaded up to failure at a rate of 0.5 N/minute. Samples of the obtained stress-strain curves are shown in Figure 38.

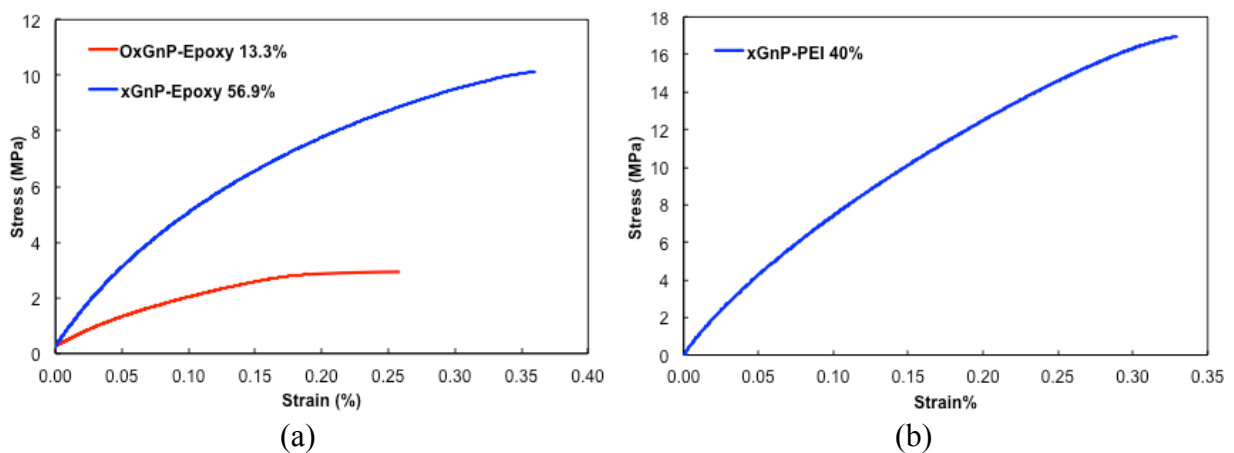


Figure 38: Stress strain response for (a) xGnP-Epoxy paper (b) xGnP-PEI paper



For epoxy-based papers, increasing the xGnP or OxGnP concentration showed improvement in the strength. However, OxGnP papers exhibit a lower strength value compared to the xGnP as displayed in Figure 39, which might be due to the agglomeration in the AFM and SEM sections.

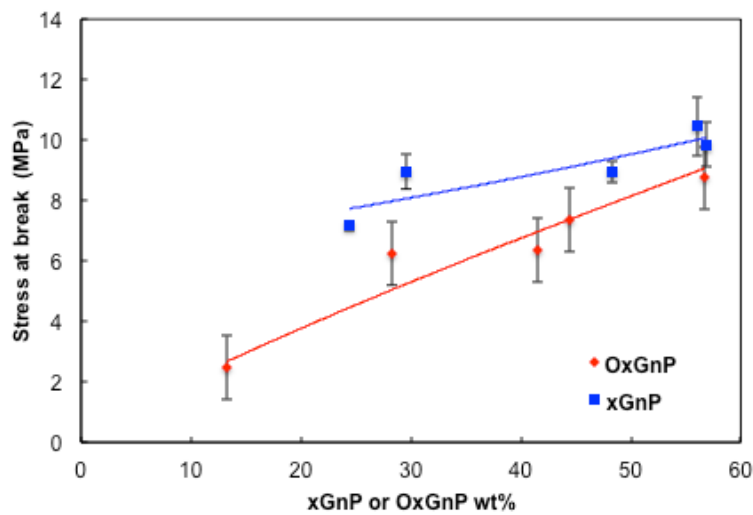


Figure 39: Stress at break for epoxy-based papers

However for xGnP-PEI nano-composites, xGnP incorporation into PEI caused a decline in both stress and strain at failure with increase of xGnP concentration, as seen in Figure 40 (a) and (b). At high concentrations of the xGnPs, the strain property of the composite paper is significantly affected by the xGnP's properties, which are brittle with almost no ductility. Therefore, xGnP-PEI papers were rigid compared with pure PEI. Additionally, the translation of xGnP's high strength to the composite paper might be limited as there is no proper chemical bond between the PEI matrix and the xGnP.

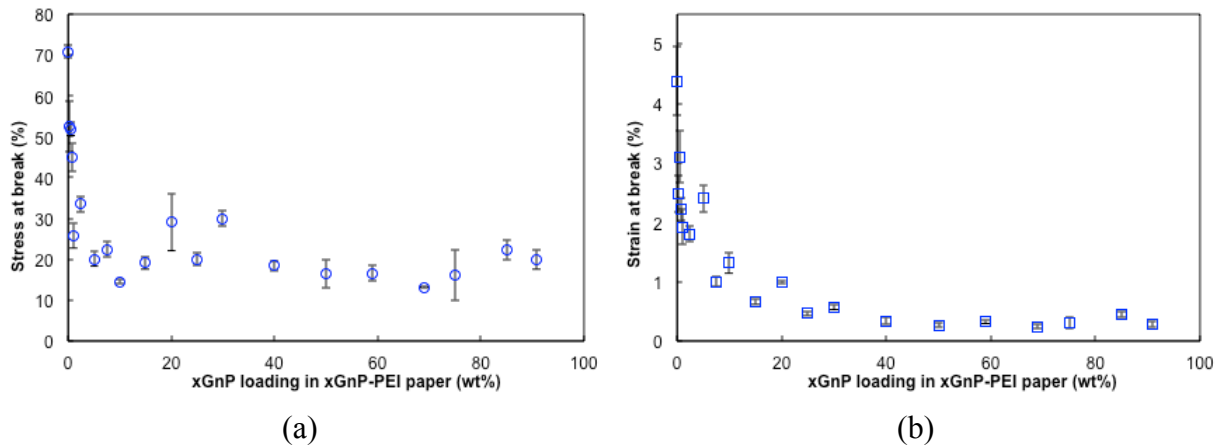


Figure 40: Stress-strain response of xGnP-PEI paper: (a) stress at break; (b) strain at break.

### 2.3.5.1.2 Temperature sweep

In this mode, DMA works by generating a sinusoidal loading wave that causes elongation to a sample of known geometry by either controlling the stress or the strain. Material elongation is directly related to its stiffness. DMA measures the storage modulus ( $E'$ ) and the loss modulus ( $E''$ ), as they represent the elastic and the viscose response of the material, respectively. The ratio of the loss modulus to the storage modulus is called Tan delta at a specified temperature (see Figure 41). It represents the ratio of the energy dissipated for the tested material. The peak of the  $\tan \delta$  curve as a function of temperature is defined as the glass transition temperature ( $T_g$ ), which is the temperature at which the material makes the transition from a solid, glassy state to a rubbery or more pliable state. At  $T_g$ , the loss modulus reaches its maximum, and the storage modulus decreases dramatically. Temperature-sweep mode in DMA is often used to characterize the glass transition temperature of a material.

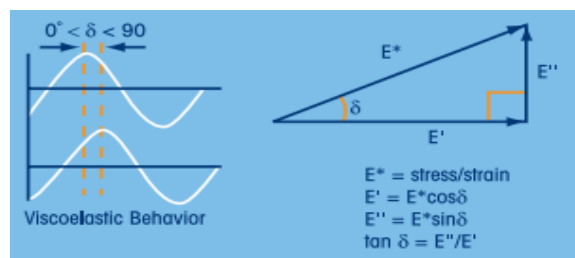


Figure 41: relation between  $E^*$ ,  $E'$ ,  $E''$ , and  $\tan(\delta)$

Epoxy-based nano-composite tests were conducted in temperature sweep mode. A 0.01 N

preloading force was applied at 1Hz single frequency; the peak value of the strain wave was 0.05. The temperature was ramped from room temperature at a rate of 20 °C/min to a maximum temperature reaching 150 °C in an air environment; typical curves are shown in Figure 42.

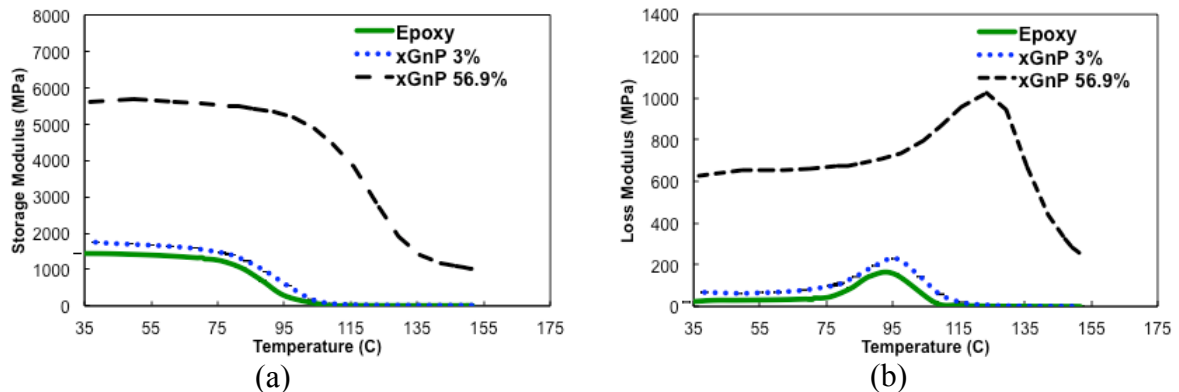


Figure 42: Typical (a) Storage (b) Loss Moduli curves obtained from DMA for epoxy based nano-composites

At higher loadings of xGnP or OxGnP, the loss and storage moduli were exponentially increased with increased loadings of graphene, see Figure 43 (b) and Figure 44 (b), which shows a promising potential in energy dissipation applications. The roll milled nano-composites exhibit improvement in these properties but not as significant as the papers, see Figure 43 (a) and Figure 44 (a). However, OxGnP papers exhibited lower loss and storage moduli values compared to the xGnP papers, which might be due to the agglomeration showed by AFM and SEM scans earlier in section 2.3.2.1 and section 2.3.2.2.

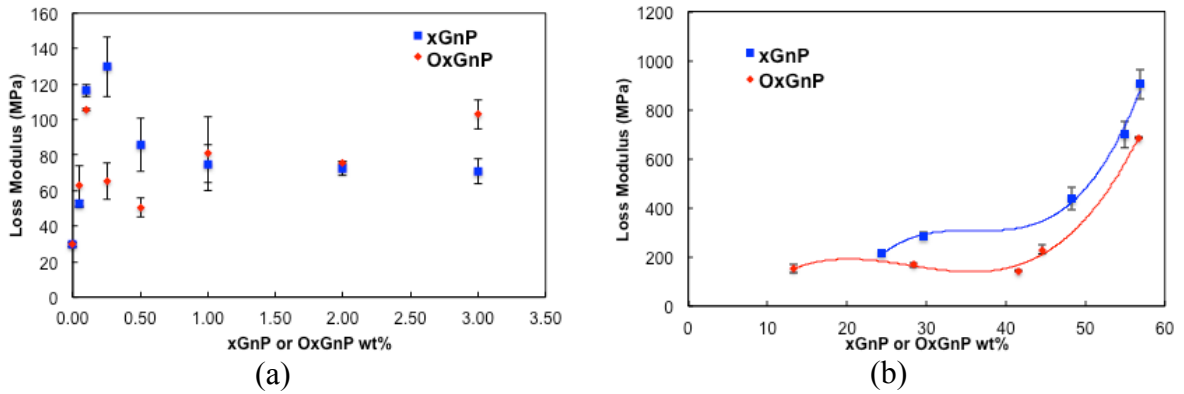


Figure 43: Loss modulus for xGnP-Epoxy or OxGnP-Epoxy at 50 °C (a) roll milled nano-composites (b) Papers at 40 °C.

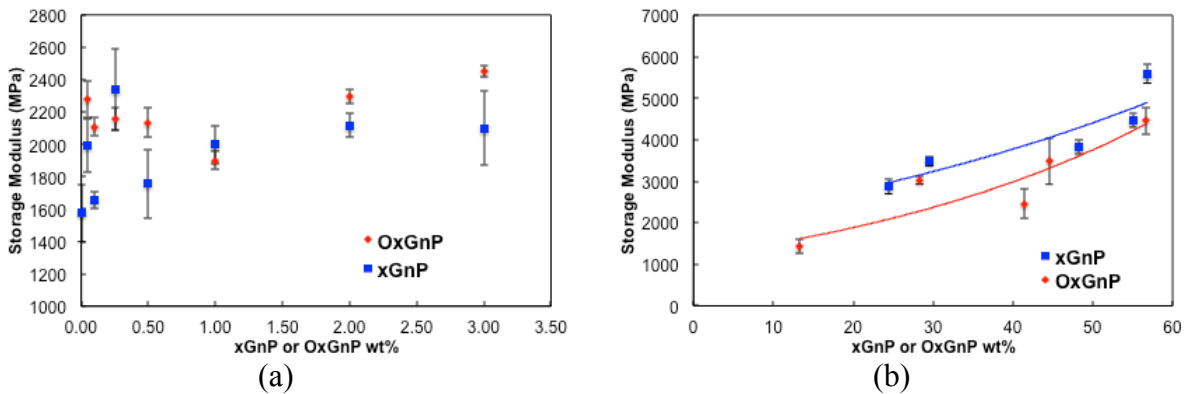


Figure 44: Storage modulus for xGnP-Epoxy or OxGnP-Epoxy (a) roll milled nano-composites (b) Papers at 40 °C.

The glass transition temperature ( $T_g$ ) was determined from the peak of the  $\tan \delta$  curve. The glass transition temperature for the roll milled nano-composites remained close to the neat epoxy value, the peak values are around  $\sim 2\%$  for both xGnP and OxGnP (Figure 45 (a)). However, for the xGnP papers, there was up to  $\sim 28^\circ\text{C}$  improvement at 57% xGnP loading. The improvement of the OxGnP papers  $T_g$  was almost constant at all OxGnP loadings up to  $\sim 17^\circ\text{C}$  (see Figure 45 (b)). The  $\tan \delta$  peak for the roll milled nano-composites showed marginal improvement at  $\sim 0.1\%$  for both xGnP or OxGnP, which vanished linearly as the loading approached 3% (see Figure 46 (a)). However, the  $\tan \delta$  at  $T_g$  for the papers showed significant reduction compared to the neat epoxy, and this reduction was noticed for OxGnP rather than xGnP. Also, the percentage of reduction increased with the increase of xGnP or OxGnP loading (Figure 46 (b)).

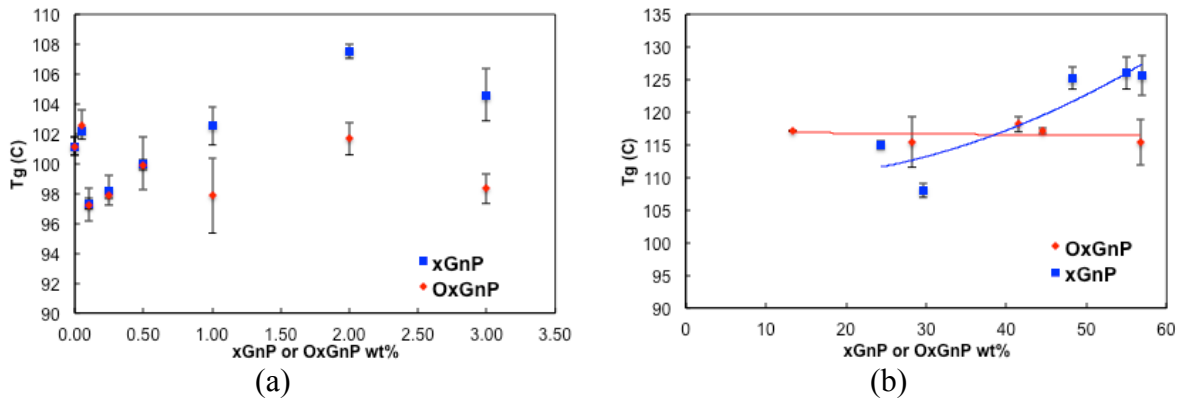


Figure 45: Tg for xGnP-Epoxy or OxGnP-Epoxy (a) roll milled nano-composites (b) Papers

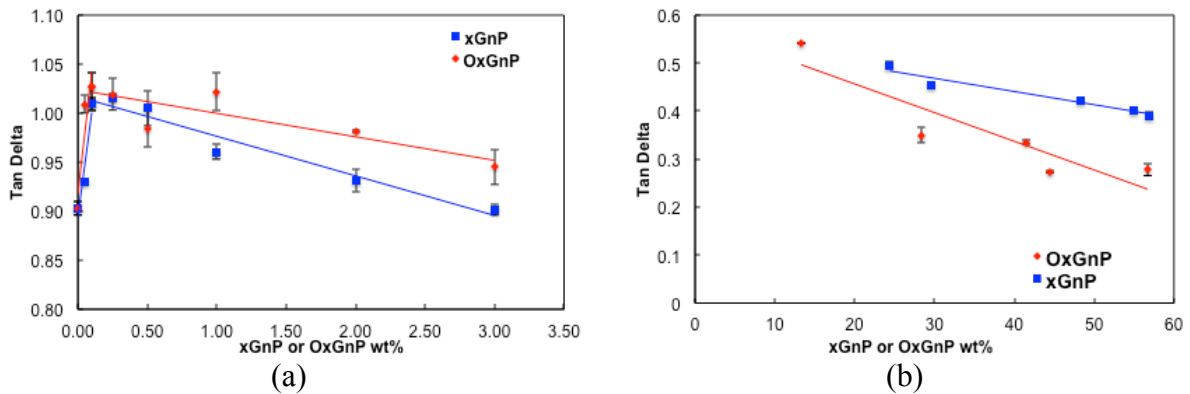


Figure 46: Max tan  $\delta$  for xGnP-Epoxy or OxGnP-Epoxy (a) roll milled nano-composites (b) Papers

The same testing parameters were employed for testing PEI-based nano-composites. However, the maximum tested temperature for the PEI based nano-composites was 315 °C compared to 150 °C for epoxy-based nano-composites; this range was fixed based on the thermal stability of the host polymer.

Figure 47 (a) displays the storage moduli of PEI, pure xGnP and representative xGnP-PEI papers. There is a significant increase if xGnPs and PEI are combined, indicating good compatibility between the PEI and xGnPs. Figure 48 (a) summarizes how this modulus is affected by the loading of xGnP in the paper. In the range of about 59 to 97 wt. %, the xGnP dramatically enhanced the storage modulus. The maximum falls between 60 and 85 wt. %. When the xGnP loading increased above that range, there was not enough PEI as a binder material. As anticipated, the 100% GNP paper was weak because the interaction among

xGnP only relied on the mechanical interlocking from the xGnP defects and the van der Waals forces. Compared with pure PEI, the increase in modulus for the xGnP-PEI paper should be attributed to the translation of the graphene's property to the xGnP-PEI paper since graphenes are highly rigid and possess an exceptionally high modulus.

On the other hand, interesting results can be extracted from the loss moduli. Typical curves are shown in Figure 47 (b); comparison of the results is summarized in Figure 48 (b). The loss modulus value for the pure PEI or xGnP paper is 50-80 MPa. These values remain almost constant from room temperature up to 200 °C. Figure 48 (b) shows that for the xGnP-PEI papers with different high xGnP concentrations, the increase in loss modulus is 2,000%-3,000%. By definition, loss modulus is the capacity of a certain amount of material to dissipate dynamic loading to heat, which means the applied mechanical energy is dissipated to heat. This indicates a damping capability of these materials.

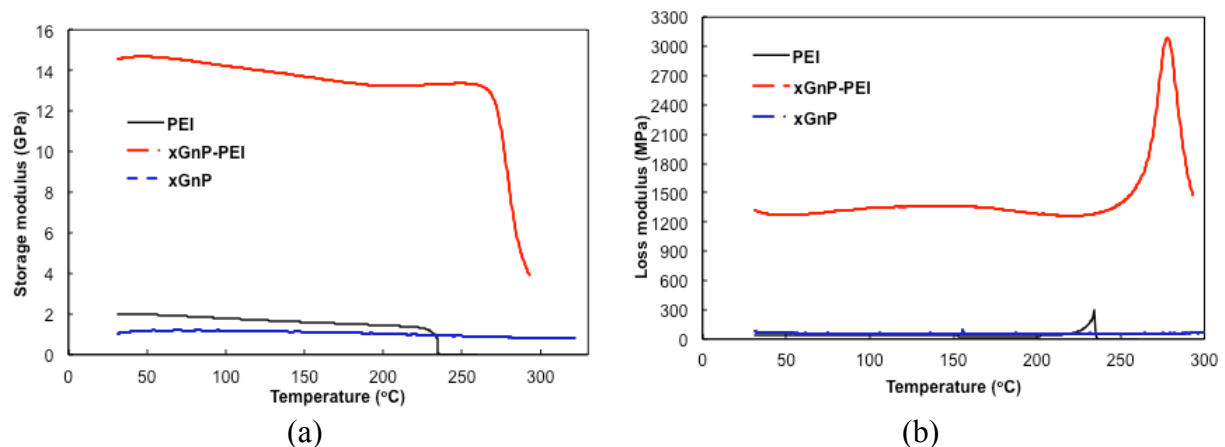


Figure 47: Comparison of (a) storage modulus (b) loss modulus of PEI, xGnP-PEI (59 wt. %), and pure xGnP papers

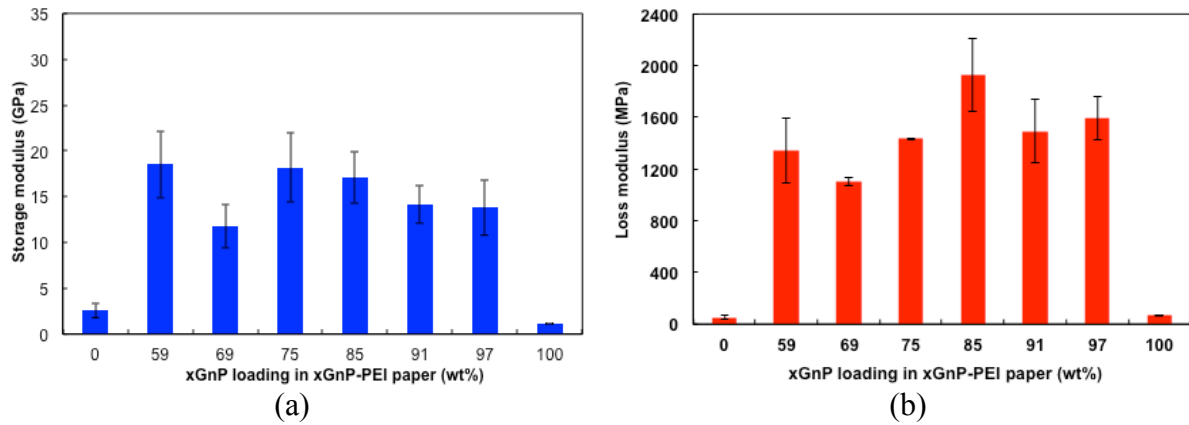


Figure 48: Effect of xGnP content on (a) the storage modulus (b) loss modulus of of xGnP-PEI paper at 40 °C.

The inclusion of reinforcements may also improve the glass transition temperature ( $T_g$ ) because in the transition temperature zone, the mobility of polymeric chains may be hindered such that the same level of mobility can only be achieved at a higher temperature range, especially if there are good interactions between the reinforcements and polymeric matrix. Figure 49 reveals considerable increases in  $T_g$  for all xGnP-PEI papers in this study.

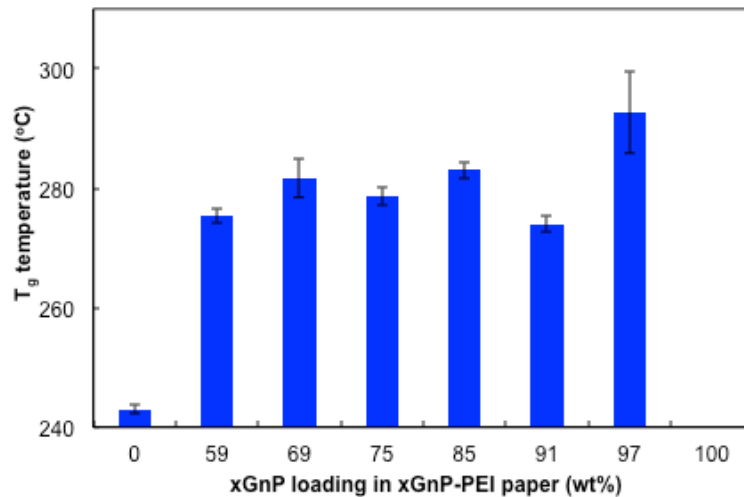


Figure 49: Effect of xGnP loading in xGnP-PEI on glass transition temperature.

This study indicates that xGnP at high concentrations remarkably improves the damping behavior in terms of  $\tan \delta$  (Figure 50) and loss modulus as discussed above.  $\tan \delta$  value for high xGnP-PEI papers increases more than 500% compared to PEI, and more than 100% over pure xGnP paper was achieved.

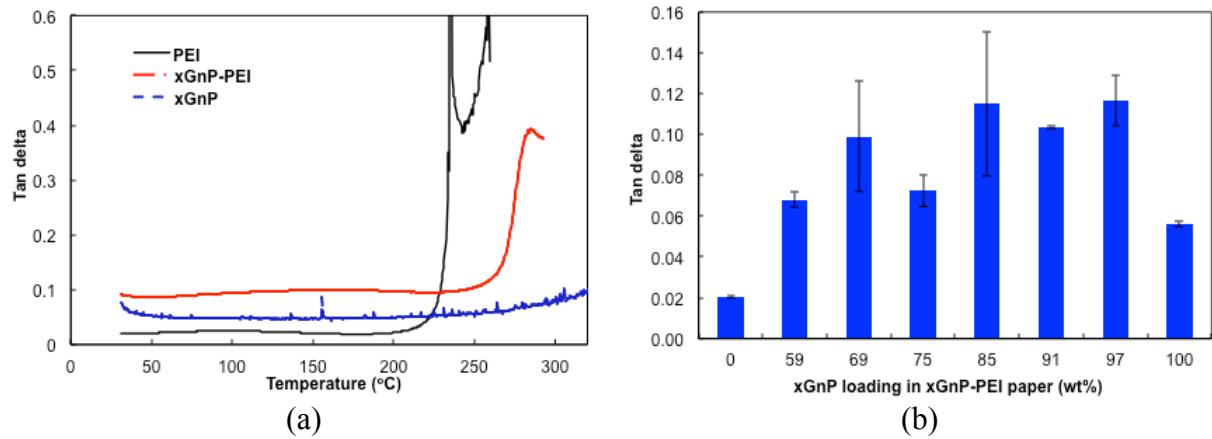


Figure 50: Tan  $\delta$  of xGnP-PEI papers (a) Typical response (b) tan  $\delta$  at different xGnP loadings.

In summary, the damping effect of graphenes on the nano-composites has been discussed in some publications [52] [53]. The damping effect of the xGnP in the host polymer may attribute to the introduced heterogeneity; when the specimen is under dynamic loading, higher inconsistency in the molecular movement causes collisions between molecules from the rigid phase (xGnP) and the softer phase (polymer molecule). The collision is evidenced by the higher loss modulus, which indicates that heat dissipates from the applied dynamic force in the DMA test. This energy-dissipation mechanism is similar to what is reported by other research for polyurea [54] [55], in which there is a co-existence of both hard domain and soft domain. Rigid xGnP represents the hard domain while the host polymer represents the soft domain, which is much softer than xGnP. Another possible explanation for the improvement in the damping properties xGnP nano-composite is that graphenes proved to have an excellent intrinsic damping property according to experimental study [56]. This damping property should transmit to the xGnP papers. Considering the fact that both the neat xGnP film and the neat polymer had much damping compared with the nano-composite papers made from both demonstrates the heterogeneity importance and co-existence of both material phases (Hard and soft domains) in damping improvement.

### 2.3.5.1.3 Multi-Frequency Mode



In this testing mode, the same sinusoidal displacement wave was generated as the one discussed in the previous section. However, the frequency at which the load applied was ramped instead of ramping the temperature. The frequency sweep was run at a constant temperature of 35°C. The frequency varied for each sample of either xGnP-Epoxy or OxGnP-Epoxy.

The preloading force applied was 0.01 N using multiple frequencies. The frequencies were varied from 1, and increased to 200 Hz in 50 Hz increments. The peak value of the applied strain wave was 0.05. Three specimens are cut from each sample; width and thickness were measured throughout and entered into the DMA software. Then, the specimen was placed in the film tension clamp. Next, the DMA measured the length of specimen, and the frequency sweep was run. The frequency sweep results were averaged for all three specimens that run on the same frequency. Typical results of the frequency sweep test are shown in Figure 51.

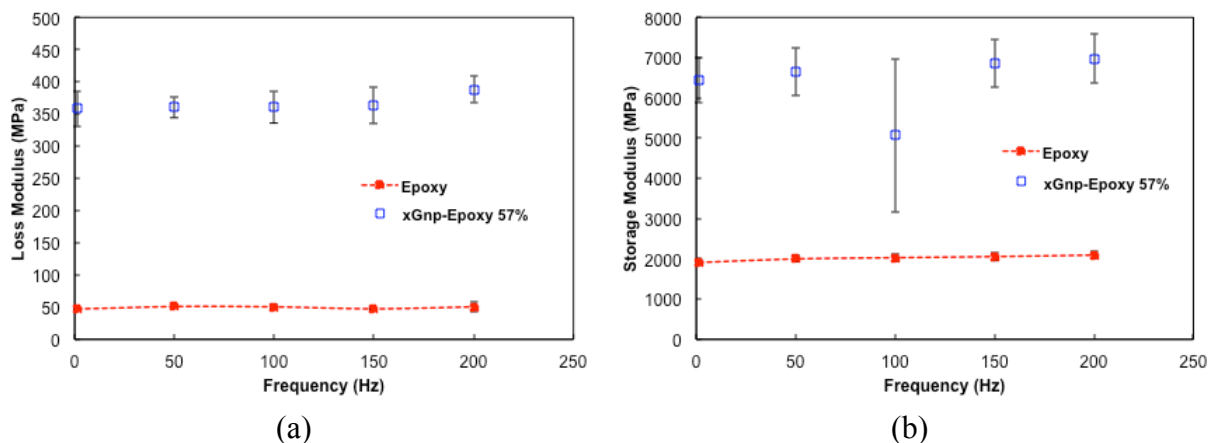


Figure 51: Frequency sweep comparison between neat epoxy and xGnP-Epoxy paper like 57 wt. % (a) loss modulus (b) storage modulus

Adding different amounts of xGnP or OxGnP has a slight effect on strain rate sensitivity of the storage modulus. Figure 52 and Figure 53 plot the storage modulus results for all the samples at different frequencies. The improvement of adding xGnP or OxGnP to Epoxy in terms of storage modulus was noticeable, which agrees with the results obtained from the DMA temperature sweep test.

Figure 54 and Figure 55 show the loss modulus frequency sweep results for all the samples. For the roll-milled nano-composite, the loss modulus increased with increasing frequency at all xGnP or OxGnP loadings (Figure 54 (a) and (b)).

For graphene papers (Figure 55), the loss modulus improvement compared to the neat epoxy was more significant, 150-350% for xGnP (Figure 55 (a)) and 300-700% for OxGnP (Figure 55 (b)). Loss modulus of xGnP-Epoxy paper nano-composited increased slightly with increasing frequency (Figure 55 (a)). However, loss modulus values for OxGnP-Epoxy paper first increased, and then decreased with increasing frequency with peak value around 150 Hz (Figure 55 (b)).

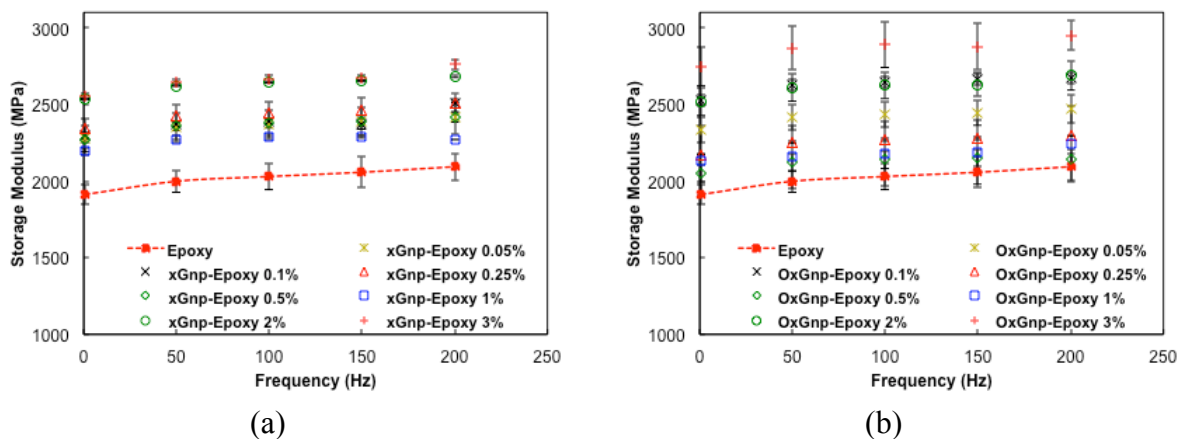


Figure 52: Storage Modulus for roll-milled nano-composite (a) xGnP-Epoxy (b) OxGnP-Epoxy

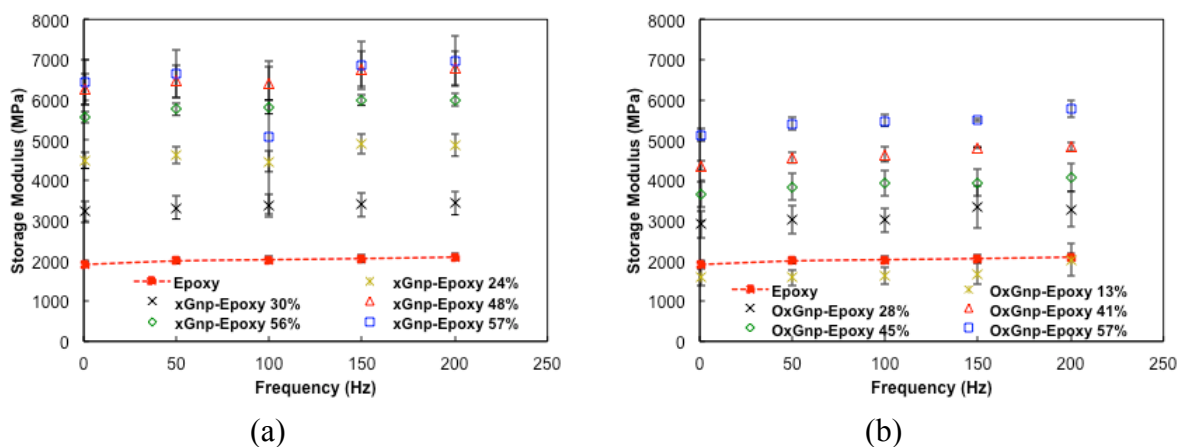


Figure 53: Storage Modulus for paper nano-composite (a) xGnP-Epoxy (b) OxGnP-Epoxy

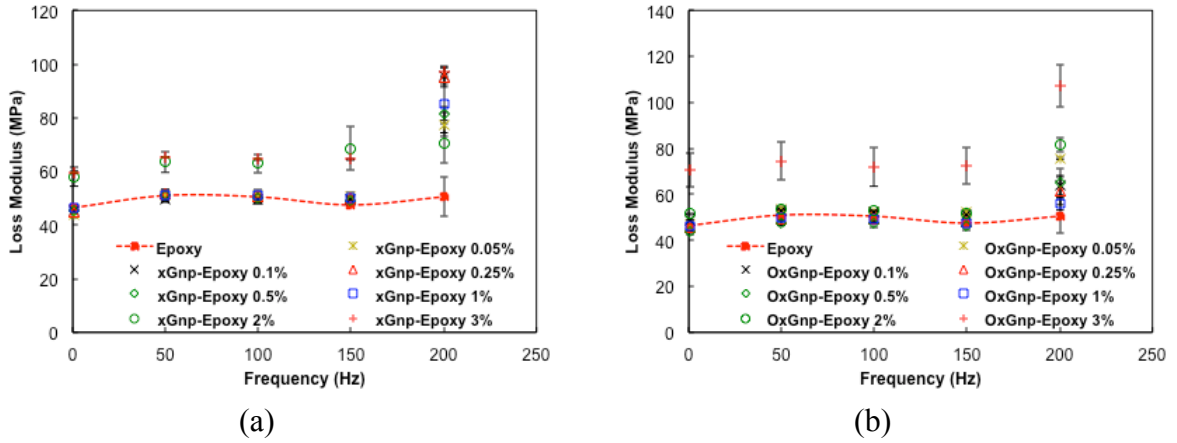


Figure 54: Loss Modulus for roll-milled nano-composite (a) xGnP-Epoxy (b) OxGnP-Epoxy

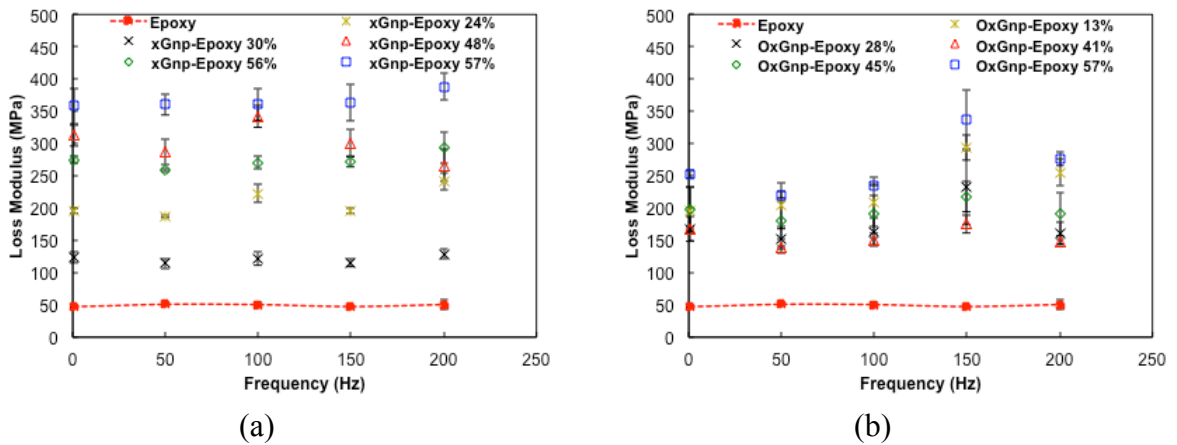


Figure 55: Loss Modulus for paper nano-composite (a) xGnP-Epoxy (b) OxGnP-Epoxy

### 2.3.5.2 Tensile Test

The most common type of test used to measure the mechanical properties of a material is the tension test. The tension test is widely used to provide basic design information on the strength of materials. Epoxy was the primary base polymer chosen in this investigation. In addition to the host polymer, xGnP or OxGnP were added to the polymer at different replacement % wt. The main goal of static mechanical evaluation is to determine the effect of adding xGnP or OxGnP materials to mechanical responses of polymers used and to investigate the lamination effect of the produced xGnP-Epoxy papers. It is essential to

determine the optimum percentage of xGnP or OxGnP that gives the base polymer the greatest improvement in mechanical properties.

Roll milled nano-composites were casted in a silicon mold resulting in dog bone shaped specimens for tensile testing (see Figure 56 (a)). However, the xGnP or OxGnP papers were laminated to get a thicker nano-composite, as described in section 2.2.2.1.3. The laminated nano-composites were prepared with suitable tabbing for gripping into the jaws of the testing machine (see Figure 56 (b)). The specimen's cross sectional area within which elongation measurements were done was approximately uniform. The cross sectional area was calculated based on measurements. Just before testing, specimen thicknesses were recorded using a caliper. Experimental response was recorded from an MTS machine; an extensometer was attached for measurement of strain change in the longitudinal and traverse directions (see Figure 57).



Figure 56: Dog bone shaped specimen (a) Roll-milled casted in silicon mold (b) Laminated tabbed with epoxy



Figure 57: MTS and extensometer for stress-strain and Poisson's Ratio measurement

Tensile displacement was applied at a rate of 1 mm/min until fracture. During the test, the load required to apply a certain displacement on the material was recorded. The collected data were the axial displacement and load. A typical stress-strain curve is shown in Figure 58 (a). Poisson's ratio can be obtained from the slope of the axial- traverse strain curve (see Figure 58 (b)).

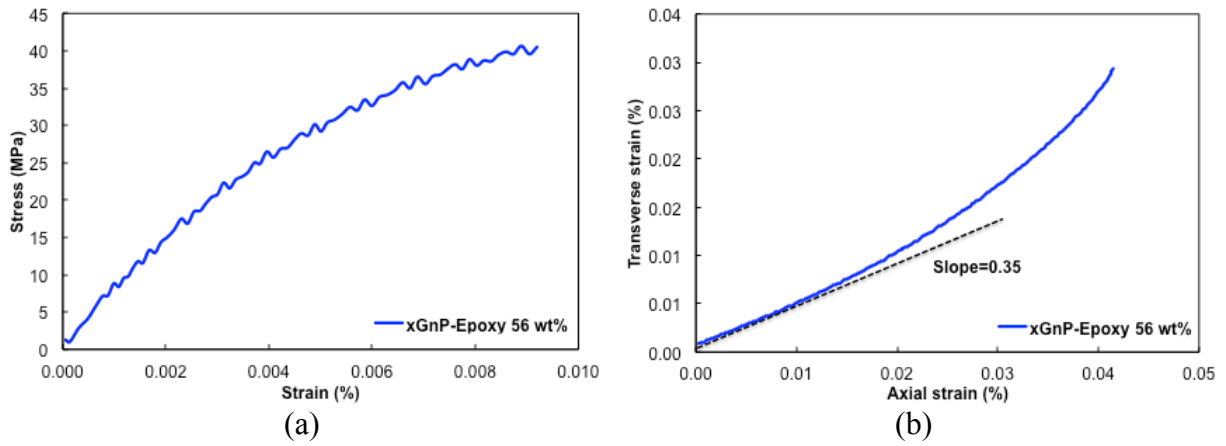


Figure 58: Typical (a) stress-strain curve (b) axial-traverse strain curve for xGnP-epoxy nano-composite

Many useful properties of the material can be obtained from this test. These properties include elastic modulus, yield and ultimate strengths, yield and ultimate strain, Poisson's ratio, bulk modulus, etc. Reduced data of stresses and strains are shown in Figure 59 and Figure 60.

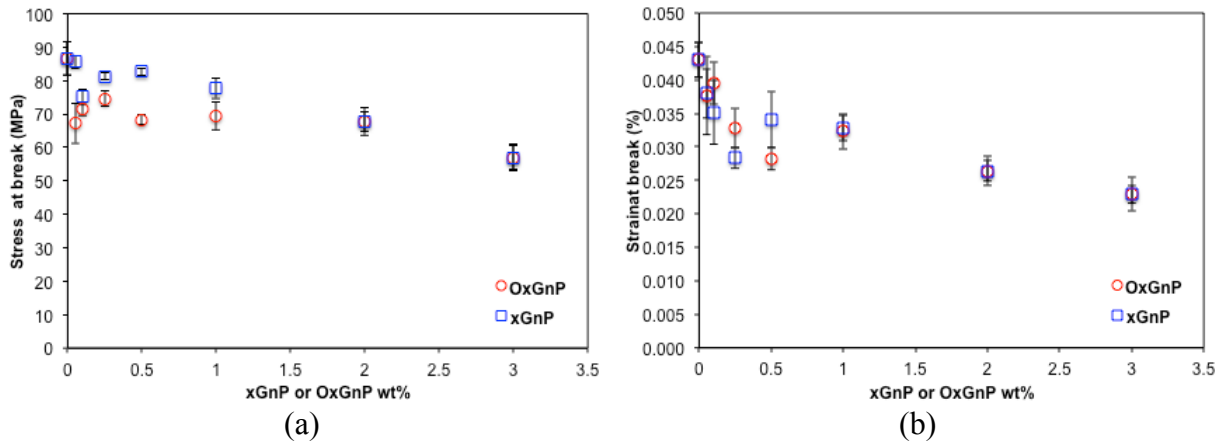


Figure 59: Stress-strain response of xGnP-Epoxy roll-milled nano-composite (a) stress at break (b) strain at break.

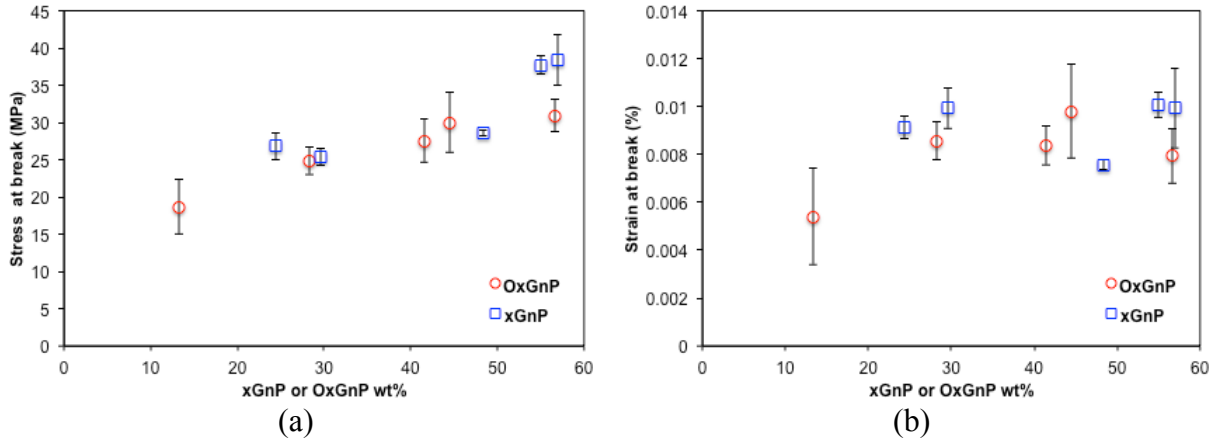


Figure 60: Stress-strain response of xGnP-Epoxy laminated nano-composite (a) stress at break (b) strain at break.

The incorporation of xGnP into Epoxy caused a decline in both stress and strain at failure for both the roll nano-composite and the laminated nano-composite, as seen in Figure 59 and Figure 60. With increase of xGnP concentration, the roll nano-composite showed further decrease in the maximum strain and stress (Figure 59). OxGnP did not show a clear improvement in terms of mechanical properties compared to xGnP.

The laminated nano-composites showed some decrease in strength compared to neat epoxy. However, the lamination of the xGnP or OxGnP papers showed improvement in the strength compared to a single paper. This may be due to the increase in the length of fracture path, which falls between the layers. Slight improvement in strength was noticed with the increase of xGnP or OxGnP loadings in Figure 60 (a). The same behavior is noticed for the maximum strain value in Figure 60 (b). At high concentrations of the xGnPs, the translation of xGnP's high strength to the nano-composite is limited, which might be the result of chemical bond absence between the Epoxy matrix and the xGnP.

Poisson's ratio for the roll-milled nano-composites value remained almost similar compared to neat epoxy in Figure 61 (a) the deviation of Poisson's ratio value was within the experimental error. However, at high xGnP or OxGnP loadings, Poisson's ratio value dropped, as seen in Figure 61 (b)

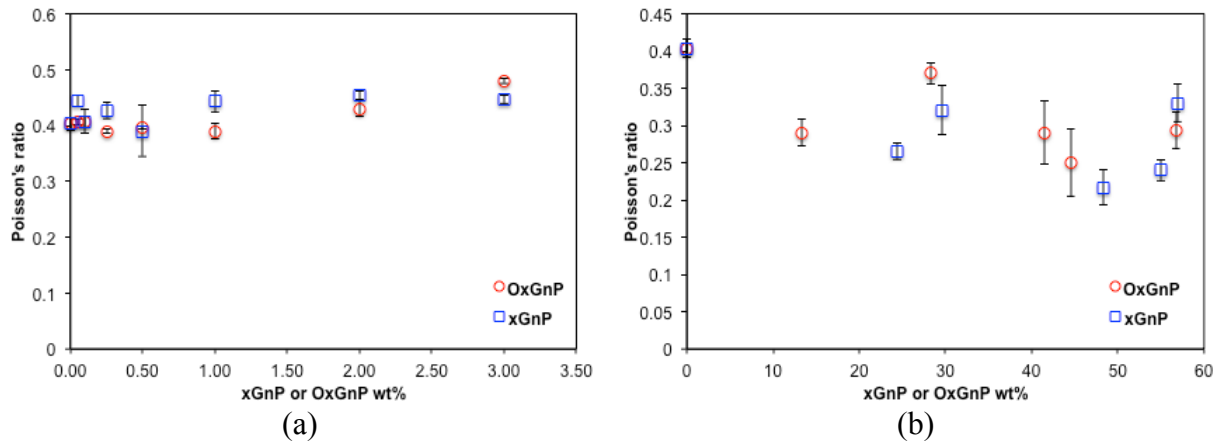


Figure 61: Poisson's ratio of (a) Roll-milled (b) laminated xGnP-Epoxy nano-composite

### 2.3.5.3 High strain rate utilizing SHPB

#### 2.3.5.3.1 Compression test

SHPB, also called Kolsky bar, which was first developed by Kolsky in 1949 [57], is a well-known technique for investigating materials at high strain-rates. The dynamic experiments were conducted at the blast and impact dynamics lab at the University of Mississippi, using steel bars for striker, incident, and transmitted, with diameters of 19.02 mm. The length of the striker bar is 91.4 cm (see Figure 62). The pressure of the gas gun was varied from 10-55 psi. Nine repeated experiments were conducted for each material at a strain rate of 800-6600  $S^{-1}$ . 1.6 annealed copper disks were employed as pulse shapers to conduct tests at constant strain rates with a linear incident ramp, while allowing the sample to be loaded under dynamic stress equilibrium. Small amounts of petroleum jelly were applied to hold the pulse shaper in place.

Two strain gages were mounted in the middle of incident and transmitted bars. The strain gauge attached on the incident bar was used to record the incident and reflected waves. The other strain gauge is needed to measure the wave transmitted through the specimen. The sample sits sandwiched between the incident and transmitted bars. The signals from the strain gauges were recorded by the data acquisition system shown in Figure 63.



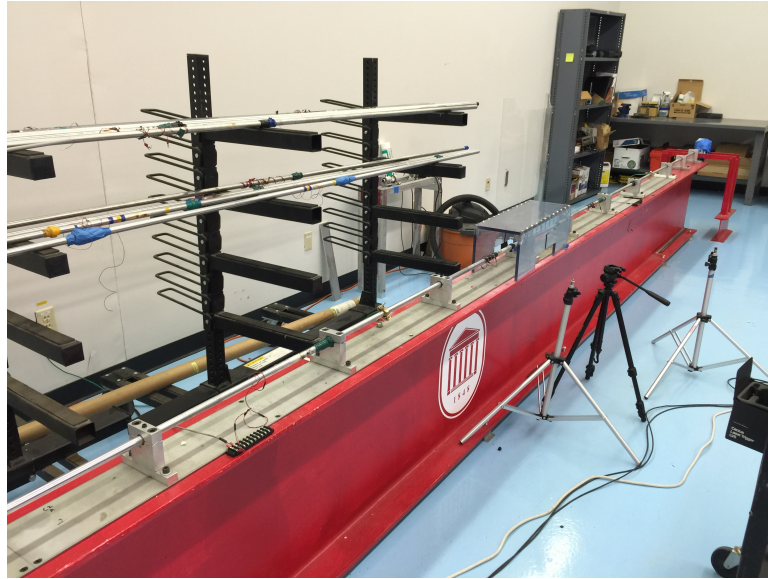


Figure 62: SHPB setup used to conduct the experiments

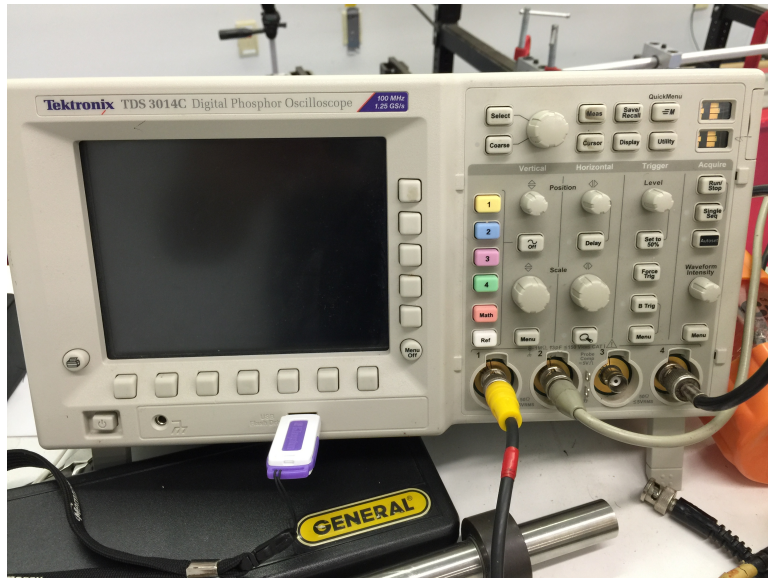


Figure 63: SHPB data acquisition system

A HyperVision HPV-2 High-Speed Video Camera (purchased from Shimadzu Scientific Instruments) was used to record the compression test. This camera is capable of recording up to 1 million frames per second (fps), with fixed resolution (312 Å~ 260 pixels). Two 1000 W strobes (purchased from Photogenic PowerLights, PL2500DR) were employed to properly expose the samples for high frame-rate recording, Figure 64 shows the setup of strobes and camera. The camera and strobes were triggered using a sound trigger system based on the impact sound of striker and incident bars.

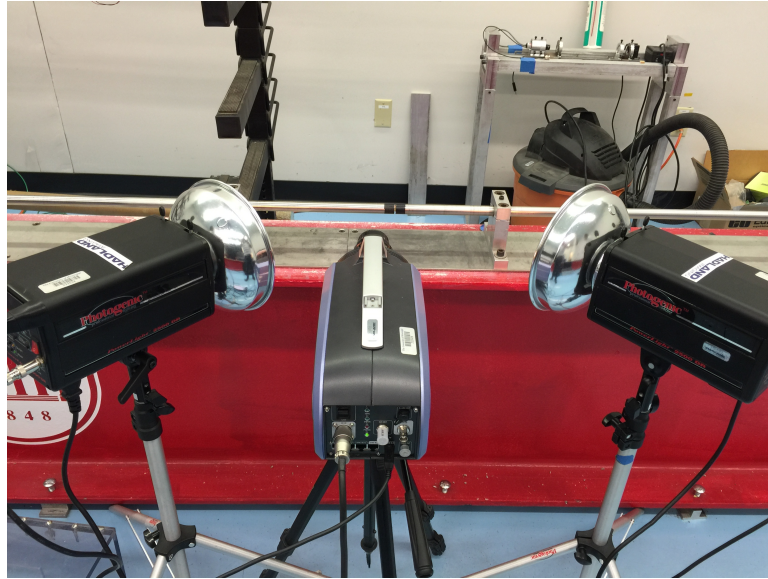
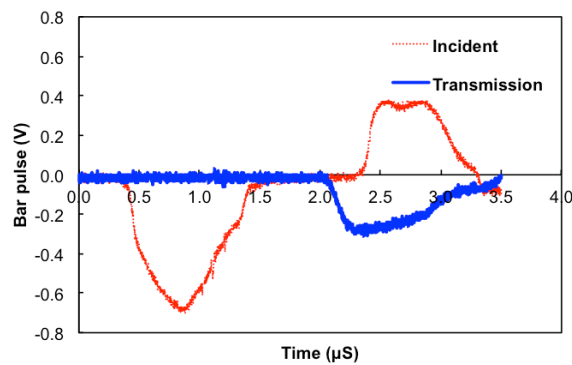


Figure 64: Camera and strobes configuration during SHPB test.

The graphene-based composites were cut into cuboid specimens for dynamic compression testing. The specimens had a side length of  $\sim 7\text{mm}$  and  $\sim 3\text{mm}$  thick. Dynamic compression tests utilizing SHPB, were carried out on specimens xGnP-Epoxy, OxGnP-Epoxy, xGnP-PU, OxGnP-PU and xGnP-PEI at several strain rates to compare their dynamic mechanical behavior in terms of energy absorption, peak stress and peak strain. Typical stress wave pulses (incident, reflected, and transmitted) acquired from strain gages attached to the incident and transmission bars are shown in Figure 65 (a)



(a)

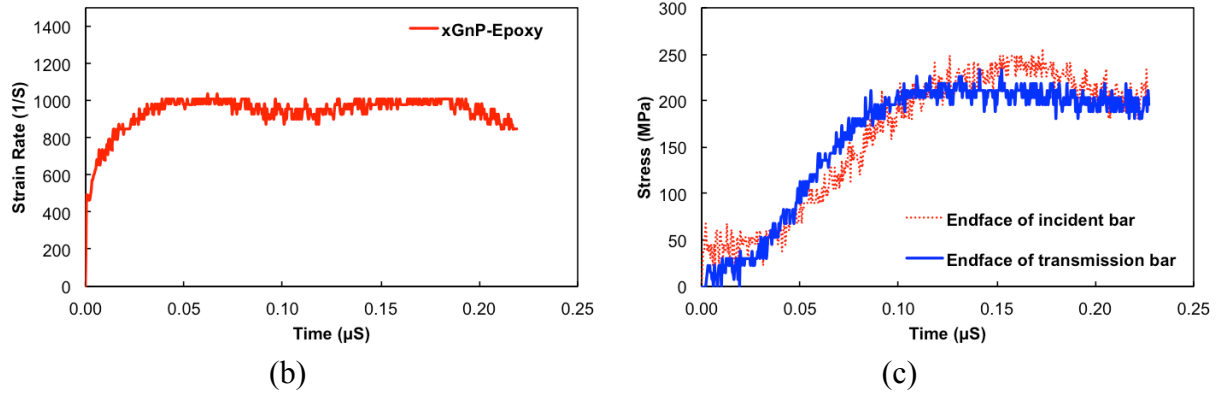


Figure 65: Typical test results of epoxy specimen (a) Incident, reflected and transmitted pulses (b) Strain rate (c) Validation of the equilibrium stress state

Based on 1-D wave propagation, under stress equilibrium, the resultant stress-strain data can be calculated using the following equations, which are:

$$\dot{\epsilon} = -2 \frac{C_0}{L_s} \epsilon_r(t) \quad (2)$$

$$\epsilon = -2 \frac{C_0}{L_s} \int_0^t \epsilon_r(t) dt \quad (3)$$

$$\sigma = \frac{A_0}{A_s} E_0 \epsilon_t(t) \quad (4)$$

Where:

$\epsilon_r(t)$  and  $\epsilon_t(t)$ : Reflected and transmitted strain histories, respectively.

$A_0$ : The cross-sectional area of the bars.

$E_0$  and  $C_0$ : Young's modulus and elastic wave speed in the bar material, respectively.

$L_s$  and  $A_s$ : Initial cross-sectional area and length of the specimen, respectively.

By calculating the developed stresses at opposite faces of all specimens, the state of dynamic equilibrium has been achieved during most of the tests. Figure 65 (b) shows a typical validation of the stress equilibrium obtained by SHPB compression test. Tests that failed to meet the stress equilibrium condition are not reported in this study. Figure 65 (c) shows the

typical curve of the generated strain rate. The curve confirms that reasonably constant strain rate is achieved during most of the pulse duration. Stress strain curves reported up to failure of each specimen and were recorded by the camera.

By implementing SHPB dynamic compressive test results, it was possible to calculate the true stress-strain curve for each material using equations (5) and (6). The material model developed was compared with experimental results reported in section 2.4.2. All results are based on the true values of stress, strain and strain rate (see equations (5)-(7)).

$$\sigma_t = \sigma_e(1 - \varepsilon_e) \quad (5)$$

$$\varepsilon_t = -\ln(1 - \varepsilon_e) \quad (6)$$

Where:

$\sigma_t$ : True stress

$\varepsilon_t$ : True strain

$\sigma_e$ : Engineering stress

$\varepsilon_e$ : Engineering strain

Then the true strain rate ( $\dot{\varepsilon}_t$ ) can be converted from an engineering strain rate, using equation (7) we get:

$$\dot{\varepsilon}_t = \dot{\varepsilon}_e / (1 - \varepsilon_e) \quad (7)$$

Figure 66 shows typical true stress–strain curves for xGnP 0.5 wt. % with each polymer at strain-rates of ~3400/s. The high-speed camera video was synced with the stress-strain curve. Once cracks initiate, the stress-strain curves were trimmed for Epoxy and PEI based nanocomposites as the material response when cracks exist includes complex behavior that is beyond the scope of this study (Figure 67 (d) and Figure 68 (d)). However, PU did not fail under compressive load (Typical for hyperelastic material), but excessive deformation was seen at a certain stage of loading. At this stage of loading, PU starts getting outside of the

bars. This will affect the calculated stress, which is based on total sample area. The stress strain curves for PU were trimmed once the video showed a significant portion of the PU getting outside the bar diameter (Figure 69 (e)). The high-speed images associated with the SHPB loading process shown in Figure 66 are listed in Figure 67 through Figure 69.

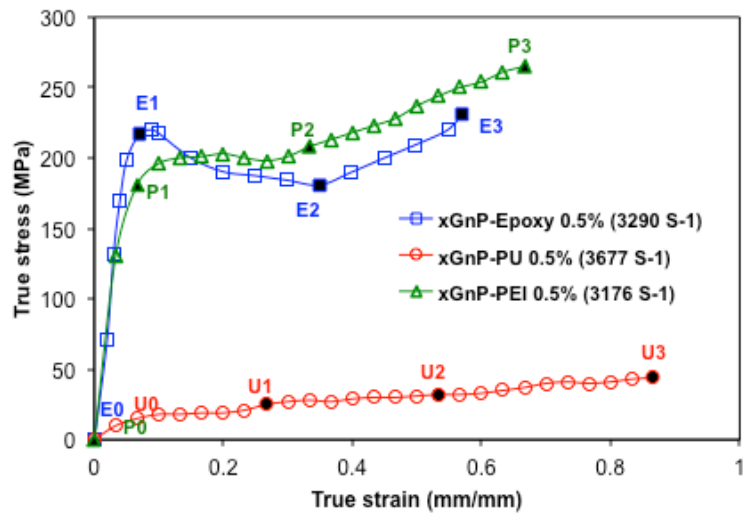


Figure 66: Typical dynamic compressive true stress-strain curve of xGnP-Polymer

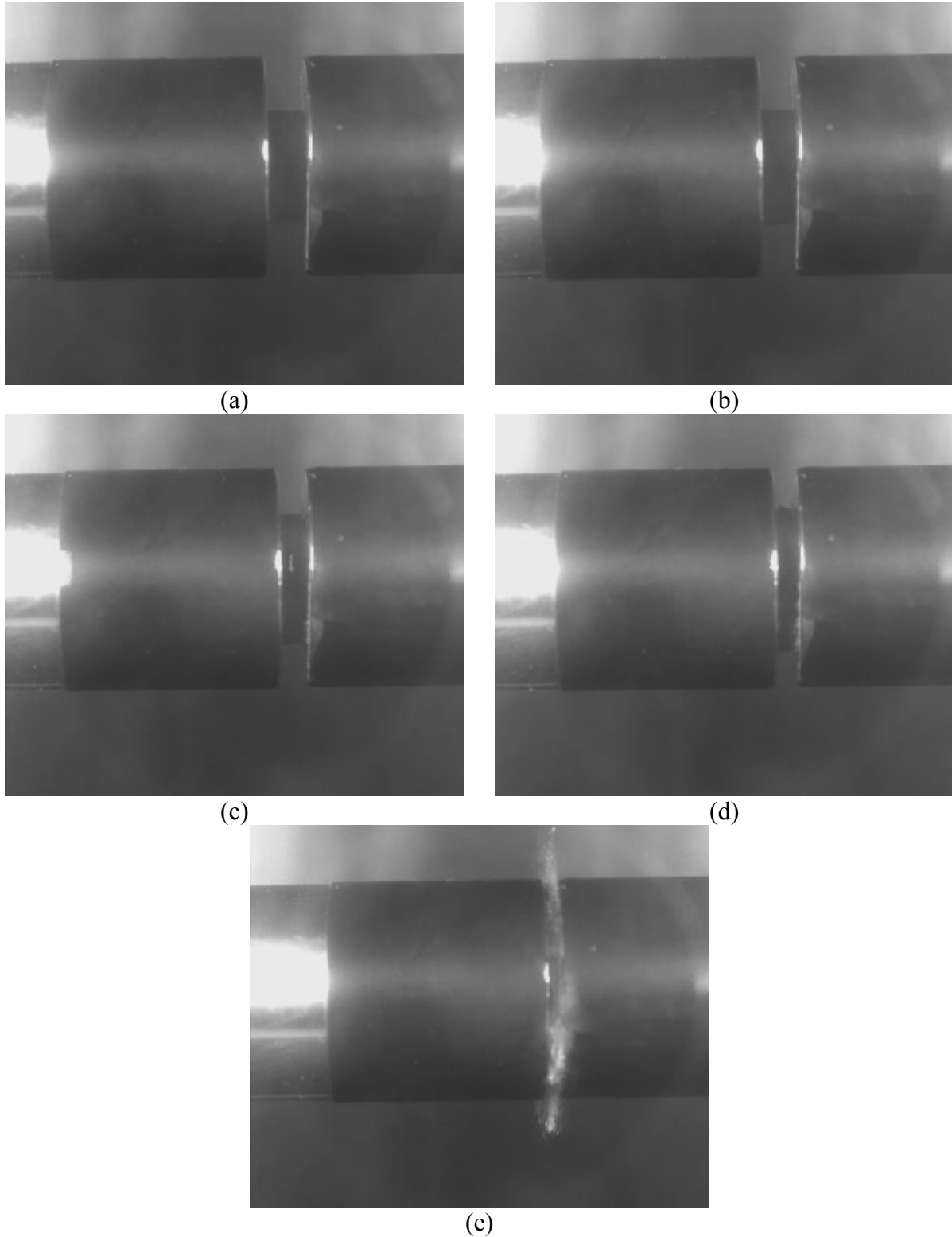


Figure 67: High-speed images associated with stress history during SHPB compression loading process of xGnP-Epoxy 0.5 wt. % specimen at strain-rate of 3290/s (a) E0 (b) E1 (c) E2 (d) E3 (e) Beyond failure

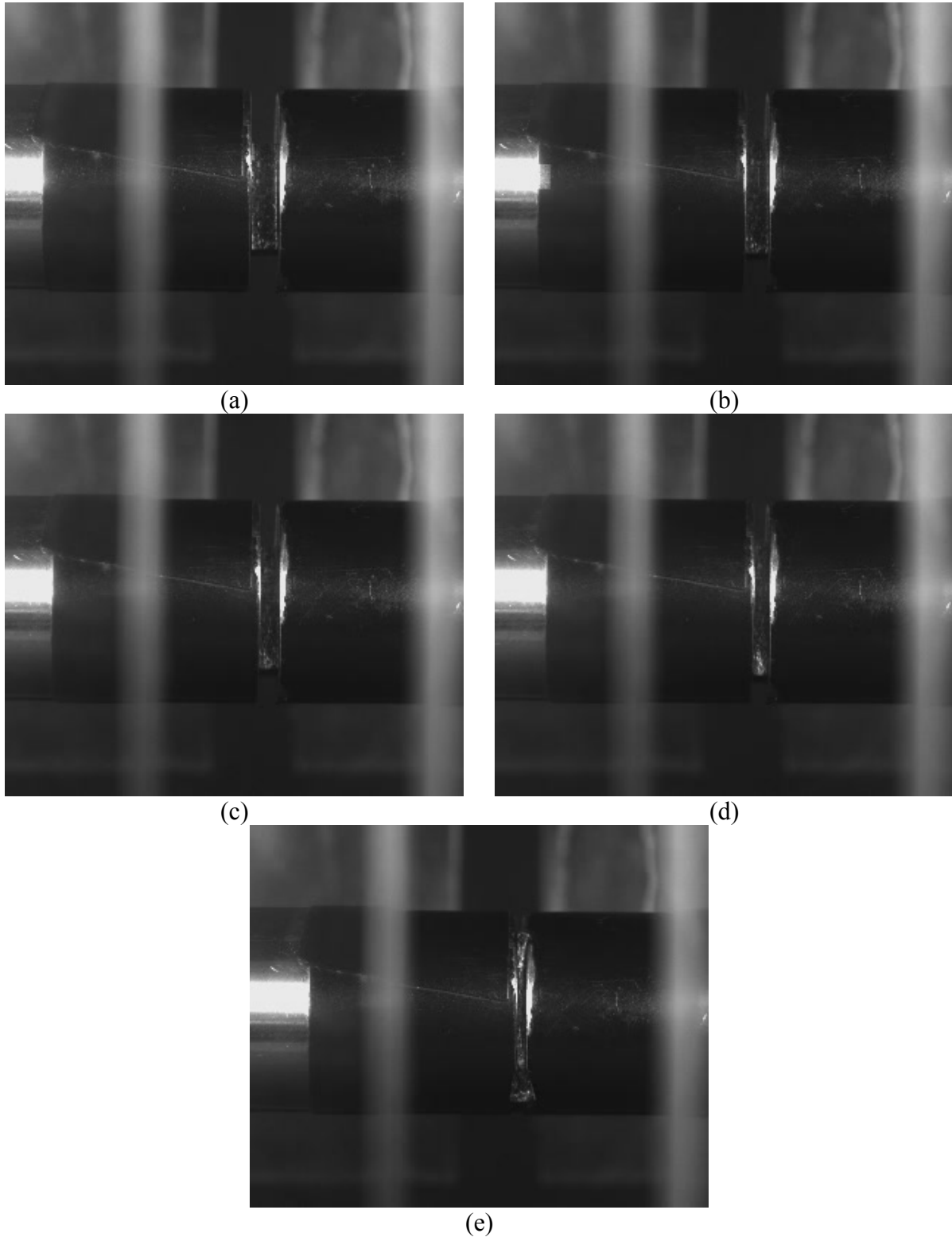


Figure 68: High-speed images associated with stress history during SHPB compression loading process of xGnP-PU 0.5 wt. % specimen at strain-rate of 3677/s (a) U0 (b) U1 (c) U2 (d) U3 (e) Sample out of SHPB

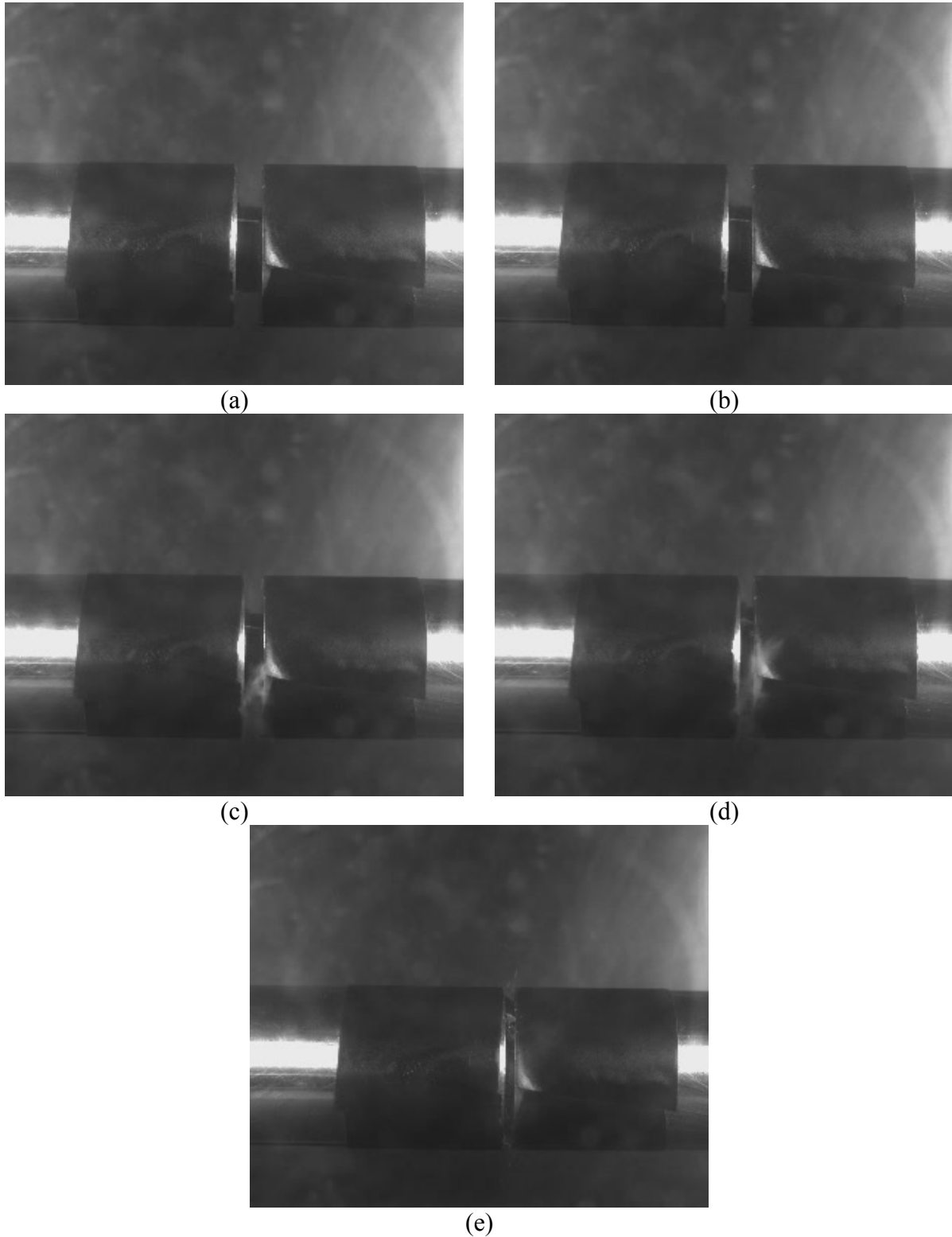


Figure 69: High-speed images associated with stress history during SHPB compression loading process of xGnP-PEI 0.5 wt. % specimen at strain-rate of 3176/s (a) P0 (b) P1 (c) P2 (d) P3 (e) Beyond failure



Toughness for all tested samples was calculated based on the area under the stress-strain curve, and values are shown in Figure 70 through Figure 72. Samples loaded at strain rate less than  $2000 \text{ S}^{-1}$  did not fail. Thus, the toughness values for these samples were extrapolated from the material model developed in section 2.4.2 for fair comparison.

Substituting epoxy by 0.5 wt. % xGnP showed slight improvement in toughness at all strain rates. However, substituting by 1% xGnP showed decrease in toughness at strain rates below  $2900 \text{ S}^{-1}$ . In contrast, there was improvement above that strain rate. The steeper slope of the trend line indicates more sensitivity to strain rate. The xGnP-Epoxy papers at 57 wt. % showed significant reduction in the toughness value at all strain rates (Figure 70 (a)).

For OxGnP-Epoxy nano-composite, substituting epoxy by either 0.5 or 1 wt. % OxGnP showed slight improvement in toughness at all strain rates with slight increase in sensitivity. However, The OxGnP-Epoxy papers at 57 wt. % showed significant reduction in the toughness value at all strain rates (Figure 70 (b)).

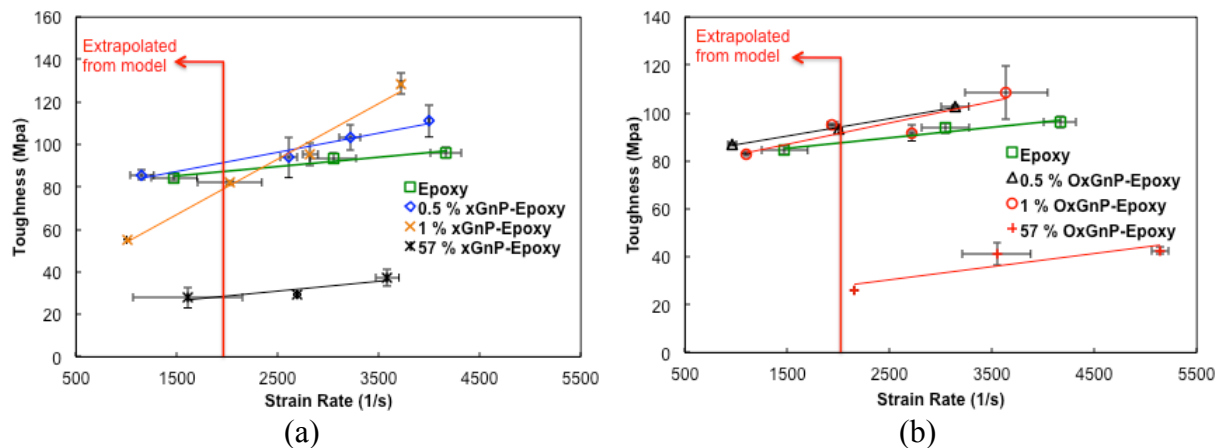


Figure 70: Toughness sensitivity to strain rate for (a) xGnP-Epoxy (b) OxGnP-Epoxy

Substituting PU by 0.2, 0.5 or 1.0 wt. % xGnP showed decrease in toughness at all strain rates coupled with decrease in sensitivity (Figure 71 (a)). The same trend is seen for OxGnP at 0.2 or 1.0 wt. % OxGnP-PU. However, 0.2 wt. % OxGnP-PU showed increase in both toughness value and sensitivity to strain rate (Figure 71 (b)).

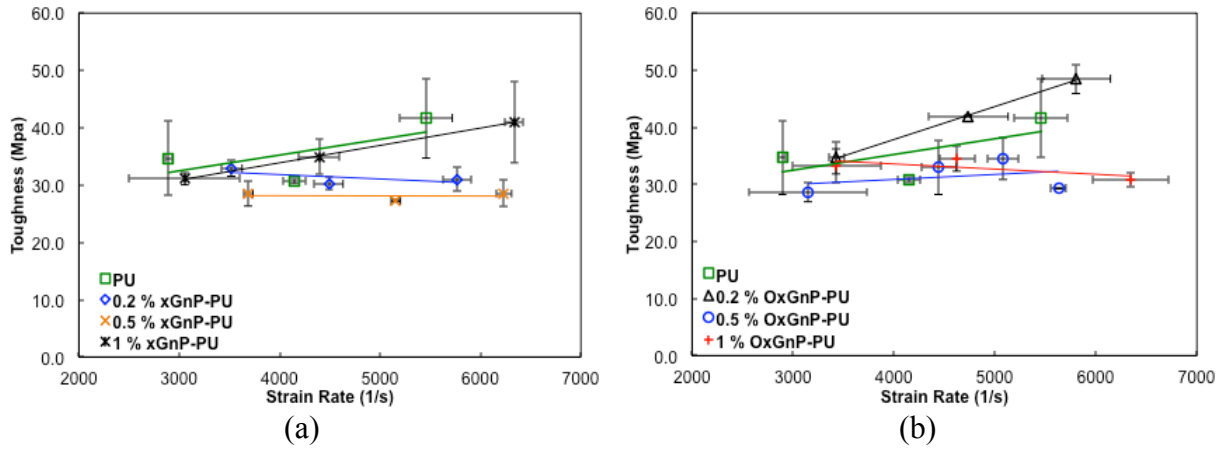


Figure 71: Toughness sensitivity to strain rate for (a) xGnP-PU (b) OxGnP-PU

Replacing PEI by 0.5 wt. % xGnP showed slight improvement in toughness at strain rates above  $2700 \text{ S}^{-1}$  and decrease below that strain rate. That change is associated with higher sensitivity to strain rate. xGnP-PEI 0.5 wt. % showed similar behavior as neat PEI. The xGnP-PEI 50 wt. % showed significant reduction in the toughness value at all strain rates (Figure 72).

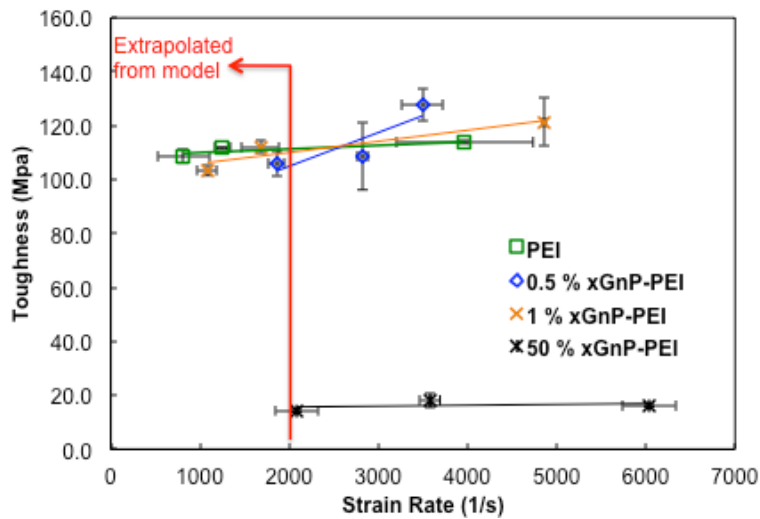


Figure 72: Toughness sensitivity to strain rate for xGnP-PEI

## 2.4 Material modeling

To model materials in Autodyn, strength model, equation of state (EoS), and failure model parameters need to be defined.

### 2.4.1 Equation of state

Equation-of-state governs the thermodynamic properties of a material (e.g. pressure and energy) to the density and temperature. Hypervelocity impacts generate high pressures and temperatures, leading to possible phase changes based on the material properties. At the maximum simulated impact velocity of 10 km/s, a phase change is expected to occur.

In this research, linear EoS was used to represent the nano-composite. Equation (8) shows the EoS used to model the nano-composites.

$$p = k\mu \quad (8)$$

Whereas,  $k$  is the material bulk modulus,  $\mu$  is volumetric strain, as given by Equations (9) and (10) respectively.

The Material bulk modulus  $k$  for isotropic material can be obtained from the following equation:

$$k = \frac{E}{3(1 - 2\nu)} \quad (9)$$

$\rho$  is the material density; and  $\rho_0$  is the reference density.

$$\mu = \frac{\rho}{\rho_0} - 1 \quad (10)$$

Where  $E$  is the elastic modulus,  $\nu$  poisson's ratio

### 2.4.2 Constitutive model

Constitutive models for material provide the foundation of finite element analysis and are an intrinsic part of computer simulation processes; multiple constitutive material models were developed to precisely define the stress-strain relationship of polymeric materials [58]-[67]. The DSGZ model is suited for prediction of stress-strain responses of glassy and semi-

crystalline polymers under different strain rates and temperatures. This model was proposed by Duan et al. [62], where the DSGZ model was employed to describe the mechanical response of polymers at varying temperatures and strain rates. Many studies proved that the DSGZ model could successfully predict the entire range of stress–strain responses of various glassy and semi crystalline polymers [62], [61], [67].

The DSGZ constitutive model is used to predict the dynamic plastic flow behavior of polymers at varying strain rates. The experimental outcomes from SHPB provide sufficient help in calibrating the constitutive material model to predict the mechanical response under various loading conditions. The empirical model is given by equation (11).

$$\sigma(\varepsilon, \dot{\varepsilon}, T) = K. f(\dot{\varepsilon}, T) \{ \sigma_h(\varepsilon) + [\sigma_{ey}(\varepsilon, \dot{\varepsilon}, T) - \sigma_h(\varepsilon)] e^{\varepsilon \{ \ln(g(\dot{\varepsilon}, T)) - C_4 \}} \} \quad (11)$$

Where:

$$\sigma_h(\varepsilon) = (e^{C_0 \cdot \varepsilon} + \varepsilon^{C_1} - C_2)(1 - e^{-\alpha \cdot \varepsilon})$$

$$\sigma_{ey}(\varepsilon, \dot{\varepsilon}, T) = \varepsilon \frac{\left[ 1 - \frac{\varepsilon}{C_3 \cdot f(\dot{\varepsilon}, T)} \right]}{C_3 \cdot f(\dot{\varepsilon}, T)}$$

$$f(\dot{\varepsilon}, T) = (\dot{\varepsilon})^m \cdot e^{\frac{a}{T}}$$

Yield strain, which corresponds to yield stress  $\sigma_y$  before softening.

$$\varepsilon_y = C_3 \cdot (\dot{\varepsilon})^m \cdot e^{\frac{a}{T}} \quad (12)$$

Yield stress at any strain rate:

$$\sigma_y(\varepsilon_y, \dot{\varepsilon}, T) = K. f(\dot{\varepsilon}, T) \{ \sigma_h(\varepsilon_y) + [\sigma_{ey}(\varepsilon_y, \dot{\varepsilon}, T) - \sigma_h(\varepsilon_y)] e^{\varepsilon_y \{ \ln(g(\dot{\varepsilon}, T)) - C_4 \}} \} \quad (13)$$

In this study, the temperature effect was not investigated; thus the multiple  $e^{\frac{a}{T}}$  was assumed to be constant A. The equation parameters were calibrated by analysis and regression of SHPB experimental results based on the true plastic stress-strain.

Figure 73 through Figure 75 show the stress-strain relationship obtained from SHPB for the tested material at different strain rates and compare them with the DSGZ prediction. The model parameters are summarized in Table 4 through Table 5. The results show that the DSGZ model successfully characterized the deformation during compressive dynamic loading of nano-composites, with fair agreement with the experimental results obtained from SHPB. The DSGZ model can be implemented in Autodyn simulations using the Fortran 90 code described in APPENDIX A.

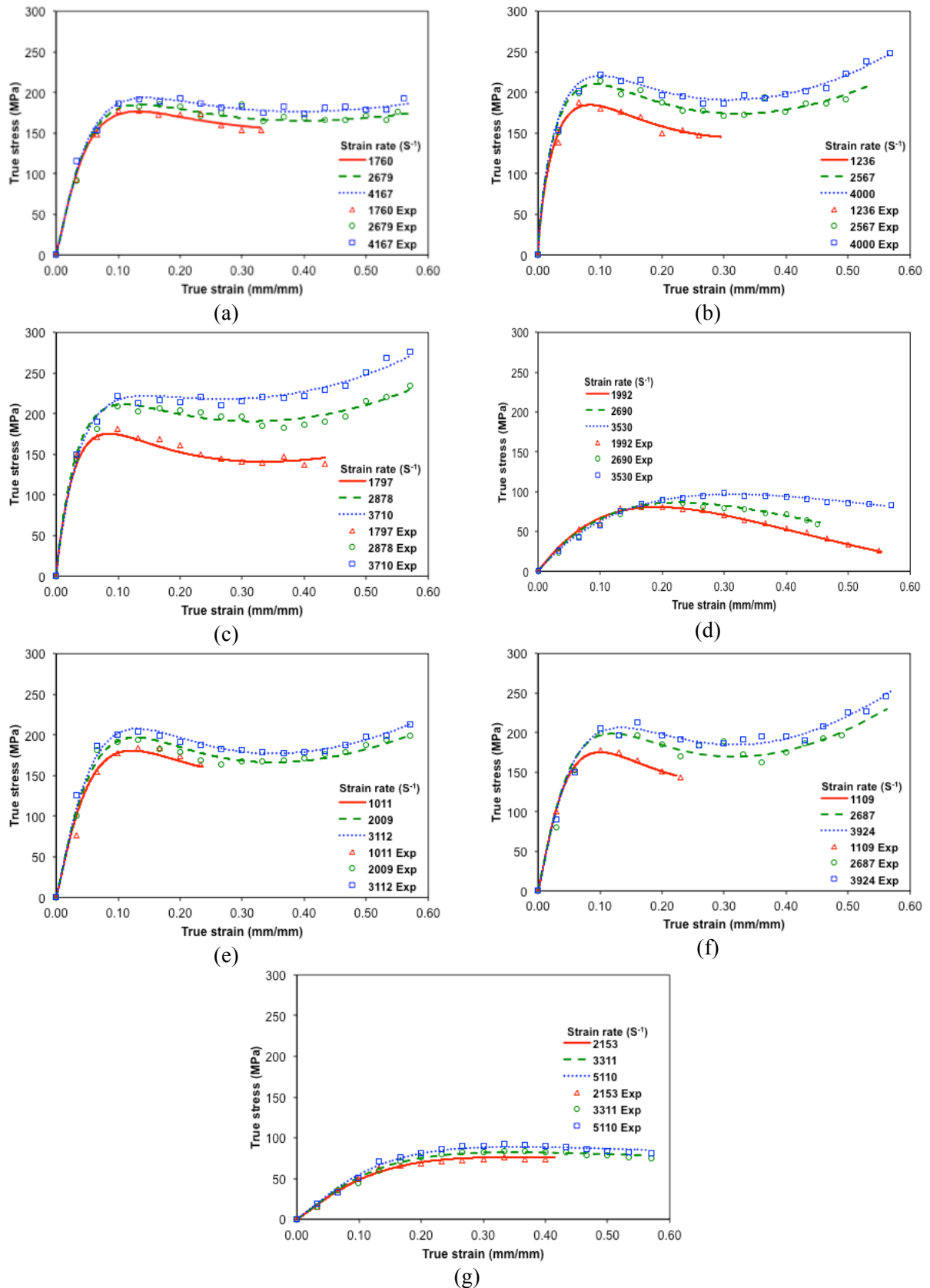


Figure 73: DSGZ Model fit model for (a) Epoxy (b) xGnP-Epoxy 0.5 wt. % (c) xGnP-Epoxy 1 wt. % (d) xGnP-Epoxy 57 wt. % (e) OxGnP-Epoxy 0.5 wt. % (f) OxGnP-Epoxy 1 wt. % (g) OxGnP-Epoxy 57 wt. %

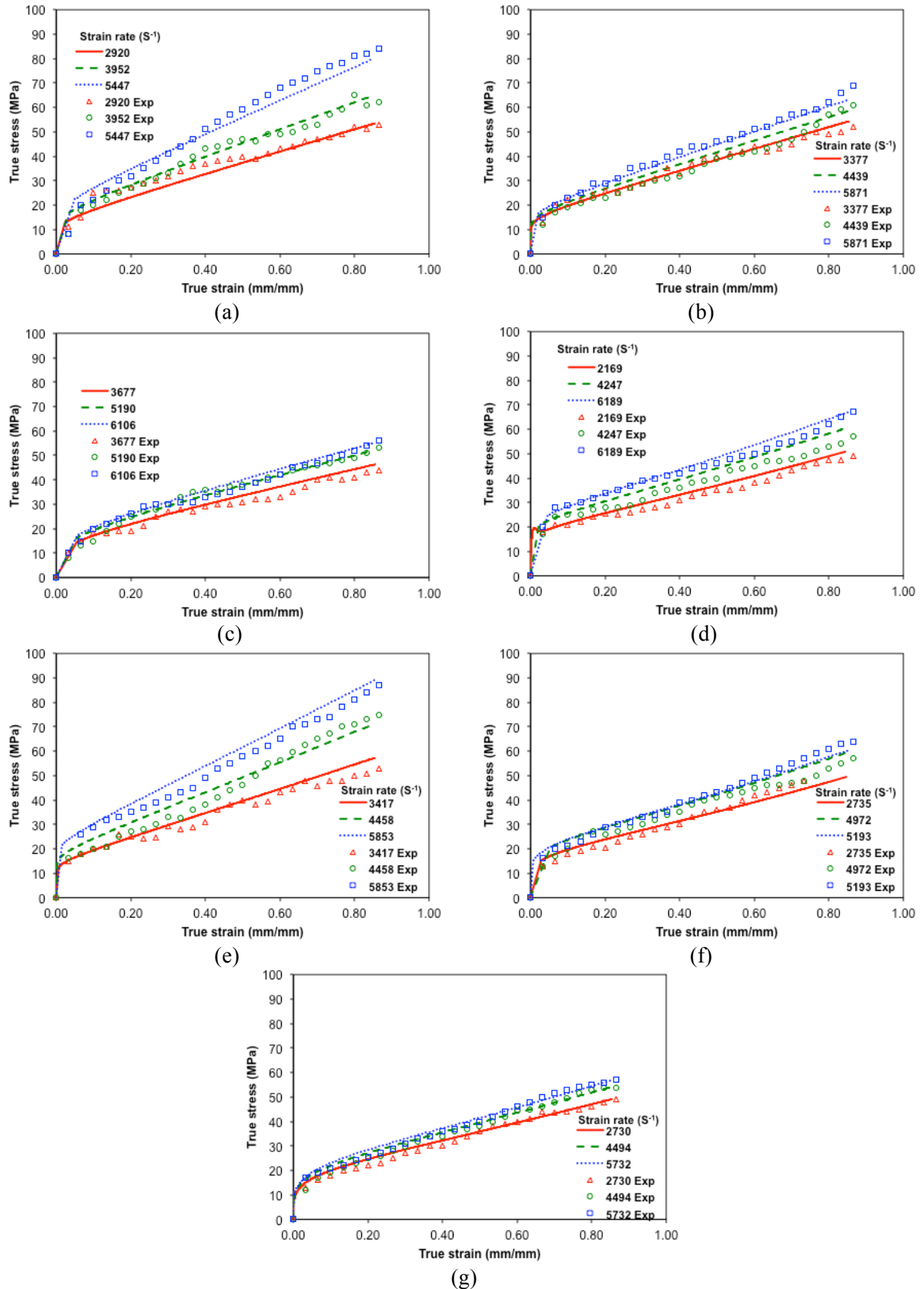


Figure 74: DSGZ Model fit model for (a) PU (b) xGnP-PU 0.2 wt. % (c) xGnP-PU 0.5 wt. % (d) xGnP-PU 1 wt. % (e) OxGnP-PU 0.2 wt. % (f) OxGnP-PU 0.5 wt. % (g) OxGnP-PU 1 wt. %

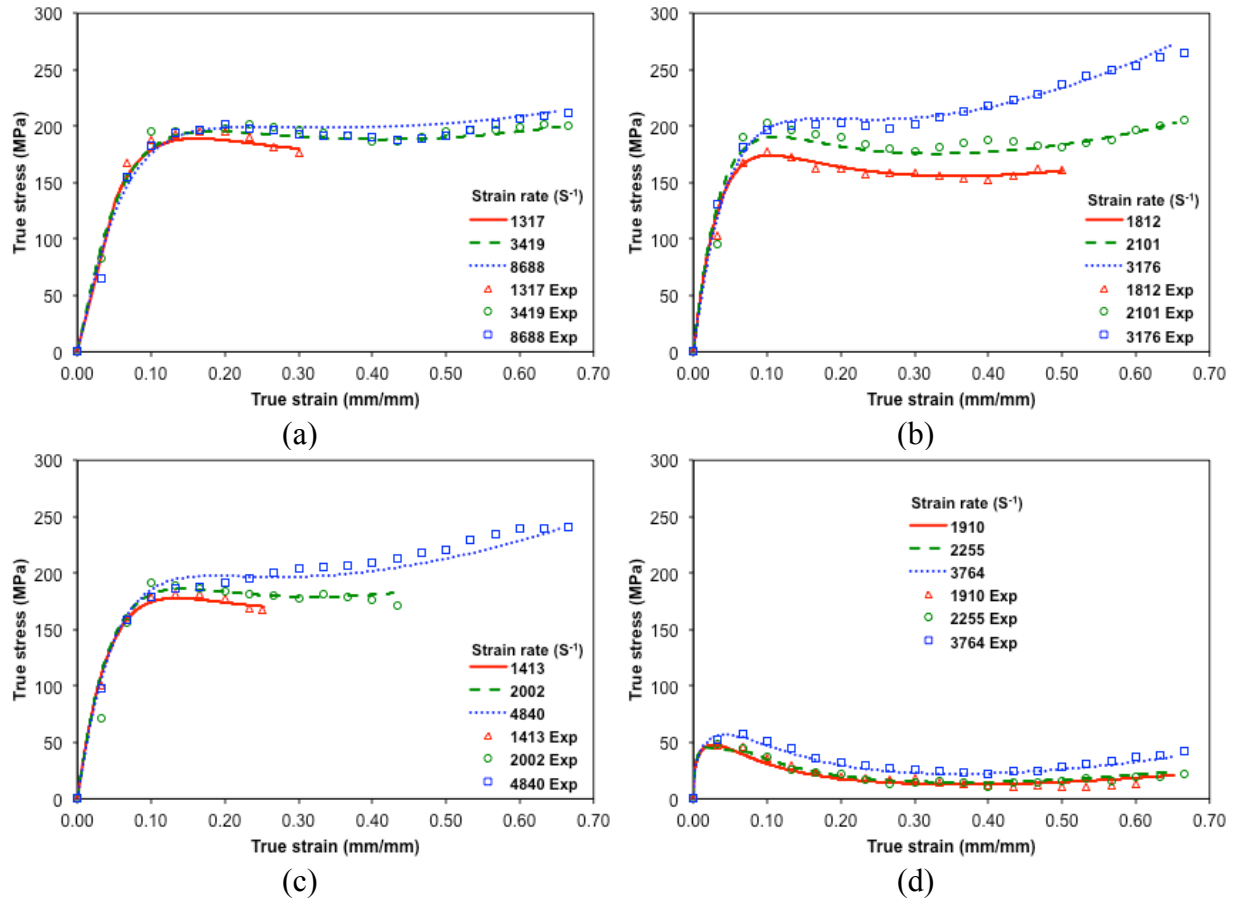


Figure 75: DSGZ Model fit model for (a) PEI (b) xGnP-PEI 0.5 wt. % (c) xGnP-PEI 1 wt. % (d) xGnP-PEI 50 wt. %

Table 4: Fitting parameters for Epoxy based nano-composites

Name	C0	C1	C2	m	A	K	C3	C4	$\alpha$
Epoxy	1.571	-0.671	0.162	0.153	5.535	2.515	0.006	32.97	17.90
0.5 % xGnP-Epoxy	1.190	-0.542	-0.431	0.131	2.892	6.017	0.014	26.85	21.90
1 % xGnP-Epoxy	3.156	-1.039	-4.025	0.667	0.084	1.134	0.006	29.73	23.61
57 % xGnP-Epoxy	-2.438	-0.575	1.615	0.292	1.027	8.438	0.024	10.78	6.16
0.5 % OxGnP-Epoxy	1.566	-0.584	2.054	0.149	1.272	28.587	0.042	11.93	16.06
1 % OxGnP-Epoxy	1.749	-0.549	2.258	0.268	1.221	13.082	0.019	15.99	26.07
57 % OxGnP-Epoxy	-1.693	-0.518	-3.531	0.186	1.040	3.197	0.023	14.87	9.88

Table 5: Fitting parameters for PU based nano-composites

Name	C0	C1	C2	m	A	K	C3	C4	$\alpha$
PU	0.03	0.00	1.987315	0.648929	0.037886	195.6132	0.010419	404781.4	393843
0.2 % xGnP-PU	0.025159	0.000771	1.988901	0.275293	1.226461	144.6943	0.005225	64800.18	113545.9
0.5 % xGnP-PU	0.016275	0.001084	1.990468	0.348119	1.08273	104.9328	0.00212	64800.18	113545.9
1 % xGnP-PU	0.408109	0.021185	1.68845	0.257627	1.372768	7.114182	0.004027	178.4168	2646.497
0.2 % OxGnP-PU	0.115202	0.002632	1.9555	0.821507	0.002489	195.0467	0.030144	4388.418	912.8154
0.5 % OxGnP-PU	0.598773	0.057774	1.466444	0.30561	0.020187	184.1425	0.264678	2255.533	5492.588
1 % OxGnP-PU	0.521258	0.091802	1.397383	0.195371	0.038602	236.2139	0.011171	1741.084	1953.068



Table 6: Fitting parameters for PEI based nano-composites

Name	C0	C1	C2	m	A	K	C3	C4	$\alpha$
PEI	1.306419	-0.61154	-0.58265	0.073834	20.34668	1.271657	0.002313	49.60687	19.09083
0.5 % xGnP-PEI	1.757806	-0.93455	-0.60591	1.02812	0.001944	7.81596	0.016094	10.73155	28.77562
1 % xGnP-PEI	1.520754	-0.935	-0.63273	0.267126	0.626761	9.404709	0.022197	9.149204	25.14796
50 % xGnP-PEI	1.79178	-0.65773	2.808651	0.842776	0.017778	1.174937	0.00483	27.99883	56092.86

### 2.4.3 Artificial Neural Networks

The Artificial Neural Network (ANN) approach is used to model the behavior of the material by varying the added graphene content and strain rate. ANNs are used in diverse disciplines including: statistics, psychology, software development, and engineering. Pham et al. [68] used ANN modeling, with the Purlin function as an activation function, to calculate the compressive strength and strain of fiber reinforced polymer confined square columns. The proposed model showed excellent correlation to the experimental data, performing better than the mechanical models developed before. Setti et. al.[69] Proposed an ANN model to predict the stress-strain curve of titanium alloy as a function of the volume fractions of  $\alpha$  and  $\beta$ . They used a combination of activation functions (tan-sigmoid, log-sigmoid, and Purlin) and training algorithms (cascade-forward back-propagation, feed-forward back-propagation, and layer recurrent). The best performing network was a combination of the log sigmoidal activation function and the layer recurrent training algorithm. Najjar et. al. [70] implemented the recurrent (dynamic) ANN to predict the stress-strain behavior of soils under various initial confining pressures, densities, and compaction states. In their work, the proposed ANN model was used to overcome the complexity, practicality and accuracy of the available mechanical constitutive models. The final ANN model showed excellent statistical accuracy measures when compared to the experimental data.

ANN emulates the human brain structure. An ANN network comprises many computational nodes called neurons spread over multiple (input, hidden and output) layers. The neurons are connected by links, which have their own connection weights. The connection weight is

modified during the training process until a satisfying mapping of the relationship between the inputs and the outputs is obtained [71]. ANN is a data-driven computational tool that excels at mapping the relationships between specific inputs and desired outputs. Typical ANN architecture used in this study is shown in Figure 76.

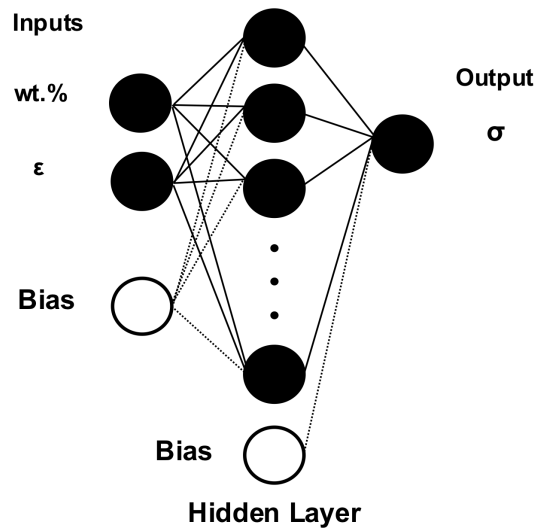


Figure 76: Sample of ANN architecture for strain-controlled model

Formulating the ANN models relies on training the network with enough examples in order for the network to capture the governing relationships between the desired inputs and expected outputs. The feed-forward back-propagation algorithm implemented in this study that has proven to be very efficient in modeling various engineering applications as discussed in references [71]-[73]. The proposed networks are composed of three layers: input, hidden and output. The nodes (i.e. neurons) in the input layer are connected to all nodes in the hidden layer, which, in turn, are connected to all nodes in the output layer. In ANN modeling, there are many variables to be considered other than the connection weights, such as: the number of hidden layers, number of hidden nodes in each layer, and many others. In engineering problems, it is recommended to use one hidden layer [71]-[73]. The maximum number of hidden nodes can be calculated by using equation (14)

$$HN = \frac{D-NO}{C \cdot (IN+NO+1)} \quad (14)$$

Where:

D: the number of training data sets.

NO: the number of outputs.

IN: the number of inputs

C: the constant determining the number of data points allocated to each connection weight.

In this study, the optimum number of hidden nodes is chosen using the procedure outlined in Najjar et. al. [70]. The network is trained starting from 1 hidden node and for 20,000 iterations on the specified structure. Then, hidden nodes are added one by one until the maximum number of hidden nodes allowed is reached. The network with the best Averaged Squared Error (ASE) is chosen as the best prediction network for this scenario. Then, the same process is performed for the structure starting with two hidden nodes, and so on, until the maximum number of hidden nodes is reached. The best of the best prediction network structures is chosen as the final ANN prediction model.

In order to prevent the ANN models from being biased towards a specific input, the values of all the inputs are normalized using equation (15).

$$X_n = \frac{X - X_{\max}}{X_{\max} - X_{\min}} \quad (15)$$

Where:

$X_n$ : the normalized value

X: the actual value

$X_{\max}$  and  $X_{\min}$ : the anticipated maximum and minimum values of X, respectively.

#### 2.4.3.1 Quasi static stress-strain

In this section, the mechanical behavior of xGnP-PEI nano-composites is investigated and modeled utilizing the ANN approach. The xGnP-PEI manufactured films were tested using

(DMA) employing standard stress controlled tension module for several xGnP loadings ranging from 0~97 wt.%. Extra details about the testing are available in section 2.3.5.1.1.

Each stress-strain curve contained its corresponding wt. %, stress and strain data values, due to the fact that there was significant variation in the number of data points available for each experimental response, as shown in section 2.3.5.1.1. Therefore, all stress-strain responses were interpolated based on their respective ranges to provide an equal number of data points.

Two ANN-based models were developed. The first simulated a stress-controlled experiment while the second simulated a strain-controlled experiment. In order to aid the developed models in their predictions, another ANN-based model was utilized to predict the maximum strain at any given xGnP content. This model was utilized as a stopping criterion for the ANN-based strain and stress controlled models. For example, to predict the stress-strain behavior for a given graphene content, the stopping criterion model is utilized first to predict the anticipated maximum strain for this case. After this step, both ANN-based stress and strain controlled models are simulated within the predicted maximum strain range.

The results obtained from DMA show a significant variation in the mechanical response of the manufactured papers based on the xGnP loading. This variation was the motivation for using ANN to predict the behavior of the material with varying wt. %.

#### 2.4.3.1.1 Stress-controlled model

In this model, the strain is predicted as a function of stress and weight percent of xGnP loading, after performing the training process discussed earlier, by adaptively starting at 1 hidden node and stopping at 7 hidden nodes with 19,900 iterations optimized model. The model produced a very good representation of the stress-strain curves involved with a coefficient of determination  $R^2 = 0.874$  and an ASE = 0.001714. Accordingly the final ANN model can be represented as shown in equation (16).

$$\varepsilon\% = \text{ANN}_{2-[1-7-19,900]-1}[\sigma, \text{wt.\%}] \quad (16)$$

Where:

2: the number of input variables [ $\sigma$  in MPa, wt. %]

1-7-19,900: represents the starting hidden node, the final hidden node and corresponding iterations, respectively.

1: represents the number of output variables ( $\varepsilon$  %).

The connection weight and threshold values are represented in tables form. Figure 77 shows a visual representation of the data reported in Table 7. A Full set of connection weight and threshold values tables for all models networks is reported in APPENDIX B.

. Table 7: sample ANN Table results reporting.

	HN1	HN2	HN3	
input 1	I1-1	I1-2	I1-3	
input 2	I2-1	I2-2	I2-3	Output
HN threshold	TH1	TH2	TH3	threshold
Output	H1-O1	H2-O1	H3-O1	TO1

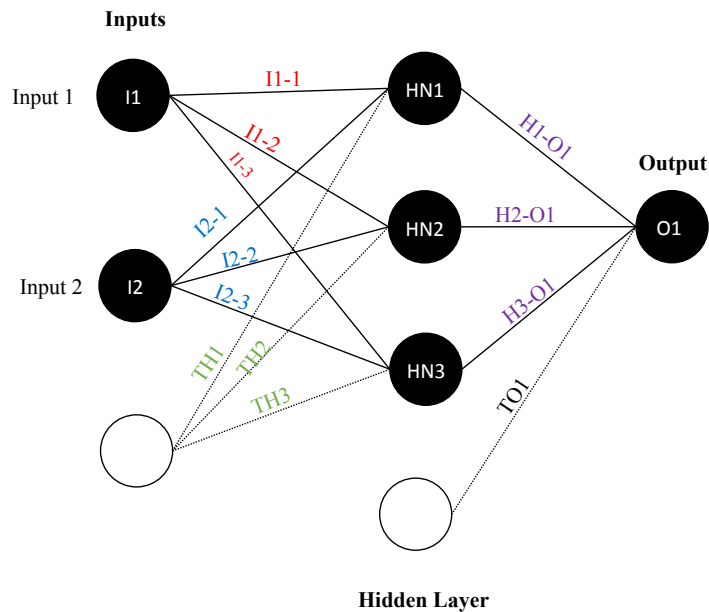


Figure 77: Visual representation of the simulation results.

#### 2.4.3.1.2 Strain-controlled model

This model predicts the strain as a function of stress and wt. % of xGnP loading. The final model was obtained by adaptively training the network starting from 1 hidden node and stopping at 9 hidden nodes and 20,000 iterations. The model produced an excellent representation of the stress-strain curves involved with an ASE = 0.001714 and a coefficient of determination  $R^2 = 0.927$ . Accordingly, the final ANN model structure can be represented as shown in equation (17).

$$\sigma = \text{ANN}_{2-[1-9-20,000]-1}[\varepsilon, \text{wt.}\%] \quad (17)$$

Similarly:

2: is the number of input variables [ $\varepsilon$  %, wt. %].

1-9-20,000: represents the starting hidden node and the final hidden node and corresponding iterations respectively.

1: represents the number of output variables ( $\sigma$  in MPa).

#### 2.4.3.1.3 Stopping criterion model

In this model, the maximum strain is predicted as a function of the weight percent of xGnP loading. After performing the training process similar to the one used in the earlier models, the best performing model was obtained at 9 hidden nodes and 3,000 iterations. The model showed good prediction accuracy of the strain value at failure. The corresponding accuracy measures are  $R^2 = 0.842$  and ASE = 0.00511. Accordingly, the final ANN model can be represented as shown in equation (18).

$$\varepsilon_{max}\% = \text{ANN}_{1-[1-9-3,000]-1}[\text{wt.}\%] \quad (18)$$

Once the ANN model is fixed, the stress-strain responses can be predicted using the ANN approach. Using the ANN simulations based on the developed models, the results can be compared with the experimental responses. Then a sensitivity analysis is performed for a range of 0-97 wt. %. Finally, the toughness, maximum tangent modulus and maximum

strength and strain values are calculated and compared with their corresponding experimental values.

#### 2.4.3.1.4 Sensitivity analysis

Both stress-controlled and strain-controlled models are simulated and compared with the experimental responses; a sample of simulations is shown in Figure 78. As noted in Figure 78, the model simulations almost form a lower and upper bounds for their corresponding experimental responses. In this case, the stress-controlled model represents an upper-bound while the strain-controlled model depicts a lower-bound. It is to be noted that the prediction accuracy of the developed models has been impacted by the discrepancy observed in the experimental data. Moreover, at higher percentages, the strain-controlled model seems to fit the experimental data better than the stress-controlled model. This observation is in accordance with the statistical accuracy measures ( $R^2$  & ASE) reported. In this case, the stress-controlled model tends to overestimate the stress values.

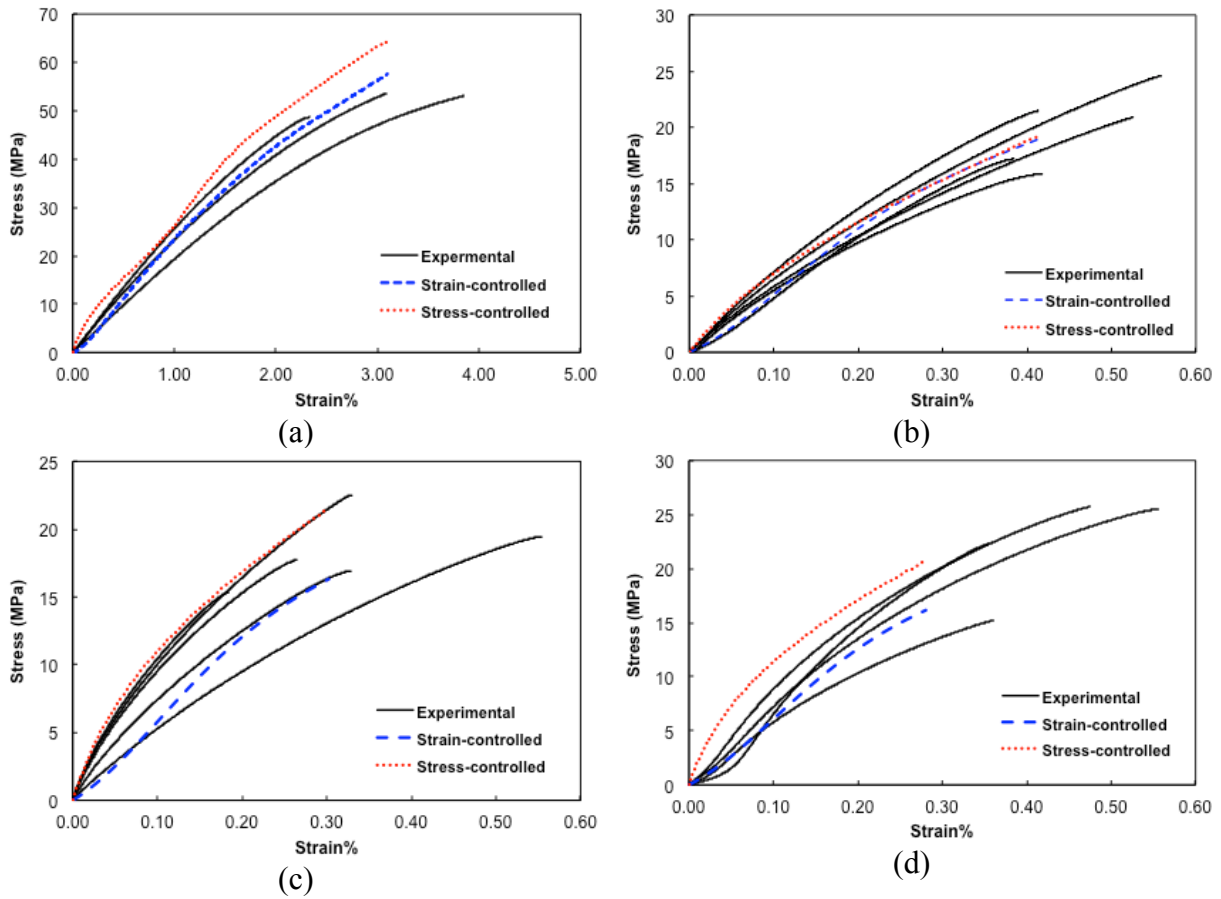


Figure 78: ANN simulations compared with experimental stress-strain curves for (a) 0.5 wt. % (b) 25 wt. % (c) 40 wt. % (d) 85 wt. %

Sensitivity analysis is performed using both models, as shown in Figure 79 and Figure 80. The analysis was performed by changing the xGnP content from 0 to 97 by weight, as observed in the figures below, both models predict a softening behavior of the material with an increase in graphene content, which may be due to graphene clustering within the nanocomposite until the weight percent reaches approximately 10%. At this point, the platelets start to mechanically interlock, which enhances the strength of the material. Finally, the material reaches a plateau where almost no more strength is developed beyond the 40 wt. %.

Moreover, it can be also observed from the figures below that the strain-controlled model seems to predict a lower strength for a given weight percent when compared with the value obtained from the stress-controlled model. This is consistent with the observation noted



earlier. Additionally, for weight percentages between 0-1%, a finer simulation is done to capture any behavioral change in the material when a fraction of a percent is added. For this range, the strain-controlled model predicts less strength loss than the stress-controlled model. At 1%, the strain-controlled model predicts a 26% reduction while the stress-controlled model predicts a 35% reduction in strength.

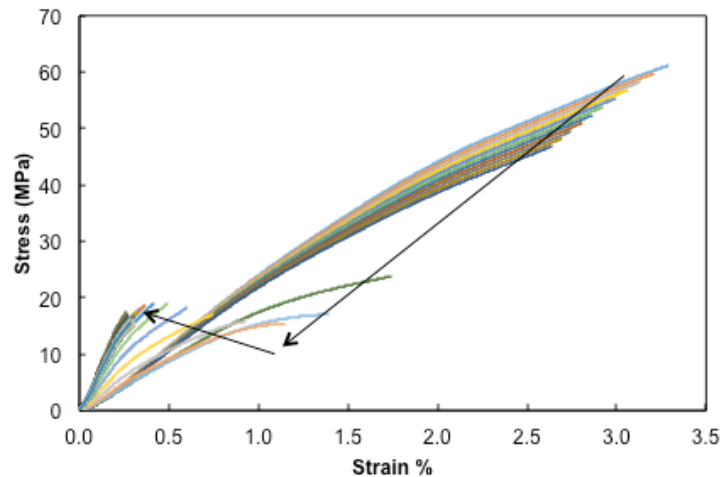


Figure 79: Sensitivity analysis simulation for the strain-controlled model

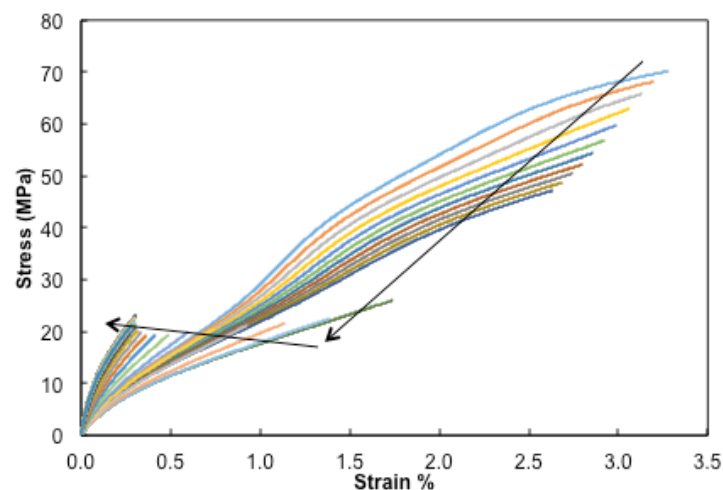


Figure 80: Sensitivity analysis simulation for the stress-controlled model

Four different mechanical properties were calculated based on the stress-strain responses simulated earlier, namely: the toughness, the maximum tangent modulus (by taking the maximum slope at each point for the entire curve) and the maximum stress and strain. These

properties are calculated based on the experimental data as well as the predicted corresponding responses, shown in Figure 81.

The toughness behavior shown in Figure 81 (a) indicates a rapid decrease in toughness until the added xGnP reaches 40 wt. %, and then it stays almost unchanged. Both ANN models fall in the center of the experimental data. It can be also noted the strain-controlled model always predicts a lower toughness than the stress-controlled model. The same behavior can be concluded from the maximum tangent modulus in Figure 81 (b), where it is more evident that the stress-controlled model defines the upper bound and the other model depicts the lower bound. At low xGnP loadings (i.e. less than 10%), the stress-controlled model predicts a higher modulus than any of the experiments, which is not the case with the other model where it almost falls right in the mid-range of the corresponding experimental-based data. The maximum strength behavior shown in Figure 81 (c) follows the same trend noted in the toughness case. The strength decreases until the added xGnP percentage reaches a minimum value at xGnP 40 wt. %. Finally, the maximum strain is shown in Figure 81 (d), which is essentially plotting the results from the stopping criterion model since the maximum strain is used to terminate the simulation for both models. The stopping criterion ANN-based model shows excellent predictions of the maximum strain. The same plateau noted earlier at 40 wt. % can also be noted in this case as well.

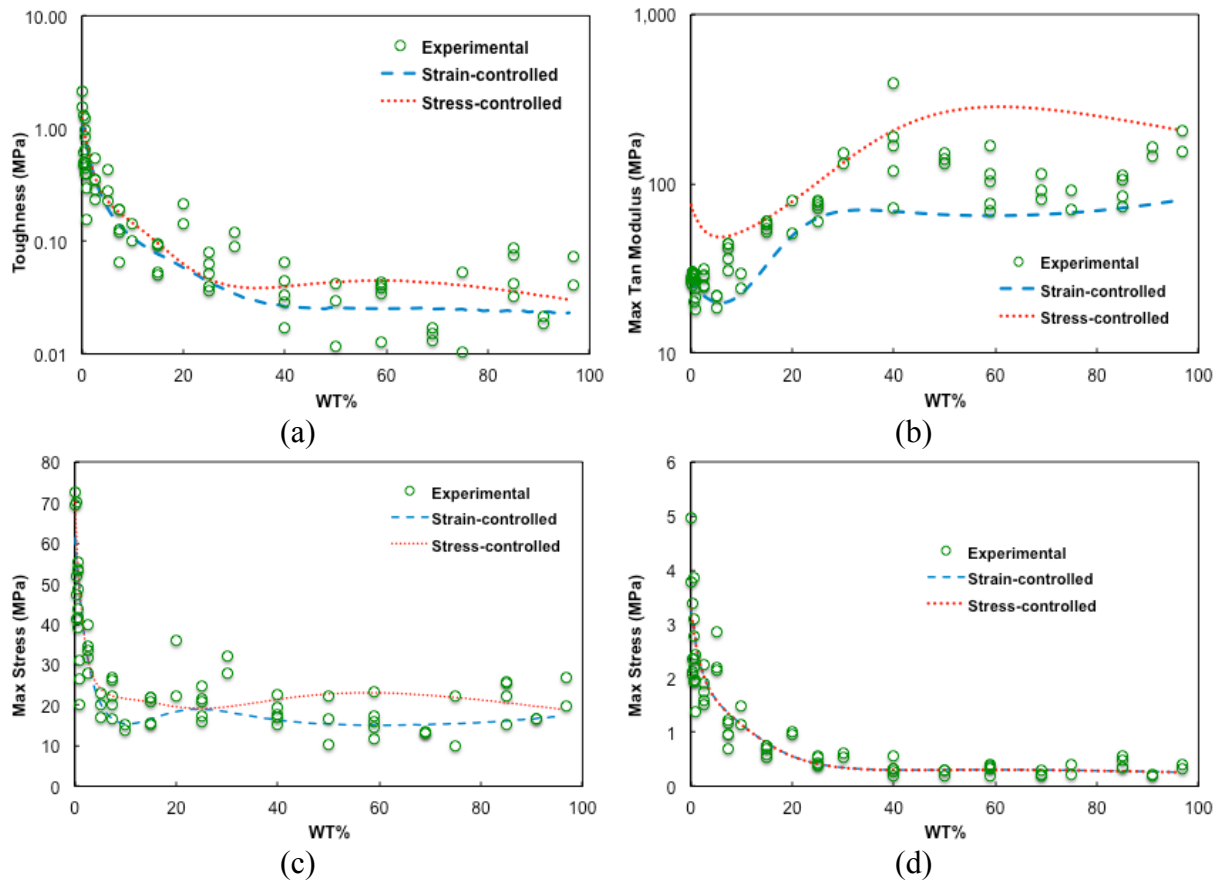


Figure 81: Mechanical properties calculated from the stress-strain responses (a) toughness (b) maximum tangent modulus (c) maximum strength (d) maximum strain

The strain-controlled model was noted to be more reliable in predicting the stress-strain behavior and the properties of the material at varying wt.%, which is consistent with its higher statistical accuracy measures. By employing both developed ANN models (stress-controlled and strain-controlled), the stress-strain behavior can be efficiently simulated at any given wt. %.

#### 2.4.3.2 High strain rate stress-strain

In this section, the stress-strain behavior of Epoxy, PU and PEI graphene based nanocomposites with varying strain rates and xGnP or OxGnP loading is modeled utilizing ANN based models. The material manufacturing, testing and data processing are discussed earlier. Each material behavior is modeled separately utilizing its own ANN model. Since the

experimental strain rate cannot be controlled directly, the resulting strain rate ranges were not the same for all the materials.

#### 2.4.3.2.1 Strain-controlled model

The final network structure for each model and its corresponding statistical accuracy measures are shown in Table 8.

Table 8: ANN models structures and statistics

Name	ANN model Structure	R <sup>2</sup>	ASE
Epoxy-OxGnP	$\sigma = \text{ANN}_{3-[1-5-20,000]-1}[\text{wt.}\%, \dot{\epsilon}, \epsilon]$	0.93	173.88
Epoxy-xGnP	$\sigma = \text{ANN}_{3-[1-5-20,000]-1}[\text{wt.}\%, \dot{\epsilon}, \epsilon]$	0.93	187.94
PU-OxGnP	$\sigma = \text{ANN}_{3-[1-5-20,000]-1}[\text{wt.}\%, \dot{\epsilon}, \epsilon]$	0.96	13.04
PU-xGnP	$\sigma = \text{ANN}_{3-[1-5-20,000]-1}[\text{wt.}\%, \dot{\epsilon}, \epsilon]$	0.97	7.29
PEI-xGnP	$\sigma = \text{ANN}_{3-[1-6-20,000]-1}[\text{wt.}\%, \dot{\epsilon}, \epsilon]$	0.95	131.81

A sample of the resulting model responses compared with the experimental response as well as the developed constitutive model are shown in Figure 82 through Figure 84. The dashed line, solid line, and markers represent the ANN model fit, DSGZ model fit and the experimental data, respectively. Also, same color lines represent the same strain rate.

The developed ANN models are in agreement with experimental results for all the studied materials. However, the ANN models were developed for the whole range graphene loadings from 0 -1 wt. % while the constitutive models were developed for specific wt. %. Comparing the ANN models to the constitutive models, both models show reasonable agreement. However, some cases shows that ANN models were more accurate than the constitutive model, such as xGnP-PU, with R<sup>2</sup> and ASE of 0.97 and 7.29 for the ANN model compared with 0.96 and 10.61 averaged over four constitutive models (one constitutive model for each weight percent e.g. 0, 0.2, 0.5 and 1%).

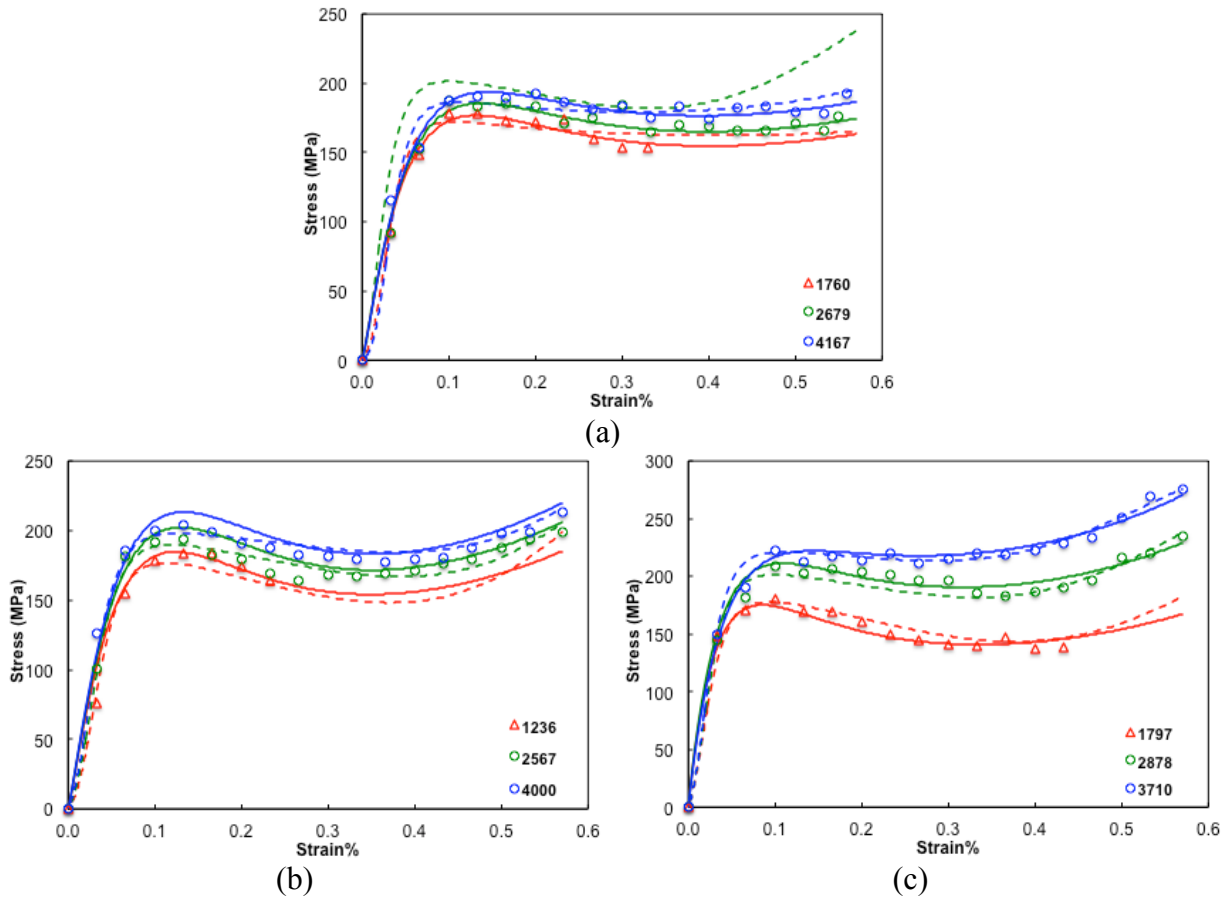


Figure 82: Epoxy-based nano-composite stress-strain response for (a) Pure Epoxy (b) 0.5% OxGnP-Epoxy (c) 1% xGnP-Epoxy

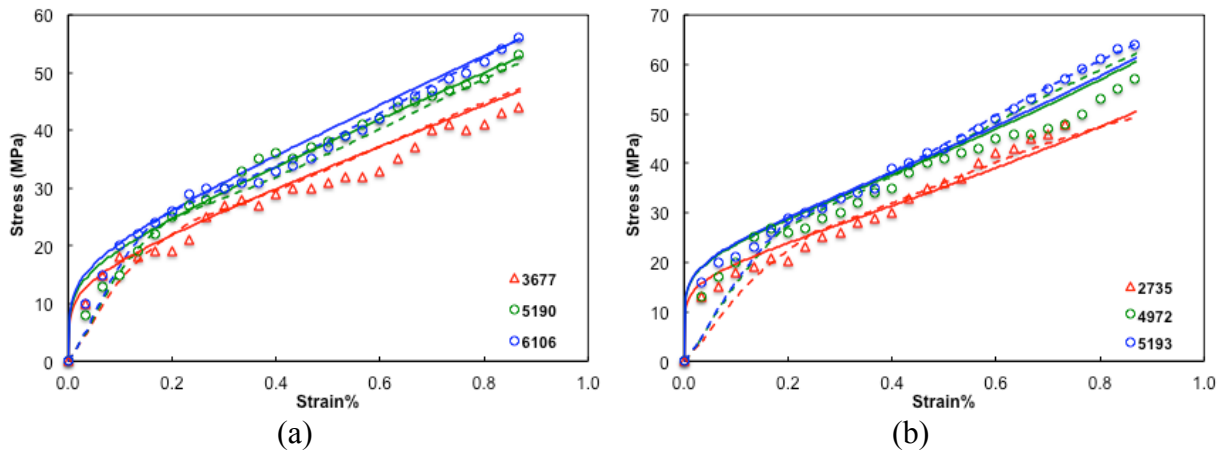


Figure 83: PU-based nano-composite stress-strain response for (a) 0.5 % xGnP-PU (b) 0.5% OxGnP-PU

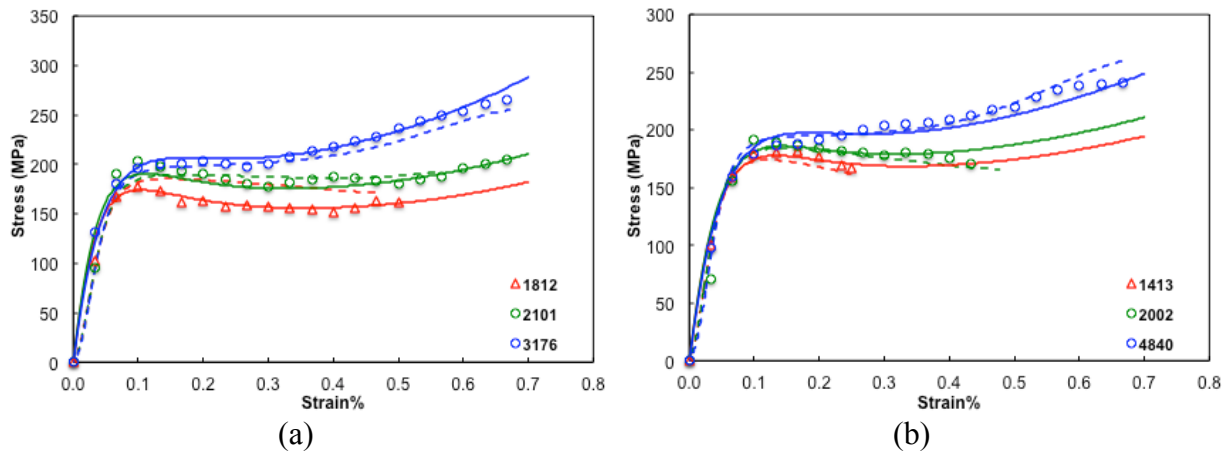


Figure 84: PEI-based nano-composite stress-strain response for a) 0.5 % xGnP-PEI b) 1 % xGnP-PEI

#### 2.4.3.2.2 Sensitivity analysis

In this section, a sensitivity analysis is performed for all the developed models. Since two inputs are considered here, the analysis is performed in two ways, the first is by changing the strain rate and fixing the weight percentage, while the other the strain rate is fixed, and the weight percentage varies. The weight percentage is varied from 0-1% and the strain rate is varied from 1000-5000  $S^{-1}$ . Note that, weight percentage sensitivity analysis cannot be performed using the DSGZ constitutive model, as each weight percentage has a separate model.

As noted in Figure 85, the materials exhibit higher toughness at higher strain rates. However, with increasing the graphene loading, the material sensitivity for strain rate increases. In Figure 85 (a), there is a ~22% deviation in the maximum stress value comparing 1000 and 5000  $S^{-1}$  strain rates for the neat PEI, while ~35% deviation is noted for 1 wt. % for the same strain rates. The sensitivity analysis figures for the whole range of graphene loading and all base polymers are reported in APPENDIX B.

Different behavior response is noticed for the OxGnP-Epoxy. The analysis showed that yield stress is more sensitive to strain rate change at higher percentages while the maximum stress is less sensitive to strain rate change at the same percentages. However, both the yield stress

and the maximum stress of xGnP-Epoxy nano-composites are sensitive to strain rate change at higher percentages. This is similar to the behavior noted for OxGnP-PU.

Finally, two trends are observed for xGnP-PU. First, reduction of the maximum stress with the increase of xGnP loading up to 0.5 wt. % is observed. Second, the maximum stress becomes more sensitive to strain rate by increasing xGnP wt. %.

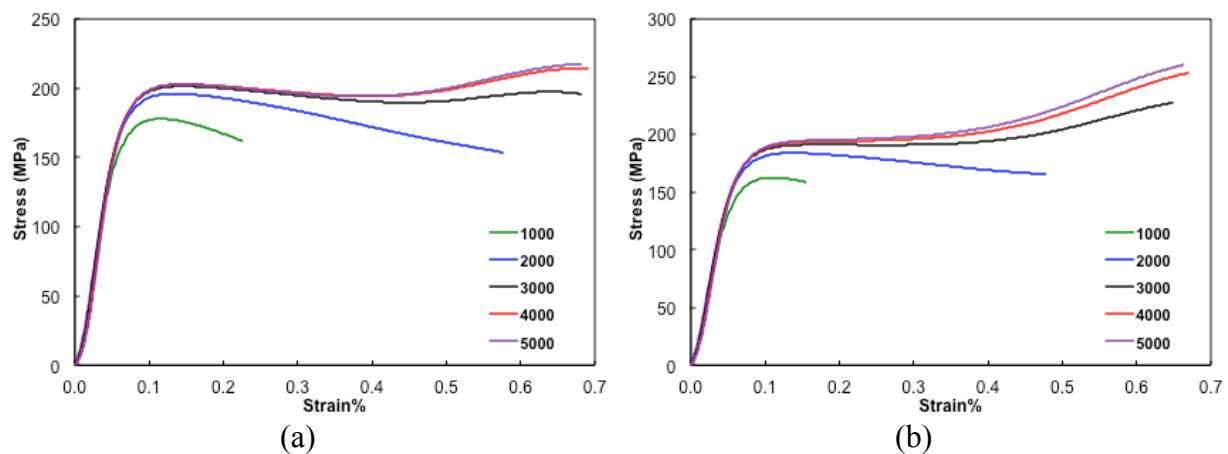


Figure 85: xGnP-PEI strain rate sensitivity analysis for (a) PEI (b) 1% xGnP-PEI

Figure 86 depicts the sensitivity analysis of the weight percentage for xGnP-Epoxy (strain rates of 1000 and 4000 S<sup>-1</sup>). At lower strain rates (Figure 86 (a)), the yield stresses decrease with the increase of the weight percentage. Additionally, a turning point is noticed for all weight percentages at strain of 0.35, where a stiffening behavior starts to become more evident. However, at higher strain rate (Figure 86 (b)), the yield stress increases with the increase of weight percentage. Moreover, the material is less sensitive to adding xGnP at higher strain rate compared to lower strain rate. Sensitivity analysis for the whole strain rate range is reported in APPENDIX B.

On the other hand, xGnP-Epoxy exhibits softening behavior with increasing weight percentage at lower strain rates, but a stiffening behavior is noticed with the increase of xGnP

loading at higher strain rates. Both OxGnP-PU and xGnP-PU nano-composites are more sensitive to the weight percentage change with the increase of strain rate.

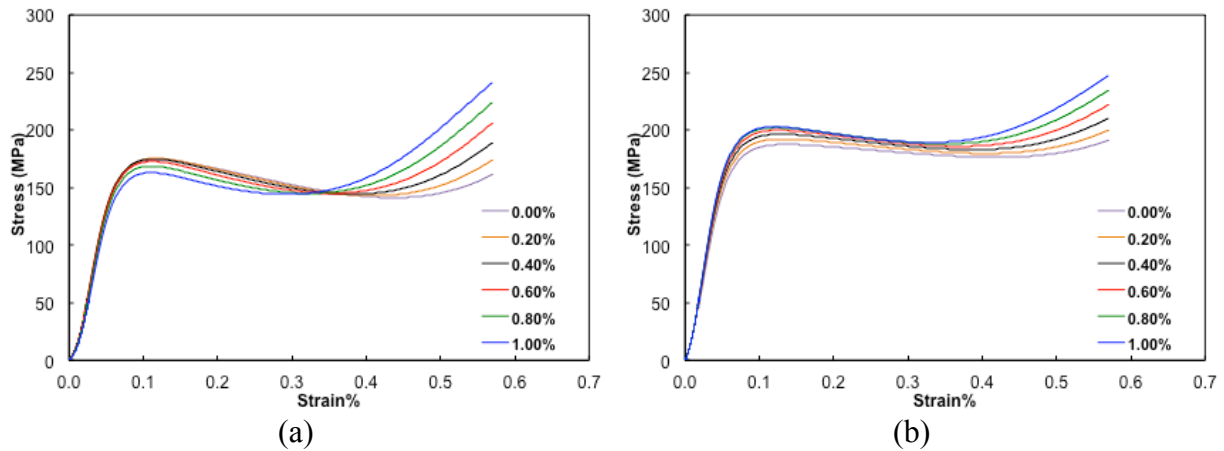


Figure 86: Sensitivity analysis of OxGnP-Epoxy based nano-composite to OxGnP loading at strain rate of (a)  $1000 \text{ S}^{-1}$  b)  $4000 \text{ S}^{-1}$

## 2.5 Finite Element Analysis

Finite element simulations have been used in this study for modeling hypervelocity impacts, which include large deformation. Autodyn has been implemented for the simulations in this research.

### 2.5.1 ANSYS Autodyn introduction

This research present hydro-code simulations performed using ANSYS Autodyn, a fully integrated and interactive code specifically designed for nonlinear dynamic problems. ANSYS Autodyn is finite element software specially designed to simulate the response of materials to short durations of severe loadings, from impact, high pressure or explosions. It is best suited for large material deformation simulations. Autodyn software has been used to model space debris impact on spacecraft, and satellites in several studies. The main solution methodology is based on explicit time integration. One unique feature of Autodyn is that it allows several parts of a problem to be simulated with available and applicable numerical formulations. This allows users to choose a solution technique suitable for the physical nature



of the problem. As well as, coupling different solution techniques for the problem in consideration.

### 2.5.2 Autodyn Hydrodynamic code

Hydrodynamic code is suited for modeling problems with large deformation, e.g blast, explosion and impact problems. Software programs that are capable of computing stresses, strains, and shock waves propagation as a function of time and location on space are known as hydro-codes. The Lagrange technique is typically used for solid continuum and structures, and the Euler technique is commonly used for modeling gases, liquids or solids subject to large deformations. Solid continuum and structures are also analyzed using smooth particle hydrodynamics.

### 2.5.3 Smooth Particles Hydrodynamics

The SPH element in Autodyn is based on the smoothed particles hydrodynamics theory. Fluid equation of motion can be modeled using the SPH meshless technique. The SPH technique can solve complicated problems that include very short duration impact loading accurately compared to the other traditional methods. The absence of mesh allows for large deformation and distortion.

The SPH technique does not suffer from tangling of the grid (typically encountered in Lagrange processor). Also, it does not require the use of an erosion algorithm (deletion of highly distorted elements to improve the numerical simulation). The SPH Code is effective in modeling several phenomena's that are associated with hypervelocity impact, including projectile breakup, debris cloud formation, and material phase change. In SPH modeling, each particle represents an interpolation point of a fluid. When solving for fluid motion, each set of particles are assumed to move at the flow velocity.

### 2.5.4 SPH parts models

For a continuum subject, the response to dynamic loading in a hydro code simulation is governed by the conservation of energy, momentum, mass. The deformations are driven by EoS and the constitutive model. An EoS then is employed to define the relationship between pressure and specific volume, while a constitutive model is used to define the fitting plastic stress-strain. In addition, a constitutive model generally includes a failure criterion.

#### 2.5.4.1 Projectile

The impacting particle is assumed to be homogenous, made of Aluminum, Spherical with diameter of 4 mm. Al 6061-T6 from the Autodyn material library was used with Polynomial EoS, Johnson-Holmquist constitutive model, and Johnson-Holmquist failure model. These models and their parameters are discussed in detail in the Autodyn theory manual. The particle size was determined from the convergence study. The projectile was represented by 559 particles to model an Aluminum sphere.

#### 2.5.4.2 Substrate

The materials for the semi-finite plates were assumed to be made from one of three materials Aluminum (AL 6061-T6), Kevlar-Epoxy (referred to in Autodyn as KEVLAR EPX), or Steel (STEEL 4340). The EoS, material model, and failure model used for these materials are shown in Table 9.

Table 9: EoS, material model, and failure model.

Material Name	EoS	Strength Model	Failure model
AL 6061-T6	Shock	Steinberg Guinan	None
KEVLAR EPX	Puff	None	Hydro (Pmin)
STEEL 4340	Linear	Johnson Cook	Johnson Cook

The plate sizes were chosen to be 50\*50 mm, and the target plates were treated as semi-infinite plates to permit the shockwaves to move through the boundaries without the effect of wave reflections. The values of all the material parameters defined here are available in the Autodyn materials library.

### 2.5.4.3 Coating

The coating was assumed to be made of graphene based composite (xGnP-Epoxy 1 wt. %). A Piece-wise Johnson-cook model was employed for simplicity. In the piece-wise version of the model, strain hardening and thermal softening parts remain the same as the JC model. However, the strain hardening part  $[A + B\varepsilon_{pl}^n]$  in the JC model is replaced by piecewise linear lines that represent the yield stress versus effective plastic strain. The model employed for reference coating (xGnP-Epoxy 1%) was a Bi-linear model. In addition, linear EoS was used. The values of the reference coating model constants are listed in Table 10.

Table 10: Model constants for reference coating.

Reference Density (g/cm3)	Bulk Modulus (Mpa)	Shear Modulus (Mpa)	Yield Stress (Mpa)	Failure stress (Mpa)	Failure Strain (Mpa)	Strain rate constant	Thermal softening Exponent	Melting Temperature (k)	Refrence strain rate (1/s)
1	4.17E+03	8.94E+02	1.70E+02	1.70E+02	0.43	0.024	1.56	597	1797

### 2.5.5 Convergence study

In finite element simulation, smaller elements typically provide more accurate results. However, when smaller elements are used, the computation time increases significantly. In order to determine the satisfactory balance point between accuracy and computational time, an element size convergence study was performed. Performing this study, we can obtain accurate results with an element size that is sufficiently small and not overly demanding of computing resources.

A simulation of a 4 mm aluminum sphere impacting an Aluminum plate (50\*50\*1mm) at different velocities was conducted. The largest, reasonable size of elements was used for the simulation. Then, a smaller element size was used, the simulation was re-run, and the average exit velocity of the current run was compared to the average exit velocity of the previous simulation. The simulation was re-run with continually decreasing element size. The change in element size did not show a noticed deviation in the results at element size smaller than

0.15mm. The results seem to converge satisfactorily at element size 0.15mm, as shown in Figure 87. This element size was employed for all other simulations.

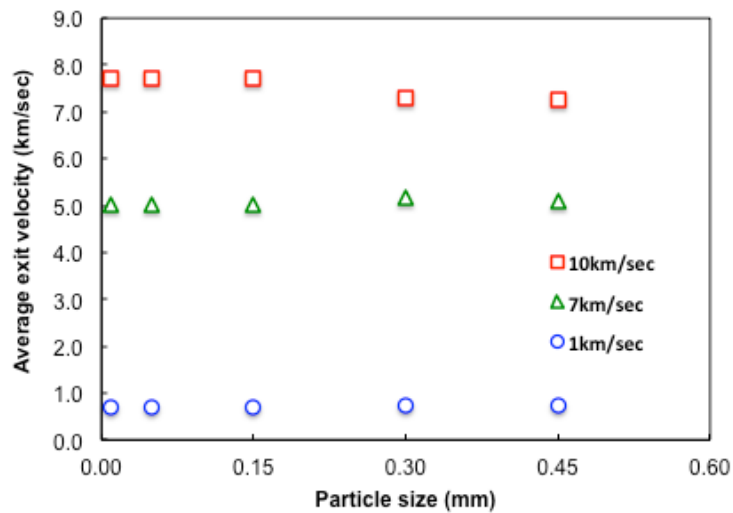


Figure 87: Average exit velocity for the different element size

## 2.5.6 Sensitivity analysis of material constants

Autodyn makes use of several constitutive material models to simulate the response of the material under a variety of thermo-mechanical conditions. In this section, a sensitivity study of the material parameters was conducted to understand their effects on the isolated performance of the graphene-based coating, and the formed crater resulted from impact by the perturbation of the coating material constants.

### 2.5.6.1 Simulations Matrix

The Aluminum (Al 6061-T6) sphere has a diameter of 4 mm simulated in Autodyn 2D hydro-code to impact plates of 1mm thick. These plates were made of Aluminum, Kevlar-Epoxy and steel, and coated with 1mm graphene-based composite (xGnP-Epoxy 1%).

Since the velocity of impact plays a significant role in the performance of the shield, simulations were run for different impact velocities. This study was performed under three different impact velocities: 1, 7, and 10 km/s. This sensitivity study parameters perturbation includes the initial yield stress, strain hardening, strain rate constant, reference density, the

Bulk and shear Moduli, reference strain rate, as well as the bonding condition between the coating and the substrate (bonded, 1mm gap, and 2mm gap). One parameter was changed in each simulation; APPENDIX C shows the values of material parameters used in the simulations, including a 50% perturbation above and below the reference values listed in Table 10. Different substrate material was used each time. The substrate plate was represented by 0.15 mm particles resulting in 2331 interpolation particles to model the substrate layer and another 2331 particles to model the coating layer.

#### 2.5.6.2 Numerical simulation results

In the present work, a dynamic analysis of the impact and penetration of three substrates plates with and without xGnP coatings is carried out in order to predict the impact response. The hydro-code model was constructed in order to predict the experimental test results. For evaluation, the coating normalized isolated performance (CNIP) was calculated; the final crater diameter and the exit velocity were compared for each simulation scenario.

The CNIP for the coatings applied to the front side of base material is calculated based on the simulation results using equation (19). The coating performance can be separated using this equation in order to understand the coating relative contribution and the change of coating material parameters. Figure 88 shows visual illustration of equation (19).

$$CNIP = \frac{Vr_{s+c} - Vr_s}{V_i} \quad (19)$$

Where:

$Vr_{s+c}$ : Average residual velocity of the impactor after impacting the coated substrate.

$Vr_s$ : Average residual velocity of the impactor after impacting the blank substrate.

$V_i$ : Impactor initial velocity.

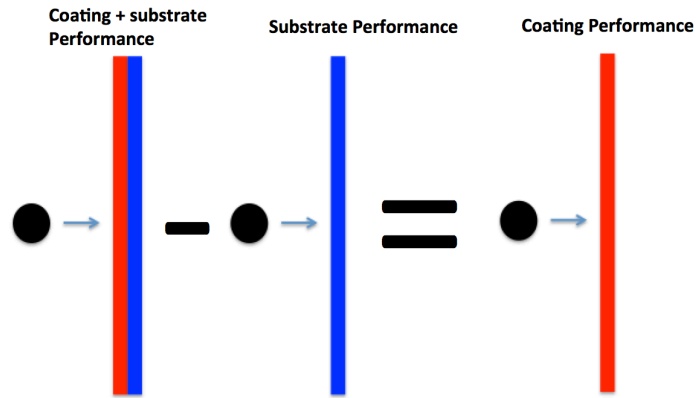


Figure 88: Coatings Isolated performance illustration

The improvement gained in terms of residual velocity as a result of adding the 1mm reference coating compared to 1mm blank substrate is shown in Figure 90. Adding the coating reduced the impact residual velocity. Though there was no reduction at lower velocity, significant reduction is observed at velocity of 7km/sec and above. This conclusion is valid for all substrates. Typical reduction in the velocity of sphere particles (after impact by Aluminum substrate with reference coating) is shown in Figure 89.

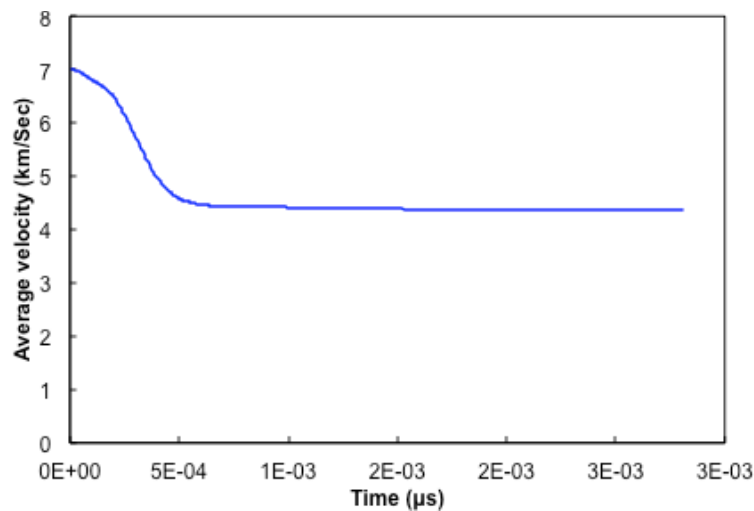


Figure 89: Typical sphere particles velocity drop after impact of Aluminum substrate coated with reference coating

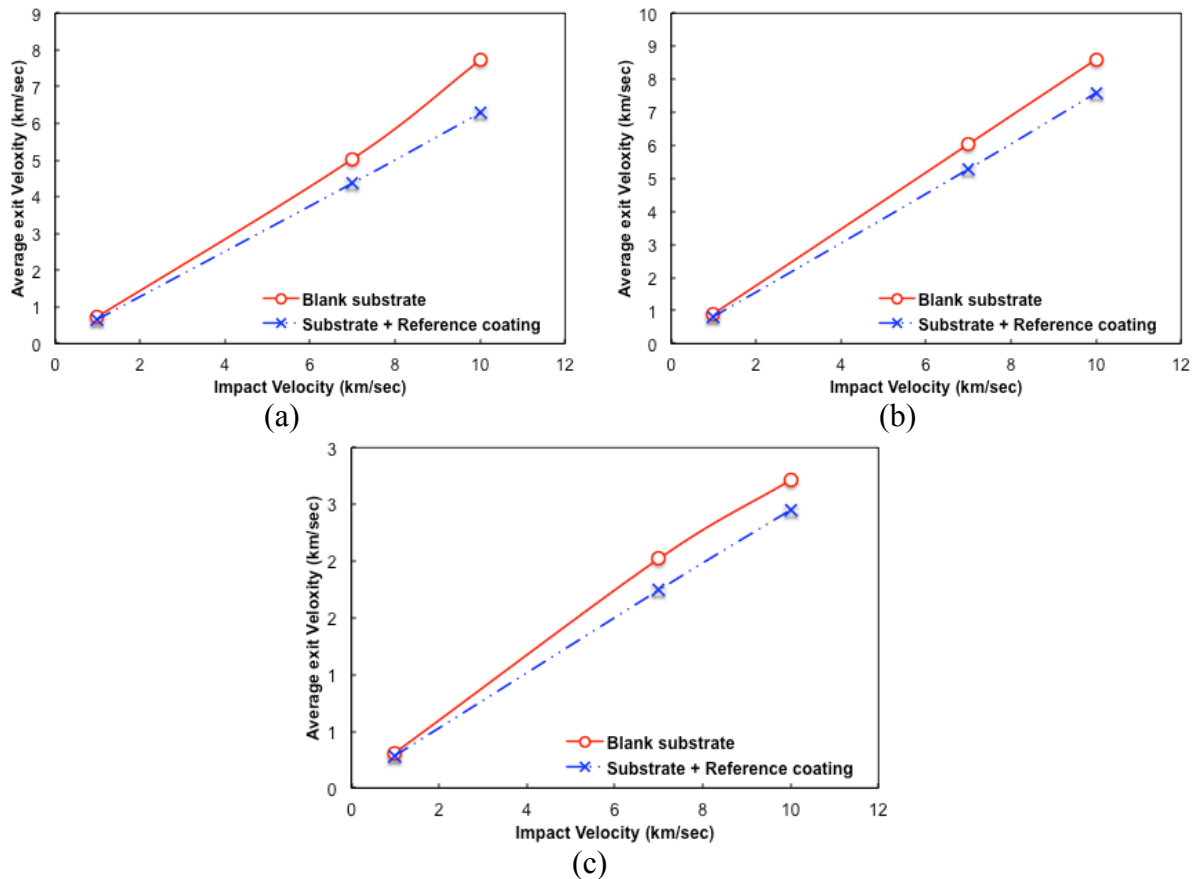


Figure 90: Average exit velocity of impactor after impact by substrate coated with reference xGnP-Epoxy 1 wt. % compared to blank substrate (a) Aluminum (b) Kevlar-Epoxy (c) Steel

After performing the simulation, the exit velocity was normalized, and the performance of the coating was separated from the total shield performance using equation (19). Then, CNIP was plotted and compared.

In order to determine the material parameters that have the biggest sensitivity to CNIP. The calculated CNIP of the reference coating is represented as the vertical zero lines in Figure 91, Figure 92, and Figure 93. The percentage deviation away from that zero is plotted in terms of CNIP. These graphs represent the CNIP deviation percentage away from the CNIP of the reference coating. The deviation values illustrated in Figure 91, Figure 92, and Figure 93 show the range at which the CNIP may change by the change in gap space and offset of coating material parameters by  $\pm 50\%$ , by employing Aluminum, Kevlar epoxy, and Steel as substrates. In the butterfly charts presented in this section, the red and green bars correspond

to decrease and increase in CNIP, while the red and green arrows on top correspond to the change of (-50%) and (+50%) in coating material parameter value, respectively. However, (+50%) and (-50%) in the gap represents 1mm and 2mm spacing, respectively (Spacing between coating and substrate). CNIP was calculated at a time where the deformations seem to be stable and no significant change noticed afterward.

In Figure 91, at impact velocity of 1 km/sec (Figure 91 (a)), the parameters that affect the CNIP the most are, respectively: coating density, the bulk modulus, and the gap between the coating and substrate (the bulk modulus and density directly control the EoS). However, the parameters that control the constitutive relation (the reference strain rate, the yield stress, the strain hardening, and the strain rate constant) have limited effect on the CNIP. With the increase of velocity at 7 and 10 km/sec (Figure 91 (b) and (c)), the bulk modulus effect becomes limited as well as the reference strain rate, the yield stress, the strain hardening, and the strain rate constant. In contrast, the gap deviation increases with the increase of impact velocity.





Figure 91: CNIP deviation from reference coating on Aluminum substrate after impact velocity of (a) 1km/sec (b) 7km/sec (c) 10km/sec

Comparing the CNIP deviation using Kevlar-Epoxy substrate (Figure 92) with Aluminum substrate (Figure 91), similar behavior is observed. However, the deviation of the CNIP at 1km/sec (Figure 92 (a)) due to change in density was greater for Aluminum substrate compared to Kevlar-Epoxy substrate. The opposite relation is seen at velocity of 7 and 10 km/sec (Figure 92 (b) and (c)). Moreover, introducing a gap showed greater deviation of the CNIP in the case of Aluminum compared to Kevlar-Epoxy at all velocities.



Figure 92: CNIP deviation from reference coating on Kevlar-Epoxy substrate after impact velocity of (a) 1km/sec (b) 7km/sec (c) 10km/sec

The deviation of CNIP from the unperturbed parameters value using Steel substrate reveals distant behavior at 1km/sec (Figure 93 (a)). All parameters showed significant deviation in terms of CNIP. Nonetheless, at 7 and 10 km/sec (Figure 93 (b) and (d)), density and gap affect the CNIP the most with outstanding deviation compared to Aluminum (Figure 91 (b) and (c)) and Kevlar-epoxy (Figure 92 (b) and (c)).



Figure 93: CNIP deviation from reference coating on Steel substrate after impact velocity of (a) 1km/sec (b) 7km/sec (c) 10km/sec

Increasing the crater diameter is of great benefit in the case of the Whipple shield being employed [11]. Debris cloud Images exported from Autodyn were used to estimate the final crater diameter. The Distance tool in MATLAB image viewer was employed to measure the crater diameter; the tool specifies the distance in pixels units. Since the shield dimensions are known, the crater diameter in mm can be calculated based on the number of pixels by liner proportion to the shield length in pixels. Figure 94 Shows a typical crater pixel measurement using Distance tool in MATLAB. The complete set of debris cloud plots for all simulations is reported in APPENDIX D.

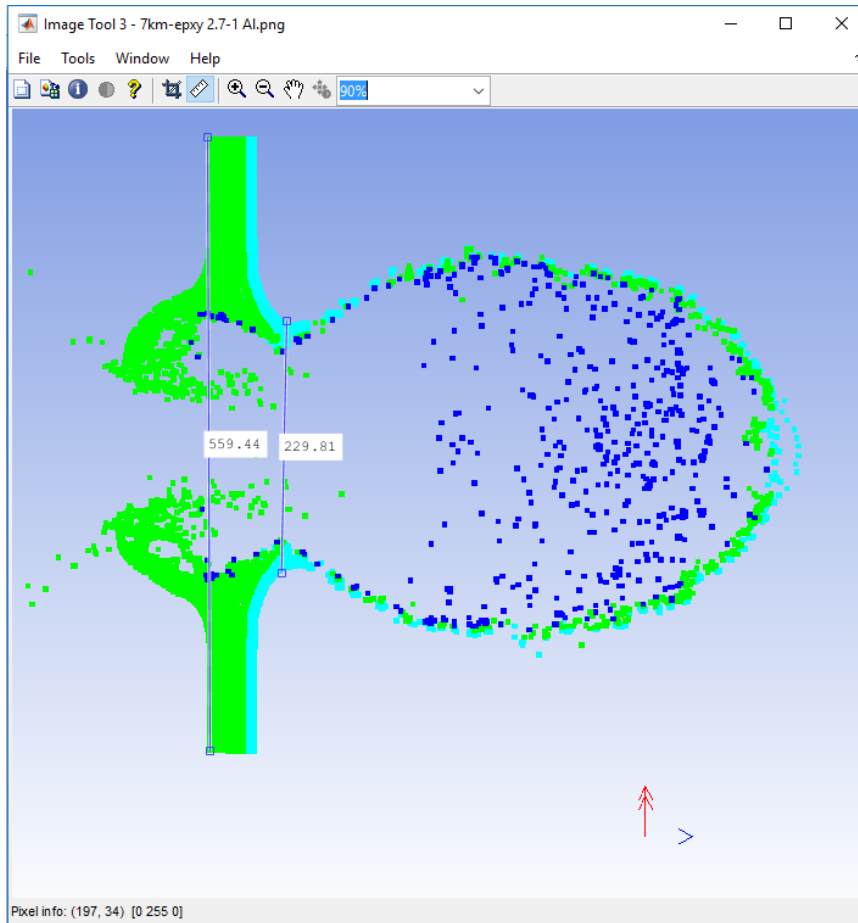


Figure 94: Measurement of crater diameter from simulation

The consequence on the crater diameter by adding the 1mm coating compared to 1mm blank substrate is shown in Figure 95. Generally, placing coating at the impact front side of the substrate increased the final crater diameter. For Aluminum substrate, the increase was more dominant at impact velocity below 7km/sec (Figure 95 (a)). However, increase in the crater diameter for Kevlar-Epoxy substrate is more significant, while for Steel substrate, the improvement was limited.

The final crater diameter of the shield (coating and substrate) was normalized to the crater diameter that resulted from the impact of the shield with reference coating in order to identify the parameters that have the biggest sensitivity to the crater diameter. The crater diameter resulting from the impact of substrate with reference coating is represented as the vertical zero lines in Figure 96 through Figure 98. The percentage deviation away from zero is plotted

in terms of crater diameter. These graphs represent the deviation in the crater diameter as a percentage from the substrate with reference coating. The deviation values illustrated in Figure 96 through Figure 98 show the range at which the crater diameter may change by the change of gap spacing and the offset of the coating material parameters by  $\pm 50\%$  using Aluminum, Kevlar epoxy, and Steel as substrate. In the butterfly charts (Figure 96 through Figure 98), the red and green bars correspond to the decrease and the increase in the crater diameter value, while the red and green arrows on top corresponds to the change in material parameters value by (-50%) and (+50%), respectively. (Similar to the charts used to report the CNIP).

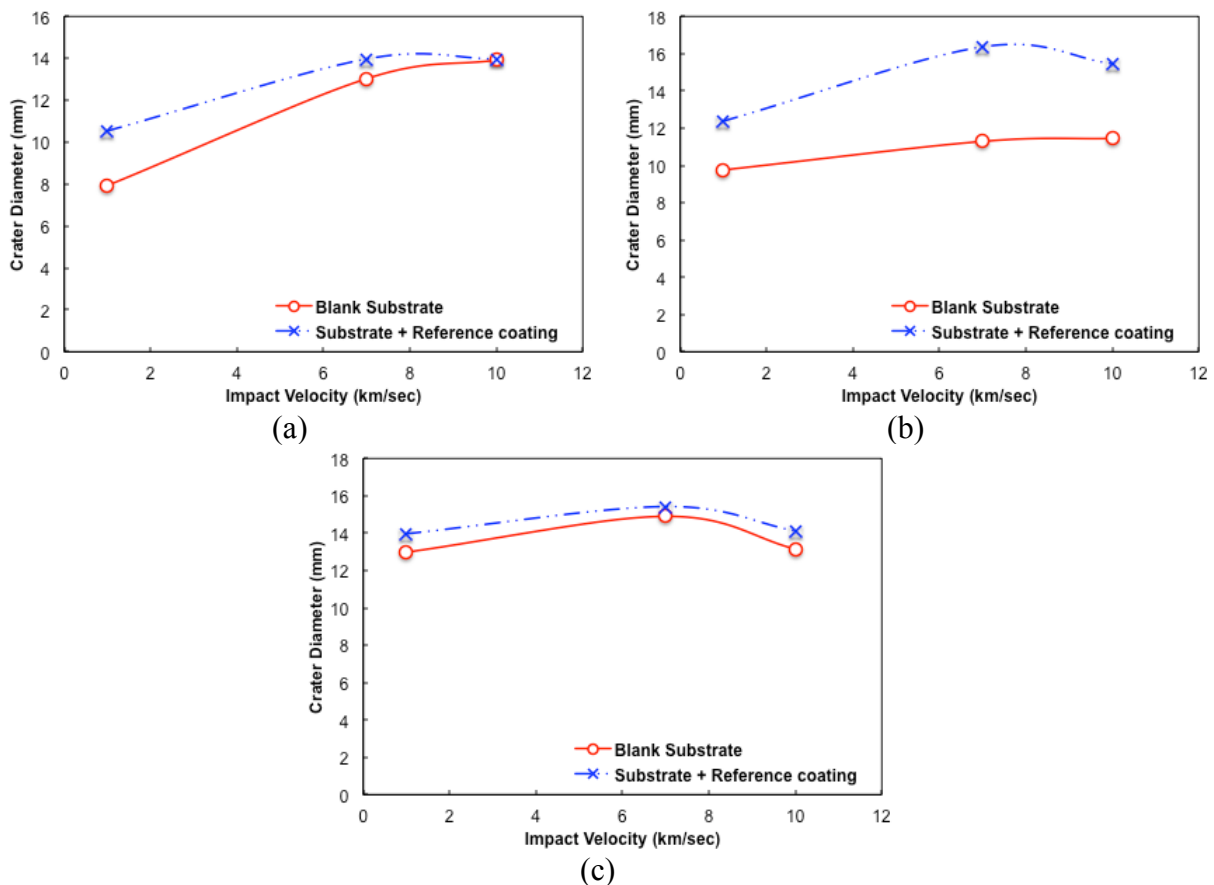


Figure 95: Crater diameter resulting from impact of substrate coated with reference xGnP-Epoxy 1 wt. % compared to blank substrate (a) Aluminum (b) Kevlar-Epoxy (c) Steel



Figure 96: Crater diameter deviation from Aluminum substrate with reference coating after impact velocity of (a) 1km/sec (b) 7km/sec (c) 10km/sec

It must be recognized that the crater's diameter measurements were taken at different times. At the chosen time, the deformation seems to be stable, and no significant change noticed afterward.

For the Aluminum substrate (Figure 96), perturbation in coating material parameters showed decrease in crater diameter at 1km/sec. Oppositely, the increase in density and the yield stress showed increase in crater diameter, though the increase was limited (Figure 96 (a)). At 7km/sec (Figure 96 (b)), either increase or decrease of the material parameters value showed increase in crater diameter and the strain hardening was more dominant at this speed. The same behavior was seen at 10km/sec (Figure 96 (c)). However, the bulk modulus was more dominant.

For Kevlar-Epoxy substrate (Figure 97), perturbation in coating material parameters showed mainly decreases in crater diameter at all velocities.

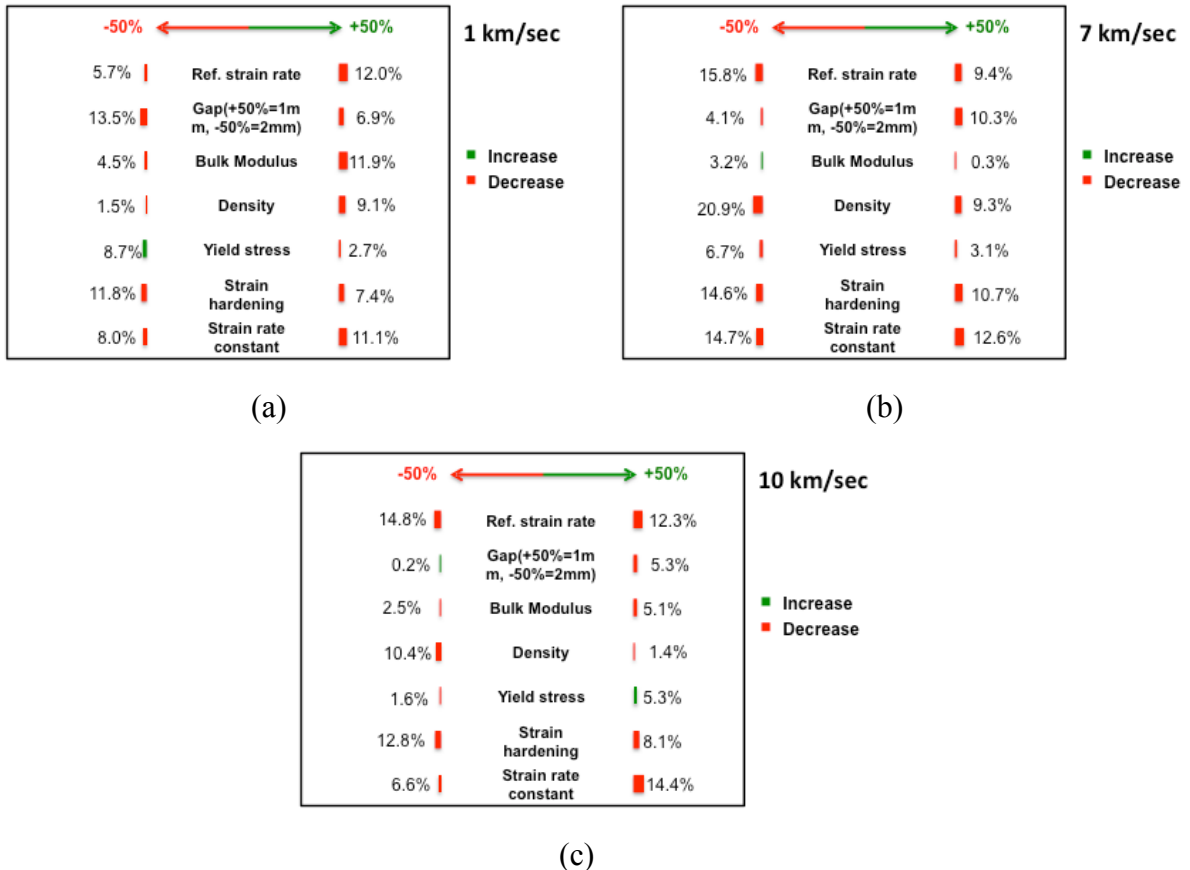


Figure 97: Crater diameter deviation from Kevlar-Epoxy substrate with reference coating after impact velocity of (a) 1km/sec (b) 7km/sec (c) 10km/sec

For Steel substrate (Figure 98), perturbation in coating material parameters showed comparable effects to the Kevlar-Epoxy substrate, mainly decreases in crater diameter at all velocities.



Figure 98: Crater diameter deviation from Steel substrate with reference coating after impact velocity of (a) 1km/sec (b) 7km/sec (c) 10km/sec

### 2.5.7 Layer stacking effect

Impact of target consisting of layered media of different materials was employed in protective structure design where materials of different mechanical properties and densities were used in order to reduce the impact intensity [28].

The effect of layer stacking is investigated in this section. A series of simulations were performed wherein the shield target was assumed to be made of two, four, and eight layers of coating and the substrate while maintaining the total weight and thickness fixed. However, smaller particle size was used in order to fit into the sub layer's small thickness. Both the substrate and the coating were represented by 0.1 mm particles, resulting in 8000 particles to model all layers (both substrate and coating).



The CNIP for all number of layers at various impact velocities is shown in Figure 99. With the increase of the number of layers, the CNIP decreases. The solid blank plate of steel performed even better than adding the coating and layering (negative CNIP). Similar behavior can be seen for Kevlar-Epoxy substrate at impact speed of 1km/sec. Even though the layers that make the multilayer shield have the same areal density and material properties as the two-layered target, there is still significant decrease anticipated in the CNIP. These results aligns with Nixdorff's [74] finding for shields that were layered into n layers of equal thickness: "The residual velocity has always turned out to be higher, and the ballistic limit velocity has always turned out to be lower than for a monolithic target of the same total thickness." This is apparent when the number n of sub-layers is raised while fixing the total thickness.

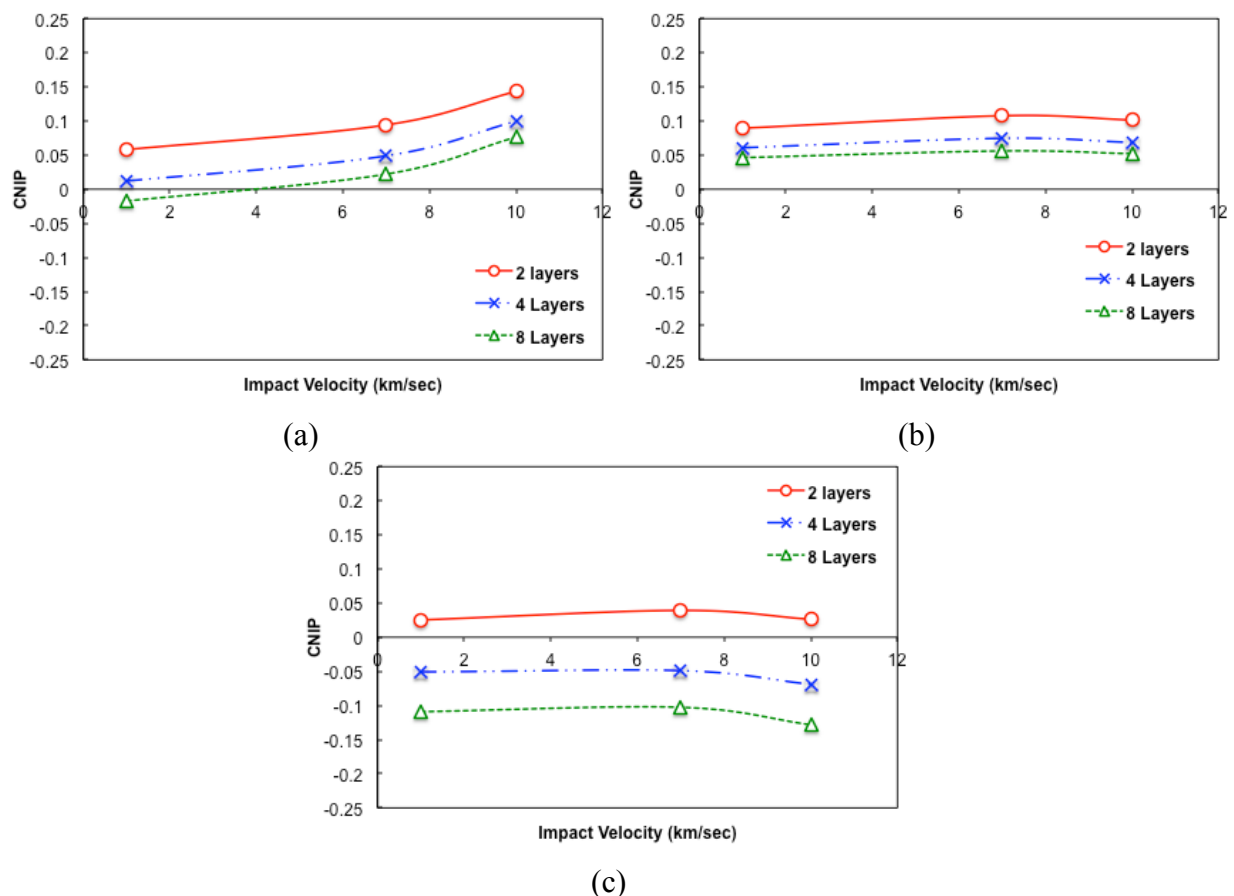


Figure 99: CNIP variation with shield layering (a) Aluminum (b) Kevlar-Epoxy (c) Steel

The variation of crater diameter can be seen in Figure 100. In Figure 100 (a), with a four-layered target, the increase in crater diameter compared to the two-layered target (Coating +Aluminum) is peaking at 7km/sec. The crater diameter continues to increase (at a lower rate) with the increase of layers number. Figure 100 (b) shows that increasing the number of layers decreases the diameter at velocities of 7km/sec and above. However, at impact velocity of 1km/sec, the diameter tends to increase. For steel substrate (Figure 100 (c)), the maximum crater diameter can be achieved by employing two layers at 1km/sec. However, at impact velocity of 10 km/sec, four layers results in larger crater diameter. The full set of the formed debris cloud shape is reported in APPENDIX E.

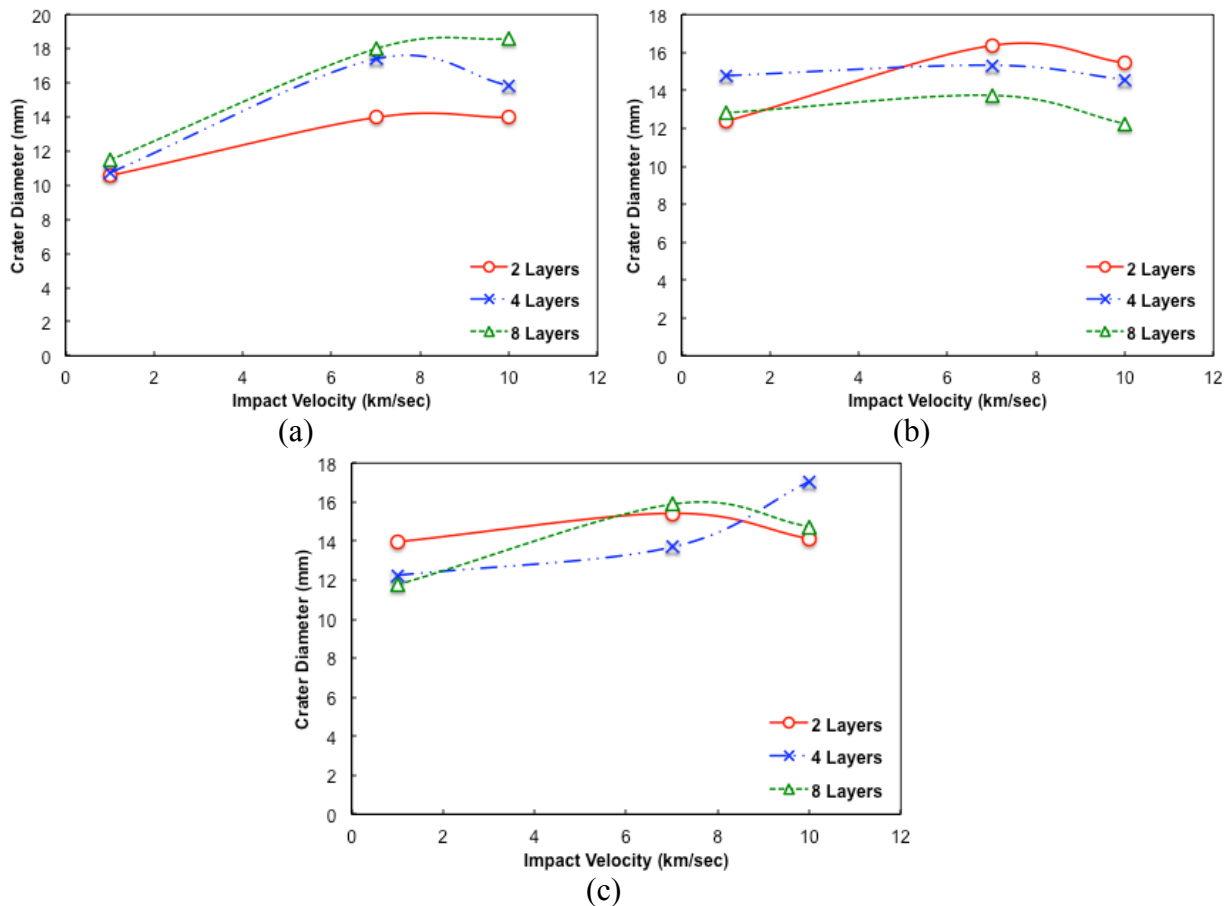


Figure 100: Variation of crater diameter with shield layering (a) Aluminum (b) Kevlar-Epoxy (c) Steel

### 2.5.8 Varying coating thickness

In this part, the same substrate materials were employed, and a series of simulations was started with 2mm of blank substrate. Then, 0.25mm of the substrate thickness was replaced by equivalent weight of coating. Thus, the total shield weight remains constant. Next, an additional 0.25 mm of substrate thickness was replaced in the next simulation. This continues until reaching only coating, resulting in a 9-shield configuration for each substrate material. The impact velocities varied between 1-7km/sec. Figure 101 shows the normalized exit velocity for all substrates. For Aluminum substrate, shown in Figure 101 (a), all configurations showed small to no deviation between the 9 shield configurations at velocities above 7km/sec. However, using thicker substrate showed slight improvement at 1km/sec. For Kevlar-Epoxy (Figure 101 (b)), the increase in coating thickness resulted in slight reduction in the exit velocity. However, Steel substrate showed different behavior (Figure 101 (c)) at 1km/sec velocity. The shield was able to stop the impactor when thickness of substrate ranged between 1-2mm. However, optimum performance at velocity greater than 7km/sec can be seen at 0.5mm thick substrate.

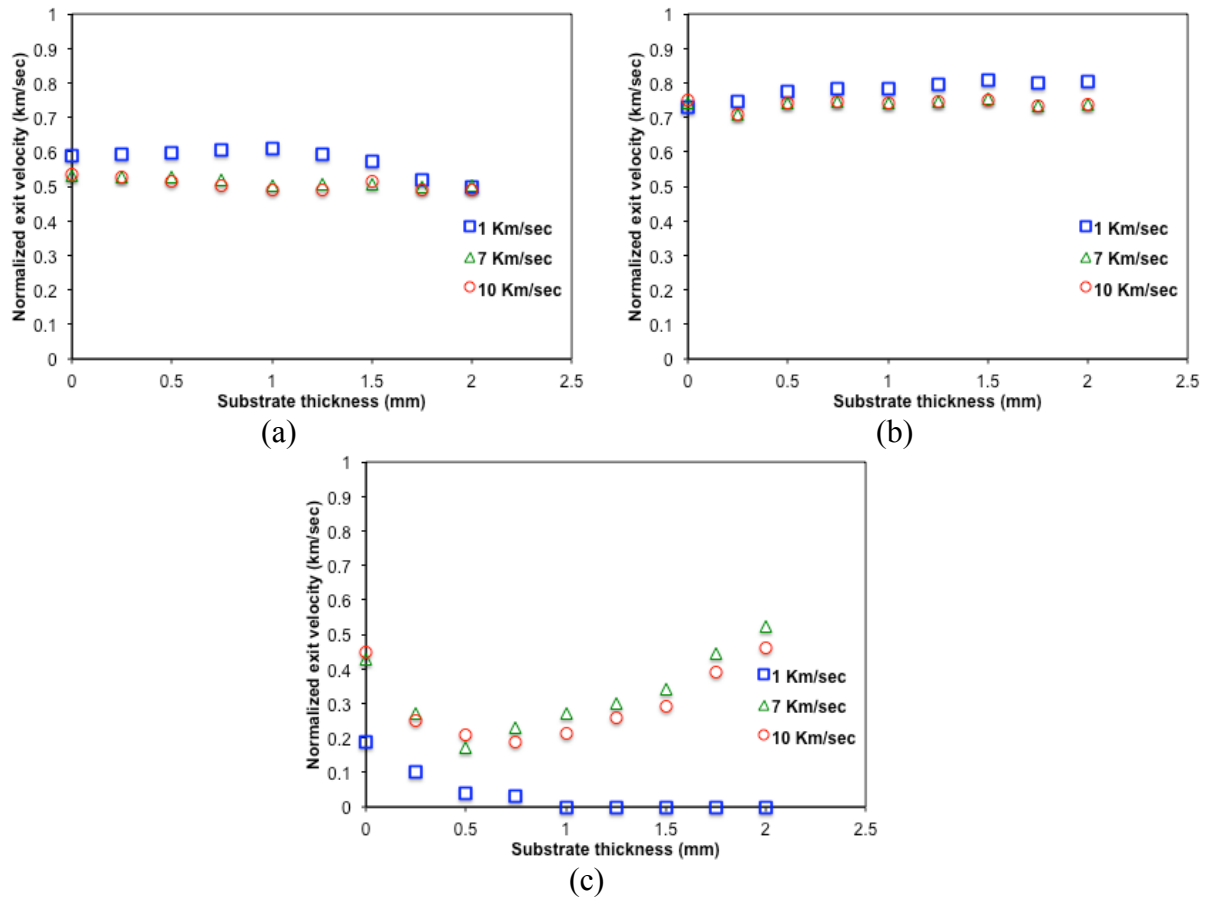


Figure 101: Normalized exit velocity variation by replacing certain substrate thickness by coating (a) Aluminum (b) Kevlar-Epoxy (c) Steel

Varying the coating thickness showed variation in crater diameter, as seen in Figure 102. Aluminum substrate, represented in Figure 102 (a), shows a trend of declination in the crater diameter with the increase of substrate thickness. This is valid at all impact velocities. The crater diameter showed variation in the case of Kevlar-Epoxy substrate. However, there is no clear trend with varying the coating thickness (Figure 102 (b)). Finally, Steel substrate, shown in Figure 102 (c) showed steep exponential declination in crater diameter with the increase in steel thickness. The full set of the formed debris cloud and crater resulted from the numerical simulation is reported in APPENDIX F.

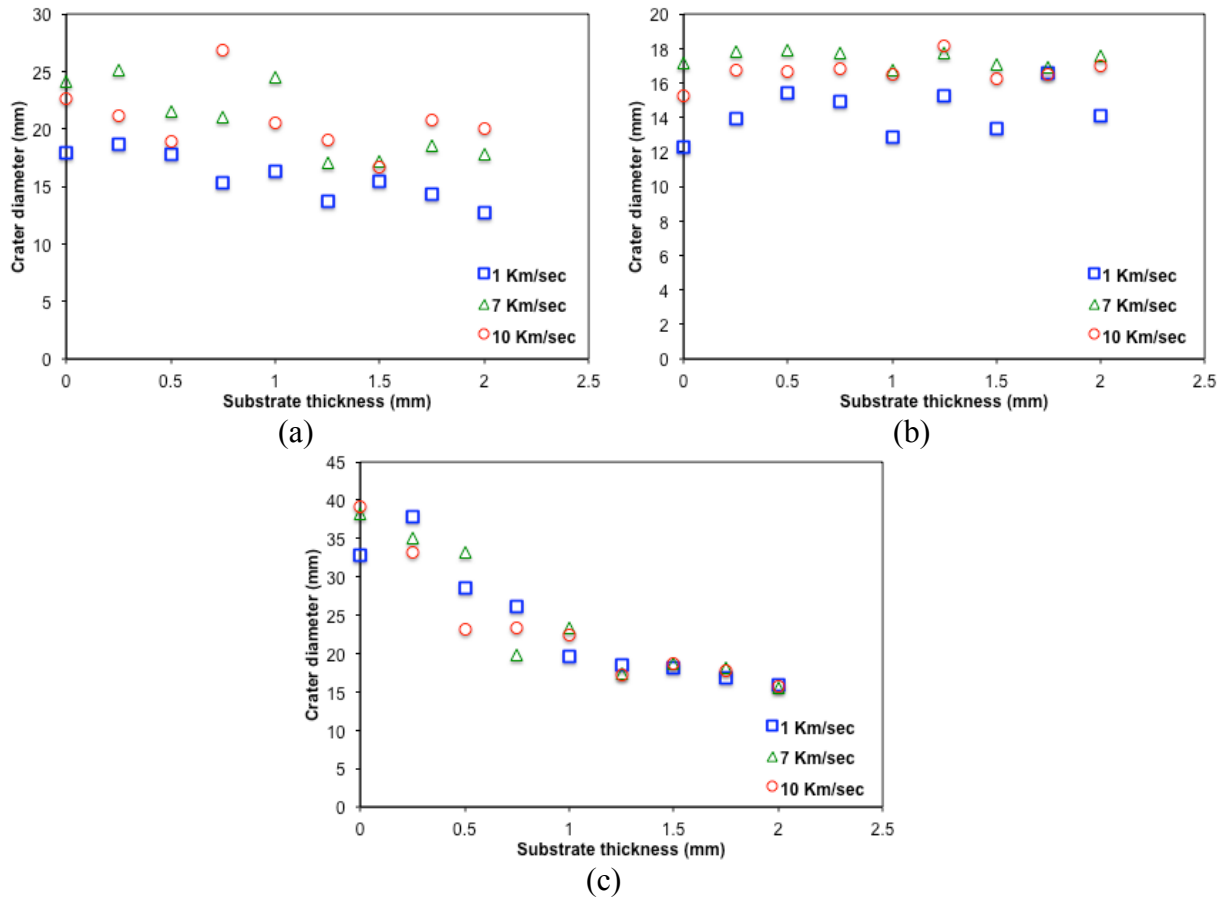


Figure 102: Variation of crater diameter by replacing certain substrate thickness by coating  
 (a) Aluminum (b) Kevlar-Epoxy (c) Steel

### 3. Conclusions and Recommendations

#### 3.1 Conclusions

The main critical issue with the development of nano-materials is our limited ability to model, simulate and bridge the behavior of the material from the nano-scale to structural-scale. Material modeling and computer-aided simulations help to understand the issue, guide the laboratory manufacturing effort, and understand the effect of the material's properties.

In this research, coupled experimental-computational technique was employed in order to study the performance of newly developed graphene-polymer nano-composites for applications in hypervelocity impact shielding. The preliminary characterization results show a potential for other applications, including, lightning strike energy dissipation, energy damping application, electronic device conductors, etc. Based on the outcome of this research, the following conclusions are made:

- Graphene oxidation seems to bond the xGnP with each other rather than enhancing the bond between the platelets and the host polymer. This was clear in the SEM and AFM scans. xGnP showed better dispersion in the polymer compared to OxGnP. This platelet-to-platelet bonding caused by the oxidation process resulted in agglomeration and clustering of the graphene platelets. Thus, the deviation between xGnP and OxGnP bulk properties was insignificant and sometimes resulted in degradation of the properties.
- Graphene-based paper was successfully manufactured; alignment of the platelets can be seen in SEM images.

- The graphene content in graphene papers can be controlled by indirect methods, in the case of xGnP-PEI, by controlling PEI concentration in the DMAc, for OxGnP or xGnP-Epoxy by pressing pressure. TGA was successfully employed to determine the xGnP or OxGnP loadings in the manufactured nano-composites.
- DMA results showed that increasing the graphene content increased the damping (loss modulus) of the material significantly.
- Based on tension tests using DMA and MTS, adding graphene platelets to all polymers clearly decreased both the strength and the toughness. However, some of the strength can be recovered by lamination. That laminated composite showed improvement in strength compared to single paper by 400%.
- SHPB dynamic testing showed that adding xGnP to the host polymer increased the strain rate sensitivity and in some cases, increased toughness.
- Implementing ANN models to predict the behavior of the material with varying graphene contents made it possible to capture the material behavior change with excellent prediction accuracy. ANN could be implemented where traditional constitutive models do not provide a satisfactory fit of the experimental data.
- Results from finite element simulation showed that adding an xGnP coating would enhance the shielding performance, without imposing significant additional load to the shield. However, the CNIP depends on the substrate at which the coating was applied.
- The sensitivity analysis carried by numerical simulations showed there are different contributions for coating material parameters; this contribution depends on substrate material.
- Based on numerical simulations, dividing the coating and the substrate into sub-layers and alternating them did not show any improvement in the CNIP performance.

### 3.2 Recommendations

Based on these research results and the conclusions listed above, further research becomes apparent, namely:

- The environmental degradation and aging effects of these nano-composites need to be investigated. The evaluation of these nano-composites was performed shortly after manufacturing, so the properties' degradation with time and environmental conditions needs to be investigated.
- Performing toxicity and flammability evaluation is highly recommended for potential multi-functional applications. The temperature effect was excluded from the material modeling and the simulation; more satisfactory results could be obtained based on additional funding.
- Unique impedance frequency curves could be generated for nano-composites or any material in general. This curve is considered a fingerprint for the material, and this fingerprint could be of great benefit for quality control purposes in the case of mass production in addition to determining the nano-filler concentration.
- Further improvement is needed for the constitutive model and EoS. Non-linear EoS needs be developed based on a plate impact test. In addition, a tension SHPB test is needed for the constitutive model.
- It is recommended to extend the simulations to 3D. Adding a 3<sup>rd</sup> dimension would increase the accuracy of the solution; computer resources limited this study.
- The shape of the impactor, material of the impactor, and additional impact speed can be investigated. In addition, different substrate materials could be considered.
- The use of hydro-codes simulation is recommended, since it can save a significant amount of money in experimental testing. Hydro-codes can produce very accurate simulations of the hypervelocity impact phenomena. In case of the need for



experimental testing, it is recommended to conduct a series of simulations for materials under consideration to determine effective materials and only those relevant material parameters.

- The results of this research indicate that for graphene-based coatings, the shielding performance is more sensitive to some parameters compared to others. If other material is to be evaluated, the major parameters contribute to the cratering growth and exit velocity can be identified by hydro-codes sensitivity analysis.

## REFERENCES

- [1] A. J. Piekutowski, and K. L. Poormon. "Impact Of Thin Aluminum Sheets With Aluminum Spheres Up To 9km/S." *International Journal of Impact Engineering*, Vol. 35 No. 12, PP. 1716-1722, 2008.
- [2] H. Fukushima, and L. T. Drzal. "Nylon-Exfoliated Graphite Nanoplatelet (xGnP) Nanocomposites With Enhanced Mechanical, Electrical And Thermal Properties." *NSTI Nanotech*, PP. 282-287, 2006.
- [3] [www.earthobservatory.nasa.gov](http://www.earthobservatory.nasa.gov), accessed March/5/2015.
- [4] H. Riebeek, "Catalog Of Earth Satellite Orbits: Feature Articles." *Catalog of Earth Satellite Orbits : Feature Articles*, Sept. 2009.
- [5] S. J. Tomczak, V. Vij, T. K. Minton, A. L. Brunsvold, D. Marchant, M. E. Wright, B. J. Petteys, A. J. Guenther, and J. M. Mabry, "Comparisons of Polyhedral Oligomeric Silsesquioxane (POSS) Polyimides As Space-Survivable Materials." (Postprint), *Air Force Research Lab Edwards Afb Ca Propulsion Directorate*, No. AFRL-PR-ED-TP-2006-437, 2006.
- [6] R. Verker, E. Grossman, and N. Eliaz. "Erosion Of POSS-Polyimide Films Under Hypervelocity Impact And Atomic Oxygen: The Role Of Mechanical Properties At Elevated Temperatures." *Acta Materialia*, Vol. 57, No. 4, PP. 1112-1123, 2009.
- [7] NASA Orbital Debris Program Office Webpage, <http://orbitaldebris.jsc.nasa.gov>, accessed May/20/2015.
- [8] E.D.Grayfer, A.S. Nazarov, V.G. Makotchenko, S.J.Kim, and V.E. Fedorov, "Chemically Modified Graphene Sheets By Functionalization Of Highly Exfoliated Graphite." *Journal of Materials Chemistry*, Vol. 21 No. 10, PP. 3410-3414, 2011.
- [9] National Research Council, "Orbital Debris-A Technical Assessment." *National Academy Press*, 1995.

- [10] H. F. Swift, "Impact Dynamics Mechanics Of Hypervelocity Impact." *Impact Dynamics, John Wiley and Sons*, 1982.
- [11] E. L. Christiansen, "Meteoroid/Debris Shielding." *National Aeronautics and Space Administration, Lyndon B. Johnson Space Center*, 2003.
- [12] M. B. Boslough, J. A. Ang, L. C. Chhabildas, W. D. Reinhart, C. A. Hall, B. G. Cour-Palais, E. L. Christiansen, and J. L. Crews, "Hypervelocity Testing Of Advanced Shielding Concepts For Spacecraft Against Impacts To 10 km/s." *International Journal of Impact Engineering*, Vol. 14, No. 1, PP. 95-106, 1993.
- [13] E. L. Christiansen, J. H. Kerr, H. M. DE La Fuente and W. C. Schneider, "Flexible And Deployable Meteoroid/Debris Shielding For Spacecraft." *International Journal of Impact Engineering*, Vol. 23, No. 1, PP. 125-136, 1999.
- [14] K. Thoma, F. Schafer, S. Hiermaier and E. Schneider, "An Approach To Achieve Progress In Spacecraft Shielding." *Advances in Space Research*, Vol. 34, No. 5, PP. 1063-1075, 2004.
- [15] E. P. Fahrenthold and Y.-K. Park, "Simulation Of Hypervelocity Impact On Aluminum-Nextel-Kevlar Orbital Debris Shields." *International Journal of Impact Engineering*, 2003.
- [16] R. A. Clegg, D. M. White, W. Riedel and W. Harwick, "Hypervelocity Impact Damage Prediction In Composites: Part I – Material Model And Characterization." *International Journal of Impact Engineering*, Vol. 33, No. 1, PP. 190-200, 2006.
- [17] W. Riedel, H. Nahme , D. M. White, and R. A. Clegg, "Hypervelocity Impact Damage Prediction In Composites: Part II – Experimental Investigations And Simulations." *International Journal of Impact Engineering*, Vol. 33, No. 1, PP. 670-680, 2006.

- [18] J. Eftis, C. Carrasco and R. Osegueda, "Simulations Of Hypervelocity Impact And Fracture Of Aluminum Targets Using A Constitutive-Microdamage Material Model." *International Journal of Impact Engineering*, Vol. 26, No. 1, PP. 157-168, 2001.
- [19] Justin H. Kerr and Eric P. Fahrenthold, "Three Dimensional Hypervelocity Impact Simulation For Orbital Debris Shield Design." *International Journal of Impact Engineering*, Vol. 20, No. 6, PP. 479-489, 1997.
- [20] S. Rayan, F. Schaefer and W. Riedel, "Numerical Simulation Of Hypervelocity Impact On CFRP/Al HS SP Spacecraft Structures Causing Penetration And Fragment Ejection." *International Journal of Impact Engineering*, Vol. 33, No. 1, PP. 703-712, 2006.
- [21] M. Katayama, S. Toda and S. Kibe, "Numerical Simulation Of Space Debris Impacts On The Whipple Shield." *Acta Astronautica*, Vol. 40, No. 12, PP. 859-869, 1997.
- [22] N. Kawai, K. Tsurui, D. Shindo, . Motoyashiki and E. Sato, "Fracture Behavior Of Silicon Nitride Ceramics Subjected To Hypervelocity Impact." *International Journal of Impact Engineering*, Vol. 38, No. 7, PP. 542-545, 2011.
- [23] G. Hussain, A. Hameed, I. Horsfall, P. Barton anf A. Q. Malik, "Experimental And Simulation Optimization Analysis Of The Whipple Shields Against Shaped Charge." *Acta Mechanica Sinica*, Vol. 28, No. 3, PP. 877-884, 2012.
- [24] Young-Keun Park and Eric P. Fahrenthold, "A Kernel Free Particle-Finite Element Method For Hypervelocity Impact Simulation." *International journal for numerical methods in engineering*, Vol. 63, No. 5, PP. 737-759, 2005.
- [25] J. Bonet, S. Kulasegaram, M. X. Rodriguez-Paz and M. Profit, "Variational Formulation For The Smooth Particle Hydrodynamics (SPH) Simulation Of Fluid And Solid Problems." *Computer methods in applied mechanics and engineering*, Vol. 193, No. 12, PP. 1245-1256, 2004.

- [26] S. Katz, E. Grossman, I. Gouzman, M. Murat, E. Wiesel, H. D. Wagner, "Response Of Composite Materials To Hypervelocity Impact." *International Journal of Impact Engineering*, Vol. 35, No. 12, PP. 1606-1611, 2008.
- [27] S. Ryan, F. Schafer, M. Guyot, S. Hiermaier and M. Lambert, "Characterizing The Transient Response Of CFRP/Al HC Spacecraft Structures Induced By Space Debris Impact At Hypervelocity." *International Journal of Impact Engineering*, Vol. 35, No. 12, PP. 1756-1763, 2008.
- [28] J. A. Zukas and D. R. Scheffler, "Impact Effects In Multilayered Plates." *International Journal of Solids and structures*, Vol. 38, No. 19, PP. 3321-3328, 2001.
- [29] G. R. Johnson, R. A. Stryk and S. R. Beissel, "SPH For High Velocity Impact Computations." *Computer Methods in Applied Mechanics and Engineering*. Vol. 139, No. 1, PP. 347-373, 1996.
- [30] M. C. Price, A. T. Kearsley, and M. J. Bruchell, "Validation Of Preston-Tonks-Wallace Strength Model At Strain Rates Approaching  $\sim 10^{11}$  S<sup>-1</sup> For Al 1100, Tantalum And Copper Using Hypervelocity Impact Crater Morphologies." *International Journal of Impact Engineering*, Vol. 52, PP. 1-10, 2013.
- [31] E. P. Farenthold and R. J. Hernandez, "Simulations Of Orbital Debris Impact On The Space Shuttle Wing Leading Edge." *International Journal of Impact Engineering*, Vol. 33, No. 1, PP. 231-243, 2006.
- [32] J. Eftis, C. Carrasco and R. A. Osegueda, "A Constitutive-Microdamage Model To Simulate Hypervelocity Projectile-Target Impact, Material Damage And Fracture." *International Journal of Plasticity*, Vol 19, No. 9, PP. 1321-1354, 2003.
- [33] G. Gongshun, P. Baojun, Z. Wei, and H. Yue, "Crater Distribution On The Rear Wall Of AL-Whipple Shield By Hypervelocity Impacts Of AL-Spheres." *International Journal of Impact Engineering*, Vol. 35, No. 12, PP. 1541-1546, 2008.

- [34] R. Destefanis, F. Schafer, M. Lambert, and M. Faraud, "Selecting Enhanced Space Debris Shields For Manned Spacecraft." *International Journal of Impact Engineering*, Vol. 33, No. 1, PP. 219-230, 2006.
- [35] M. J. Eller, C. Liang, S. Della-Negra, A. B. Clubb, H. Kim, A. E. Young and E. A. Schweikert, "Hypervelocity Nanoparticle Impacts On Free-Standing Graphene: A Sui Generis Mode Of Sputtering." *The Journal of Chemical Physics*, Vol. 142, No. 4, PP. 044308, 2015.
- [36] H. Shang and W. Wang, "Hypervelocity Impact Properties Of Graphene Armor Via Molecular Dynamic Simulations." *EPJ Web of Conferences*, Vol. 26, PP. 04027, 2012.
- [37] G.H. Lee, R.C. Cooper, S.J. An, S. Lee, A. van der Zande, N. Petrone, A.G. Hammerberg, C. Lee, B. Crawford, W. Oliver, and J.W. Kysar, "High-Strength Chemical-Vapor-Deposited Graphene And Grain Boundaries." *Science*, Vol. 340 No. 6136, PP. 1073-1076, 2013.
- [38] A.A. Balandin, S. Ghosh, W. Bao, I. Calizo, D. Teweldebrhan, F. Miao, and C.N. Lau, "Superior Thermal Conductivity Of Single-Layer Graphene." *Nano letters*, Vol. 8 No. 3 PP. 902-907, 2008.
- [39] S. Park, and R. S. Ruoff. "Chemical Methods For The Production Of Graphenes." *Nature nanotechnology* Vol. 4, No. 4, PP. 217-224, 2009.
- [40] Gómez-Navarro, C. M. Burghard, and K. Kern. "Elastic Properties Of Chemically Derived Single Graphene Sheets." *Nano letters* Vol. 8, No. 7, PP. 2045-2049, 2008.
- [41] S. K. Khanna, and H. TT. Phan. "High Strain Rate Behavior Of Graphene Reinforced Polyurethane Composites." *Journal of Engineering Materials and Technology*, Vol. 137, No. 2, PP. 021005, 2015.
- [42] O. Urakawa, *Encyclopedia of Polymeric Nanomaterials*, PP. 1-10, 2014.

- [43] T. Yilmaz, and T. J. Sinmazcelik, "Mater Effects Of Hydrothermal Aging On Glass–Fiber/Polyetherimide (PEI) Composites." *Journal of materials science*. Vol. 45, No. 2, PP. 399-404, 2010.
- [44] Y. Zhai, K. Xiao, J. Yu, and B. Ding, "Fabrication of hierarchical structured sio<sub>2</sub>/polyetherimide-polyurethane nanofibrous separators with high performance for lithium ion batteries." *Electrochim. Acta*, Vol. 154, No. 1, PP. 219-226, 2015.
- [45] M. Hegde, E.T. Samulski, M. Rubinstein, and T.J. Dingemans, "The Role Of Crystallinity In SWCNT–Polyetherimide Nanocomposites." *Composites Science and Technology*, Vol. 110, PP. 176-187, 2015.
- [46] X. Li, B. Sanjib, and L. T. Drzal. "High Temperature Vacuum Annealing and Hydrogenation Modification of Exfoliated Graphite Nanoplatelets." *Journal of Engineering*, 2013.
- [47] X. Li, and M. R. Coleman. "Functionalization Of Carbon Nanofibers With Diamine And Polyimide Oligmer." *Carbon*, Vol. 46, No. 8, PP. 1115-1125, 2008.
- [48] H.J. Shin, K.K. Kim, A. Benayad, S.M. Yoon, H.K. Park, I.S. Jung, M.H. Jin, H.K. Jeong, J.M. Kim, J.Y. Choi, and Y.H. Lee, "Efficient Reduction Of Graphite Oxide By Sodium Borohydride And Its Effect On Electrical Conductance." *Advanced Functional Materials*, Vo. 19, No. 12, PP. 1987-1992, 2009.
- [49] C. Mattevi, G. Eda, S. Agnoli, S. Miller, K.A. Mkhoyan, O. Celik, D. Mastrogiovanni, G. Granozzi, E. Garfunkel, and M. Chhowalla, "Evolution Of Electrical, Chemical, And Structural Properties Of Transparent And Conducting Chemically Derived Graphene Thin Films." *Advanced Functional Materials*, Vol. 19, No. 16, PP. 2577, 2009.
- [50] X. Li and M. R. Coleman, "Functionalization Of Carbon Nanofibers With Diamine And Polyimide Oligomer." *Carbon*, Vol. 46, No. 8, PP. 1115-1125, 2008.
- [51] H. J. Shin, K. K. Kim, A. Benayad, S. M. Yoon, H. K. Park, I. S. Jung, M. H. Jin, H. K.



- Jeong, J. M. Kim, J. Y. Choi, and Y. H. Lee, "Efficient Reduction Of Graphite Oxide By Sodium Borohydride And Its Effect On Electrical Conductance." *Advanced Functional Materials*, Vol. 19, No. 12, PP. 1987-1992, 2009.
- [52] H. Wu and L.T. Drzal, "Graphene Nanoplatelet Paper As A Light-Weight Composite With Excellent Electrical And Thermal Conductivity And Good Gas Barrier Properties." *Carbon*, Vol. 50, PP. 1135–1145, 2012.
- [53] M. Naebe, J. Wang, A. Amini, H. Khayyam, N. Hameed, L.H. Li, Y. Chen, and B. Fox, "Mechanical Property And Structure Of Covalent Functionalized Graphene/Epoxy Nanocomposites." *Scientific reports*, Vol. 4, PP. 1-7, 2014.
- [54] B. Li, E. Olson, A. Perugini, and W.H. Zhong, "Simultaneous Enhancements In Damping And Static Dissipation Capability Of Polyetherimide Composites With Organosilane Surface Modified Graphene Nanoplatelets." *Polymer*, Vol. 52, PP. 5606–5614, 2011.
- [55] M. Grujicic, B. Pandurangan, T. He, B.A. Cheeseman, C.F. Yen, and C.L. Rando, "Computational Investigation Of Impact Energy Absorption Capability Of Polyurea Coatings Via Deformation-Induced Glass Transition." *Materials Science and Engineering: A*, Vol. 527, No. 29, PP. 7741–7751, 2010.
- [56] D. Lahiri, S. Das, W. Choi, and A. Agarwal, "Unfolding The Damping Behavior Of Multilayer Graphene Membrane In The Low-Frequency Regime." *ACS Nano*, Vol. 6, PP. 3992–4000, 2012.
- [57] H. Kolsky, "An Investigation Of The Mechanical Properties Of Materials At Very High Rates Loading." *Proceedings of the Physical Society. Section B*, Vol. 62, No. 11, PP. 676, 1949.

- [58] J. Richeton, S. Ahzi, L. Daridon, and Y. Rémond, "A Formulation Of The Cooperative Model For The Yield Stress Of Amorphous Polymers For A Wide Range Of Strain Rates And Temperatures." *Polymer*, Vol. 46, No. 16, PP. 6035-6043, 2005.
- [59] Z.Z. Gao, Z.Q. Liu, W. Liu, and Z.F. Yue, "Experimental And Constitutive Investigation On Tensile And Compressive Behavior Of MDYB-3 At Different Temperatures And Loading Rates." *International Journal of Polymeric Materials*, Vol. 60, No. 5, PP. 340-350, 2011.
- [60] O. A. Hasan, and M. C. Boyce. "A Constitutive Model For The Nonlinear Viscoelastic Viscoplastic Behavior Of Glassy Polymers." *Polymer Engineering & Science*, Vol. 35, No. 4, PP. 331-344, 1995.
- [61] U.A. Dar, W. Zhang, Y. Xu, and J. Wang, "Thermal And Strain Rate Sensitive Compressive Behavior Of Polycarbonate Polymer-Experimental And Constitutive Analysis." *Journal of Polymer Research*, Vol. 21, No. 8, PP. 1-10, 2014.
- [62] Y. Duan, A. Saigal, R. Greif, and M.A. Zimmerman, "A Uniform Phenomenological Constitutive Model For Glassy And Semicrystalline Polymers." *Polymer Engineering & Science*, Vol. 41, No. 8, PP. 1322-1328, 2001.
- [63] K.H. Safari, J. Zamani, F.J. Ferreira, and R.M. Guedes, "Constitutive Modeling Of Polycarbonate During High Strain Rate Deformation." *Polymer Engineering & Science*, Vol. 53, No. 4, PP. 752-761, 2013.
- [64] D.J. Senden, S. Krop, J.A.W. van Dommelen, and L.E. Govaert, "Rate And Temperature Dependent Strain Hardening Of Polycarbonate." *Journal of Polymer Science Part B: Polymer Physics*, Vo. 50, No. 24, PP. 1680-1693, 2012.
- [65] R. Fleischhauer, H. Dal, M. Kaliske, and K. Schneider, "A Constitutive Model For Finite Deformation Of Amorphous Polymers." *International Journal of Mechanical Sciences*, Vol. 65, No. 1, PP. 48-63, 2012.

- [66] Y. Bai, C. Liu, G. Huang, W. Li, and S. Feng, "A Hyper-Viscoelastic Constitutive Model For Polyurea Under Uniaxial Compressive Loading." *Polymers*, Vol. 8, No. 4, PP. 133, 2016.
- [67] R. Singh, A. Saigal, and R. Greif. "Impact Behavior Of Recycled Core Composite Polymeric Enclosures." *Composite structures*, Vol. 61, No. 4, PP. 321-332, 2003.
- [68] T. M. Pham, and M. N. Hadi, "Predicting Stress And Strain Of FRP-Confined Square/Rectangular Columns Using Artificial Neural Networks." *Journal of Composites for Construction*, Vol. 18, No. 6, PP. 4014-4019, 2014.
- [69] S. G. Setti, , and R. N. Rao, "Artificial Neural Network Approach For Prediction Of Stress–Strain Curve Of Near B Titanium Alloy." *Rare Metals*, Vol. 33, No. 3, PP. 249-257, 2014.
- [70] Y. M. Najjar, and C. Huang, "Simulating The Stress–Strain Behavior Of Georgia Kaolin Via Recurrent Neuronet Approach." *Computers and Geotechnics*, Vol. 34, No. 5, PP. 346-361, 2007.
- [71] O. Itani, and Y. Najjar, "Three-Dimensional Modeling Of Spatial Soil Properties Via Artificial Neural Networks." *Transportation Research Record: Journal of the Transportation Research Board*, Vol. 1709, PP. 0-59, 2000.
- [72] R. Rojas, "Neural Networks: A Systematic Introduction." *Springer Science & Business Media*, 2013.
- [73] H. Yasarer, and Y. M. Najjar, "Characterizing The Permeability Of Kansas Concrete Mixes Used In PCC Pavements." *International Journal of Geomechanics*, Vol. 14, No. 4, PP. 4014-4017, 2013.
- [74] K. Nixdorff, "Some Applications Of The Impact Theory Of Awerbuch, J. And Bodner, Sr." *Transactions of the Canadian Society for Mechanical Engineering*, Vol. 8, No. 1, PP. 16-20, 1984.

## LIST OF APPENDICES

## APPENDIX A

```
! *****
! THIS MODULE IS A CONTAINER FOR THE INITIALISATION AND SOLUTION
! OF A USER STRENGTH MODEL
! THE FOLLOWING ROUTINES ARE INCLUDED:
! MODULE STR_USER_1
!   DEFINE VARIABLES THAT ARE COMMON BETWEEN THE ROUTINES BELOW
! SUBROUTINE INIT_STR_USER_1
!   DEFINE THE INPUT PARAMETERS FOR THE USER STRENGTH MODEL
! SUBROUTINE CHECK_STR_USER_1
!   CHECK PARAMETERS ARE VALID FOR THE USER STRENGTH MODEL
! SUBROUTINE SET_STR_USER_1
!   SET SHORTCUTS TO PARAMETERS FOR THE USER STRENGTH MODEL
! SUBROUTINE SOLVE_STR_USER_1
!   SOLVE THE USER STRENGTH MODEL
! BEFORE EACH ROUTINE IS CALLED, THE FOLLOWING POINTERS ARE SET-UP
!   MTL - POINTER TO THE CURRENT MATERIAL
!   EQ  - POINTER TO THE CURRENT FLAG/EQUATION/MATERIAL OPTION
!!!!!!!!!!!!!!!!!!!!!!!!!!!!!!!!!!!!!!!!!!!!!!!!!!!!!!!!!!!!!!!!!!!!!!!!!!!!!!
! NOTE: CARE SHOULD BE TAKEN WHEN USING THIS MATERIAL MODEL WITH THE
!       ANP TETRAHEDRAL ELEMENTS. IT IS HIGHLY RECOMMENDED THAT YOU
!       CONTACT ANSYS FOR ADVICE ON THE TYPES OF MATERIALS
!       APPLICABLE TO THE ANP TERTRAHEDRAL ELEMENT.
!!!!!!!!!!!!!!!!!!!!!!!!!!!!!!!!!!!!!!!!!!!!!!!!!!!!!!!!!!!!!!!!!!!!!!!!!!!!!!
! *****

MODULE STR_USER_1
USE kindf
IMPLICIT NONE
SAVE
REAL(REAL8), DIMENSION(10) :: SC

END MODULE STR_USER_1

SUBROUTINE INIT_STR_USER_1(IFACT)

USE material
USE str_user_1

IMPLICIT NONE

INTEGER (INT4) ::   IFACT

! *****

! THIS SUBROUTINE INITIALISES (ALLOCATES) PARAMETERS AND DATA
! FLAG - IMF_STR_USER_1
! INPUT - IFACT = 0 JUST GET NAME OF EQUATION AND DEPENDANT FLAGS
!         IFACT = 1 EQUATION IS ACTIVE HENCE ALLOCATE
```

```

! *****
! DEFINE PARAMETERS TO ALLOW ALLOCATION
EQ%EQTYPE = IMF_STR_USER_1 ! DO NOT MODIFY THIS LINE
EQ%NAME = 'User Strength #1'
EQ%NPAR = 10 ! NUMBER OF REAL INPUT PARAMETER (MINIMUM OF 1)
EQ%NUMOPT = 0 ! NUMBER OF OPTION LISTS
EQ%NDEPFLG = 0 ! NUMBER OF NON-OPTIONAL DEPENDANT (CHILD)
FLAG/MODEL OPTION

IF (IFACT==1) THEN
  CALL ALLOC_EQ ! DO NOT MODIFY THIS LINE, ALLOCATES MEMORY

  ! FOR EACH REAL INPUT PARAMETER, ASSIGN DATA
  ! ('name ' L, T,M,H, val, min,max,default,0,required)
EQ%PAR(1)=PRMT (1, 'Shear Modulus' , -1, -2, 1, 0, ZERO, -BIG, BIG, ZERO , 0, 1) !
THIS LINE MUST ALWAYS EXIST
EQ%PAR(2)=PRMT (2, 'C0' , -1, -2, 1, 0, ZERO, -BIG, BIG, ZERO , 0, 0)
EQ%PAR(3)=PRMT (3, 'C1' , -1, -2, 1, 0, ZERO, -BIG, BIG, ZERO , 0, 0)
EQ%PAR(4)=PRMT (4, 'C2' , -1, -2, 1, 0, ZERO, -BIG, BIG, ZERO , 0, 0)
EQ%PAR(5)=PRMT (5, 'm' , -1, -2, 1, 0, ZERO, -BIG, BIG, ZERO , 0, 0)
EQ%PAR(6)=PRMT (6, 'a enter a small' , -1, -2, 1, 0, ZERO, -BIG, BIG, ZERO , 0, 0)
EQ%PAR(7)=PRMT (7, 'K' , -1, -2, 1, 0, ZERO, -BIG, BIG, ZERO , 0, 0)
EQ%PAR(8)=PRMT (8, 'C3' , -1, -2, 1, 0, ZERO, -BIG, BIG, ZERO , 0, 0)
EQ%PAR(9)=PRMT (9, 'C4' , -1, -2, 1, 0, ZERO, -BIG, BIG, ZERO , 0, 0)
EQ%PAR(10)=PRMT (10, 'Alpha' , -1, -2, 1, 0, ZERO, -BIG, BIG, ZERO , 0, 0)

  ! FOR EACH OPTION LIST, ASSIGN DATA
  ! FOR EXAMPLE,
  ! EQ%OPTION(1)%NAME = 'Strain rate dependant' ! OPTION LIST NAME
  ! EQ%OPTION(1)%NUMOPT = 2 ! NUMBER OF OPTIONS IN THE LIST
  ! EQ%OPTION(1)%DEFAULT = 1 ! DEFAULT OPTION
  ! EQ%OPTION(1)%SELECTED = 1 ! SELECTED OPTION
  ! CALL ALLOC_OPTION(1) ! ALLOCATE THE MEMORY
  ! DEFINE OPTIONS
  ! ('name ', active, ' ', 0 / Dependant (child)
flag)
  ! EQ%OPTION(1)%OPTS(1) = OPTION('Yes', 'Y', ' ', 0)
  ! EQ%OPTION(1)%OPTS(2) = OPTION('No', 'Y', ' ', 0)
  ! FOR EACH NON-OPTIONAL DEPENDANT (CHILD) FLAG/MODEL OPTION, ASSIGN DEPENDANT
FLAG
  !EQ%DEPFLG(1) = IMF_YP_PCWISE
ENDIF
! SET IN ACTIVE SWITCH FOR APPROPRIATE PROCESSOR TYPE:: ALL ON BY DEFAULT
EQ%IFSOLVER(ISLV_FCT) = 0
RETURN
END SUBROUTINE INIT_STR_USER_1

SUBROUTINE SET_STR_USER_1

USE material
USE str_user_1

IMPLICIT NONE

! *****
! THIS SUBROUTINE ASSIGNS SHORTCUTS FOR DIRECT USE IN THE SOLVER
! *****

```

```

! FOR EXAMPLE
SHRMDZ = EQ%PAR(1)%VAL ! THIS LINE MUST BE PRESENT
SC(1) = EQ%PAR(1)%VAL
SC(2) = EQ%PAR(2)%VAL
SC(3) = EQ%PAR(3)%VAL
SC(4) = EQ%PAR(4)%VAL
SC(5) = EQ%PAR(5)%VAL
SC(6) = EQ%PAR(6)%VAL
SC(7) = EQ%PAR(7)%VAL
SC(8) = EQ%PAR(8)%VAL
SC(9) = EQ%PAR(9)%VAL
SC(10) = EQ%PAR(10)%VAL

RETURN

END SUBROUTINE SET_STR_USER_1

SUBROUTINE CHECK_STR_USER_1

USE material
USE str_user_1

IMPLICIT NONE

! *****
! THIS SUBROUTINE CHECKS EOS INPUT DATA
! *****

RETURN

END SUBROUTINE CHECK_STR_USER_1

SUBROUTINE SOLVE_STR_USER_1_2D
(PRES,TT1,TT2,TT3,XMUT,EPST,EPST,TEMP,T,TEMP,DAMAGE,YIELDT,IFAIL)

USE material
USE str_user_1
USE cycvar
USE edtdef
USE ijknow
USE wrapup
USE mdgrid

IMPLICIT NONE

INTEGER (INT1) :: IFAIL
INTEGER (INT4) :: IJK
REAL (REAL8) :: EPST, EPST, PRES, TEMP, TT1, TT2
REAL (REAL8) :: TT3, XMUT, YIELDT, DAMAGE
! INTEGER (INT4) :: I, IM

! *****
! THIS IS A USER SUPPLIED SUBROUTINE WHICH CAN BE USED TO COMPUTE
! THE YIELD STRESS FOR A MATERIAL
! INPUT PARAMETER

```

```

! PRES    PRESSURE
! Tnn     PRINCIPAL STRESSES
! XMUT    COMPRESSION
! EPST    EFFECTIVE PLASTIC STRAIN
! EPSD    EFFECTIVE PLASTIC STRAIN RATE
! TEMP    TEMPERATURE
! DAMAGE  DAMAGE
! IFAIL   STRESS STATE INDICATOR
! = 0     HYDRO
! = 1     ELASTIC
! = 2     PLASTIC
! = 3     BULK FAILURE (WITH HEAL)
! = 4     BULK FAILURE (NO HEAL)

! OUTPUT PARAMETERS

! YIELDT  YIELD STRESS FOR CURRENT MATERIAL
! IFAIL   STRESS STATE INDICATOR (SEE ABOVE)

! THE FOLLOWING MODULES CONTAIN INFORMATION WHICH MAY BE
! USEFUL FOR COMPUTING THE OUTPUT PARAMETERS :-

! MODULE 'IJKNOW'

! INOW - I INDEX FOR CURRENT CELL
! JNOW - J INDEX FOR CURRENT CELL
! MNOW - CURRENT SUBGRID NUMBER

! MODULE 'MATDEF'
! MATNO      - THE MATERIAL NUMBER OF THE CURRENT MATERIAL
! MATERIALS(MATNO)%NAME - THE MATERIAL NAME OF THE CURRENT MATERIAL

! MODULE 'CYCVAR'
! NCYCLE - CURRENT CYCLE NUMBER
! TIME   - CURRENT TIME
! DLTH   - TIME STEP FOR CURRENT CYCLE

! MODULE 'EDTDEF'
! NTCODE - DIMENSIONS: 2 = 2D, 3 = 3D

! EN(IJK) - CELL SPECIFIC INTERNAL ENERGY
! DAM(IJK) - DAMAGE

! TO OBTAIN THE VALUE OF THE INDEX IJK FOR THE CURRENT CELL, USE
!   IJK = IJSET(INOW,JNOW)
! THE INDEX IJK MUST ALSO BE DEFINED AS AN INTEGER: - INTEGER (INT4) :: IJK

! *****

! SUBROUTINE CALLED BY ALL STRENGTH MODELS SO SKIP OUT, BY DEFAULT
IF (NSTR/=IMF_STR_USER_1) GO TO 900
IF (EPST<=0.000000000000000000000001) THEN

    YIELDT = 0.0000000000
ELSE

    YIELDT =
SC(7)*(EPSD**SC(5))*2.718**(SC(6)/300)*(((2.718**(SC(2)*EPST)+EPST**SC(3))-SC(4))*(1-
2.718**(-1*SC(10)*EPST)))+(EPST*(2.718**(1
-
(EPST/(SC(8)*(EPSD**SC(5))*2.718**(SC(6)/300))))))/(SC(8)*(EPSD**SC(5))*2.718**(SC(6)/3

```



```
00))-(2.718**(SC(2)*EPST)+EPST**SC(3)-SC(4))*(1-2.718**(-
1*SC(10)*EPST))*2.718**(EPST*((EPSD**SC(5))*2.718**(SC(6)/300)-SC(9))))
```

```
END IF
```

```
900 RETURN
```

```
END SUBROUTINE SOLVE_STR_USER_1_2D
```

```
SUBROUTINE SOLVE_STR_USER_1_3D
(PRES,TT1,TT2,TT3,XMUT,EPST,EPSD,TEMP,T, DAMAGE, YIELDT, IFAIL)
```

```
USE material
USE str_user_1
USE cycvar
USE edtdef
USE ijknow
USE wrapup
USE mdgrid3
```

```
IMPLICIT NONE
```

```
INTEGER (INT1) :: IFAIL
INTEGER (INT4) :: IJK
REAL (REAL8) :: EPSD, EPST, PRES, TEMP, TT1, TT2
REAL (REAL8) :: TT3, XMUT, YIELDT, DAMAGE
```

```
! *****
```

```
! THIS IS A USER SUPPLIED SUBROUTINE WHICH CAN BE USED TO COMPUTE
! THE YIELD STRESS FOR A MATERIAL
```

```
! INPUT PARAMETER
```

```
! PRES    PRESSURE
! Tnn     PRINCIPAL STRESSES
! XMUT    COMPRESSION
! EPST    EFFECTIVE PLASTIC STRAIN
! EPSD    EFFECTIVE PLASTIC STRAIN RATE
! TEMP    TEMPERATURE
! DAMAGE  DAMAGE
! IFAIL   STRESS STATE INDICATOR
! = 0    HYDRO
! = 1    ELASTIC
! = 2    PLASTIC
! = 3    BULK FAILURE (WITH HEAL)
! = 4    BULK FAILURE (NO HEAL)
```

```
! OUTPUT PARAMETERS
```

```
! YIELDT  YIELD STRESS FOR CURRENT MATERIAL
! IFAIL   STRESS STATE INDICATOR (SEE ABOVE)
```

```
! THE FOLLOWING MODULES CONTAIN INFORMATION WHICH MAY BE
! USEFUL FOR COMPUTING THE OUTPUT PARAMETERS :-
```

```
! MODULE 'IJKNOW'
```

```
! INOW - I INDEX FOR CURRENT CELL
! JNOW - J INDEX FOR CURRENT CELL
! KNOW - K INDEX FOR CURRENT CELL
```

```

! MNOW - CURRENT SUBGRID NUMBER

! MODULE 'MATDEF'
! MATNO      - THE MATERIAL NUMBER OF THE CURRENT MATERIAL
! MATERIALS(MATNO)%NAME - THE MATERIAL NAME OF THE CURRENT MATERIAL

! MODULE 'CYCVAR'
! NCYCLE - CURRENT CYCLE NUMBER
! TIME   - CURRENT TIME
! DLTH   - TIME STEP FOR CURRENT CYCLE

! MODULE 'EDTDEF'
! NTCODE - DIMENSIONS: 2 = 2D, 3 = 3D

! THE FOLLOWING GRID VARIABLES MAY ALSO BE USEFUL :-
! ML(NCEN) - CELL SPECIFIC INTERNAL ENERGY
! XMU (IJK) - CELL COMPRESSION (RHO/RHOREF-ONE)
! ML(NCDM) - DAMAGE

! TO OBTAIN THE VALUE OF THE INDEX IJK FOR THE CURRENT CELL, USE
!   IJK = IJKSET3(INOW,JNOW,KNOW)
! THE INDEX IJK MUST ALSO BE DEFINED AS AN INTEGER: - INTEGER (INT4) :: IJK

! *****

! SUBROUTINE CALLED BY ALL STRENGTH MODELS SO SKIP OUT, BY DEFAULT
IF (NSTR/=IMF_STR_USER_1) GO TO 900

900 RETURN

END SUBROUTINE SOLVE_STR_USER_1_3D

SUBROUTINE SOLVE_STR_USER_1_3D_SHELL (IFAIL, DSTN1 ,DSTN2 ,DSTN3
,DSTN12,DSTN23,DSTN31, &
SSN1 ,SSN2 ,SSN3 ,SSN12 ,SSN23
,SSN31 , &
STR1N ,STR2N ,STR12N,STR23N,STR31N)

USE material
USE str_user_1
USE cycvar
USE ijknow
USE wrapup
USE mdgrid3
USE loce1m

IMPLICIT NONE

INTEGER (INT1) :: IFAIL
REAL (REAL8) :: DSTN1, DSTN2, DSTN3, DSTN12, DSTN23, DSTN31
REAL (REAL8) :: SSN1, SSN2, SSN3, SSN12, SSN23, SSN31
REAL (REAL8) :: STR1N, STR2N, STR12N, STR23N, STR31N

! *****

! THIS IS A USER SUPPLIED SUBROUTINE WHICH CAN BE USED TO COMPUTE
! THE STRESSES FOR A SUBLAYER OF SHELL ELEMENT

! INPUT PARAMETER

```

```

! IFAIL  STRESS STATE INDICATOR
! = 0   HYDRO
! = 1   ELASTIC
! = 2   PLASTIC
! = 3   BULK FAILURE (WITH HEAL)
! = 4   BULK FAILURE (NO HEAL)

! DSTN1  STRAIN INCREMENT IN LOCAL 11 DIRECTION
! DSTN2  STRAIN INCREMENT IN LOCAL 22 DIRECTION
! DSTN3  STRAIN INCREMENT IN LOCAL 33 DIRECTION (THROUGH THICKNESS)
! DSTN12 SHEAR STRAIN INCREMENT IN LOCAL 12 DIRECTION
! DSTN23 SHEAR STRAIN INCREMENT IN LOCAL 23 DIRECTION
! DSTN31 SHEAR STRAIN INCREMENT IN LOCAL 31 DIRECTION

! SSN1   TOTAL STRAIN IN LOCAL 11 DIRECTION
! SSN2   TOTAL STRAIN IN LOCAL 22 DIRECTION
! SSN3   TOTAL STRAIN IN LOCAL 33 DIRECTION (THROUGH THICKNESS)
! SSN12  TOTAL SHEAR STRAIN IN LOCAL 12 DIRECTION
! SSN23  TOTAL SHEAR STRAIN IN LOCAL 23 DIRECTION
! SSN31  TOTAL SHEAR STRAIN IN LOCAL 31 DIRECTION

! OUTPUT PARAMETERS

! STR1N  STRESS IN LOCAL 11 DIRECTION
! STR2N  STRESS IN LOCAL 22 DIRECTION
! STR12N SHEAR STRESS IN LOCAL 12 DIRECTION
! STR23N SHEAR STRESS IN LOCAL 23 DIRECTION
! STR31N SHEAR STRESS IN LOCAL 31 DIRECTION

! NOTE THAT THROUGH THICKNESS STRESS STR3N FOR SHELLS IS ALWAYS ZERO

! THE FOLLOWING MODULES CONTAIN INFORMATION WHICH MAY BE
! USEFUL FOR COMPUTING THE OUTPUT PARAMETERS :-

! MODULE  'IJKNOW'

! INOW - I INDEX FOR CURRENT CELL
! JNOW - J INDEX FOR CURRENT CELL
! KNOW - K INDEX FOR CURRENT CELL
! MNOW - CURRENT SUBGRID NUMBER

! MODULE  'MATDEF'
! MATNO           - THE MATERIAL NUMBER OF THE CURRENT MATERIAL
! MATERIALS(MATNO)%NAME - THE MATERIAL NAME OF THE CURRENT MATERIAL

! MODULE  'CYCVAR'
! NCYCLE - CURRENT CYCLE NUMBER
! TIME   - CURRENT TIME
! DLTH   - TIME STEP FOR CURRENT CYCLE

! MODULE  'LOCELM'
! IJK     - THE INDEX IJK FOR THE CURRENT CELL
! LELM(1) - THE INDEX FOR NODE 1 OF THE CURRENT CELL
! LELM(2) - THE INDEX FOR NODE 2 OF THE CURRENT CELL
! LELM(3) - THE INDEX FOR NODE 3 OF THE CURRENT CELL
! LELM(4) - THE INDEX FOR NODE 4 OF THE CURRENT CELL

! THE FOLLOWING GRID VARIABLES MAY ALSO BE USEFUL :-
! XN0(IJK) - INITIAL X CO-ORDINATE OF NODE IJK
! YN0(IJK) - INITIAL Y CO-ORDINATE OF NODE IJK
! ZN0(IJK) - INITIAL Z CO-ORDINATE OF NODE IJK
! XN(IJK)  - CURRENT X CO-ORDINATE OF NODE IJK

```

```
! YN(IJK) - CURRENT Y CO-ORDINATE OF NODE IJK
! ZN(IJK) - CURRENT Z CO-ORDINATE OF NODE IJK

! *****

! SUBROUTINE CALLED BY ALL STRENGTH MODELS SO SKIP OUT, BY DEFAULT
IF (NSTR/=IMF_STR_USER_1) GO TO 900

900 RETURN

END SUBROUTINE SOLVE_STR_USER_1_3D_SHELL
```

## APPENDIX B

### 1. Quasi static stress-strain ANN

#### I. Model network connection weight

##### a) Strain controlled

	HN1	HN2	HN3	HN4	HN5	HN6	HN7	HN8	HN9	
WT%	-0.002	-13.762	-8.570	-16.474	-0.869	3.941	-11.415	-0.384	-2.041	
Strain	53.218	7.530	17.119	8.599	9.775	13.335	7.661	5.098	2.499	Output threshold
HN threshold	2.358	-4.706	-0.260	1.602	-5.224	-6.936	-2.831	-2.625	-1.613	
Stress	29.897	13.811	4.602	-5.217	-22.890	9.176	6.873	-2.106	0.982	-31.049

##### b) Stress controlled

	HN1	HN2	HN3	HN4	HN5	HN6	HN7	
WT%	16.486	-38.437	-0.552	-0.599	-18.965	-15.979	-8.562	
Stress	-4.382	3.862	-8.981	-4.407	8.056	4.227	-4.549	Output threshold
HN threshold	5.195	-3.648	10.477	-0.537	-4.964	-4.738	2.387	
Strain	-17.901	-25.898	-13.288	-15.727	5.304	11.716	3.487	29.897

##### c) Stopping criterion

	HN1	HN2	HN3	HN4	HN5	HN6	HN7	HN8	HN9	
WT%	54.109	13.985	-8.037	-0.658	3.484	0.061	-0.127	-0.027	-0.018	Output threshold
HN threshold	1.738	-1.966	2.110	-2.233	-3.040	-1.957	-1.732	-1.444	-0.954	
Max stress	-16.442	2.665	3.876	-0.433	3.313	0.157	0.091	0.161	0.085	10.935
Max strain	-5.948	-3.005	-1.060	0.267	-0.949	0.138	0.322	0.189	0.089	5.901

### 2. High strain rate stress-strain ANN

#### I. Model network connection weight

##### a) xGnP-Epoxy

	HN1	HN2	HN3	HN4	HN5	
WT%	-0.489	3.320	4.640	-5.092	-0.631	
Strainrate	0.367	1.920	0.379	1.240	-0.820	
Strain	-44.767	5.589	-6.620	0.508	0.722	Output threshold
HN threshold	-1.046	-7.765	-1.741	3.401	-0.414	
Strain	-17.282	3.078	1.449	1.938	-0.937	-1.8152

##### b) OxGnP-Epoxy

	HN1	HN2	HN3	HN4	HN5	
WT%	0.123	-1.457	-1.494	-1.954	-0.224	
Strainrate	-0.253	0.558	1.629	0.824	-0.605	
Strain	-36.513	-6.900	-4.018	0.187	-0.058	Output threshold
HN threshold	-0.871	5.927	2.269	-0.106	-0.198	
Strain	-15.574	-4.200	2.564	-1.006	-0.625	2.7601

c) xGnP-PU

	HN1	HN2	HN3	HN4	HN5	
WT%	-0.397	-6.313	3.085	-2.076	-0.040	
Strainrate	0.404	3.426	0.813	-0.062	-0.726	
Strain	-21.033	2.444	0.389	3.631	-0.010	Output threshold
HN threshold	-1.904	-5.603	-4.492	-0.685	-0.265	
Stress	-12.578	6.009	4.250	1.754	-0.572	-1.9467

d) OxGnP-PU

	HN1	HN2	HN3	HN4	HN5	
WT%	2.357	-0.154	0.404	-0.682	-0.549	
Strainrate	-3.956	0.078	0.228	-0.707	-0.456	
Strain	-1.725	-16.484	-4.536	0.463	0.419	Output threshold
HN threshold	3.666	-1.712	1.531	-0.563	-0.379	
Strain	-3.432	-9.607	-1.539	-0.866	-0.732	3.4203

e) xGnP-PEI

	HN1	HN2	HN3	HN4	HN5	HN6	
WT%	-0.191	0.042	-0.246	-5.082	-6.353	-1.117	
Strainrate	0.561	1.039	11.562	0.885	0.747	-0.124	
Strain	-48.670	12.430	-5.943	2.536	2.523	0.684	Output threshold
HN threshold	-1.198	-6.923	3.385	-0.110	-2.196	-0.267	
Strain	-18.345	1.160	3.412	1.677	-3.867	-1.271	-2.926

II. Error statistics

a) xGnP-Epoxy

ANN				DSGZ Model			
WT%	Strain rate	R2	ASE	WT%	Strain rate	R2	ASE
0	1760	0.956	114.458	0	1760	0.991	23.075
0	2679	0.947	100.816	0	2679	0.983	33.283
0	4167	0.952	95.739	0	4167	0.988	24.152
0.5	1236	0.877	352.755	0.5	1236	0.832	482.230
0.5	2567	0.869	291.427	0.5	2567	0.875	279.811
0.5	4000	0.927	190.354	0.5	4000	0.791	545.335
1	1797	0.728	478.043	1	1797	0.981	32.483
1	2878	0.935	154.101	1	2878	0.980	48.477
1	3710	0.987	43.542	1	3710	0.990	32.521
	overall	0.934	187.937		<b>Overall</b>	0.946	155.953

b) OxGnP-Epoxy

ANN				DSGZ Model			
WT%	Strain rate	R2	ASE	WT%	Strain rate	R2	ASE
0	1760	0.914	224.603	0	1760	0.991	23.075
0	2679	0.913	166.726	0	2679	0.983	33.283
0	4167	0.961	77.201	0	4167	0.988	24.152
0.5	1236	0.877	477.124	0.5	1236	0.973	103.175
0.5	2567	0.928	147.131	0.5	2567	0.968	65.147
0.5	4000	0.940	129.259	0.5	4000	0.971	62.086
1	1797	0.918	250.262	1	1797	0.942	178.044
1	2878	0.923	199.297	1	2878	0.962	98.838
1	3710	0.958	126.734	1	3710	0.982	53.669
	<b>Overall</b>	0.934	173.875		<b>Overall</b>	0.976	62.970

c) xGnP-PU

ANN				DSGZ Model			
WT%	Strain rate	R2	ASE	WT%	Strain rate	R2	ASE
0	2920	0.965	5.606	0	2920	0.931	11.154
0	3952	0.981	5.128	0	3952	0.948	14.351
0	5442	0.992	4.155	0	5442	0.913	47.263
0.2	3377	0.920	12.415	0.2	3377	0.979	3.336
0.2	4439	0.959	8.802	0.2	4439	0.949	10.870
0.2	5871	0.968	8.552	0.2	5871	0.987	3.416
0.5	3677	0.929	7.918	0.5	3677	0.954	5.103
0.5	5190	0.978	3.980	0.5	5190	0.979	3.851
0.5	6106	0.985	2.701	0.5	6106	0.976	4.432
1	2169	0.902	11.855	1	2169	0.962	4.532
1	4247	0.946	8.670	1	4247	0.910	14.516
1	6189	0.963	7.692	1	6189	0.978	4.494
	<b>Overall</b>	0.971	7.289		<b>Overall</b>	0.957	10.610

d) OxGnP-PU

ANN				DSGZ Model			
WT%	Strain rate	R2	ASE	WT%	Strain rate	R2	ASE
0	2920	0.910	14.519	0	2920	0.931	11.154
0	3952	0.972	7.658	0	3952	0.948	14.351
0	5447	0.992	4.134	0	5447	0.914	47.082
0.2	3417	0.910	15.020	0.2	3417	0.952	7.994
0.2	4458	0.910	36.566	0.2	4458	0.966	14.040
0.2	5853	0.965	16.126	0.2	5853	0.966	15.400
0.5	2735	0.938	8.880	0.5	2735	0.968	4.605
0.5	4972	0.894	19.272	0.5	4972	0.943	10.391
0.5	5193	0.962	9.359	0.5	5193	0.984	3.894
1	2730	0.952	6.960	1	2730	0.984	2.295
1	4494	0.961	7.231	1	4494	0.983	3.094
1	5732	0.950	10.093	1	5732	0.986	2.875
	<b>overall</b>	0.957	13.036		<b>Overall</b>	0.962	11.517

e) xGnP-PEI

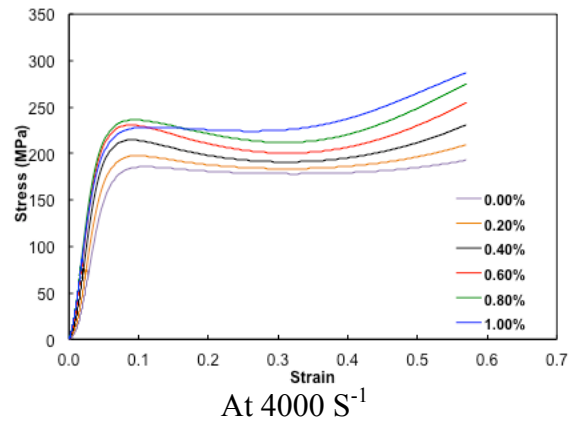
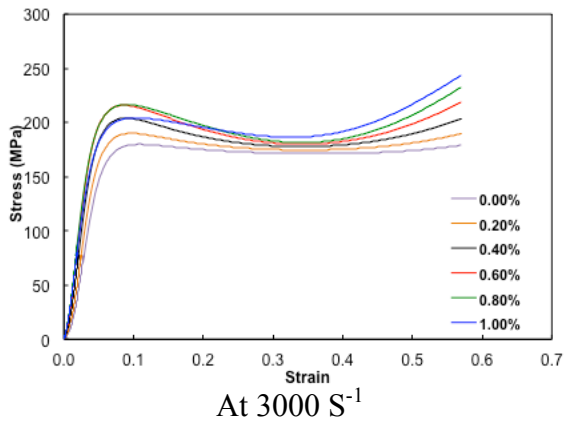
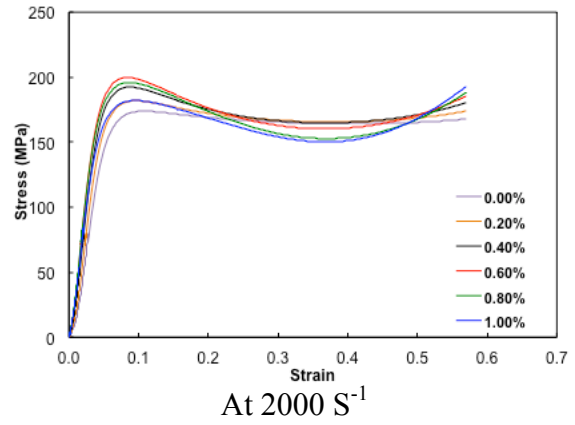
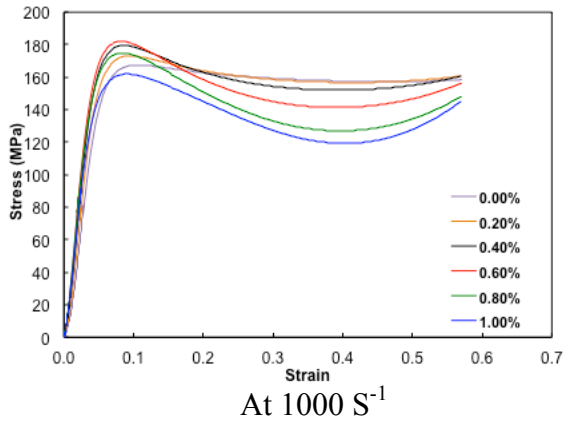
ANN				DSGZ Model			
WT%	Strain rate	R2	ASE	WT%	Strain rate	R2	ASE
0	1317	0.915	297.581	0	1317	0.987	45.892
0	3419	0.969	68.718	0	3419	0.986	31.208
0	8688	0.984	38.549	0	8688	0.972	70.104
0.5	1812	0.761	405.363	0.5	1812	0.978	37.377
0.5	2101	0.964	71.292	0.5	2101	0.948	104.677
0.5	3176	0.955	134.985	0.5	3176	0.991	26.833
1	1413	0.977	72.968	1	1413	0.992	24.612
1	2002	0.932	188.389	1	2002	0.946	149.593
1	4840	0.981	53.503	1	4840	0.980	56.465
	<b>Overall</b>	0.954	131.805		<b>Overall</b>	0.979	61.450



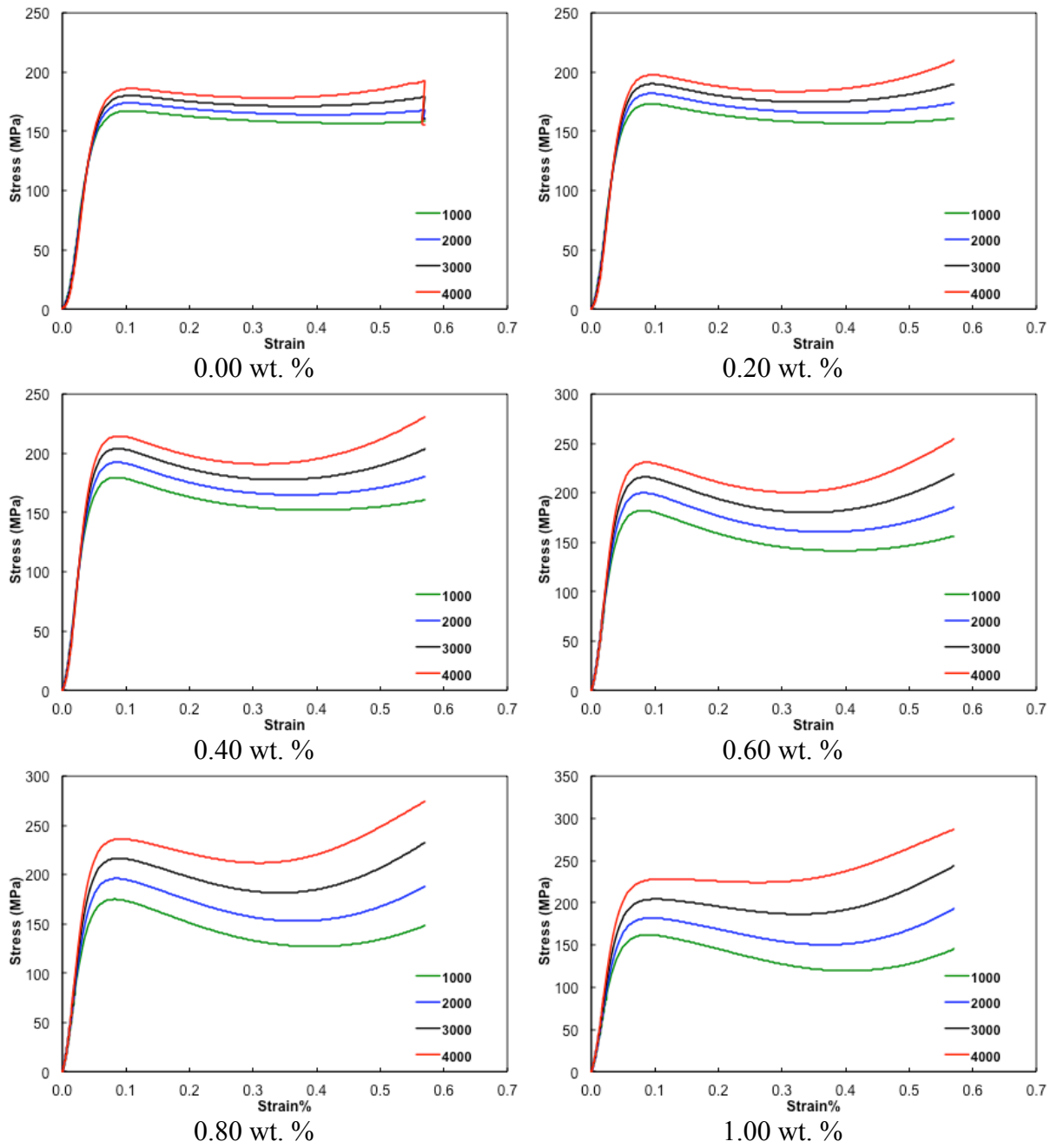
### III. Sensitivity Analysis

#### f) xGnP-Epoxy

##### 1. Change in wt. %

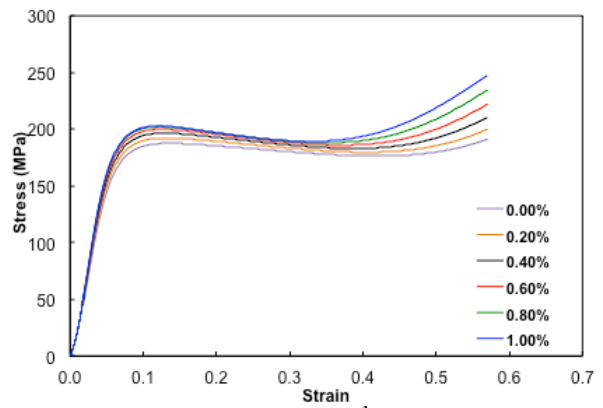
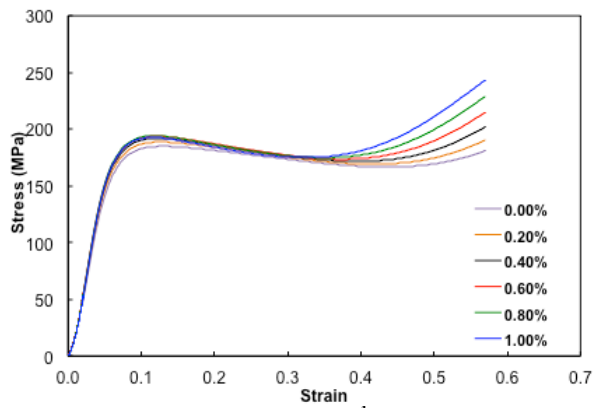
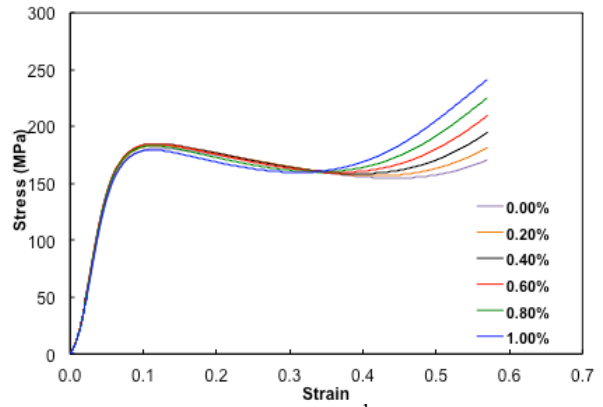
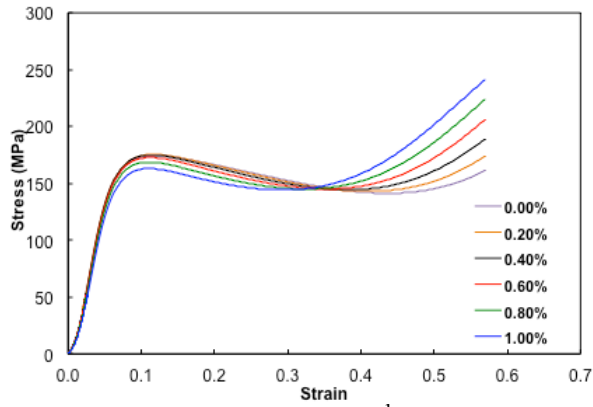


## 2. Change in strain rate

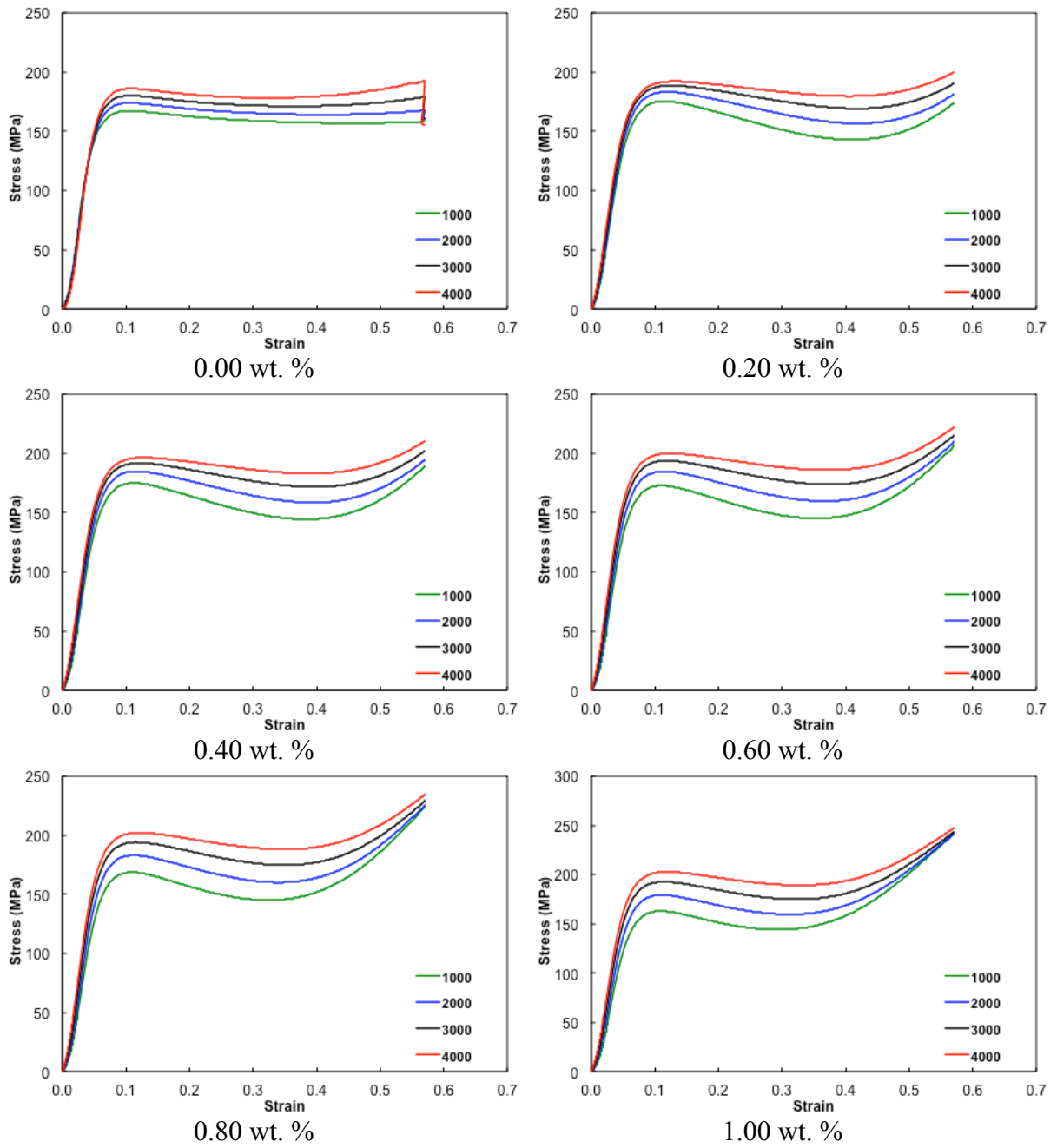


g) OxGnP-Epoxy

1. Change in wt. %

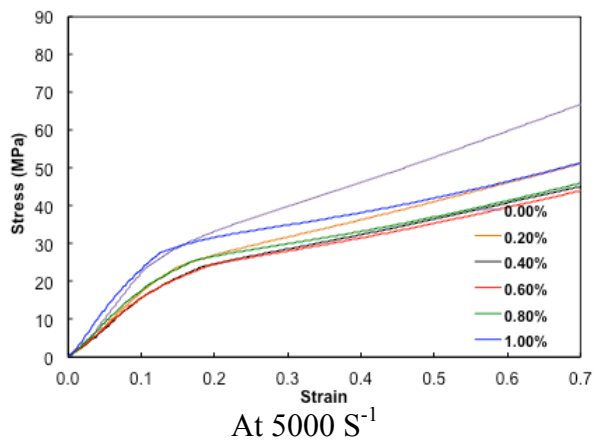
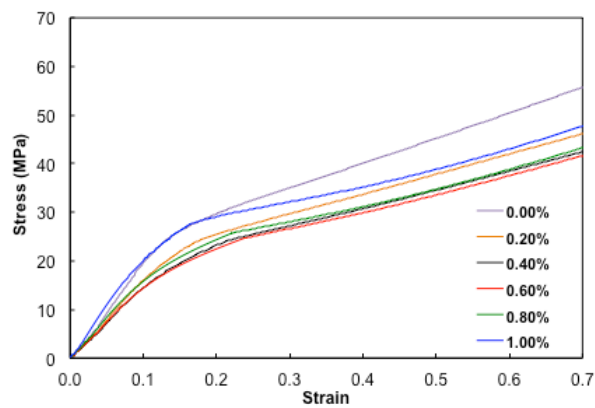
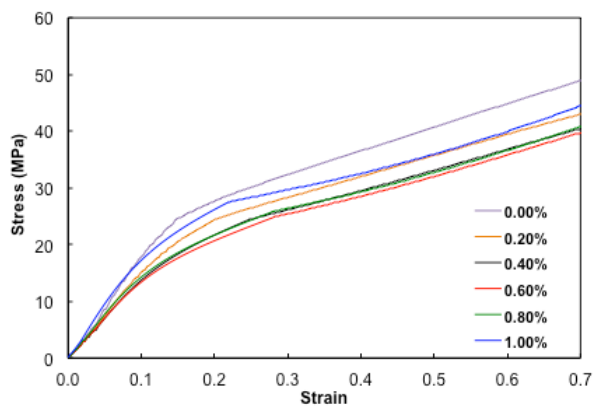
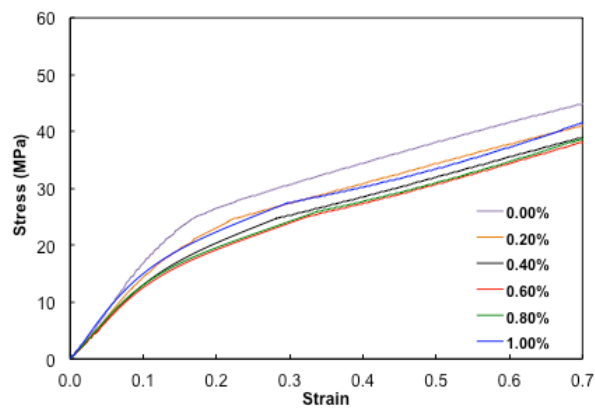
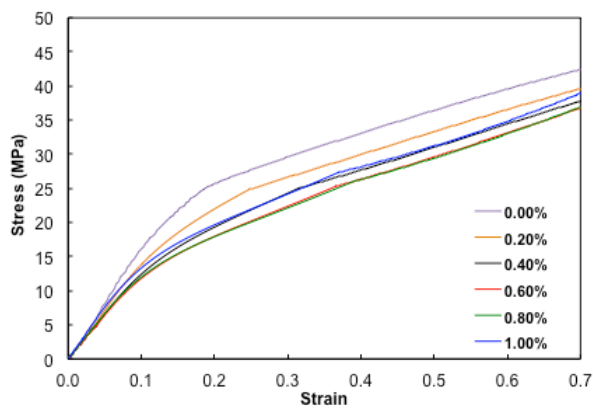


## 2.Change in strain rate

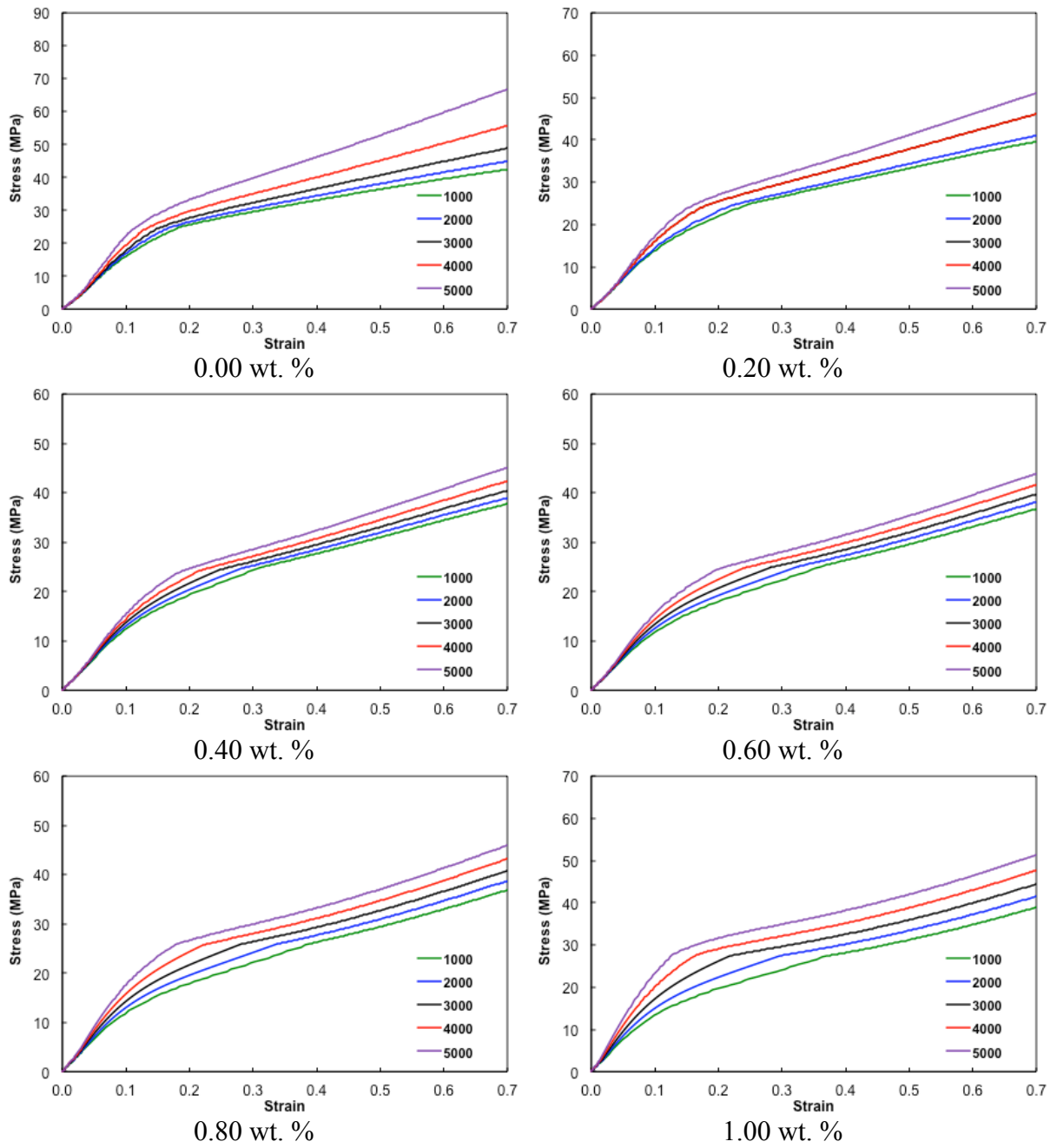


h) xGnP-PU

1. Change in wt. %

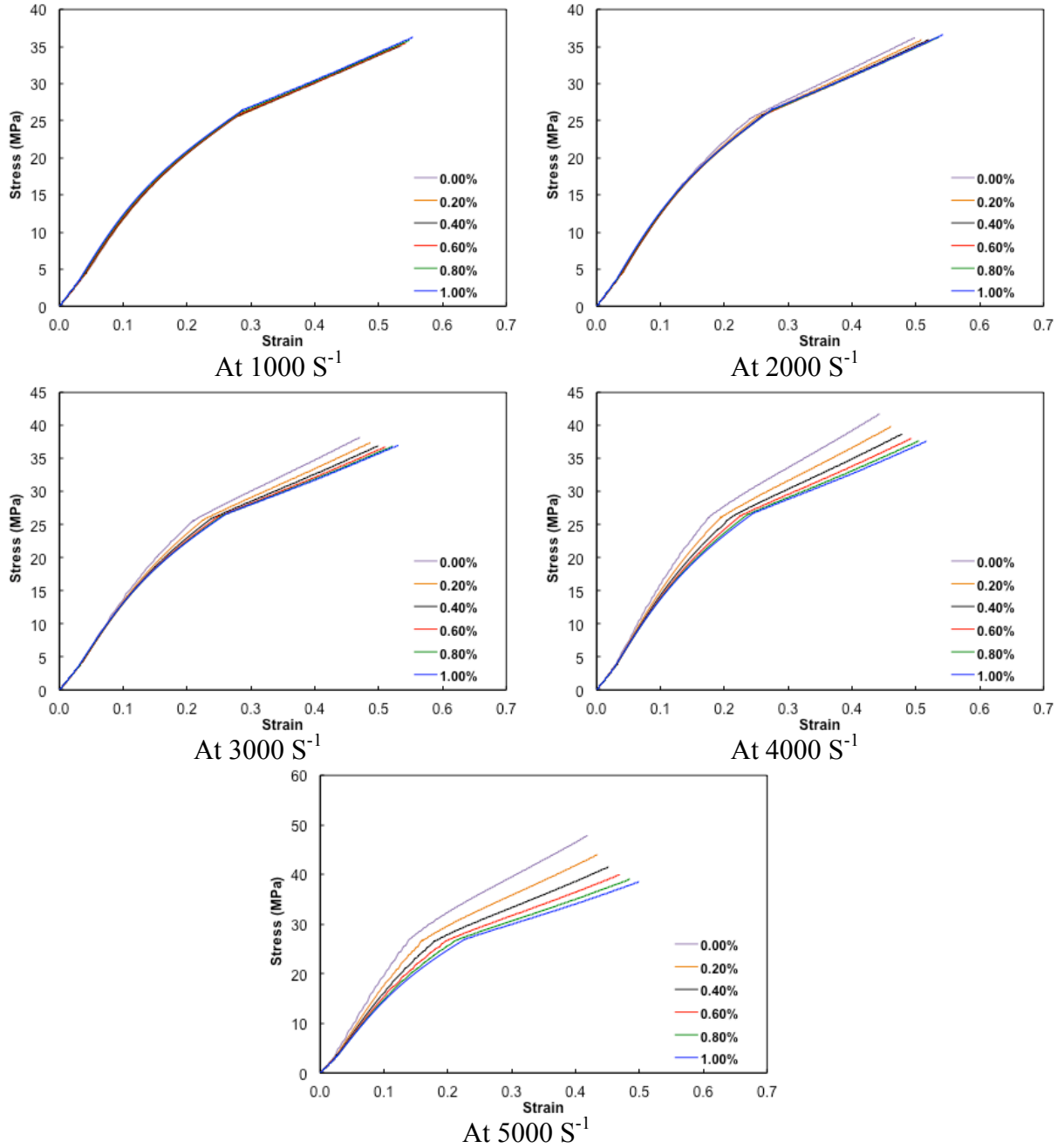


## 2.Change in strain rate

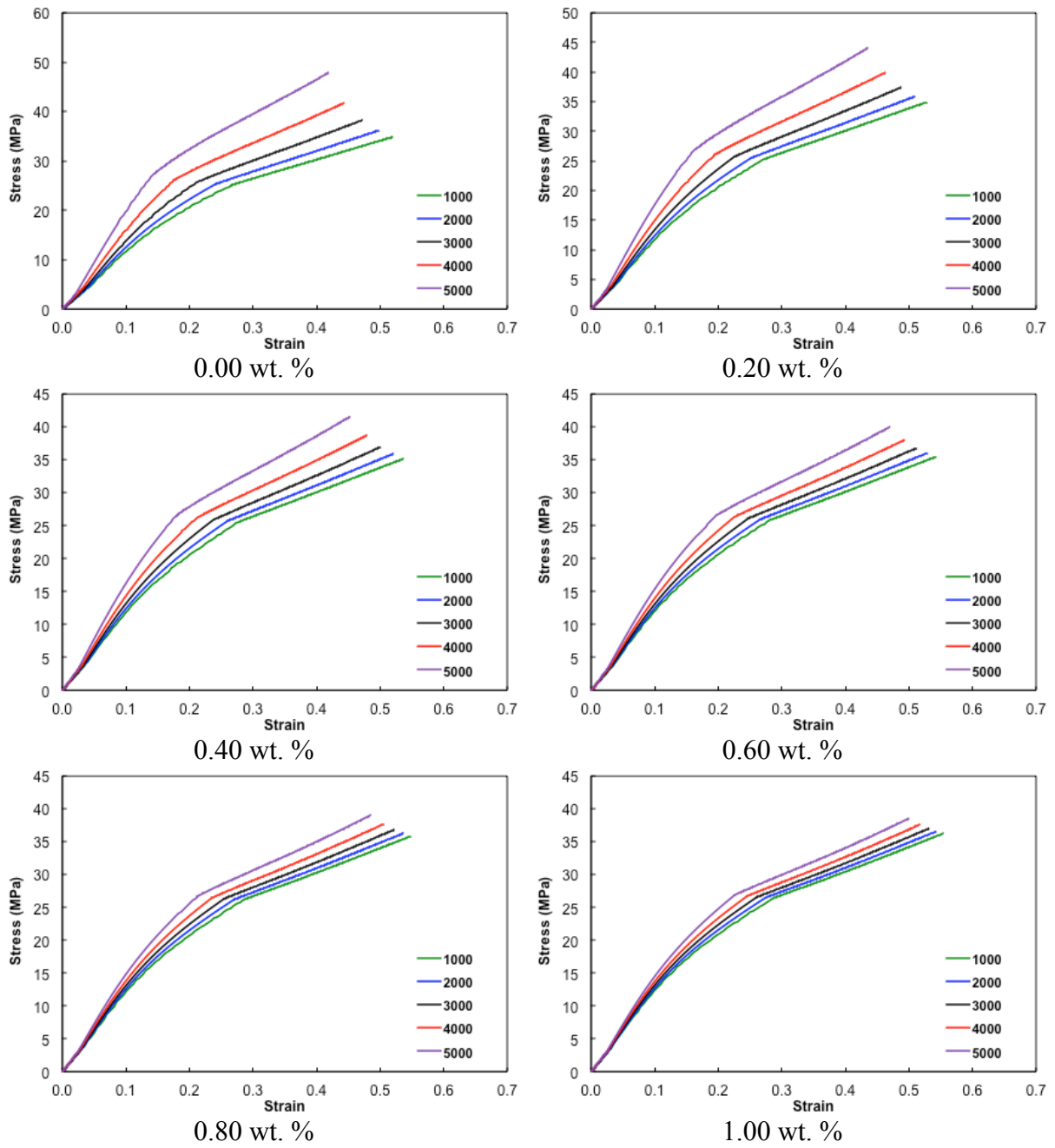


i) OxGnP-PU

1. Change in wt. %



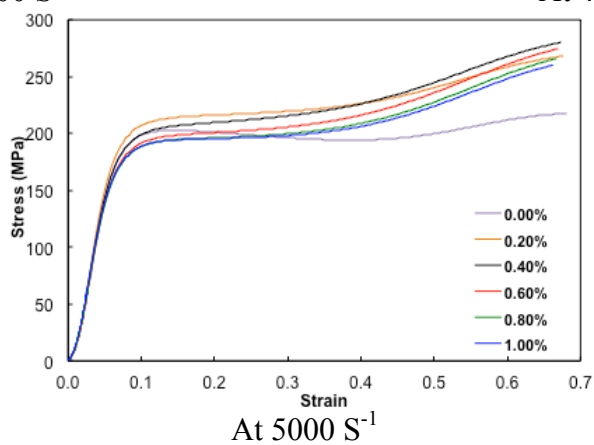
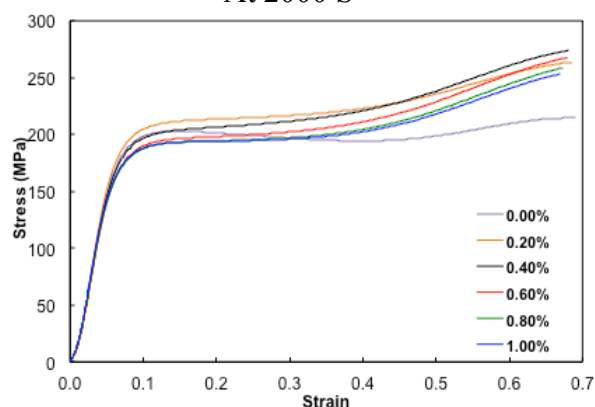
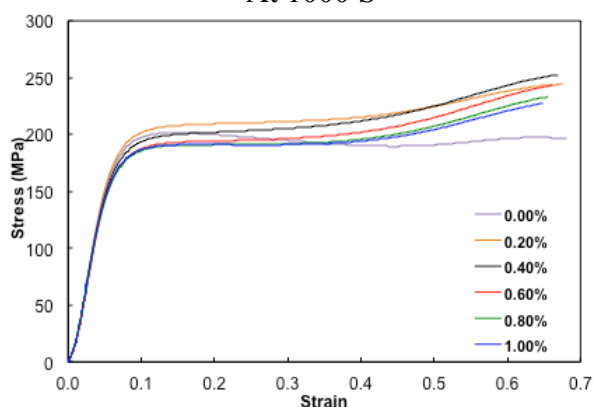
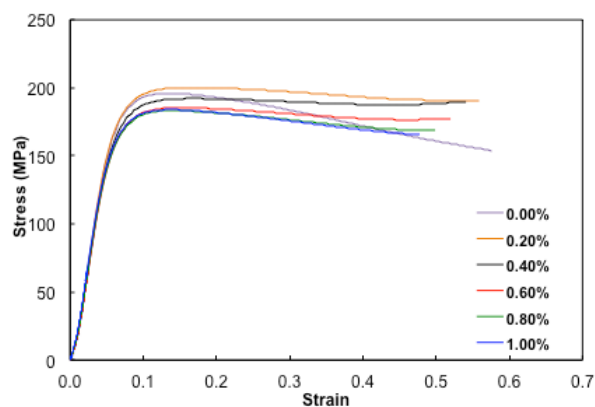
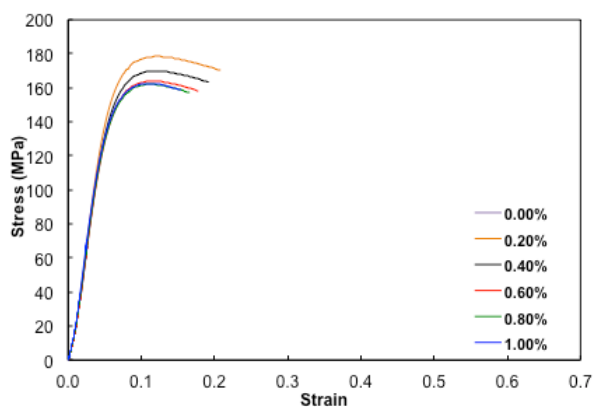
## 2.Change in strain rate



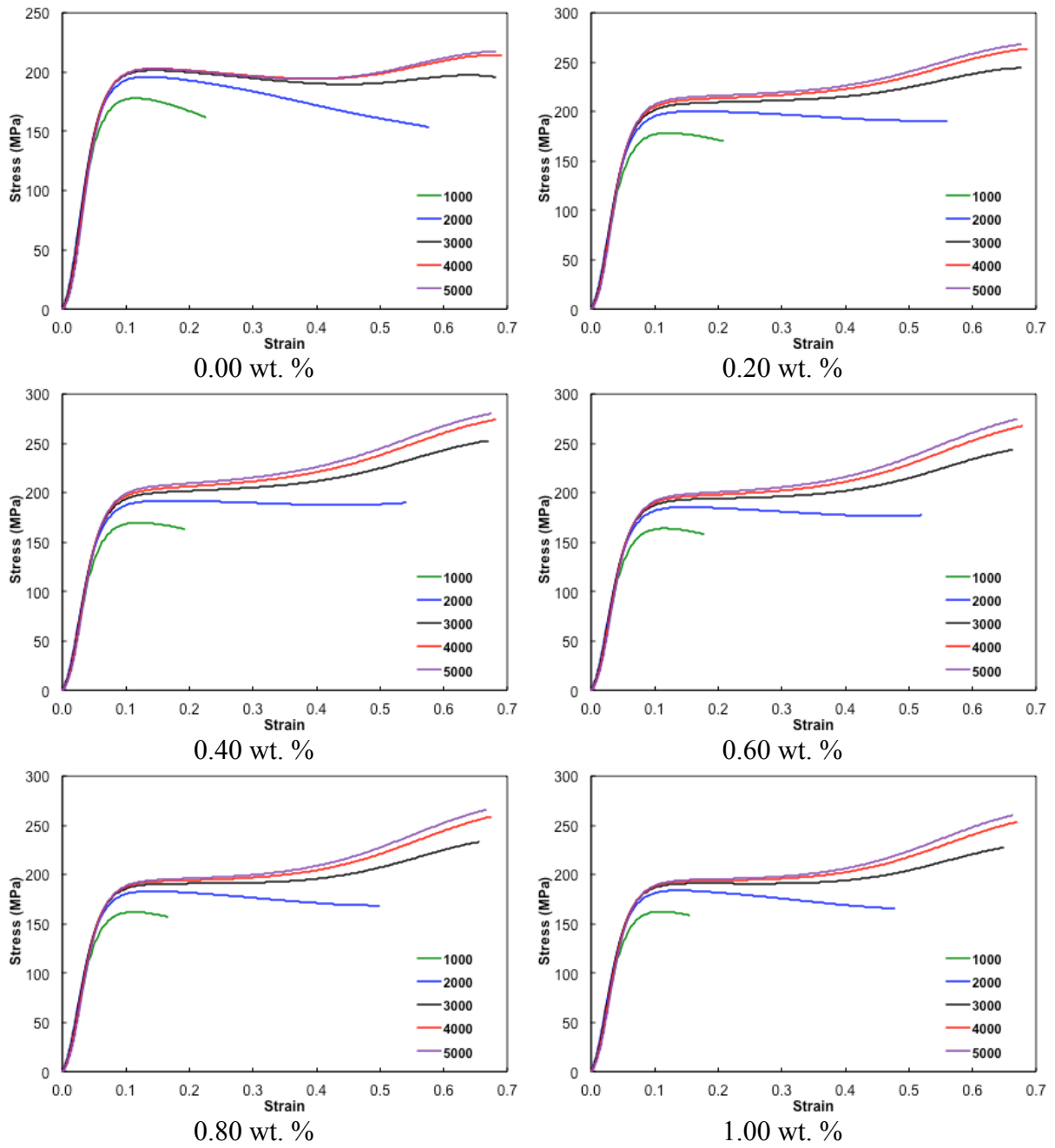


j) xGnP-PEI

1. Change in wt. %

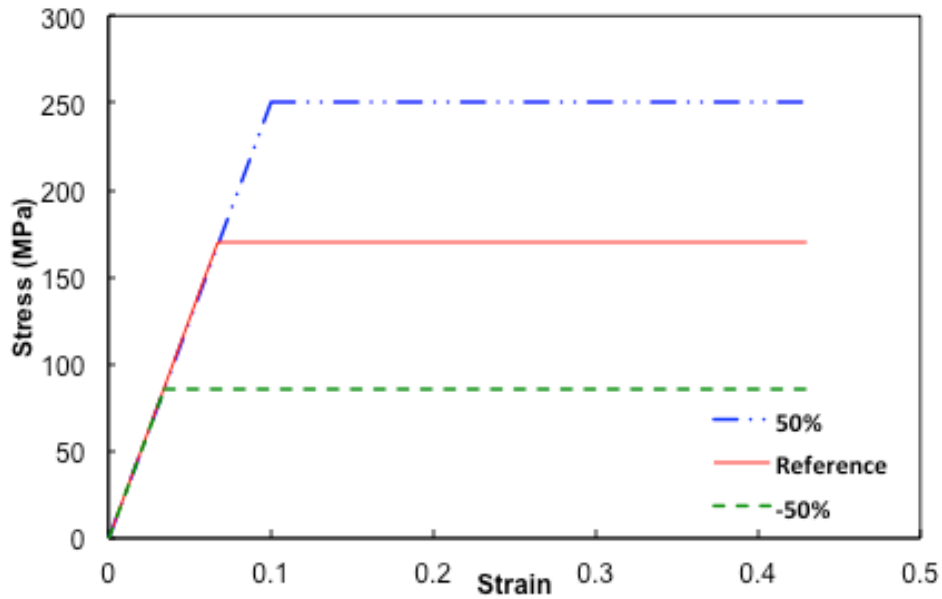


## 2.Change in strain rate



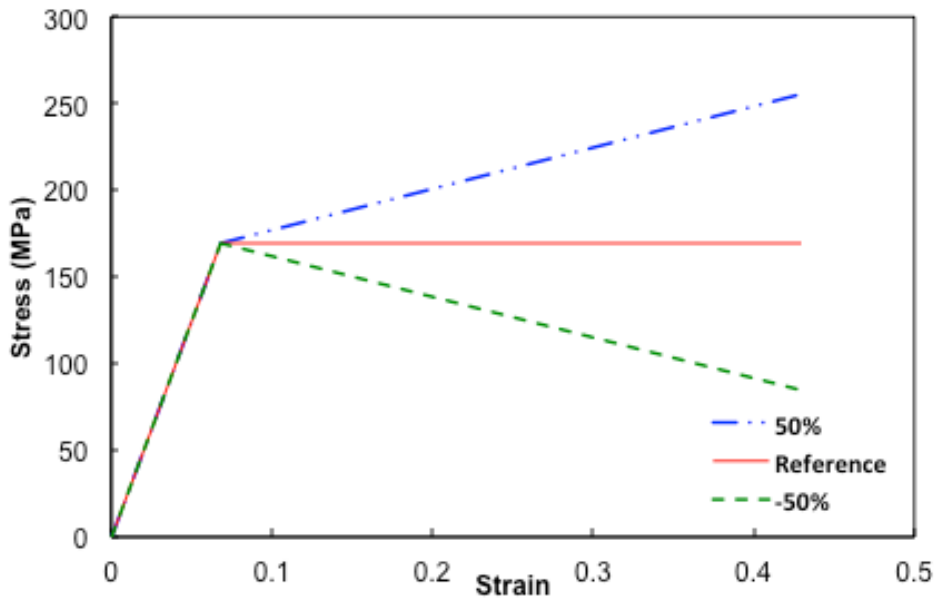
## APPENDIX C

### 1. Change in yield stress



Change %	Reference Density (g/cm <sup>3</sup> )	Bulk Modulus (Mpa)	Shear Modulus (Mpa)	Yield Stress (Mpa)	Failure stress (Mpa)	Failure Strain (Mpa)	Strain rate constant	Thermal softening Exponent	Melting Tempreture (k)	Refrence strain rate (1/s)
-50%	1	4.17E+03	8.94E+02	8.50E+01	8.50E+01	0.43	0.024	1.56	597	1797
+50%	1	4.17E+03	8.94E+02	2.55E+02	2.55E+02	0.43	0.024	1.56	597	1797

### 2. Change in Strain hardening



Change %	Reference Density (g/cm <sup>3</sup> )	Bulk Modulus (Mpa)	Shear Modulus (Mpa)	Yield Stress (Mpa)	Failure stress (Mpa)	Failure Strain (Mpa)	Strain rate constant	Thermal softening Exponent	Melting Tempreture (k)	Refrence strain rate (1/s)
-50%	1	4.17E+03	8.94E+02	1.70E+02	8.50E+01	0.43	0.024	1.56	597	1797
+50%	1	4.17E+03	8.94E+02	1.70E+02	2.55E+02	0.43	0.024	1.56	597	1797

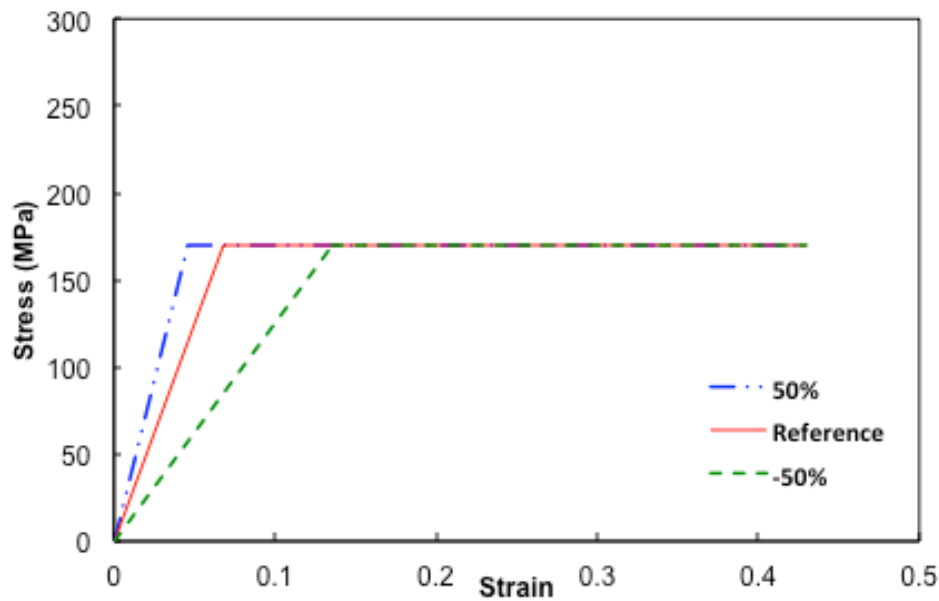
### 3. Change in Strain Rate constant

Change %	Reference Density (g/cm <sup>3</sup> )	Bulk Modulus (Mpa)	Shear Modulus (Mpa)	Yield Stress (Mpa)	Failure stress (Mpa)	Failure Strain (Mpa)	Strain rate constant	Thermal softeneing Exponent	Melting Tempreture (k)	Refrence strain rate (1/s)
-50%	1	4.17E+03	8.94E+02	1.70E+02	1.70E+02	0.43	0.012	1.56	597	1797
+50%	1	4.17E+03	8.94E+02	1.70E+02	1.70E+02	0.43	0.036	1.56	597	1797

### 4. Change in Reference density

Change %	Reference Density (g/cm <sup>3</sup> )	Bulk Modulus (Mpa)	Shear Modulus (Mpa)	Yield Stress (Mpa)	Failure stress (Mpa)	Failure Strain (Mpa)	Strain rate constant	Thermal softeneing Exponent	Melting Tempreture (k)	Refrence strain rate (1/s)
-50%	0.5	4.17E+03	8.94E+02	1.70E+02	1.70E+02	0.43	0.024	1.56	597	1797
+50%	1.5	4.17E+03	8.94E+02	1.70E+02	1.70E+02	0.43	0.024	1.56	597	1797

### 5. Change in bulk Modulus



Change %	Reference Density (g/cm <sup>3</sup> )	Bulk Modulus (Mpa)	Shear Modulus (Mpa)	Yield Stress (Mpa)	Failure stress (Mpa)	Failure Strain (Mpa)	Strain rate constant	Thermal softeneing Exponent	Melting Tempreture (k)	Refrence strain rate (1/s)
-50%	0.5	2.09E+03	4.48E+06	1.70E+02	1.70E+02	0.43	0.024	1.56	597	1797
+50%	1.5	6.26E+03	1.34E+06	1.70E+02	1.70E+02	0.43	0.024	1.56	597	1797

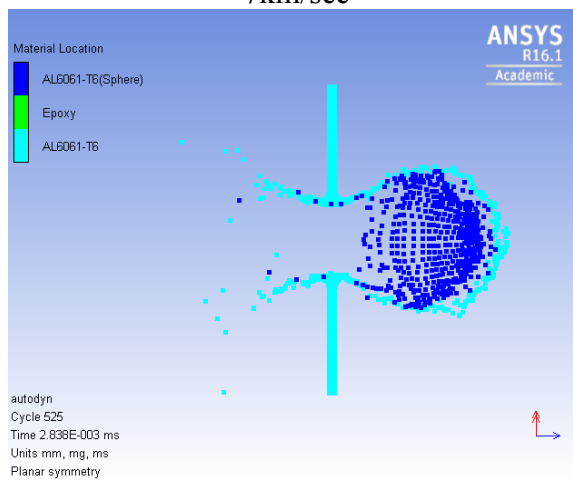
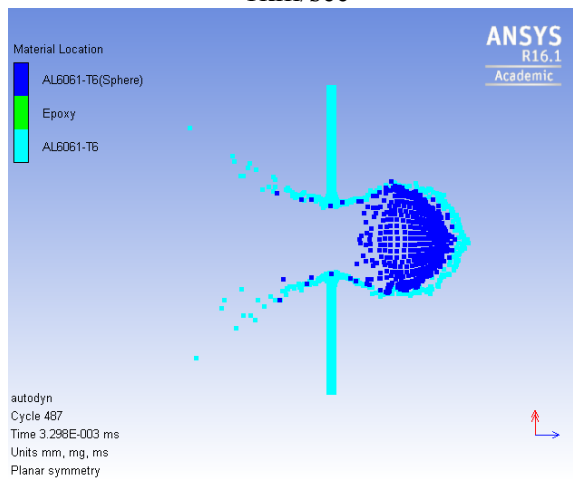
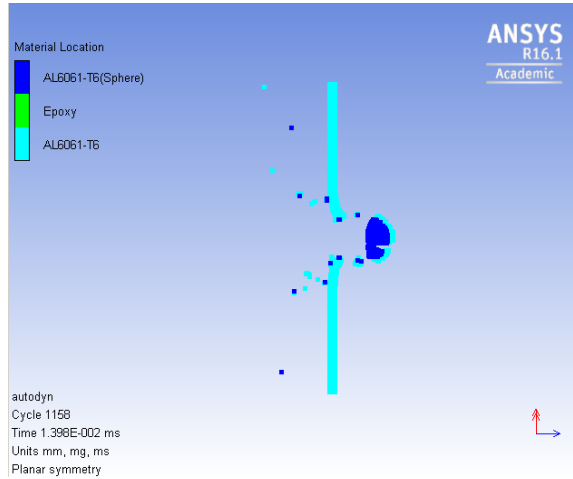
### 6. Reference strain rate

Change %	Reference Density (g/cm <sup>3</sup> )	Bulk Modulus (Mpa)	Shear Modulus (Mpa)	Yield Stress (Mpa)	Failure stress (Mpa)	Failure Strain (Mpa)	Strain rate constant	Thermal softeneing Exponent	Melting Tempreture (k)	Refrence strain rate (1/s)
-50%	0.5	4.17E+03	8.94E+02	1.70E+02	1.70E+02	0.43	0.024	1.56	597	899
+50%	1.5	4.17E+03	8.94E+02	1.70E+02	1.70E+02	0.43	0.024	1.56	597	2696

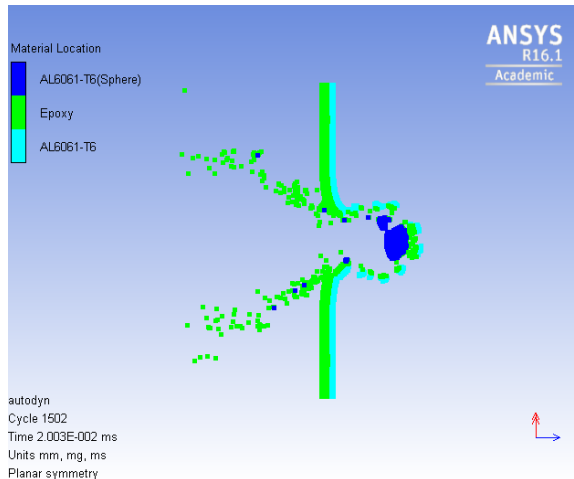
## APPENDIX D

### I. The crater image for xGnP-Epoxy 1% on Aluminum substrate

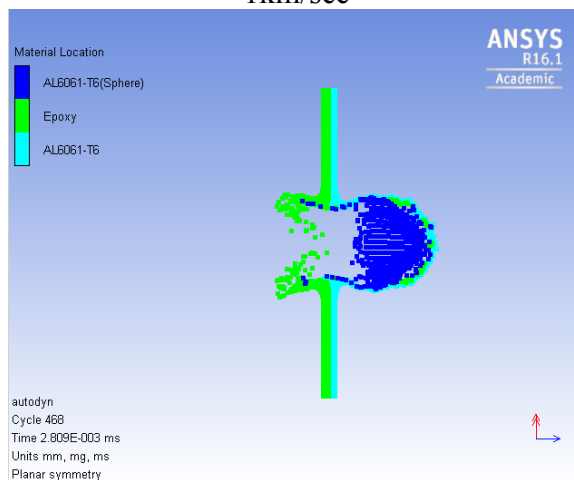
#### a) Aluminum blank substrate



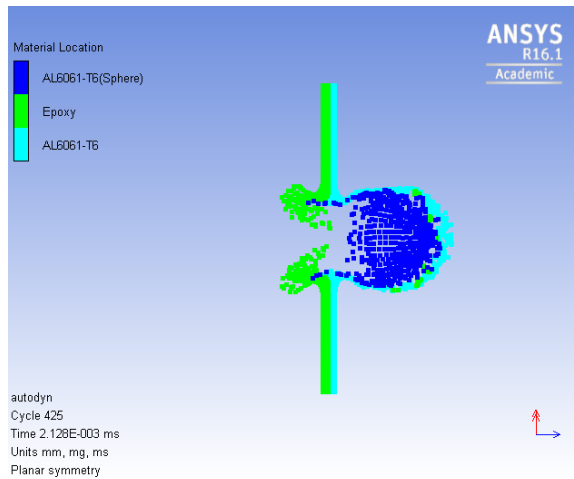
#### b) Reference xGnP-Epoxy 1% on Aluminum substrate



1km/sec

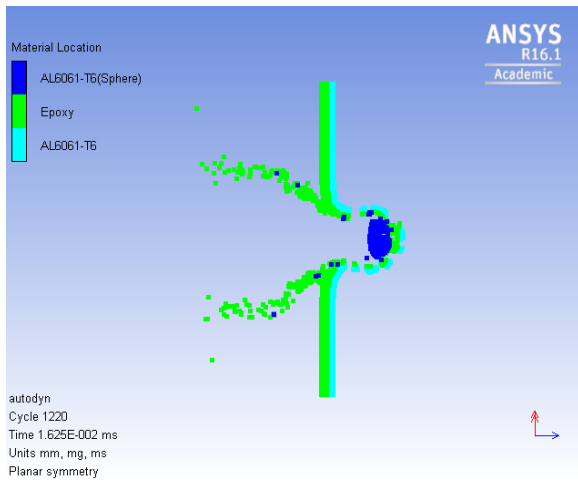


7km/sec

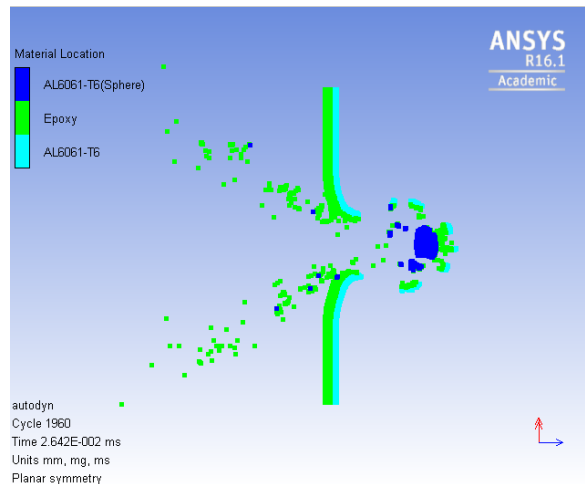


10km/sec

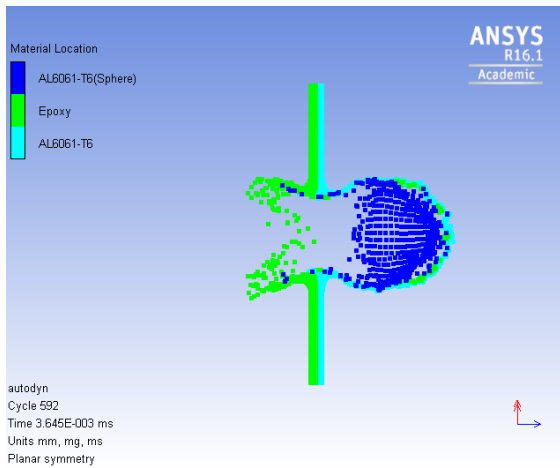
c) Change in yield stress



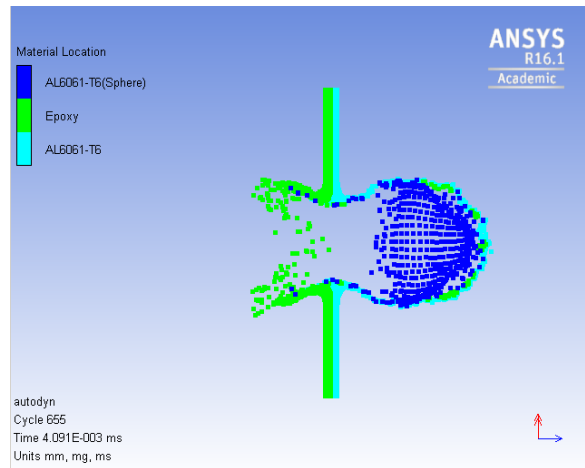
-50% at 1km/sec



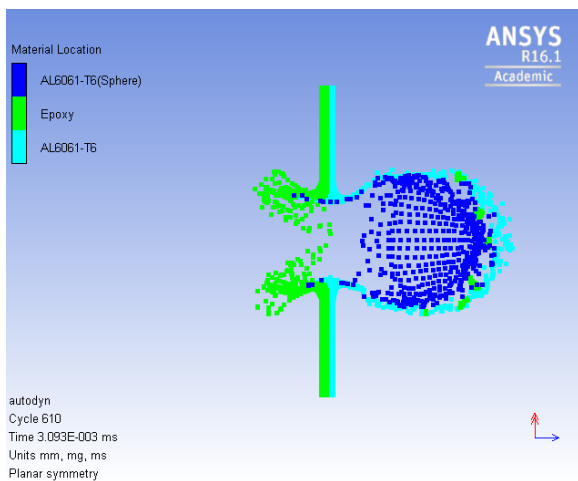
+50% at 1km/sec



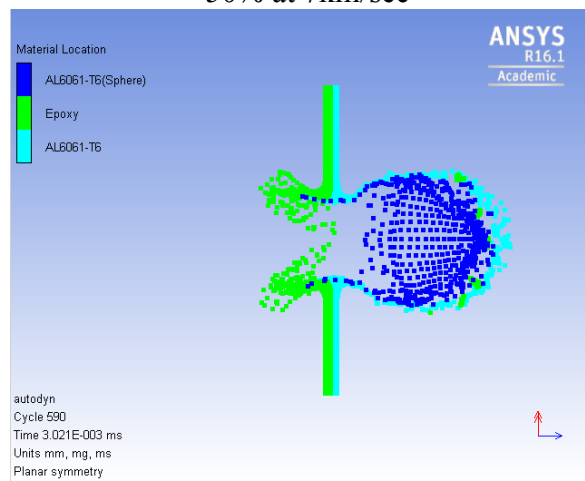
-50% at 7km/sec



+50% at 7km/sec

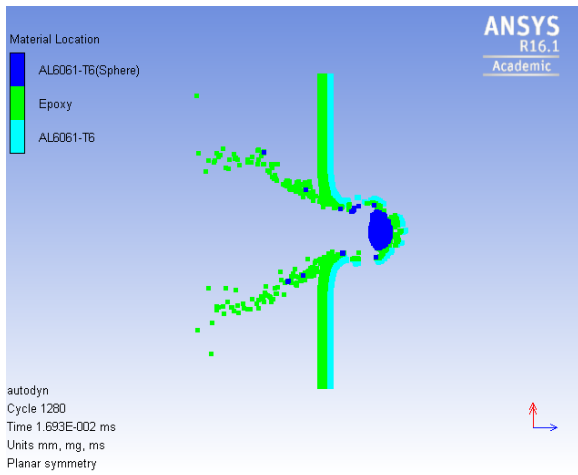


-50% at 10km/sec

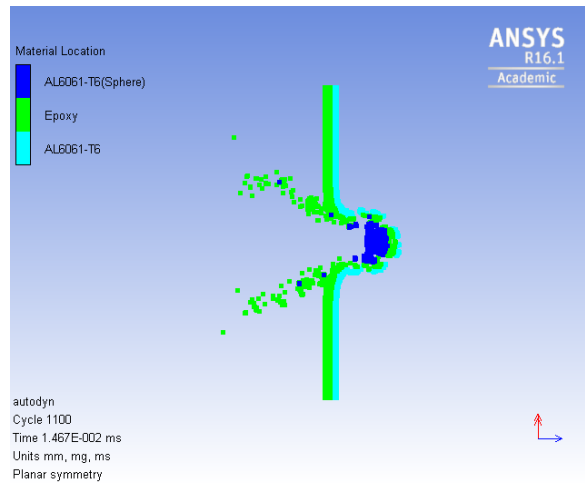


+50% at 10km/sec

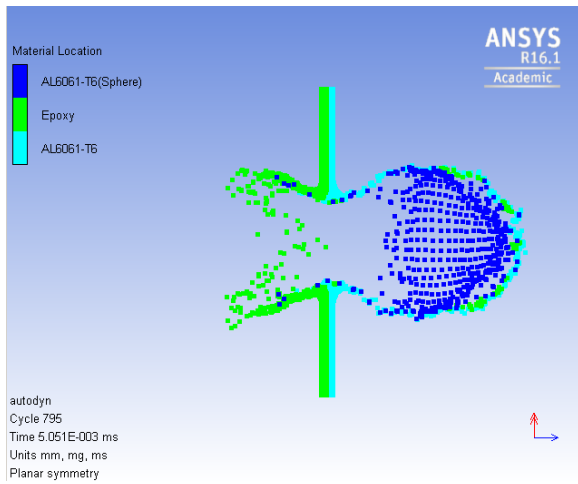
d) Change in Strain hardening



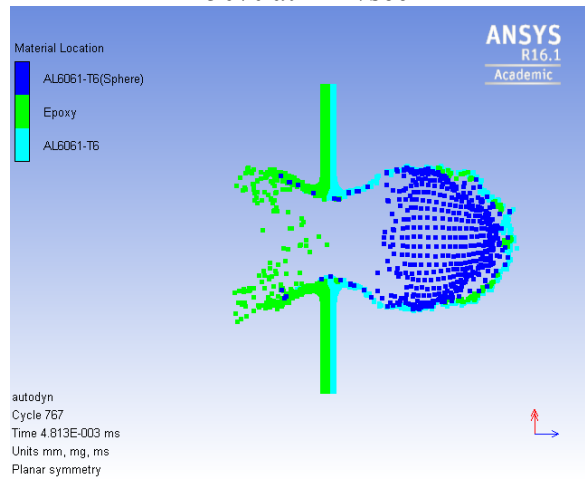
-50% at 1km/sec



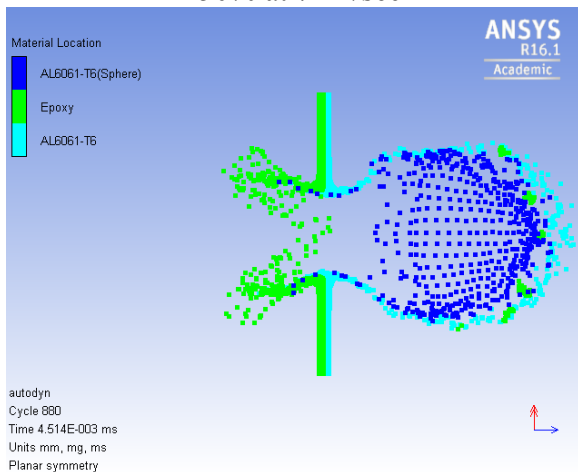
+50% at 1km/sec



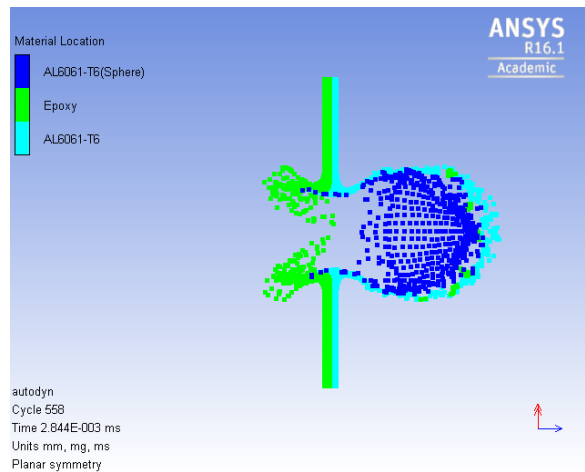
-50% at 7km/sec



+50% at 7km/sec



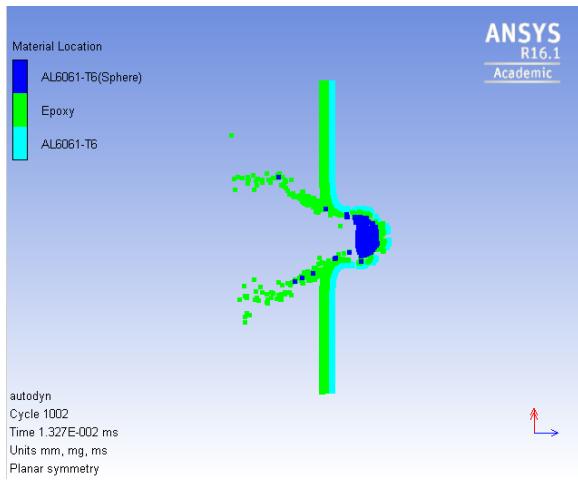
-50% at 10km/sec



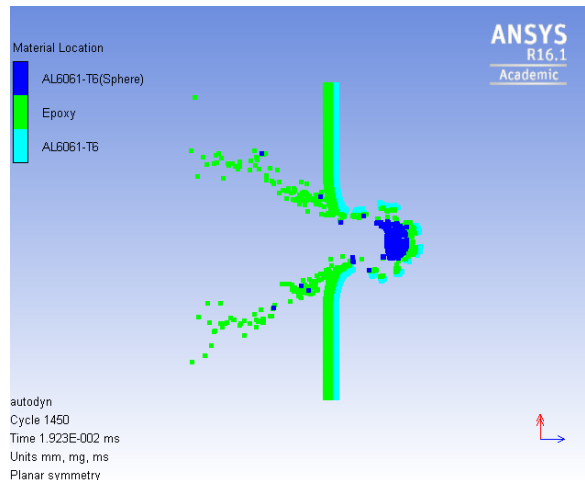
+50% at 10km/sec



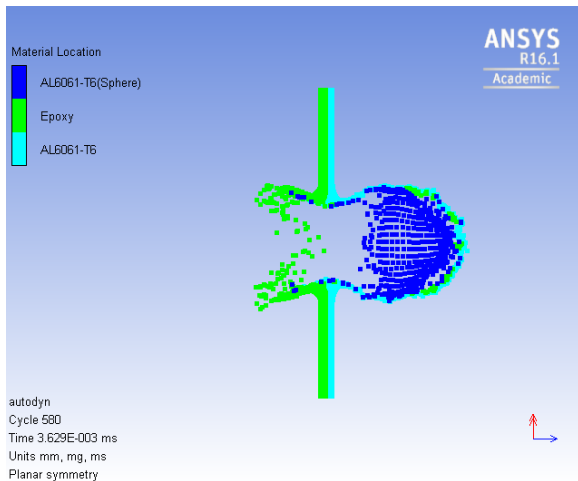
e) Change in Strain Rate constant



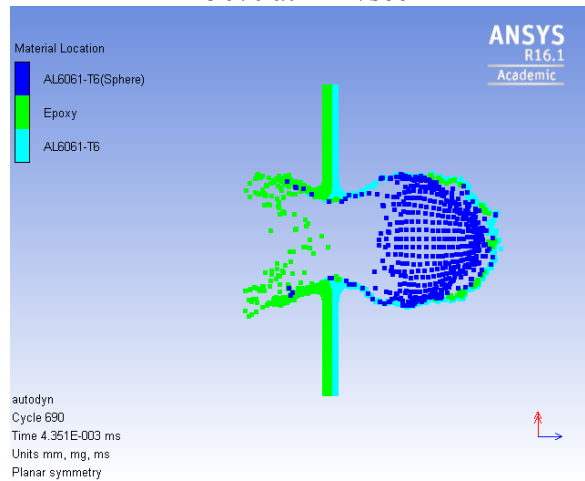
-50% at 1km/sec



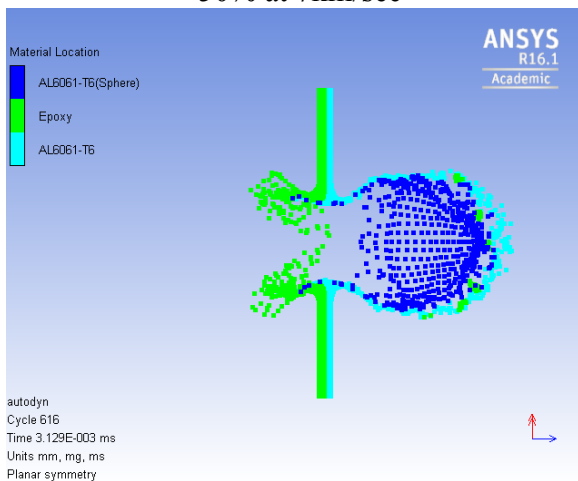
+50% at 1km/sec



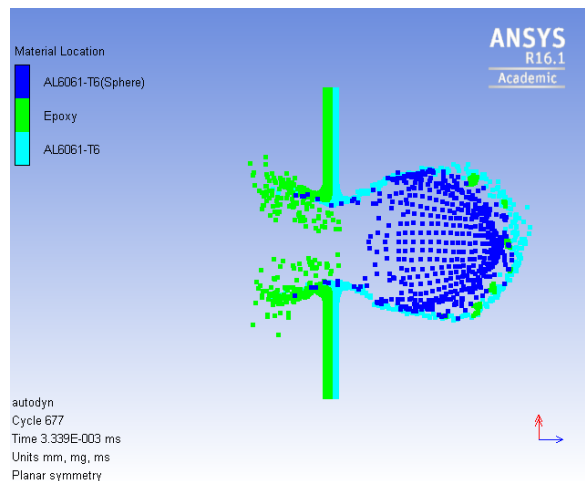
-50% at 7km/sec



+50% at 7km/sec

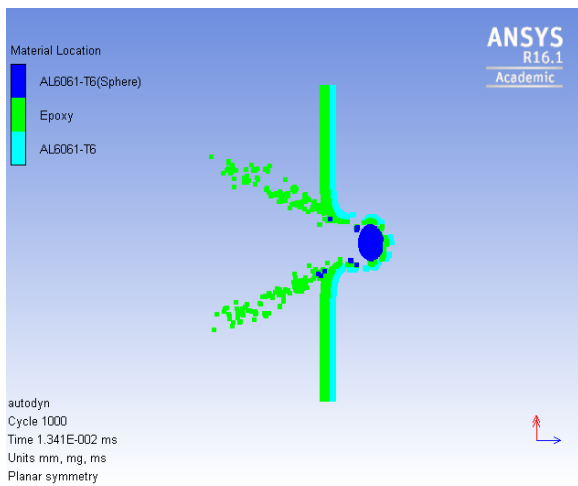


-50% at 10km/sec

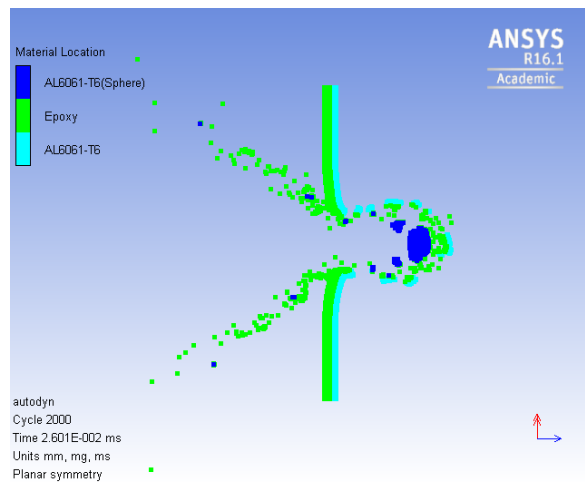


+50% at 10km/sec

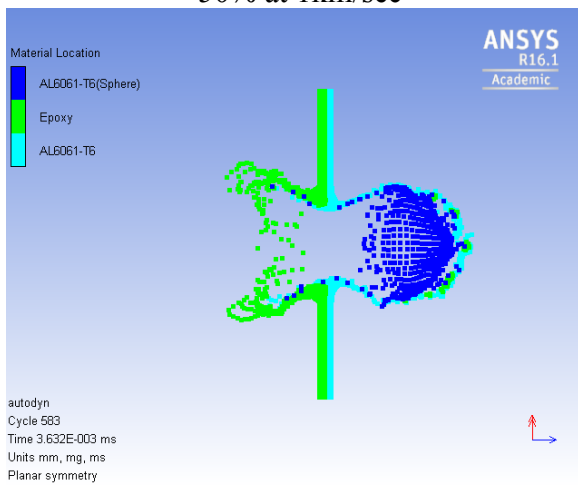
f) Change in Reference density



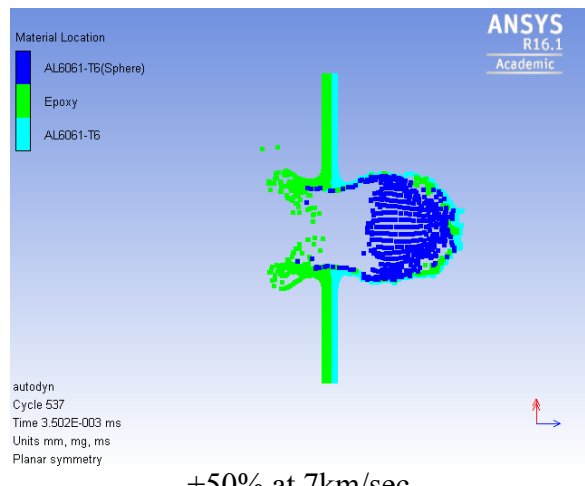
-50% at 1km/sec



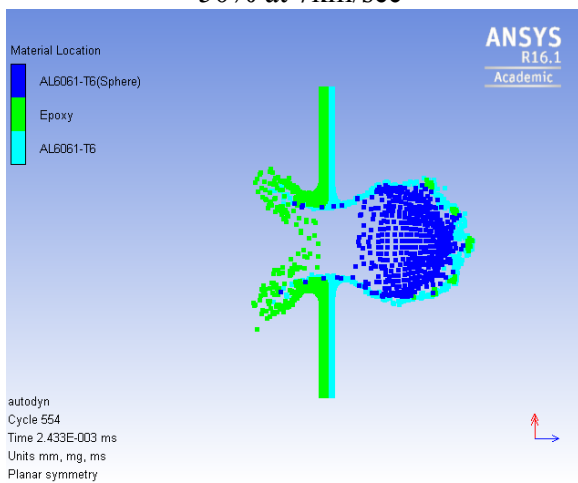
+50% at 1km/sec



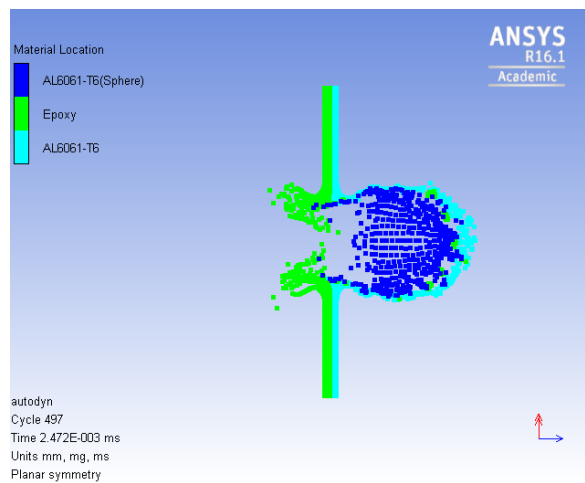
-50% at 7km/sec



+50% at 7km/sec

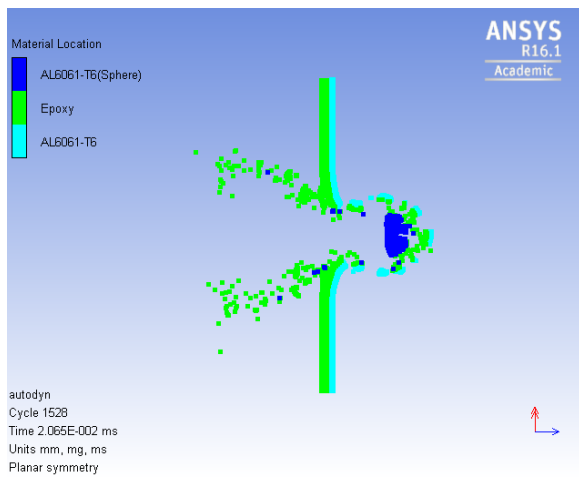


-50% at 10km/sec

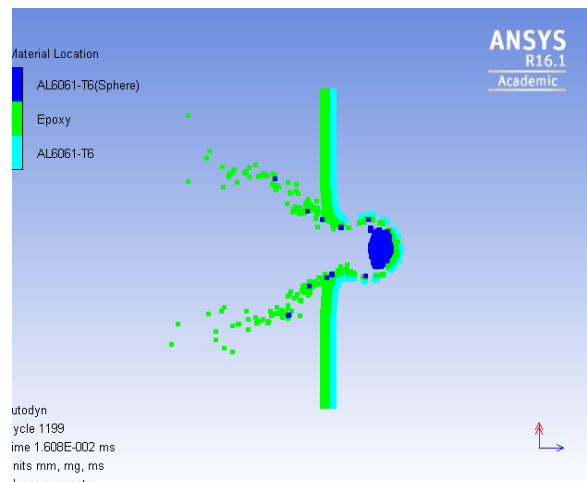


+50% at 10km/sec

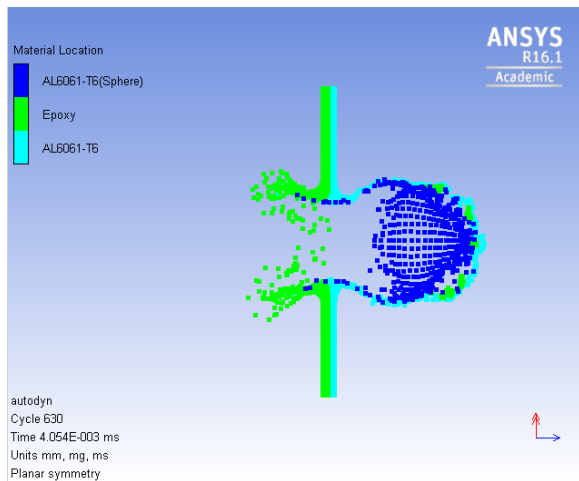
g) Change in bulk Modulus



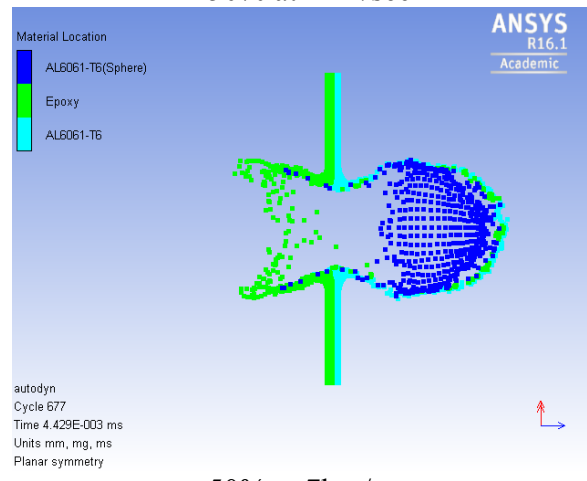
-50% at 1km/sec



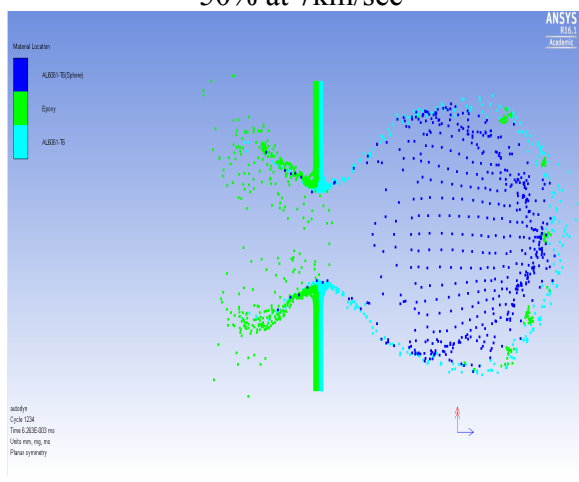
+50% at 1km/sec



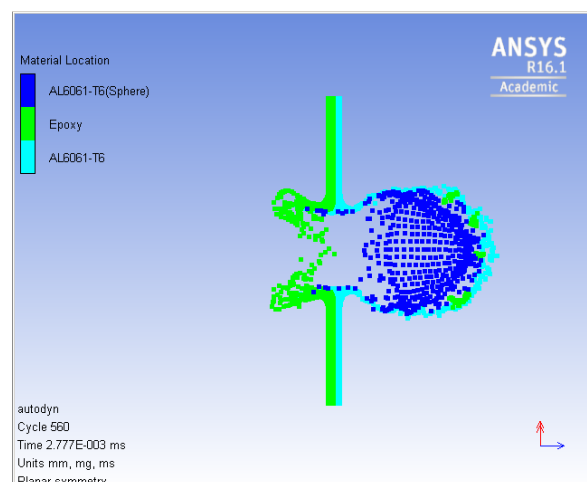
-50% at 7km/sec



+50% at 7km/sec

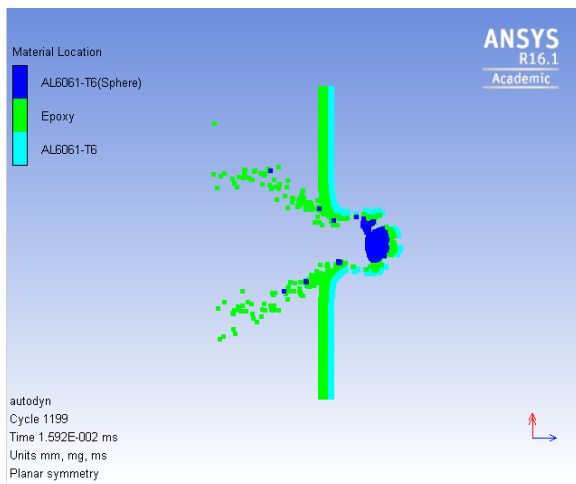


-50% at 10km/sec

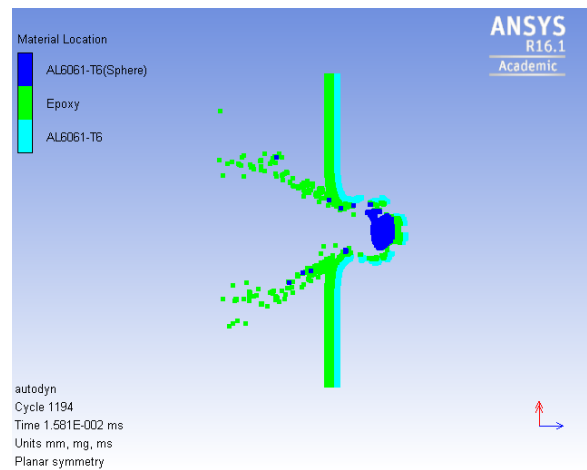


+50% at 10km/sec

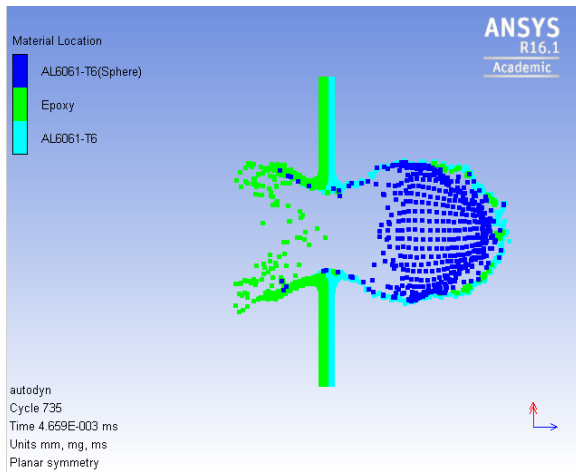
h) Reference strain rate



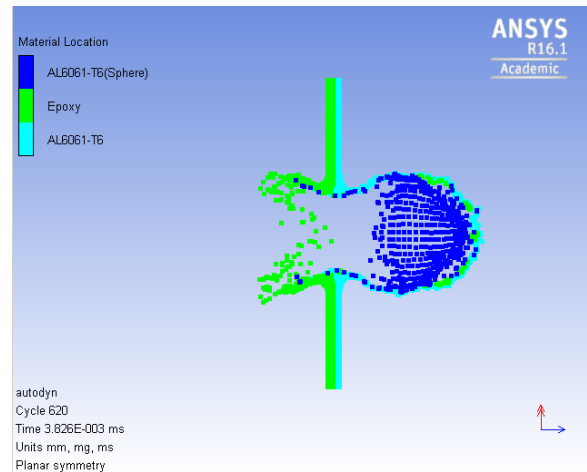
-50% at 1km/sec



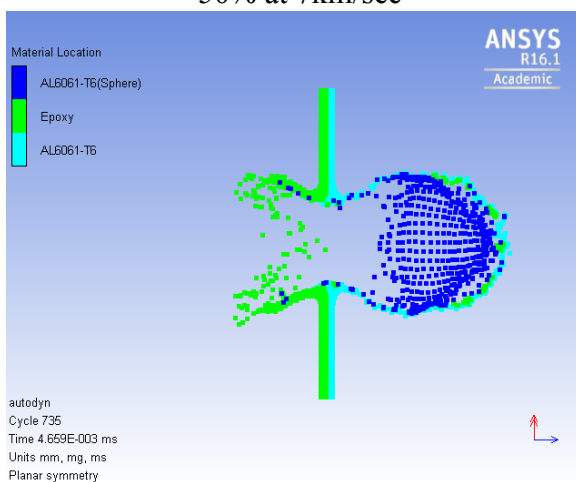
+50% at 1km/sec



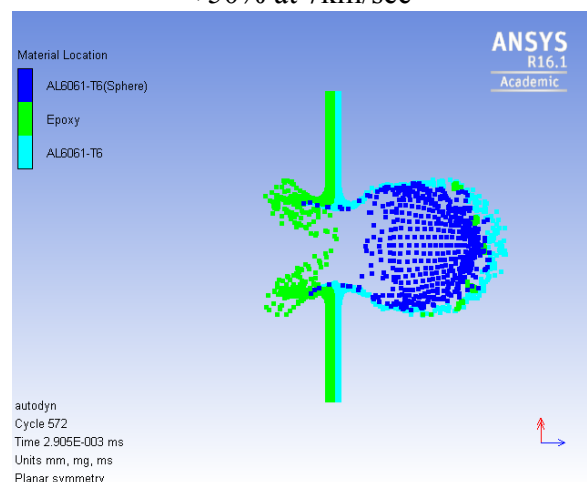
-50% at 7km/sec



+50% at 7km/sec

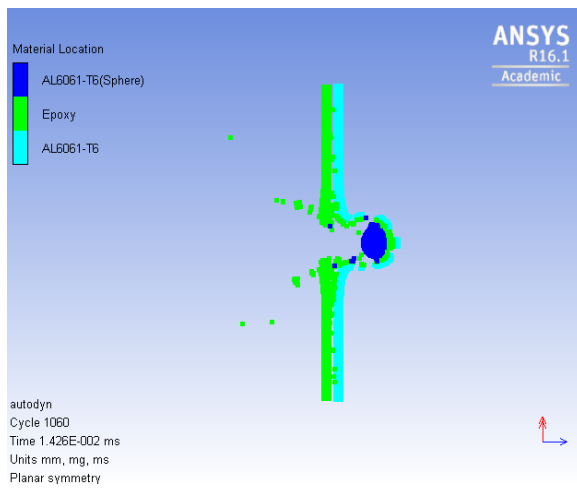


-50% at 10km/sec

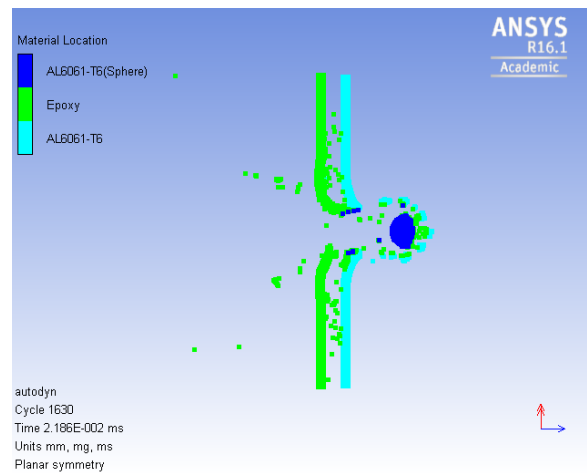


+50% at 10km/sec

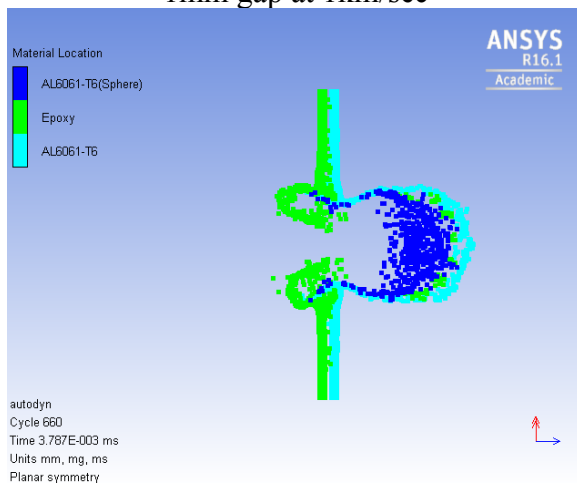
i) Change in gap distance



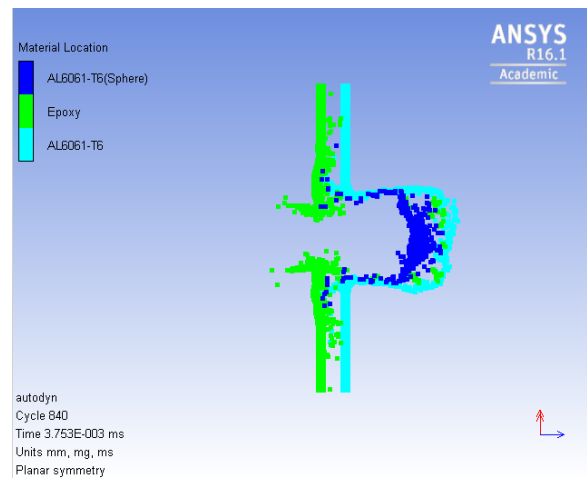
1mm gap at 1km/sec



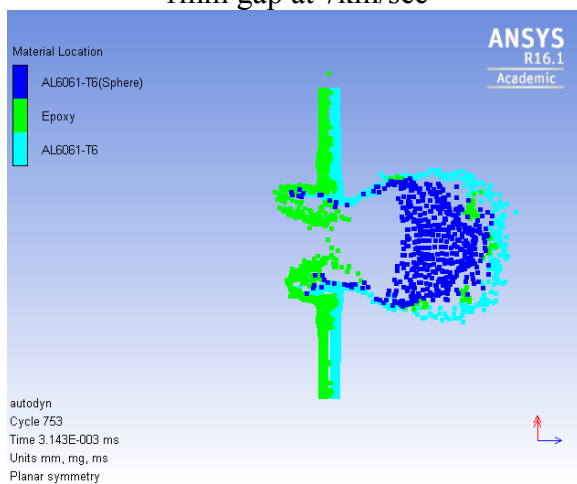
2mm gap at 1km/sec



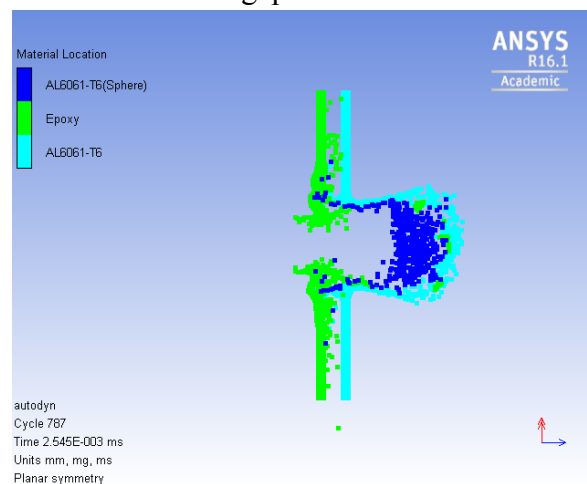
1mm gap at 7km/sec



2mm gap at 7km/sec



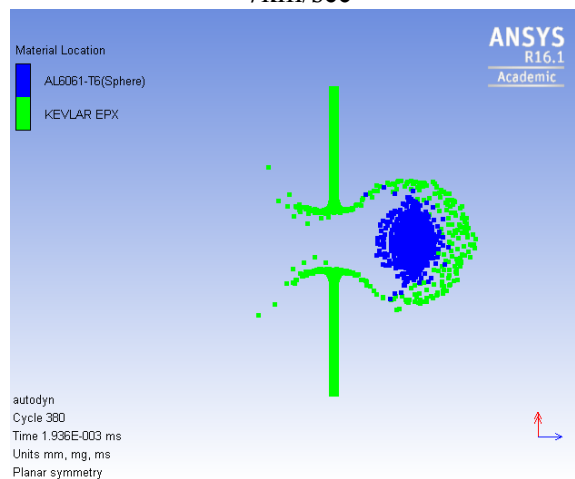
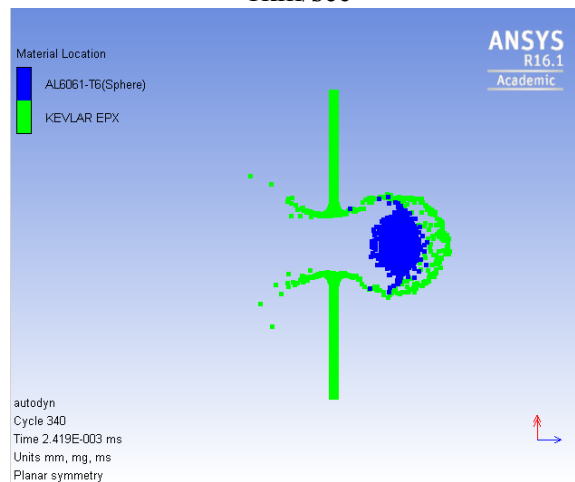
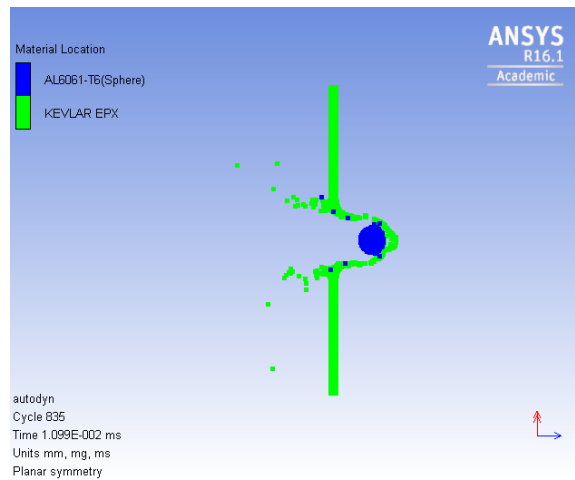
1mm gap at 10km/sec



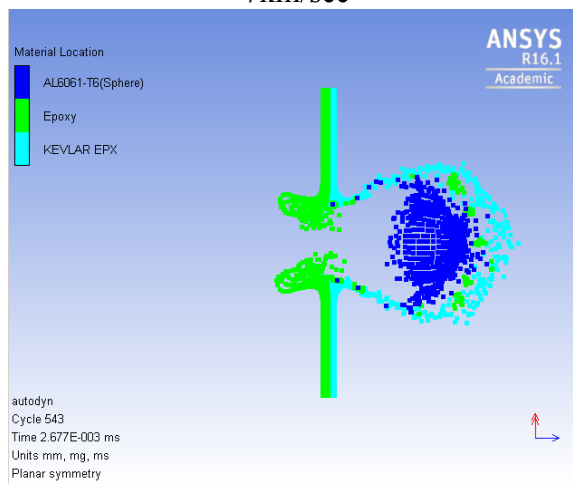
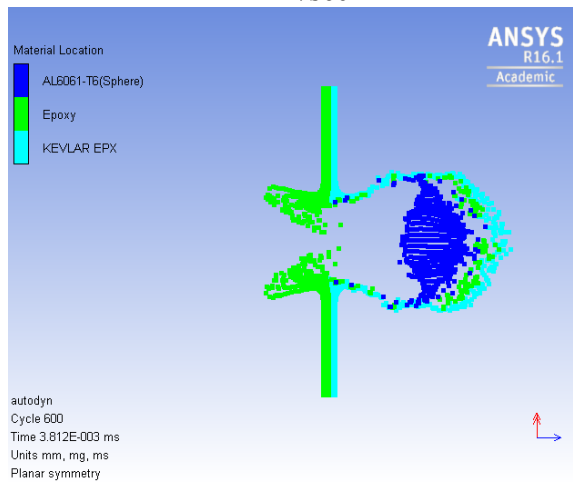
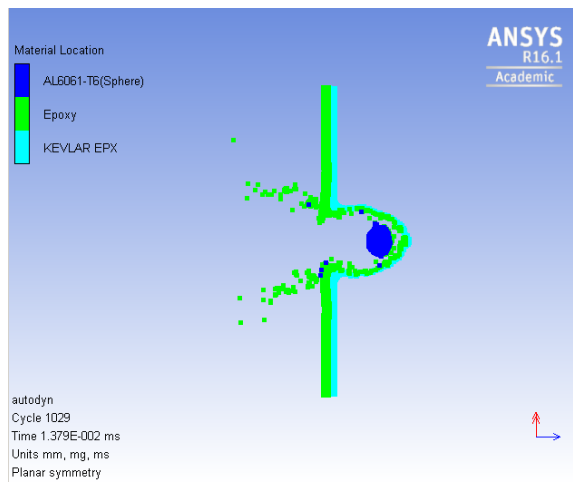
2mm gap at 10km/sec

## II. The crater image for xGnP-Epoxy 1% on Kevlar-Epoxy substrate

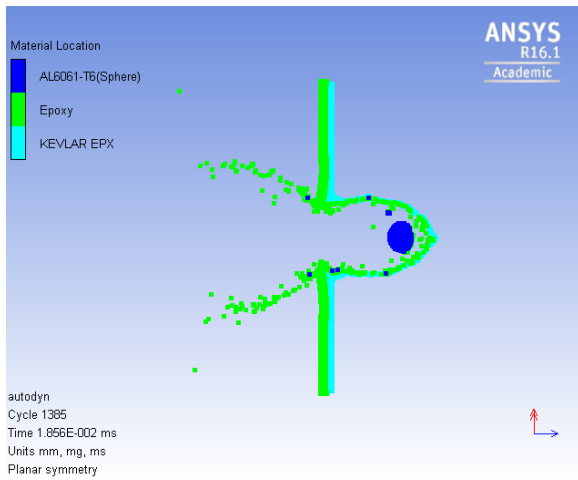
### a) Kevlar-Epoxy blank substrate



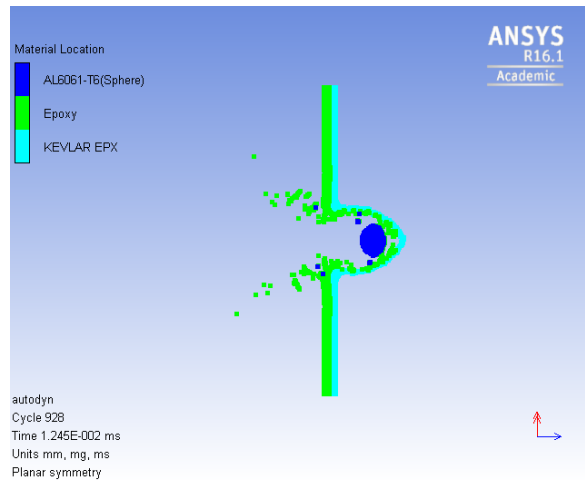
b) Reference xGnP-Epoxy 1% on Kevlar-Epoxy substrate



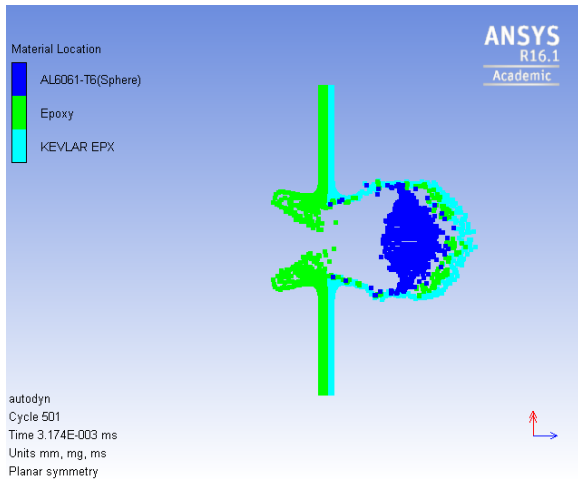
c) Change in yield stress



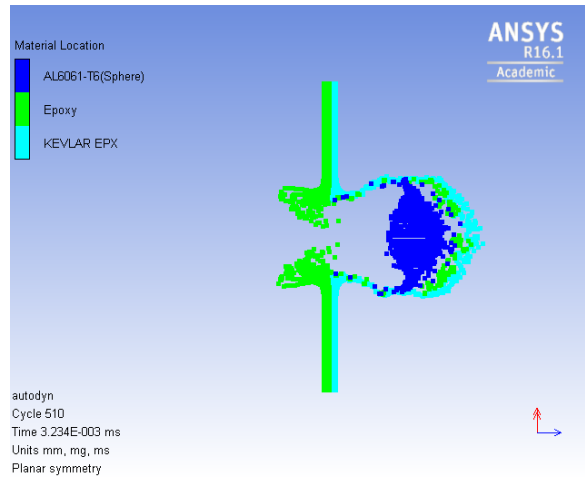
-50% at 1km/sec



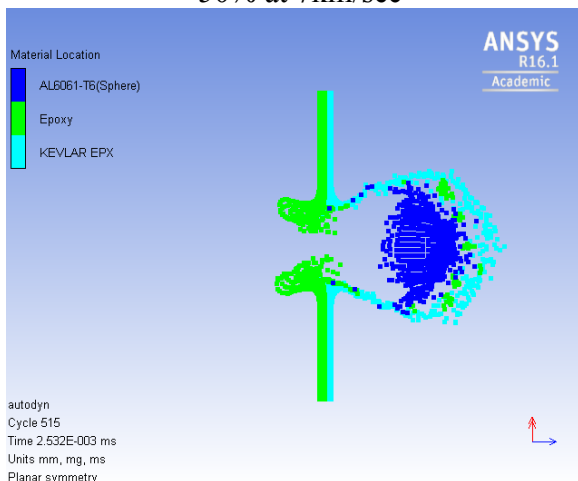
+50% at 1km/sec



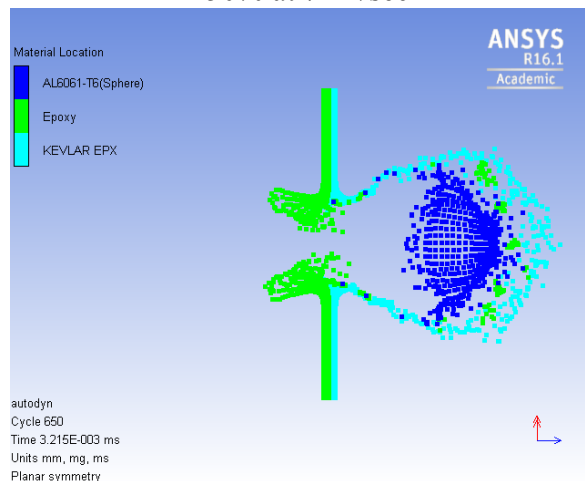
-50% at 7km/sec



+50% at 7km/sec



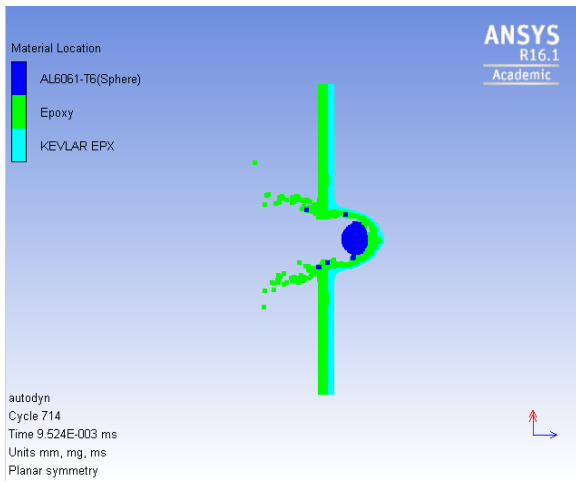
-50% at 10km/sec



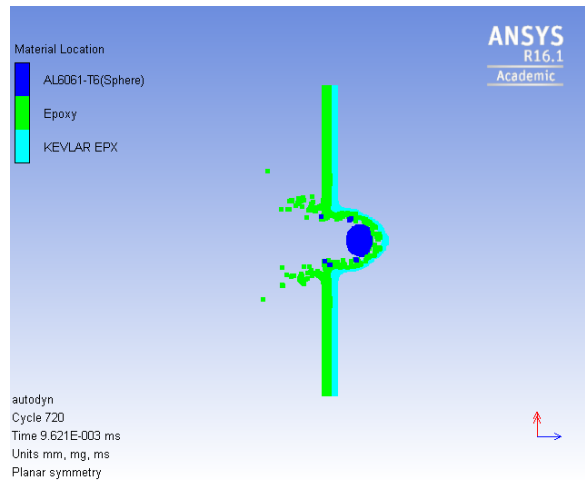
+50% at 10km/sec



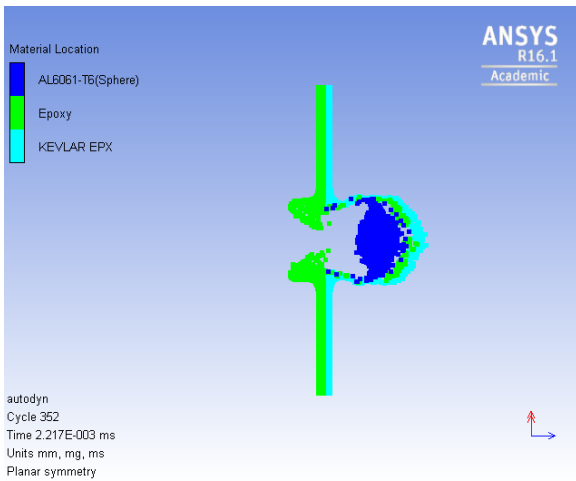
d) Change in Strain hardening



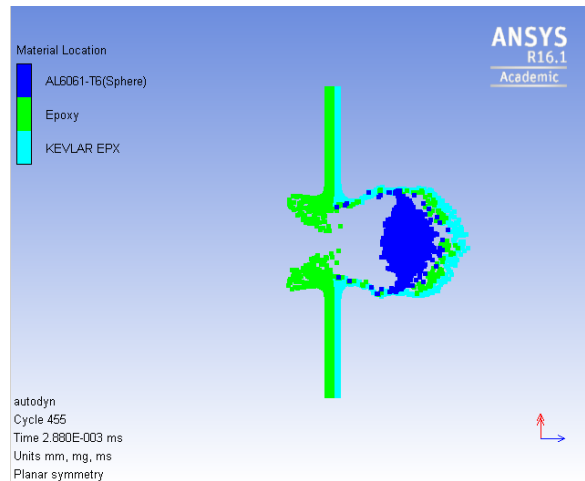
-50% at 1km/sec



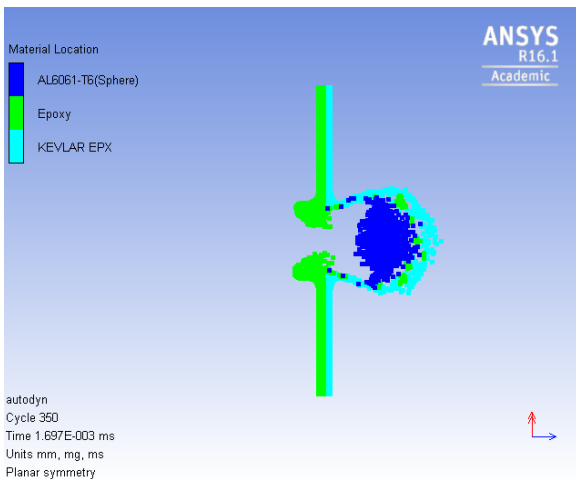
+50% at 1km/sec



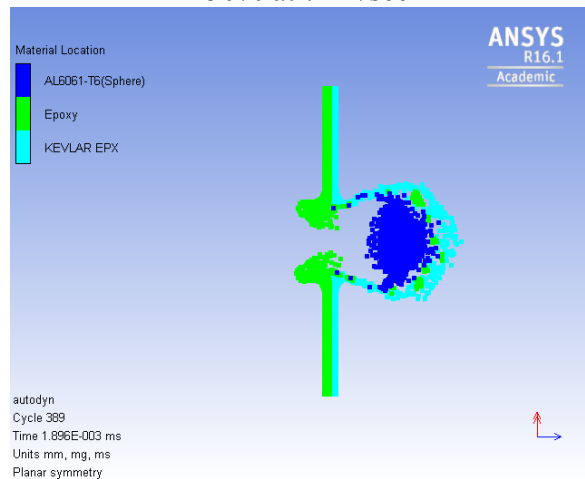
-50% at 7km/sec



+50% at 7km/sec

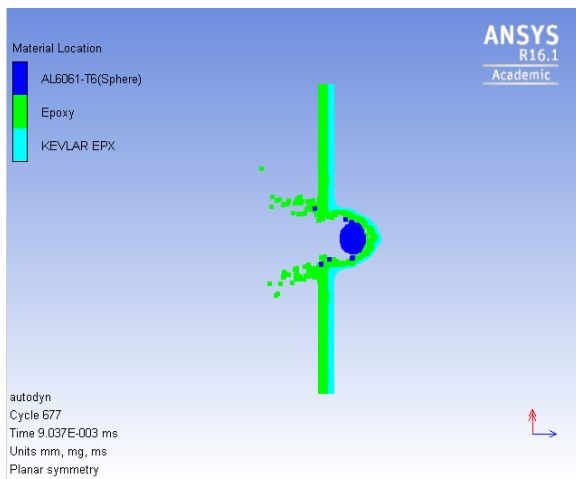


-50% at 10km/sec

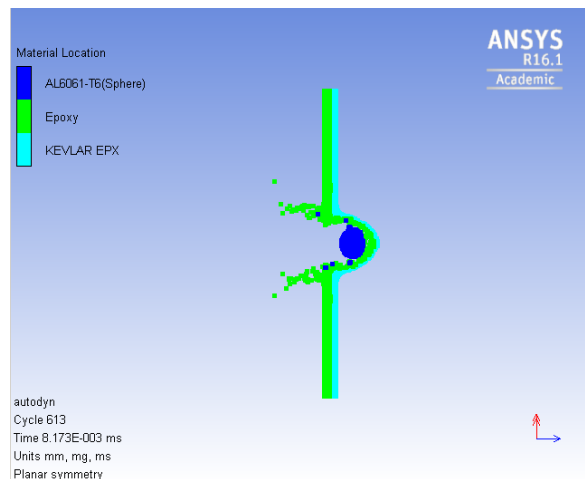


+50% at 10km/sec

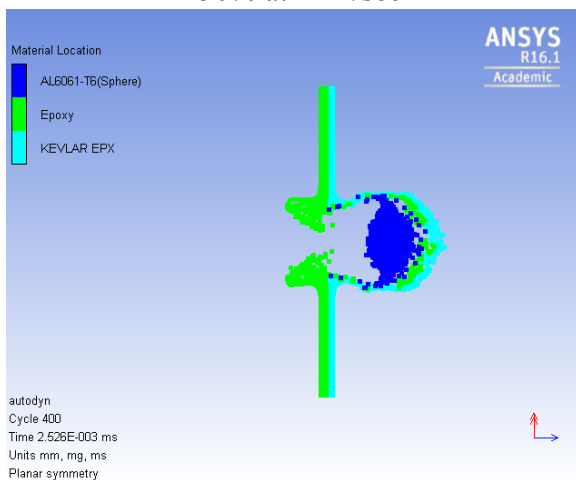
e) Change in Strain Rate constant



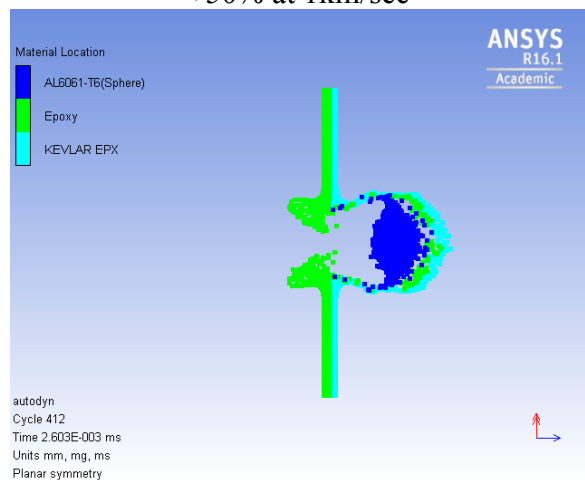
-50% at 1km/sec



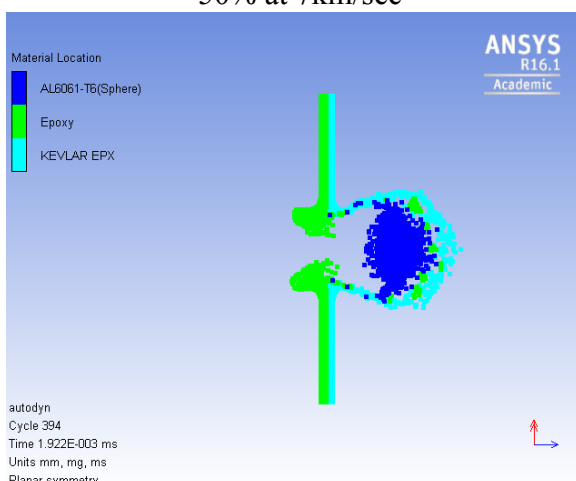
+50% at 1km/sec



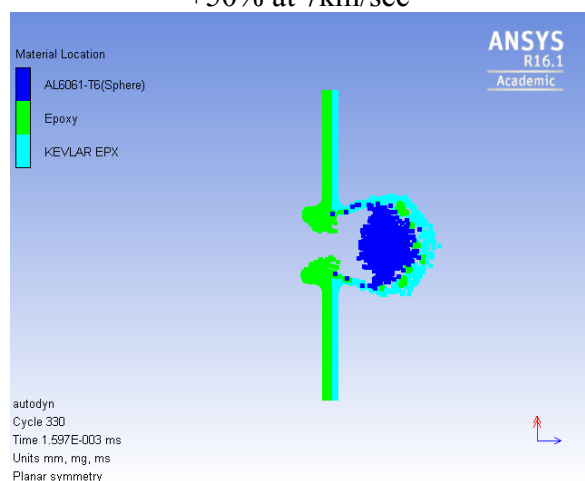
-50% at 7km/sec



+50% at 7km/sec

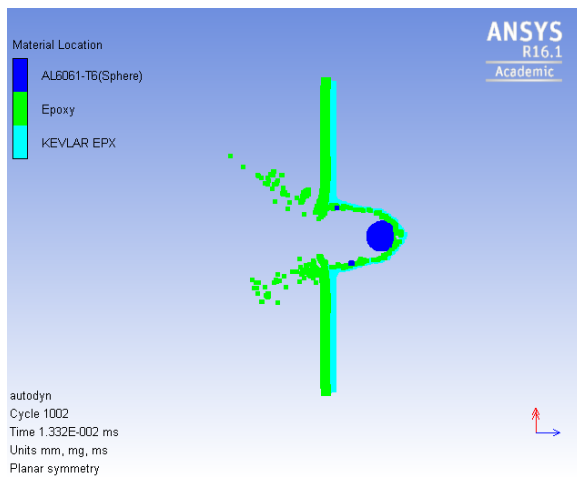


-50% at 10km/sec

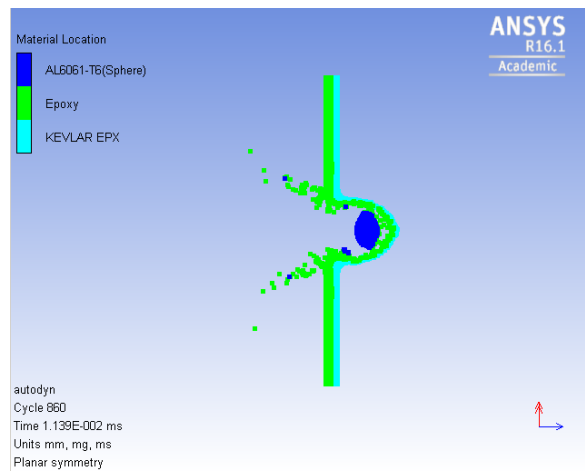


+50% at 10km/sec

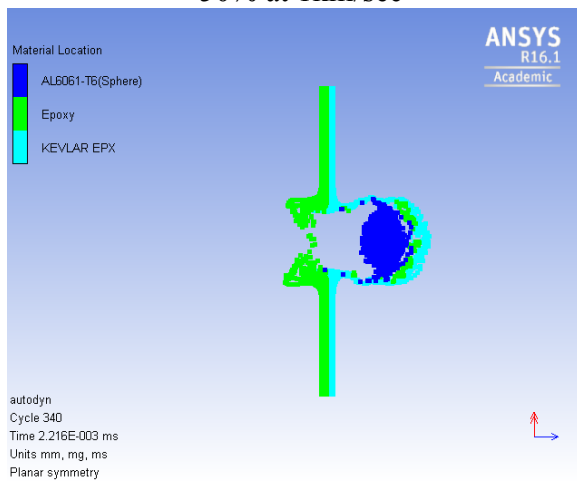
f) Change in Reference density



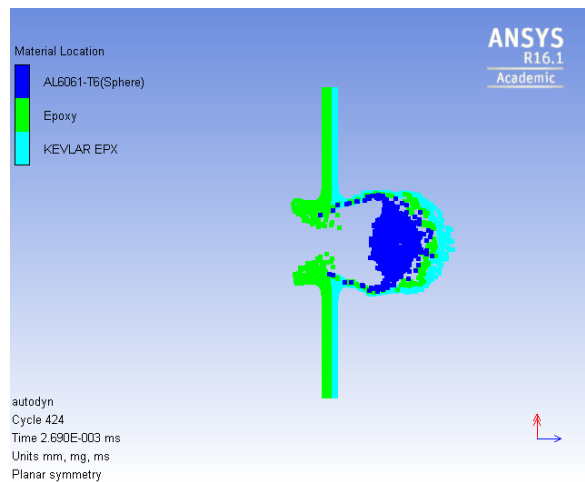
-50% at 1km/sec



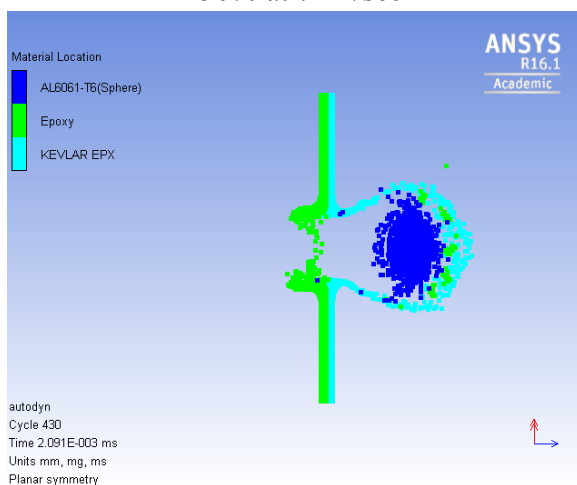
+50% at 1km/sec



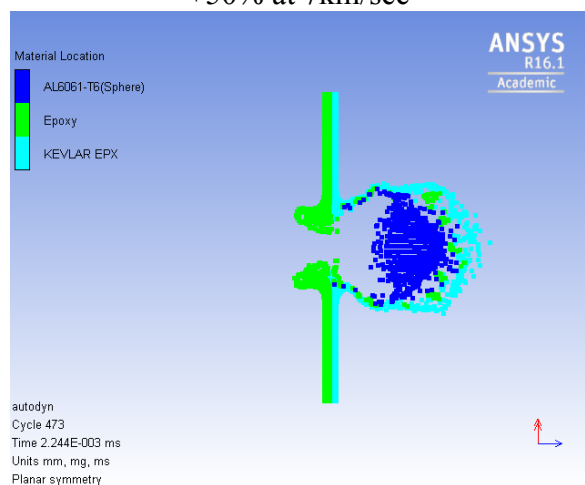
-50% at 7km/sec



+50% at 7km/sec

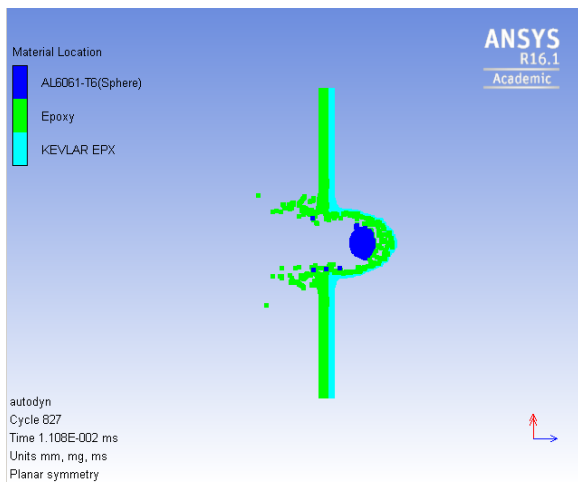


-50% at 10km/sec

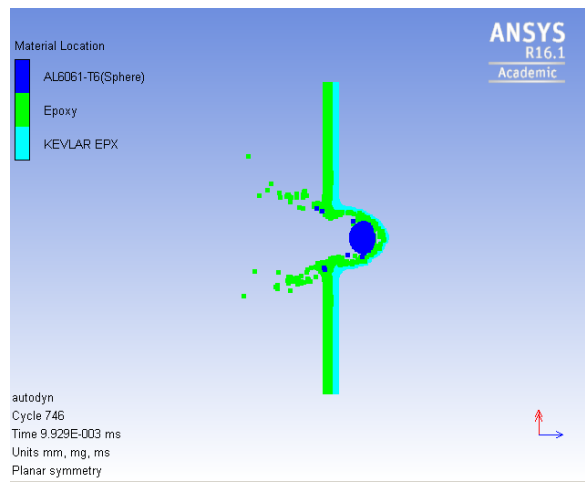


+50% at 10km/sec

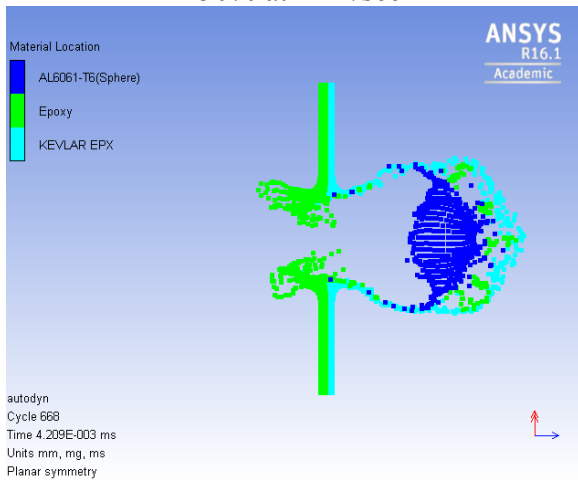
g) Change in bulk Modulus



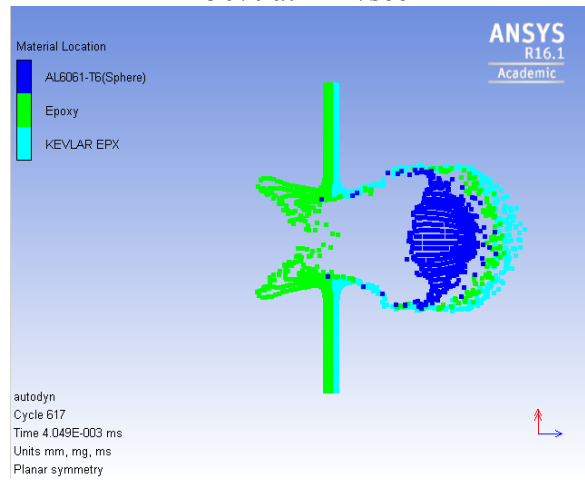
-50% at 1km/sec



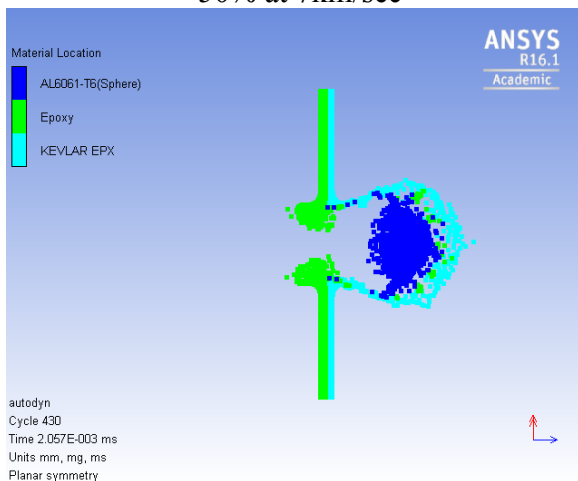
+50% at 1km/sec



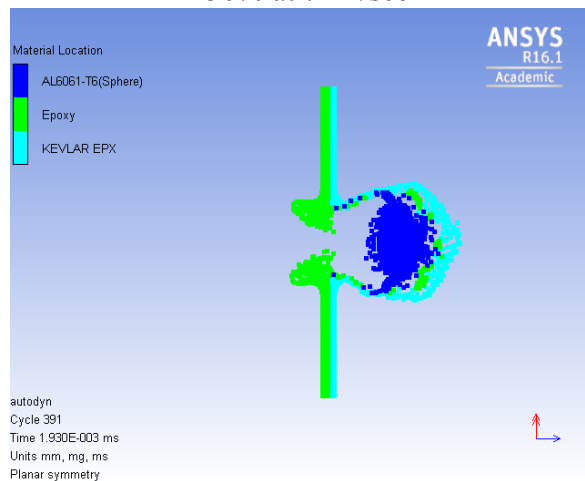
-50% at 7km/sec



+50% at 7km/sec

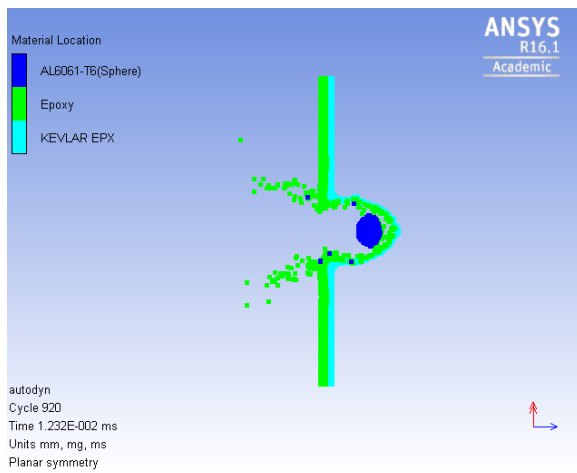


-50% at 10km/sec

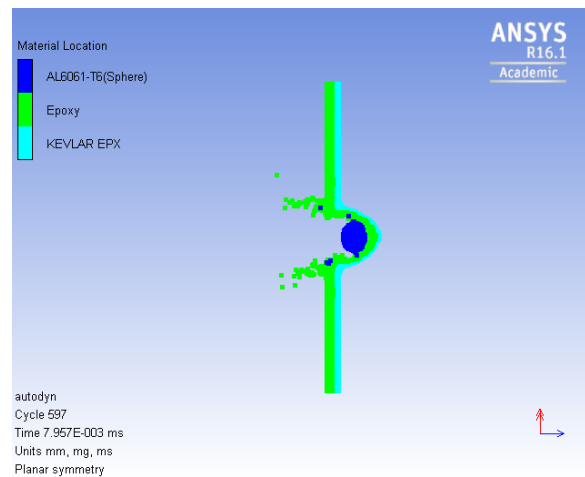


+50% at 10km/sec

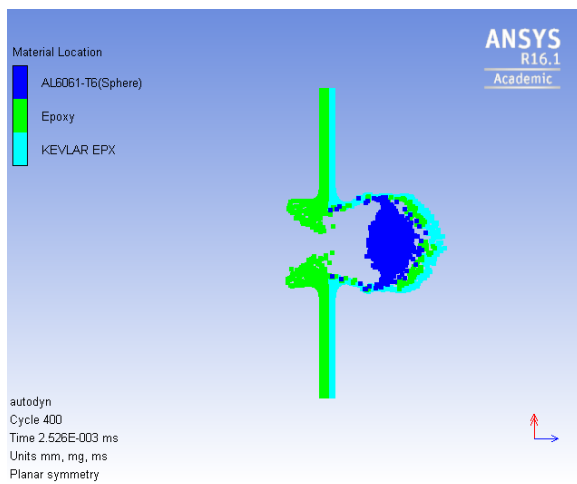
## h) Reference strain rate



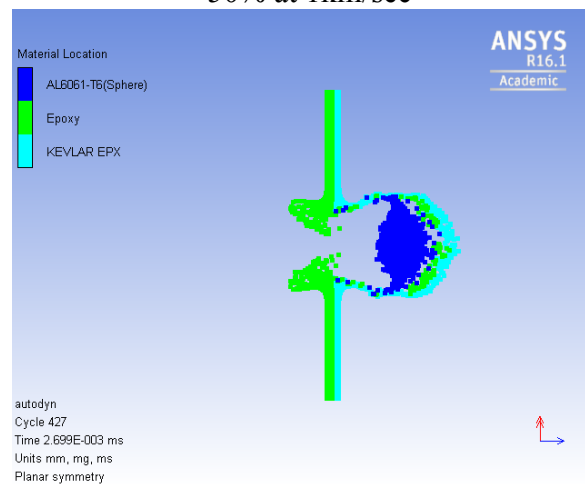
-50% at 1km/sec



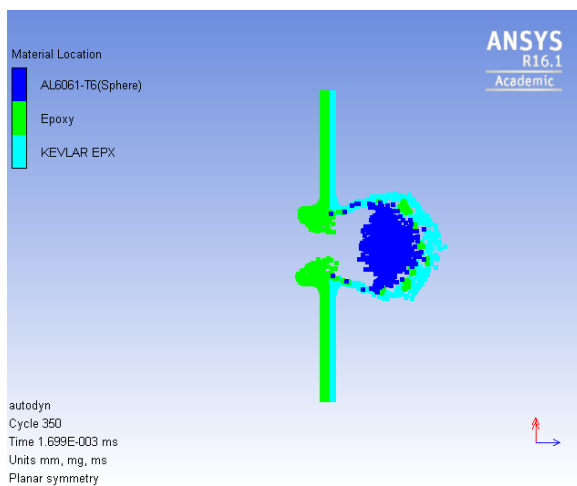
+50% at 1km/sec



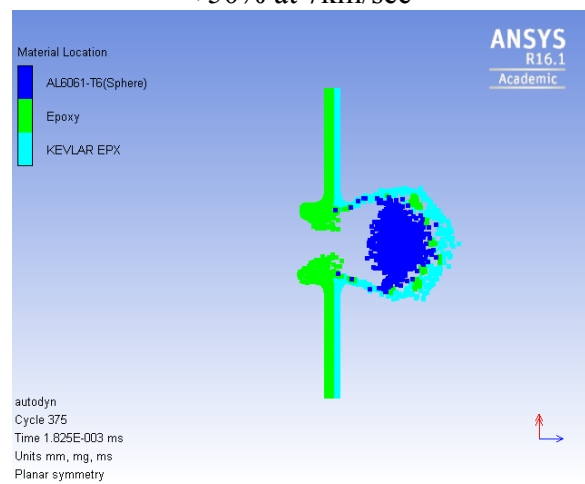
-50% at 7km/sec



+50% at 7km/sec

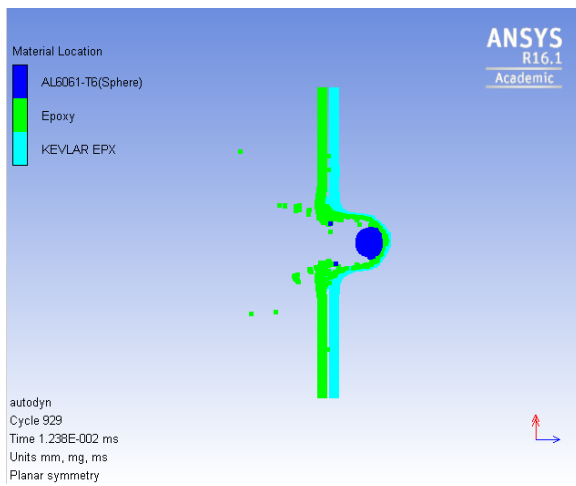


-50% at 10km/sec

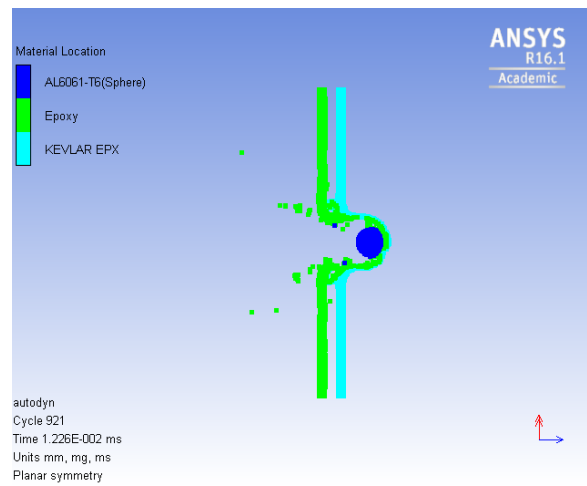


+50% at 10km/sec

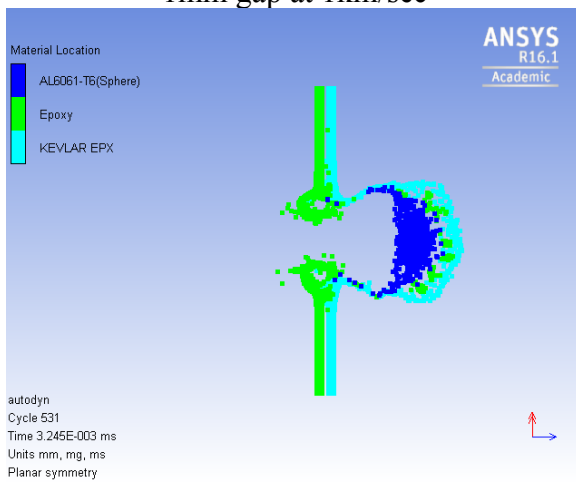
i) Change in gap distance



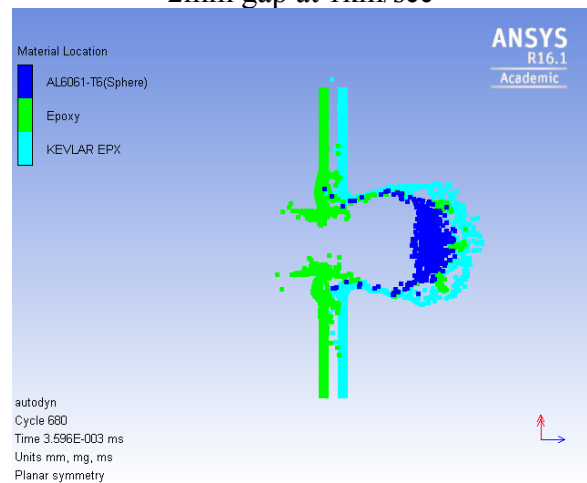
1mm gap at 1km/sec



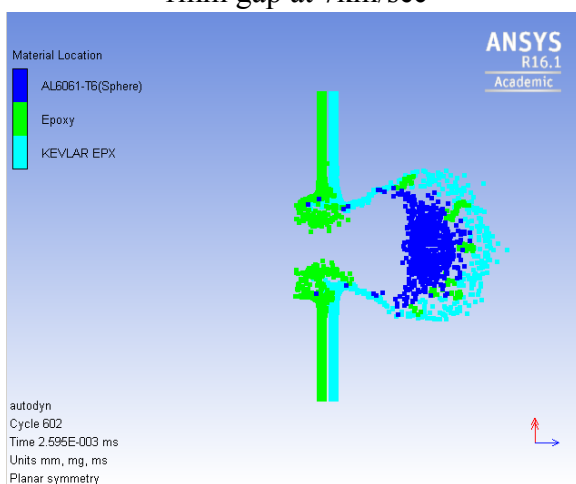
2mm gap at 1km/sec



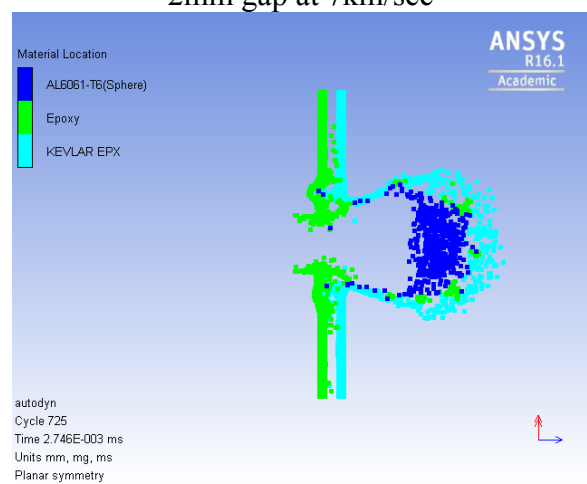
1mm gap at 7km/sec



2mm gap at 7km/sec



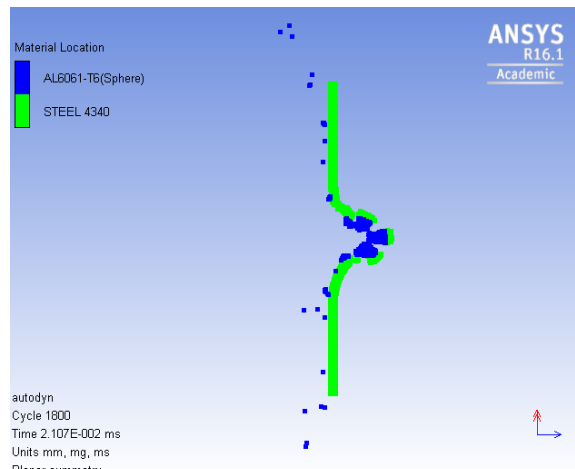
1mm gap at 10km/sec



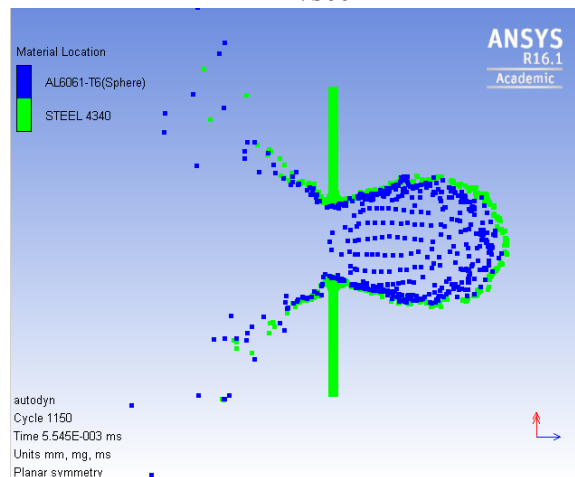
2mm gap at 10km/sec

### III. The crater image for xGnP-Epoxy 1% on Steel substrate

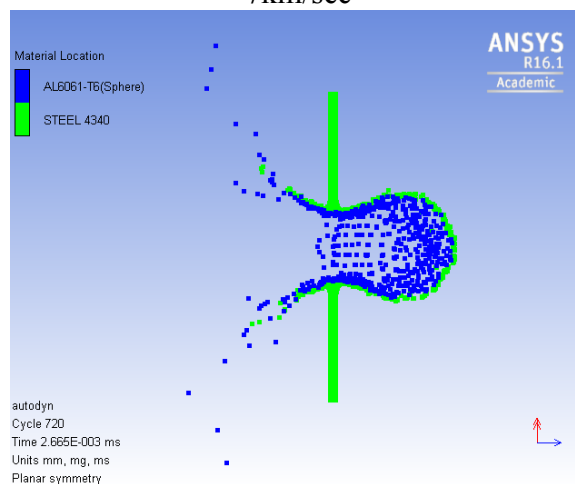
a) Steel blank substrate



1km/sec

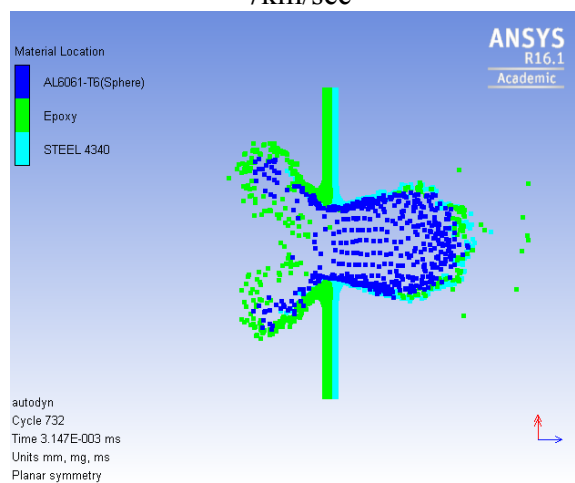
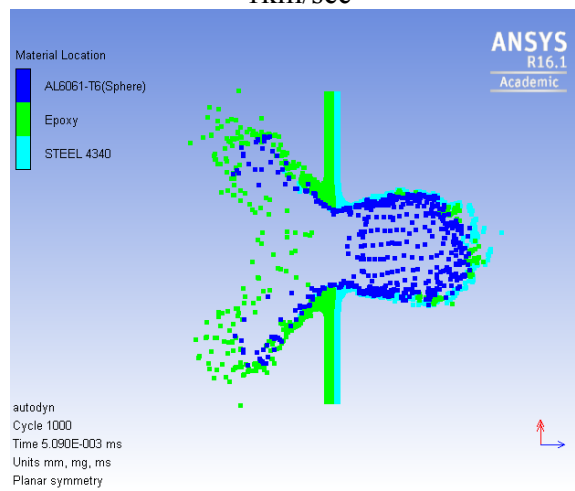
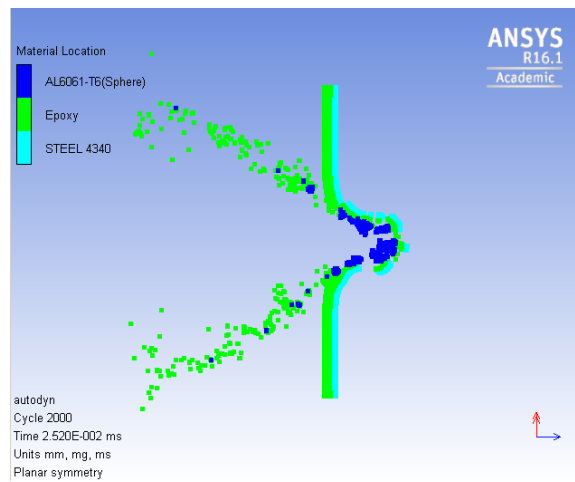


7km/sec



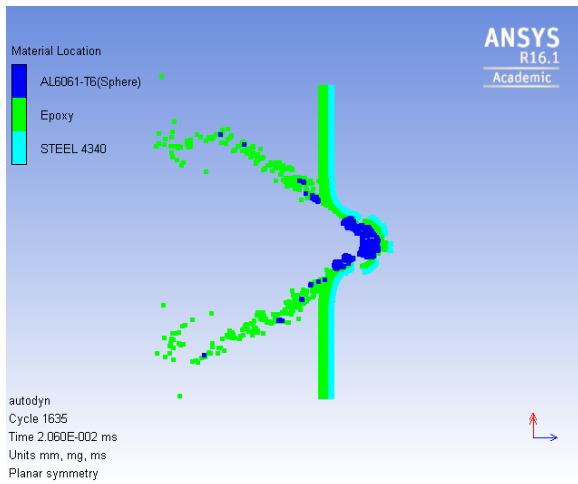
10km/sec

b) Reference xGnP-Epoxy 1% on Steel substrate

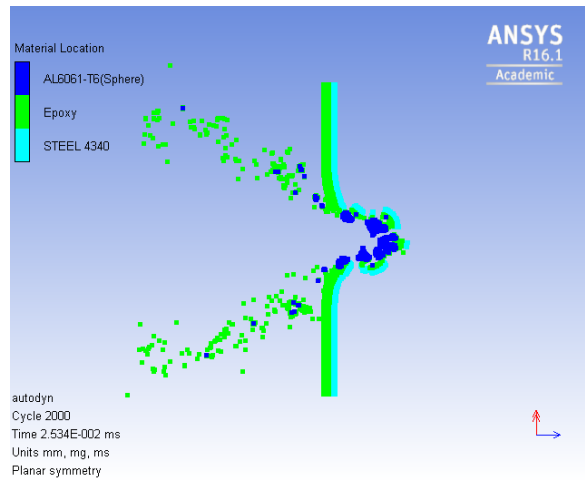




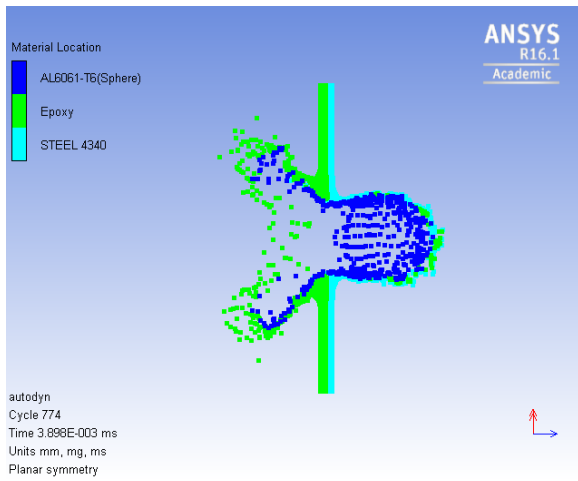
c) Change in yield stress



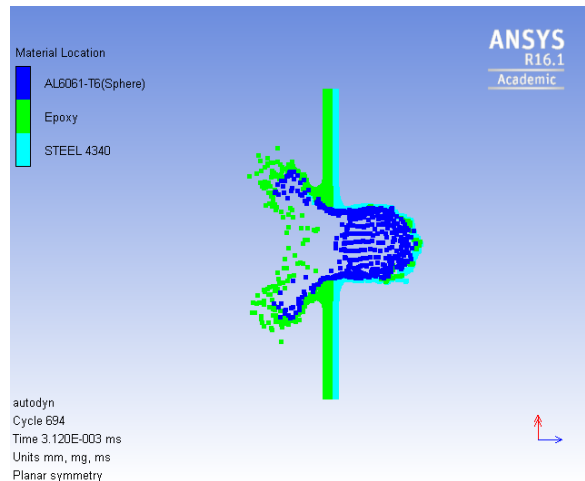
-50% at 1km/sec



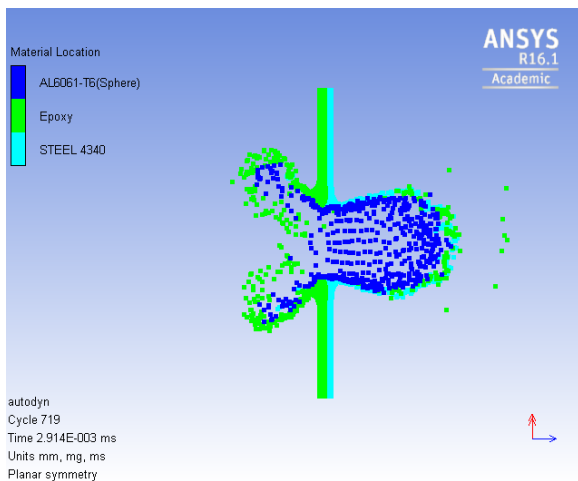
+50% at 1km/sec



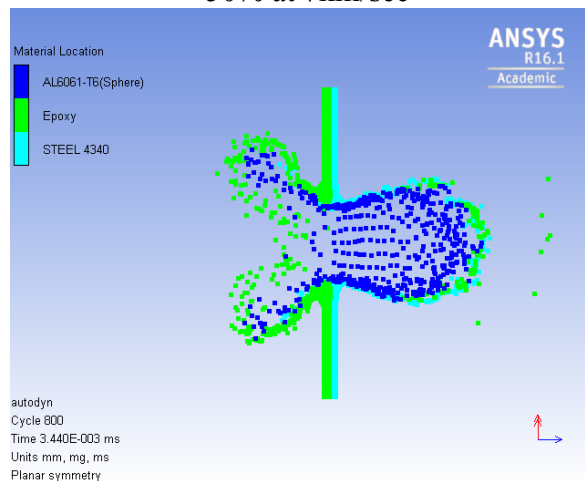
-50% at 7km/sec



+50% at 7km/sec

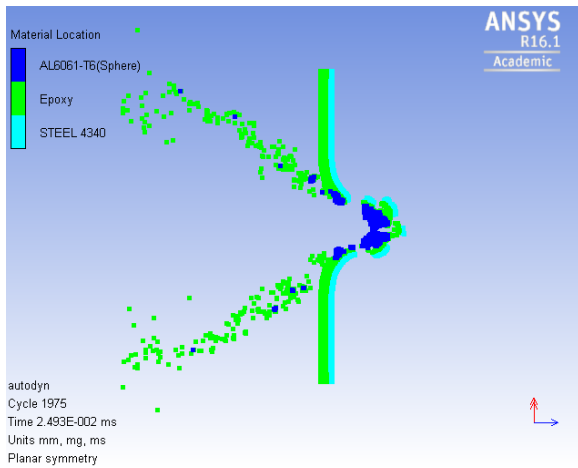


-50% at 10km/sec

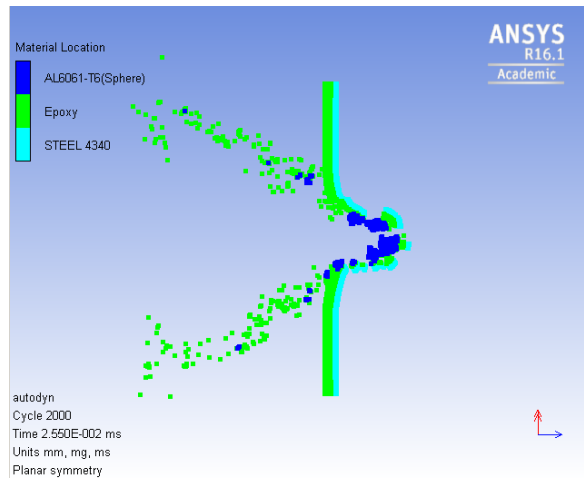


+50% at 10km/sec

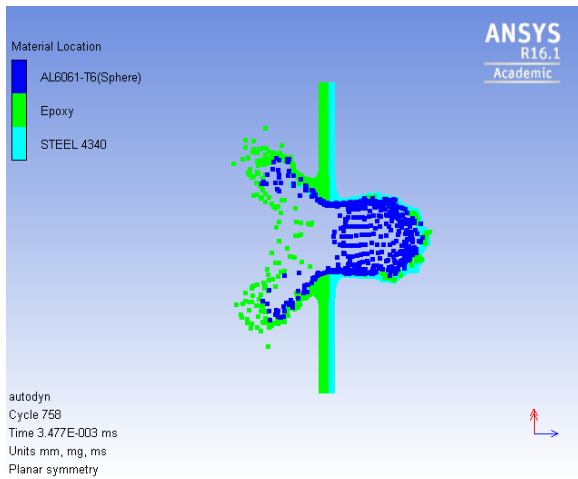
d) Change in Strain hardening



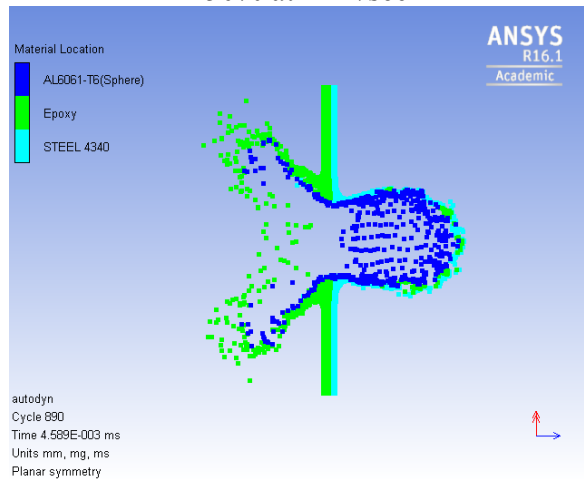
-50% at 1km/sec



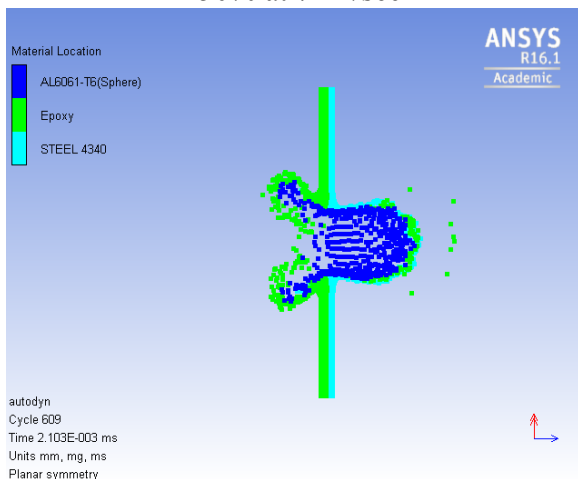
+50% at 1km/sec



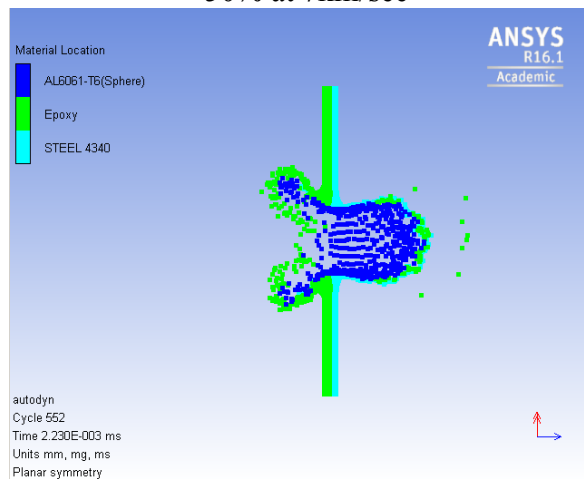
-50% at 7km/sec



+50% at 7km/sec

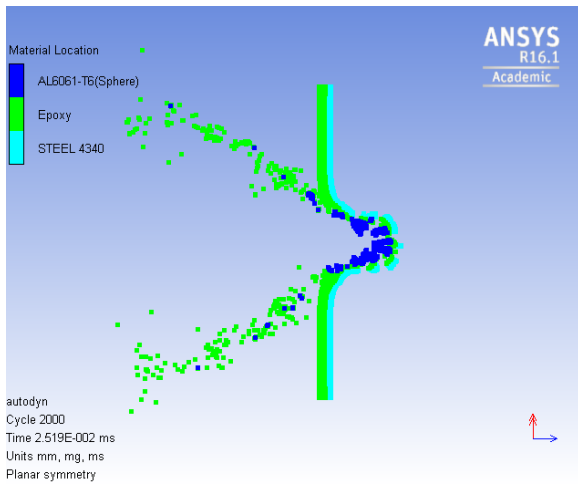


-50% at 10km/sec

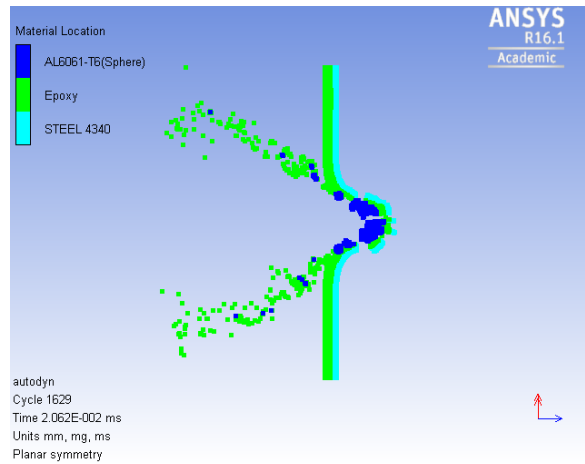


+50% at 10km/sec

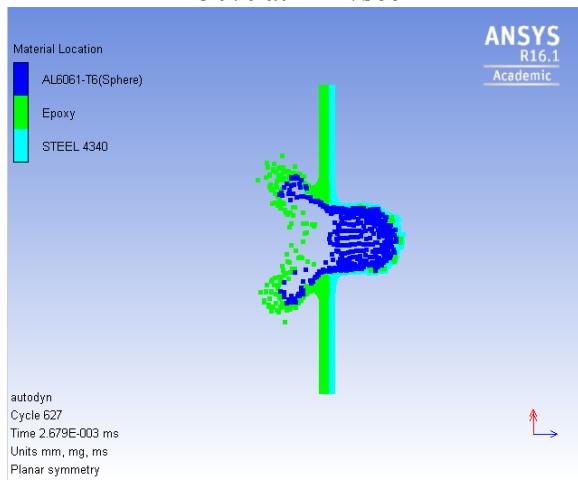
e) Change in Strain Rate constant



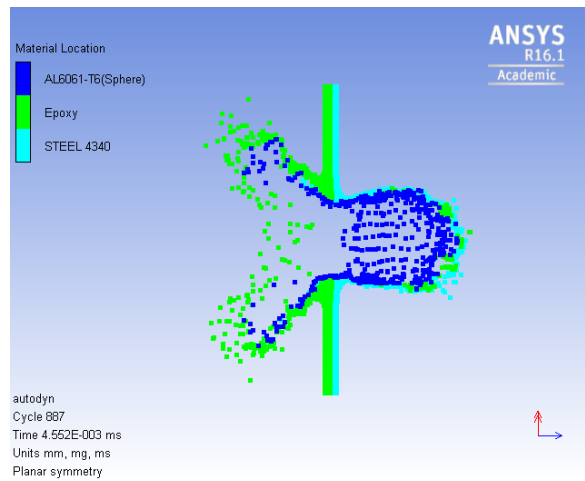
-50% at 1km/sec



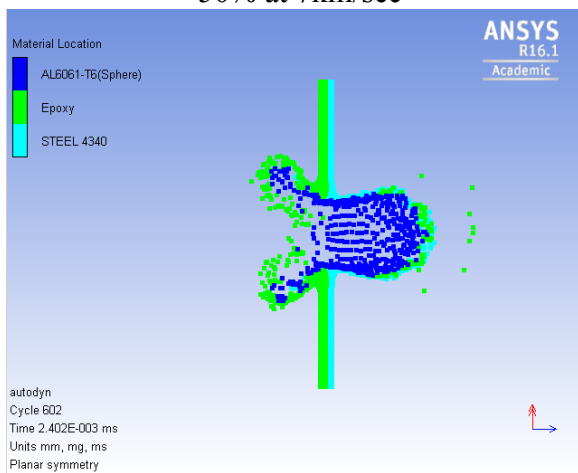
+50% at 1km/sec



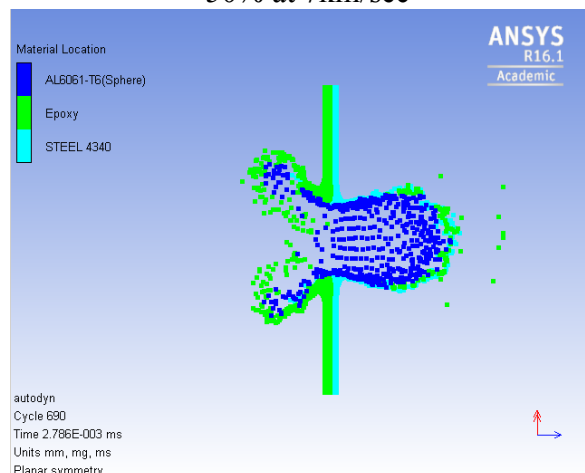
-50% at 7km/sec



+50% at 7km/sec

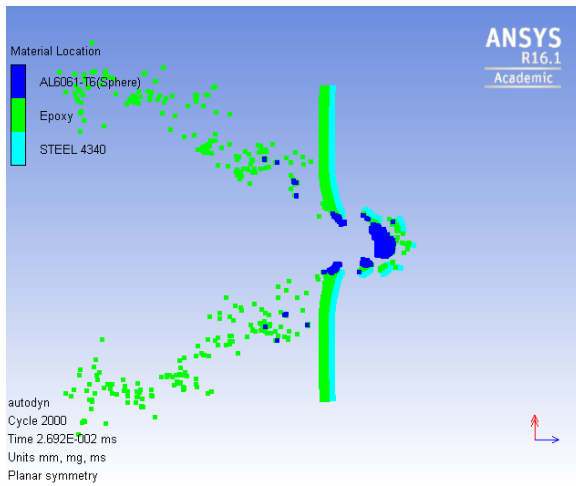


-50% at 10km/sec

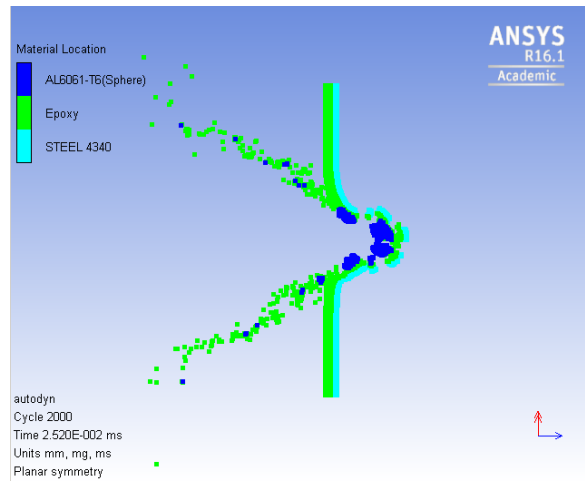


+50% at 10km/sec

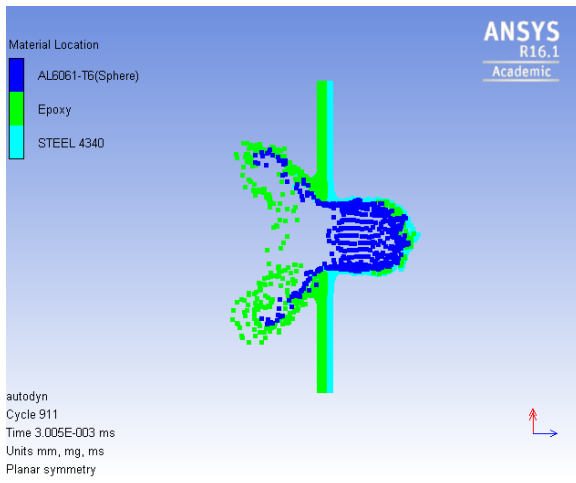
f) Change in Reference density



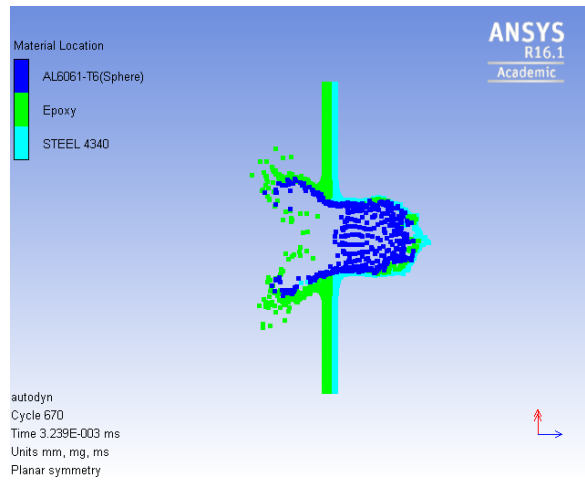
-50% at 1km/sec



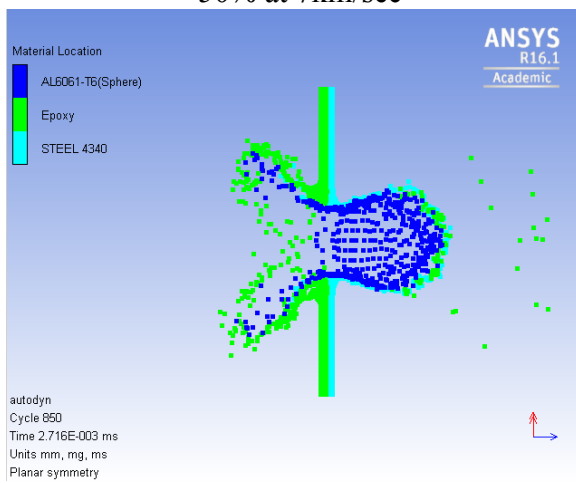
+50% at 1km/sec



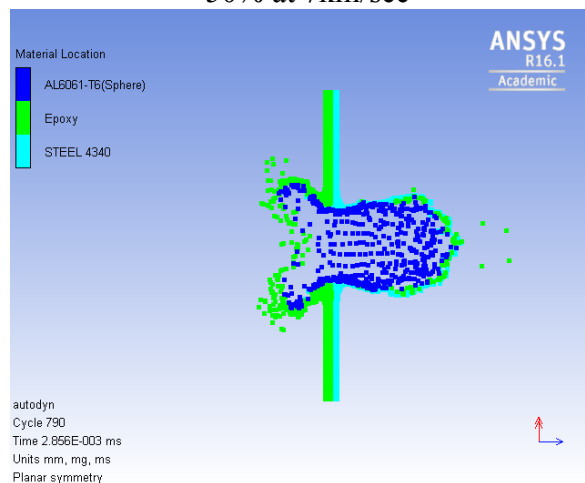
-50% at 7km/sec



+50% at 7km/sec

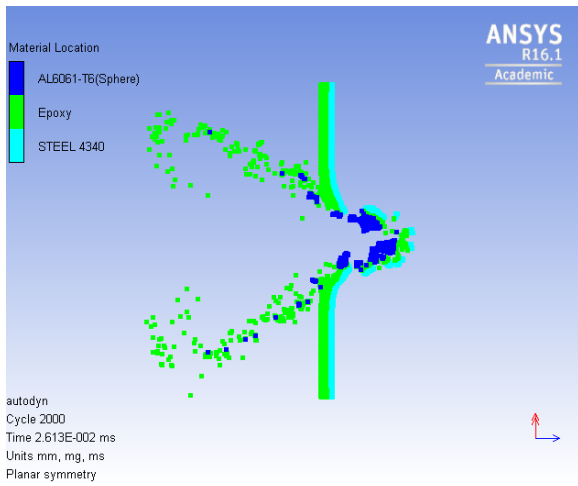


-50% at 10km/sec

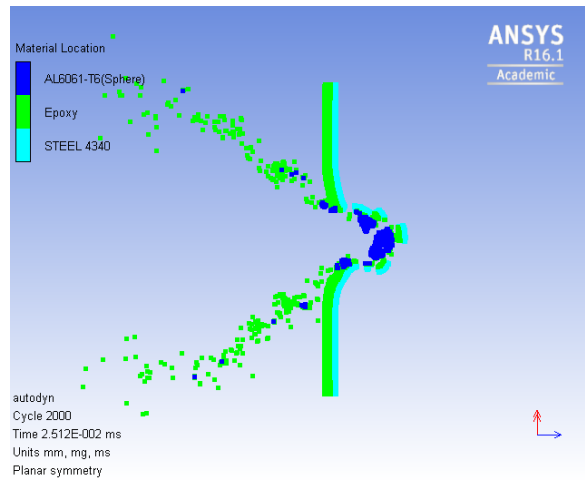


+50% at 10km/sec

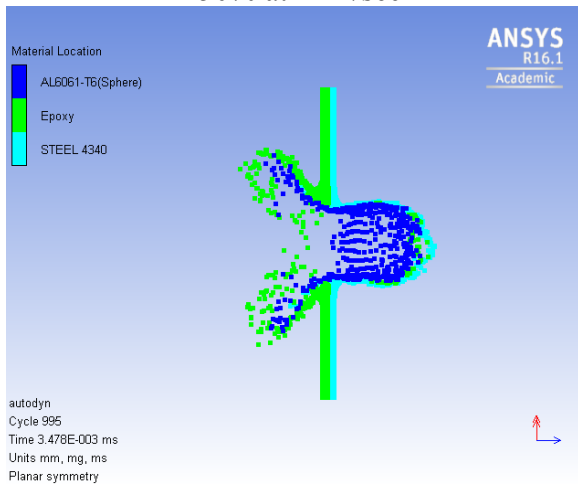
g) Change in bulk Modulus



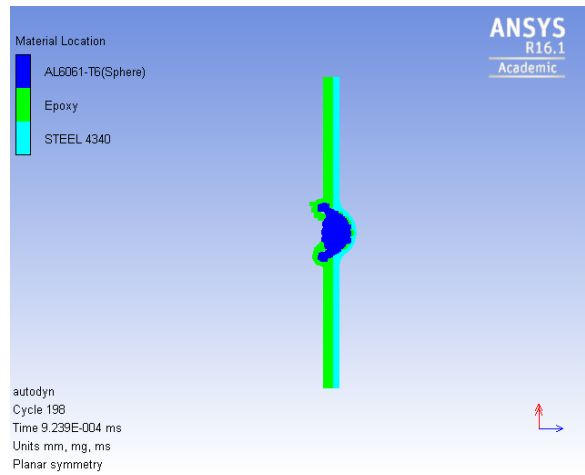
-50% at 1km/sec



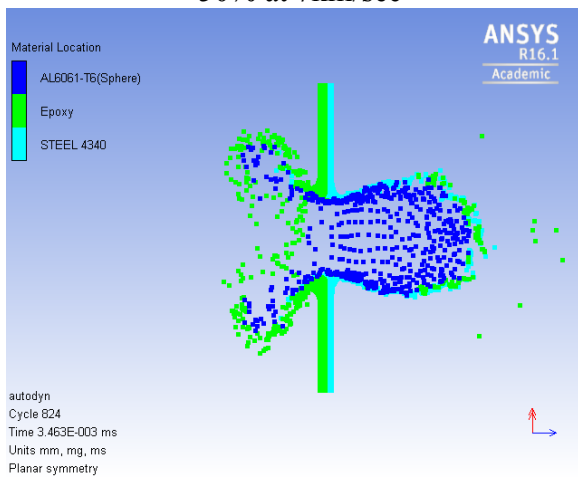
+50% at 1km/sec



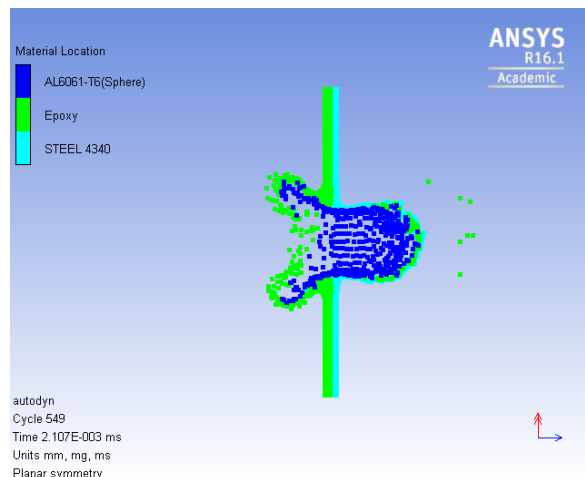
-50% at 7km/sec



+50% at 7km/sec

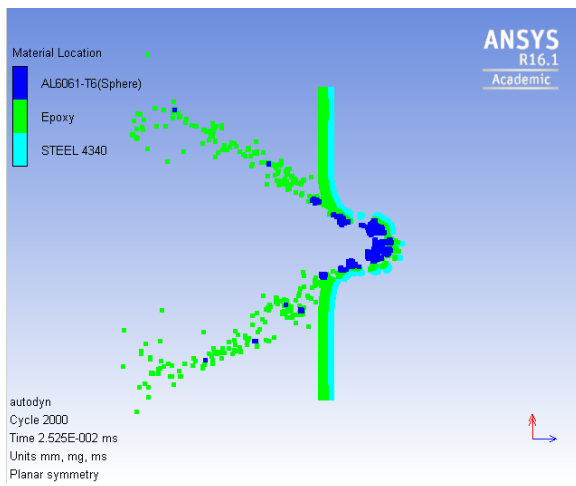


-50% at 10km/sec

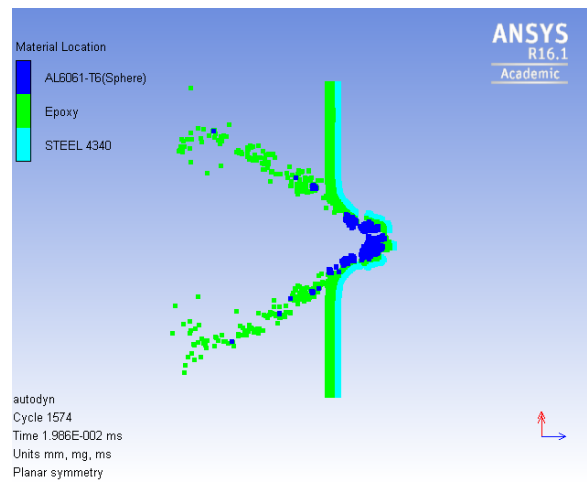


+50% at 10km/sec

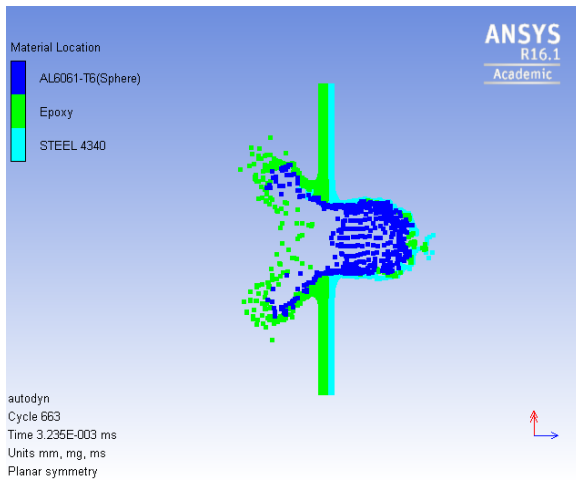
### h) Reference strain rate



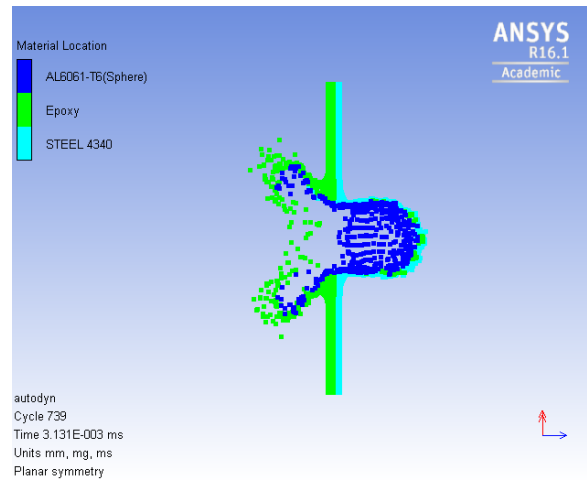
-50% at 1km/sec



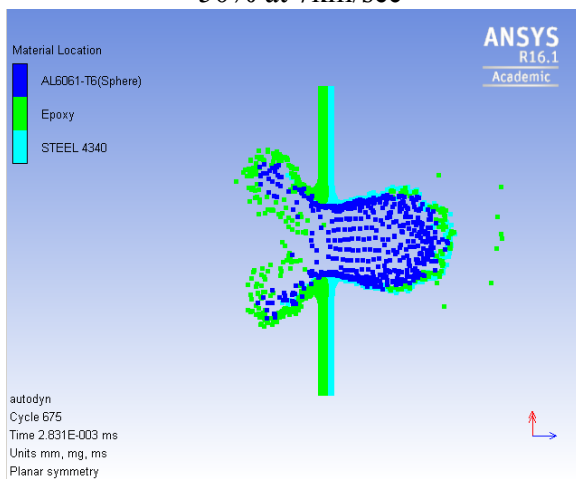
+50% at 1km/sec



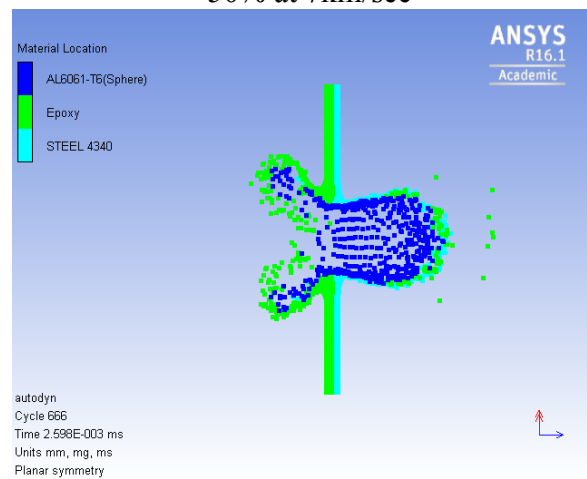
-50% at 7km/sec



+50% at 7km/sec

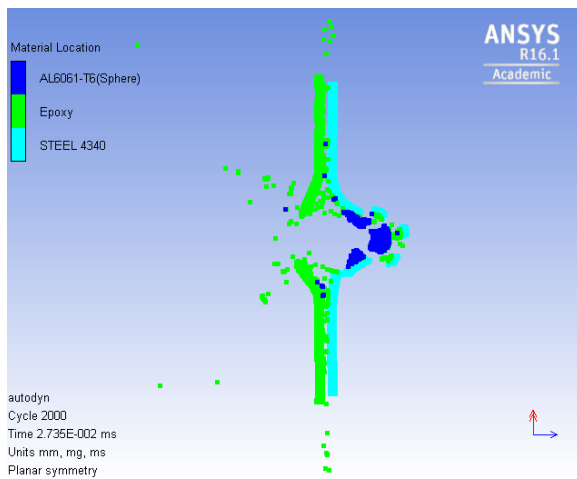


-50% at 10km/sec

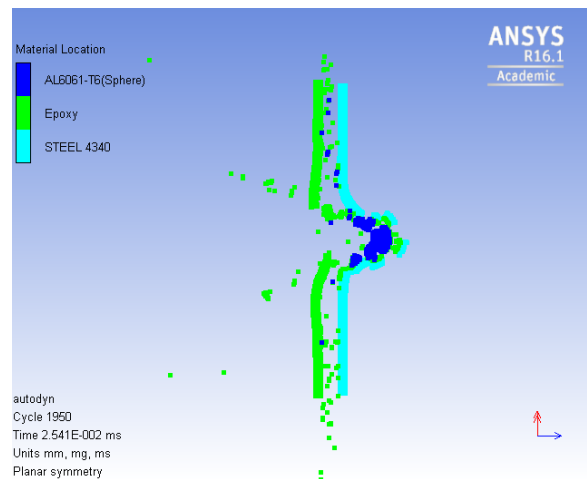


+50% at 10km/sec

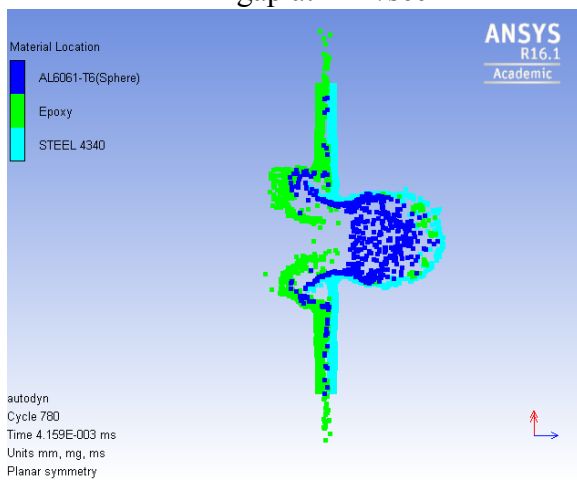
i) Change in gap distance



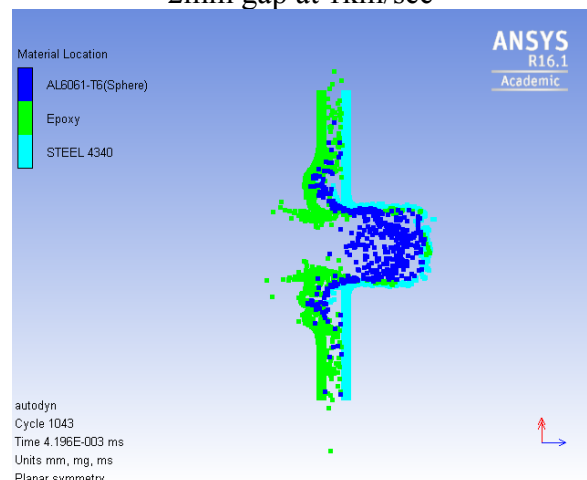
1mm gap at 1km/sec



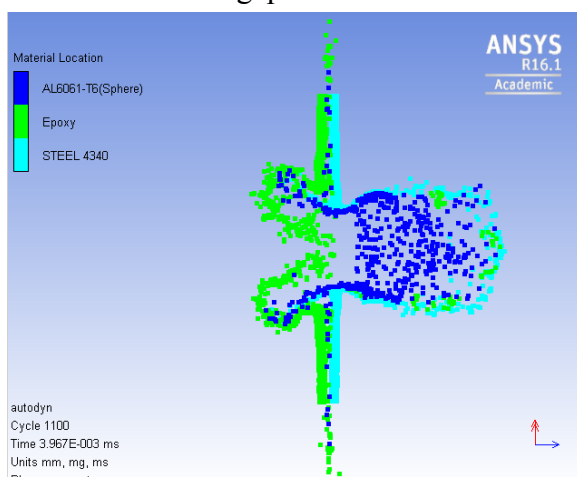
2mm gap at 1km/sec



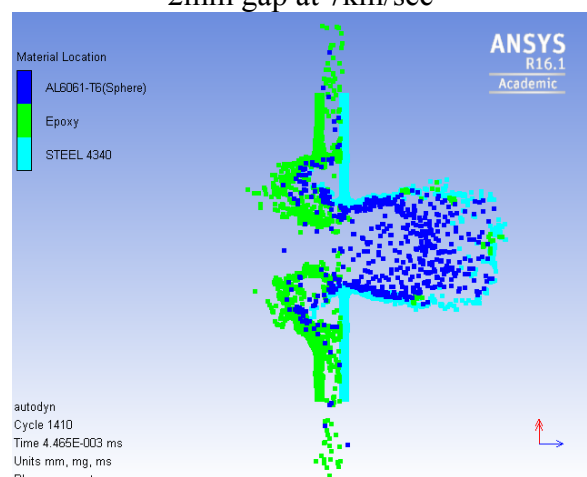
1mm gap at 7km/sec



2mm gap at 7km/sec



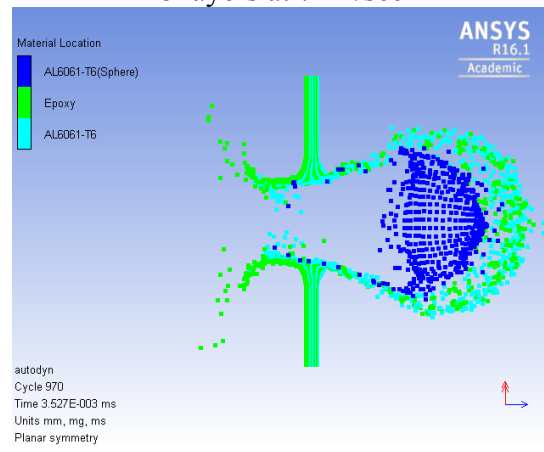
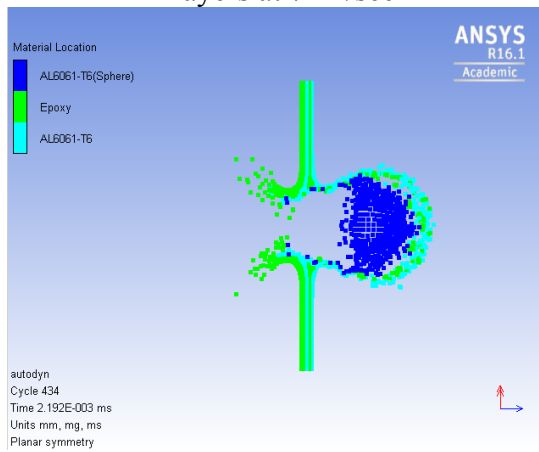
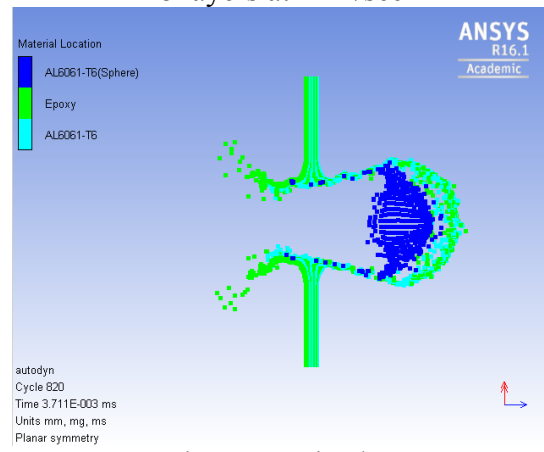
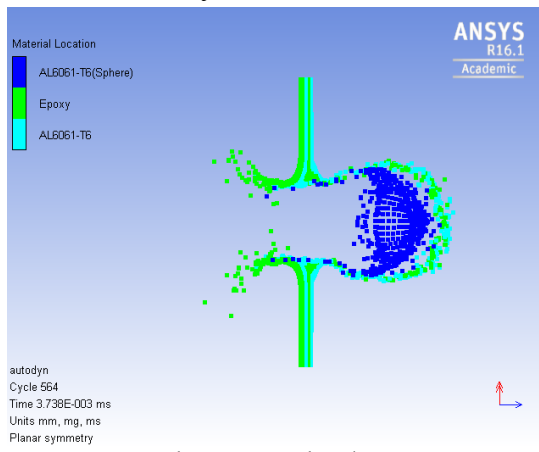
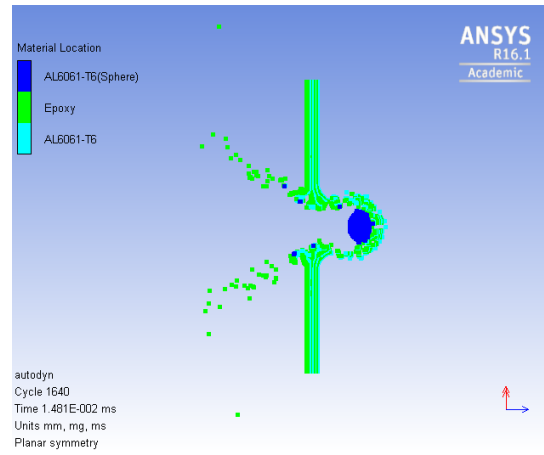
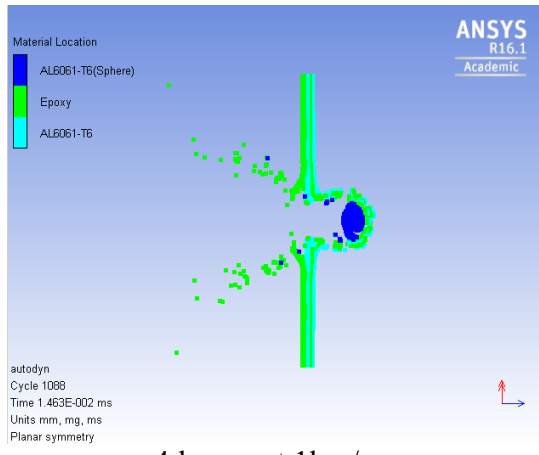
1mm gap at 10km/sec



2mm gap at 10km/sec

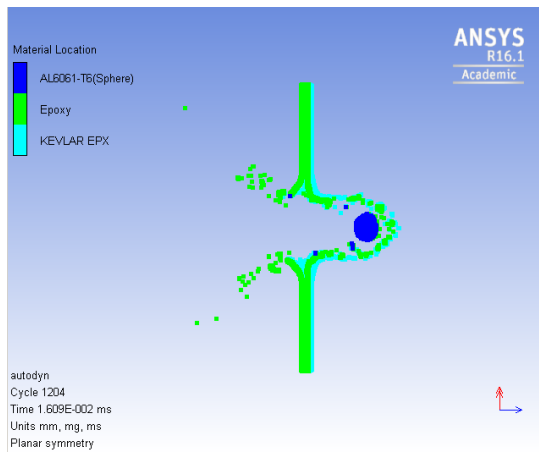
# APPENDIX E

## 1. Coating with Aluminum

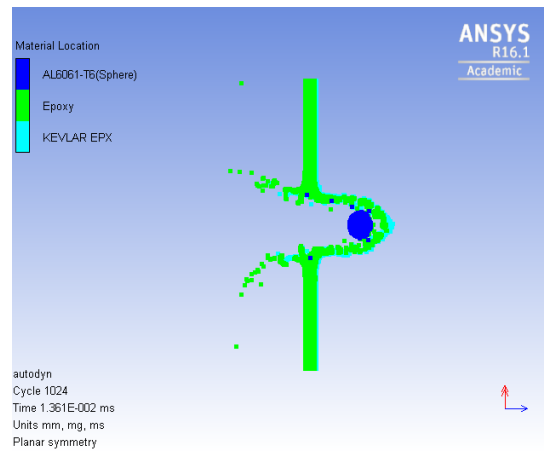




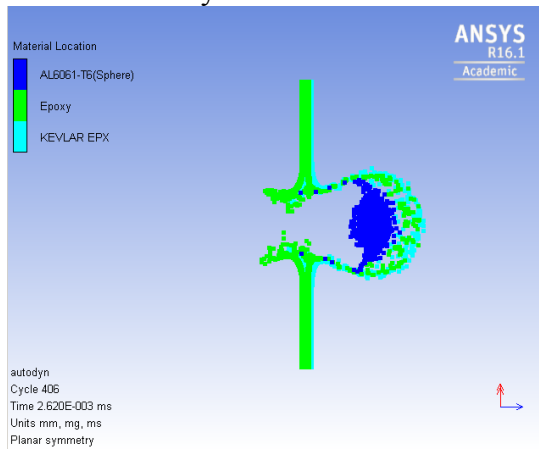
## 2. Coating with Kevlar-Epoxy



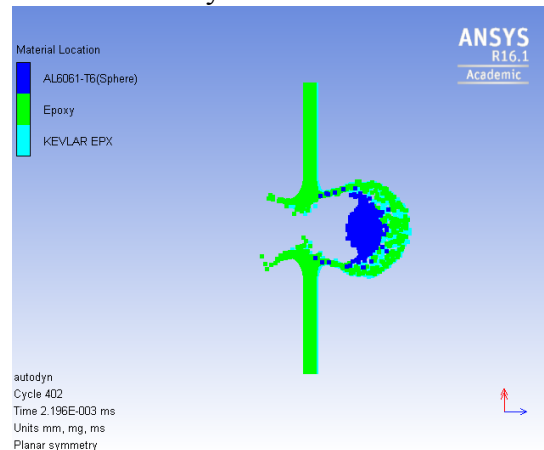
4 layers at 1km/sec



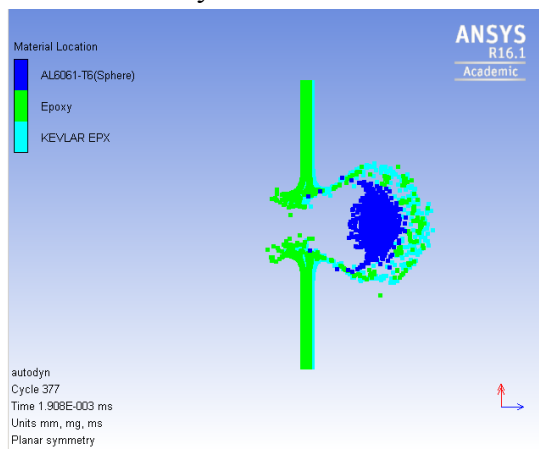
8 layers at 1km/sec



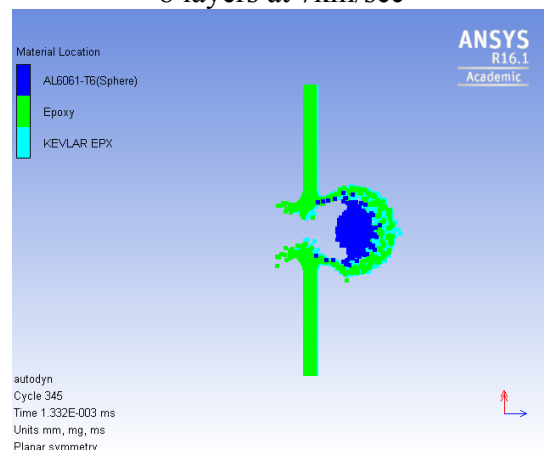
4layers at 7km/sec



8 layers at 7km/sec

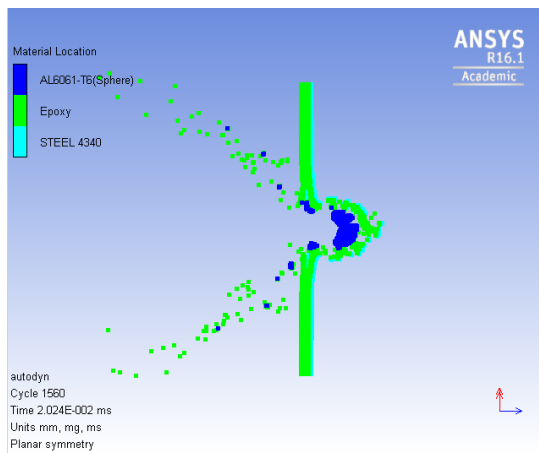


4 layers at 10km/sec

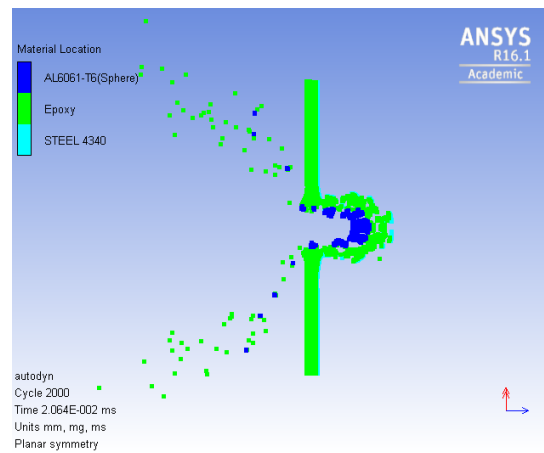


8 layers at 10km/sec

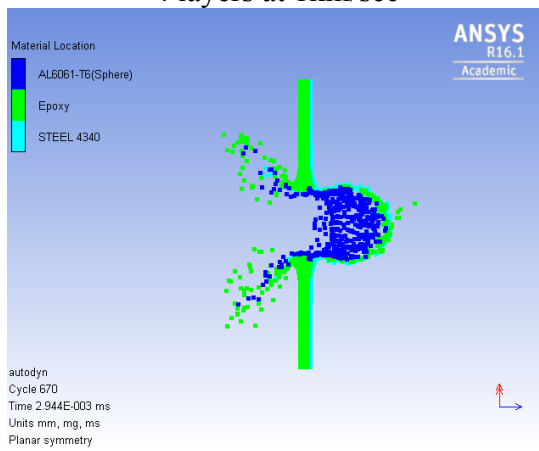
### 3. Coating with Steel



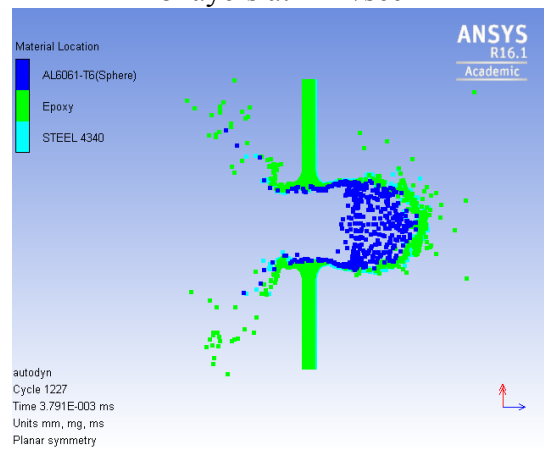
4 layers at 1km/sec



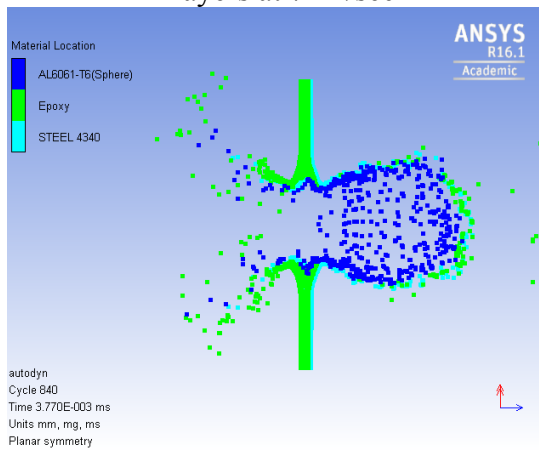
8 layers at 1km/sec



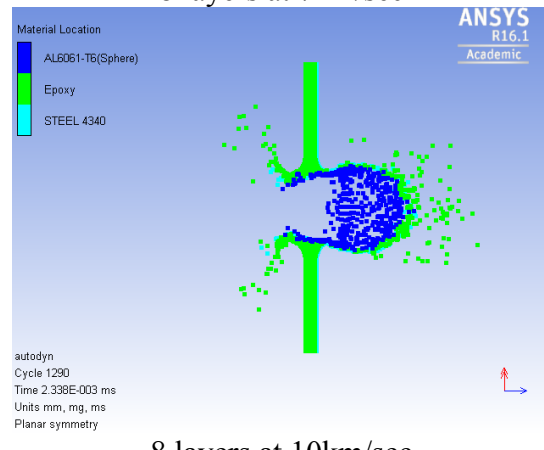
4layers at 7km/sec



8 layers at 7km/sec



4 layers at 10km/sec

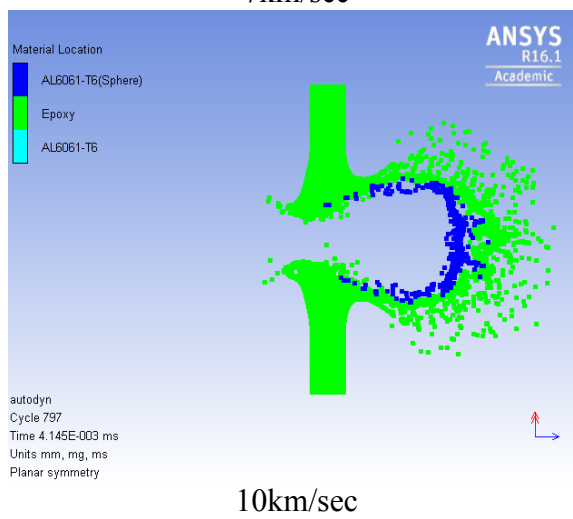
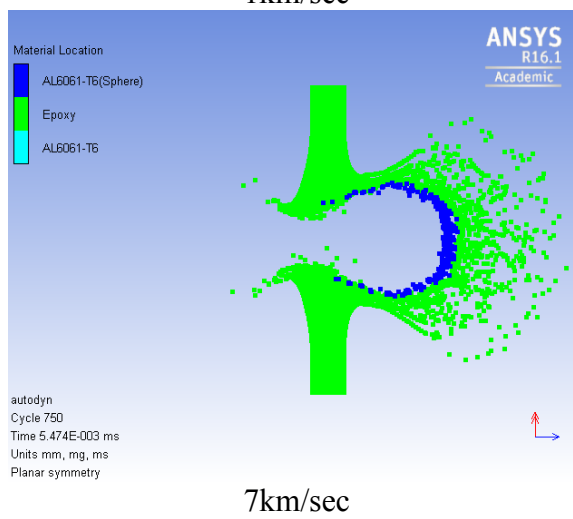
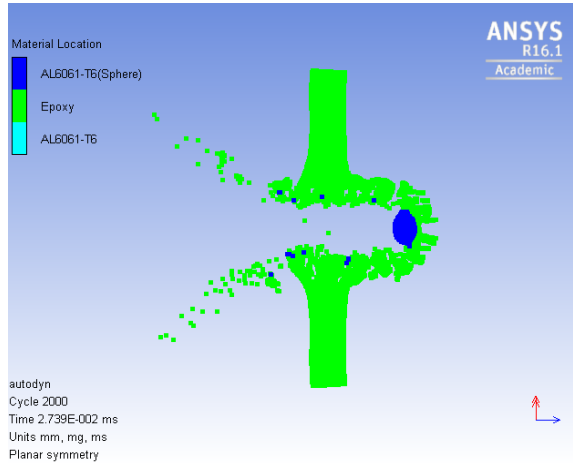


8 layers at 10km/sec

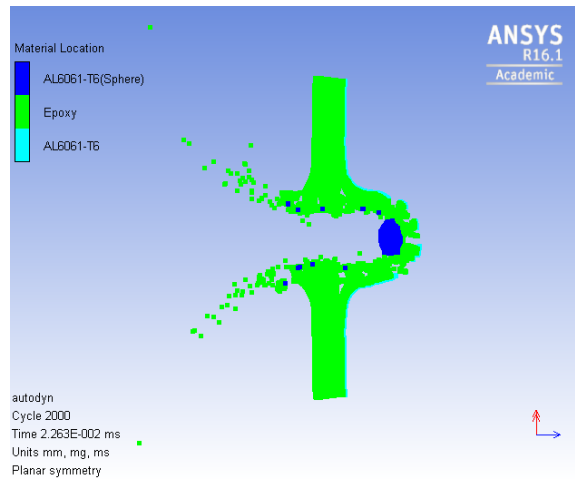
# APPENDIX F

## I. Aluminum substrate

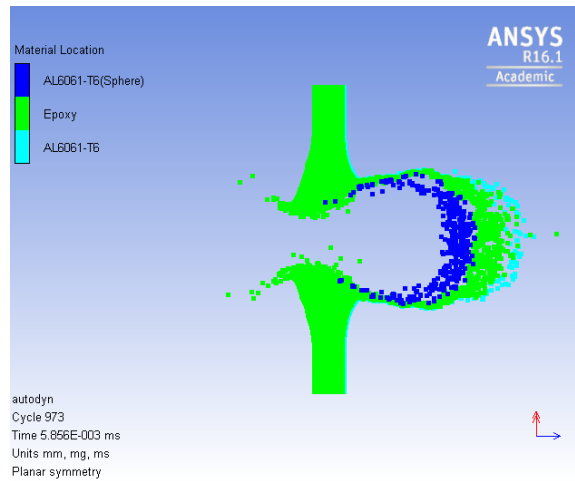
### 1. 5.41mm coating



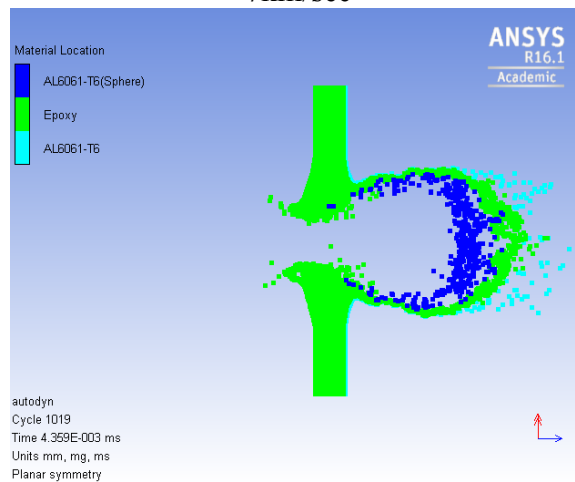
## 2. 4.73mm coating with 0.25mm Aluminum



1km/sec

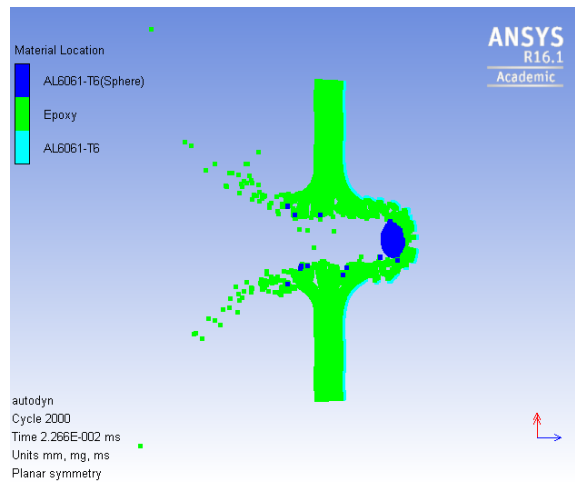


7km/sec

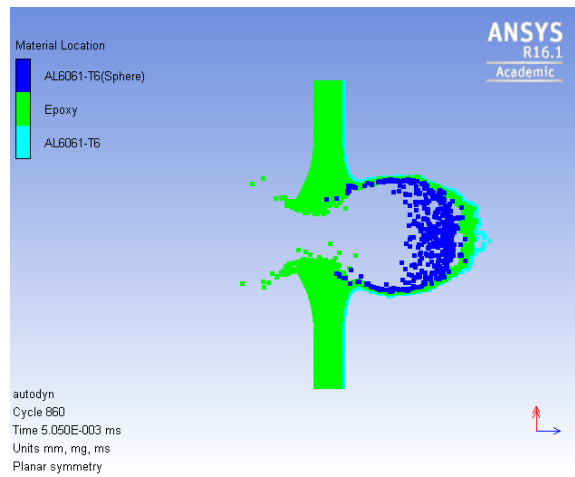


10km/sec

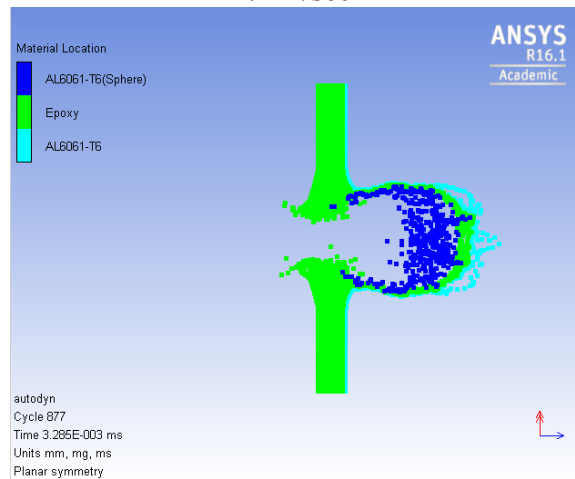
### 3. 4.06mm coating with 0.50mm Aluminum



1km/sec

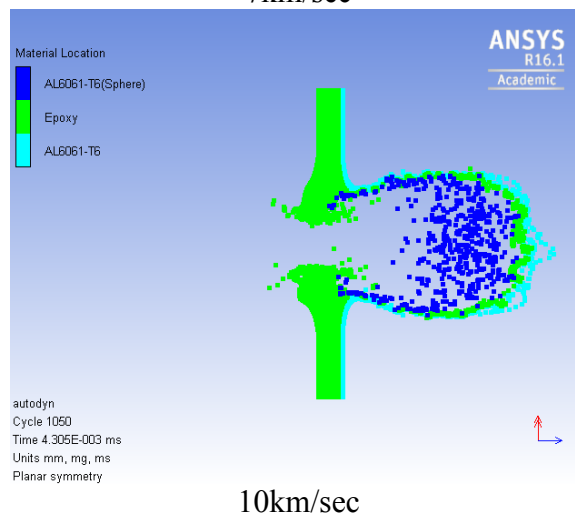
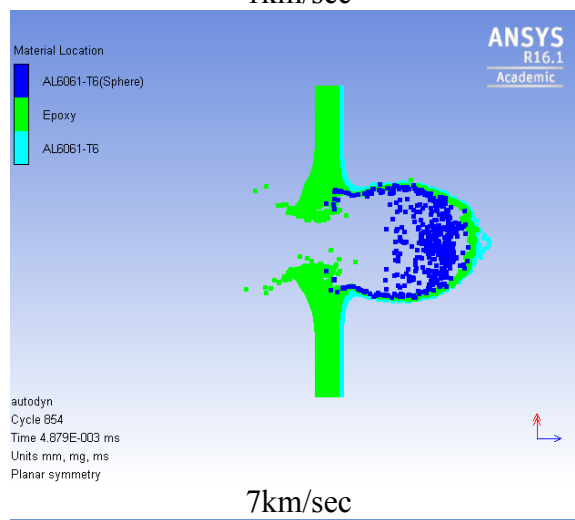
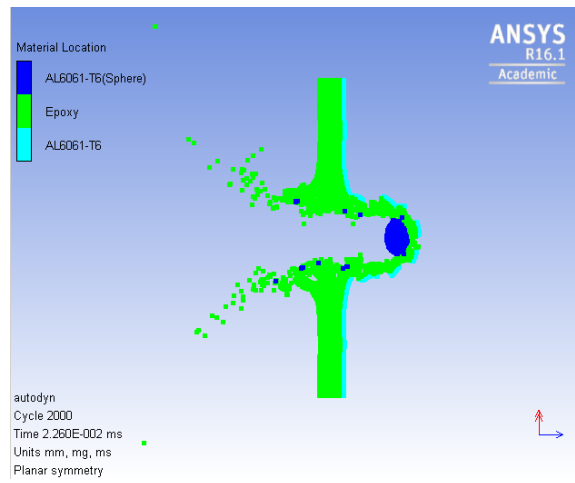


7km/sec

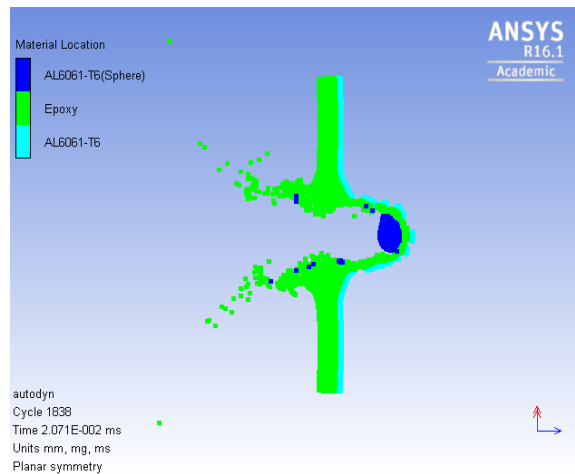


10km/sec

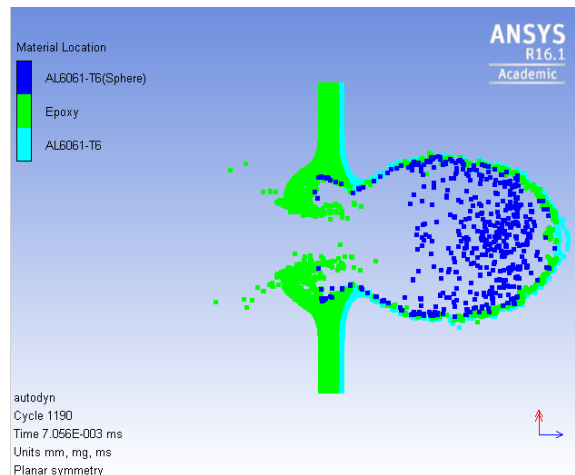
#### 4. 3.38mm coating with 0.75mm Aluminum



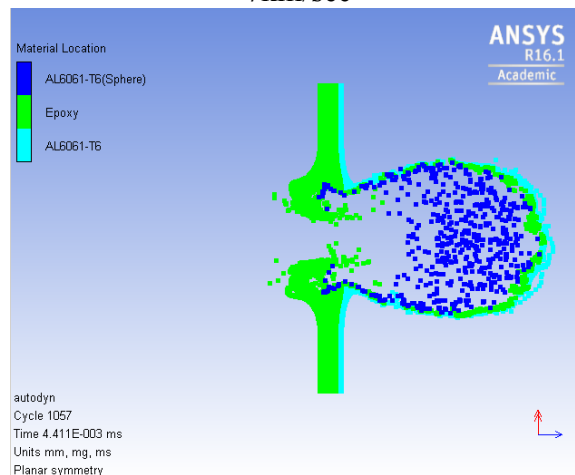
## 5. 2.7mm Coating with 1.00mm Aluminum



1km/sec

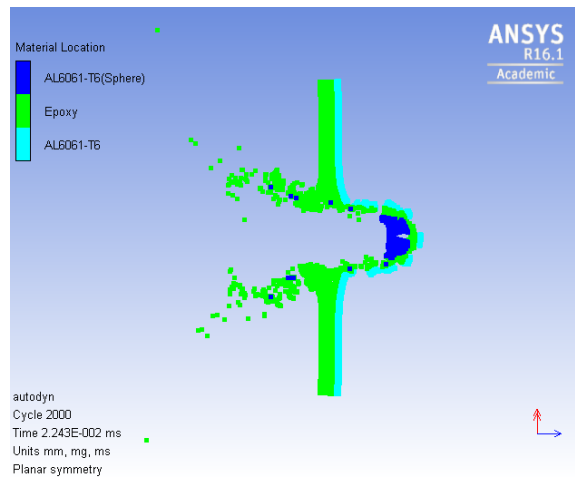


7km/sec

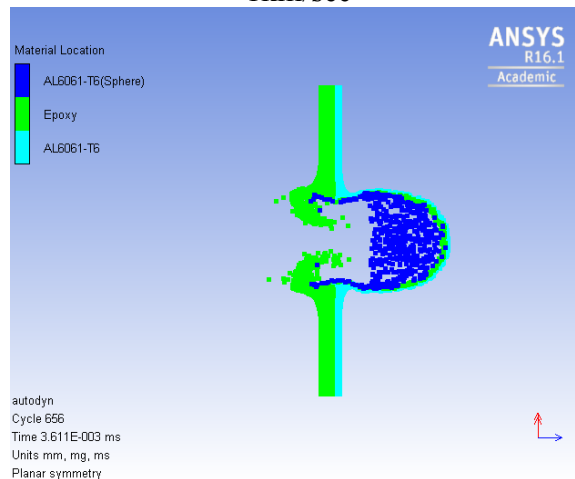


10km/sec

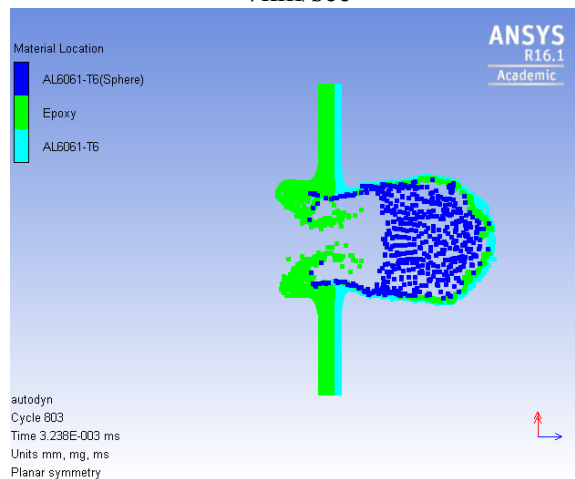
## 6. 2.03mm coating with 1.25mm Aluminum



1km/sec



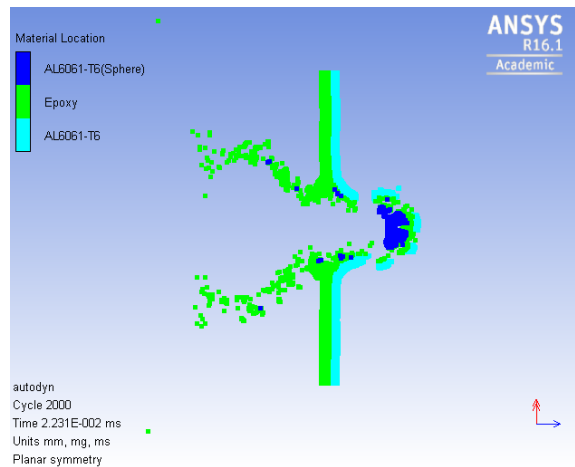
7km/sec



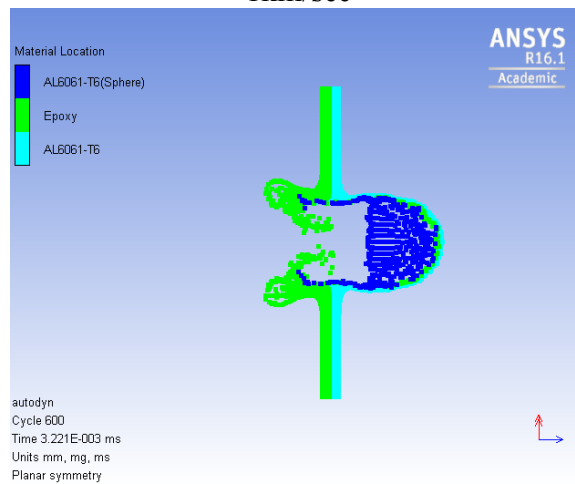
10km/sec



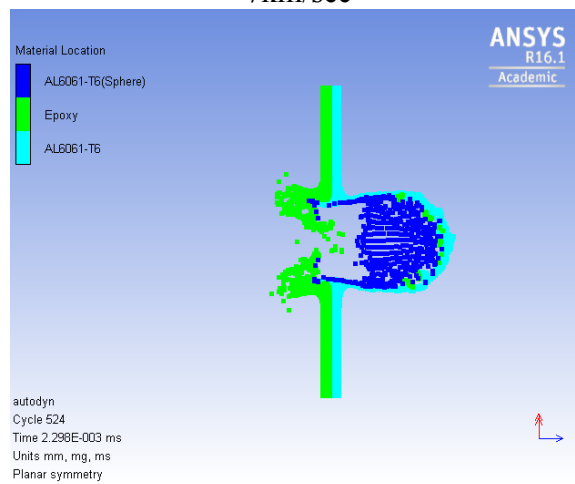
## 7. 1.35 coating with 1.50mm Aluminum



1km/sec

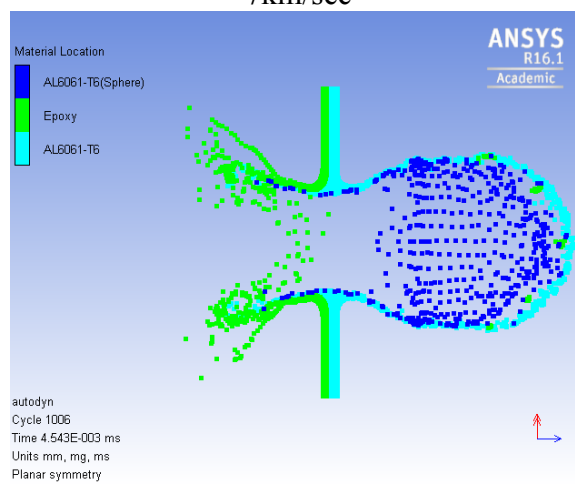
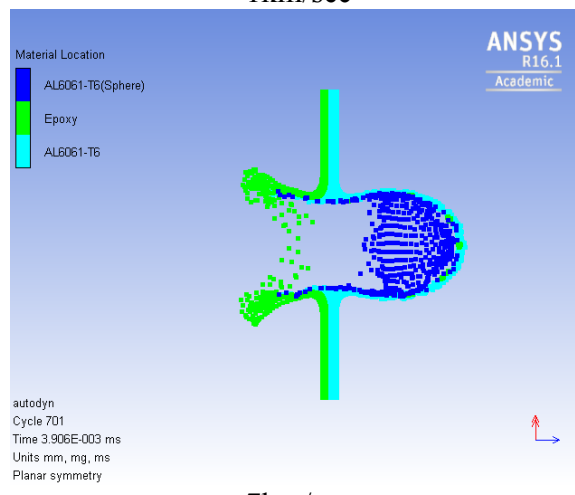
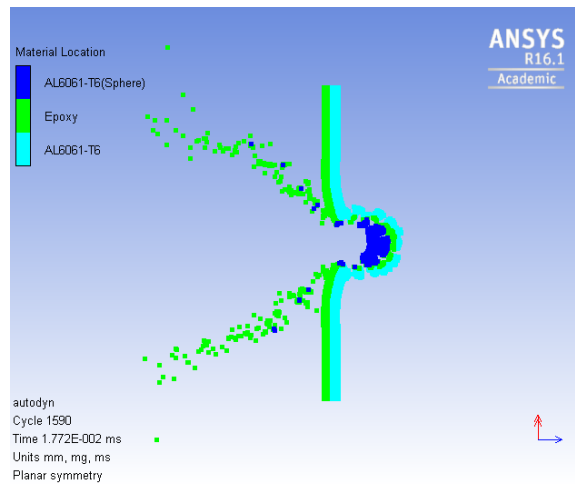


7km/sec

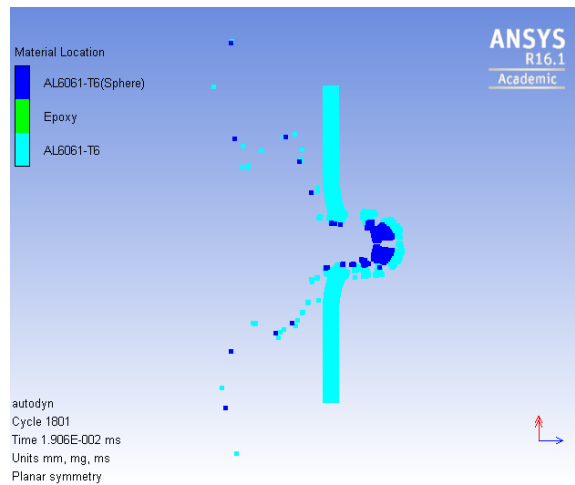


10km/sec

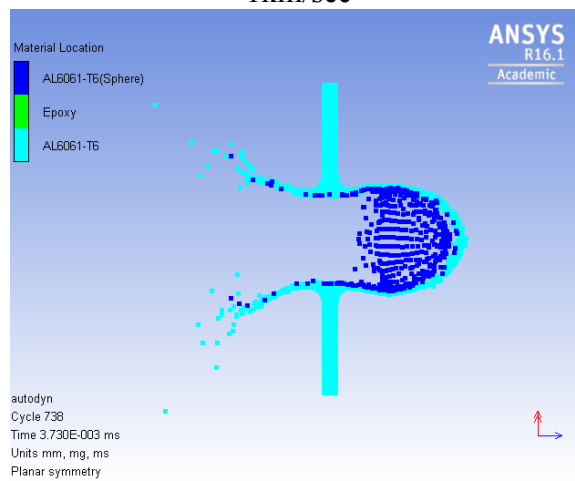
## 8. 0.68mm coating with 1.75mm Aluminum



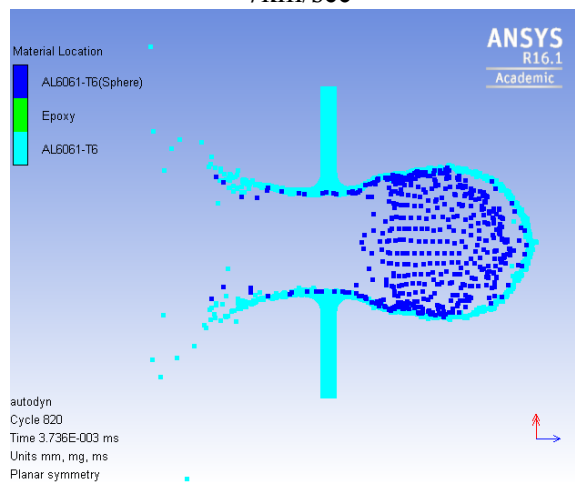
## 9. 2.00 Aluminum



1km/sec



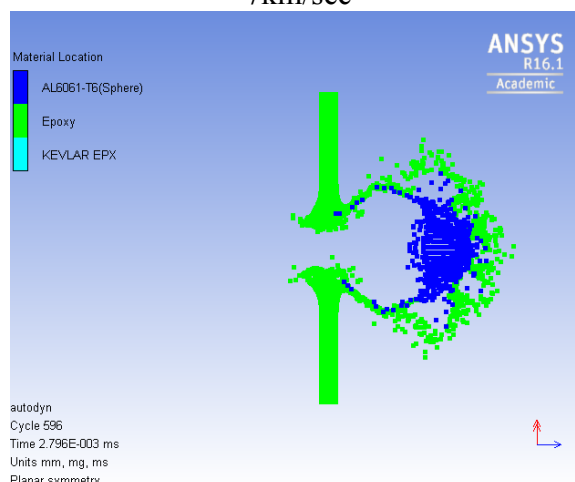
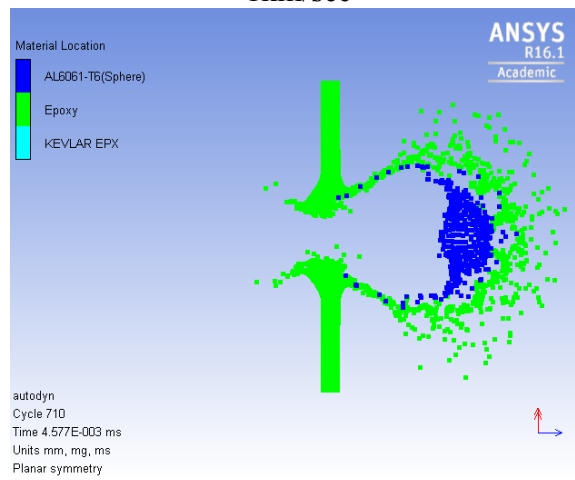
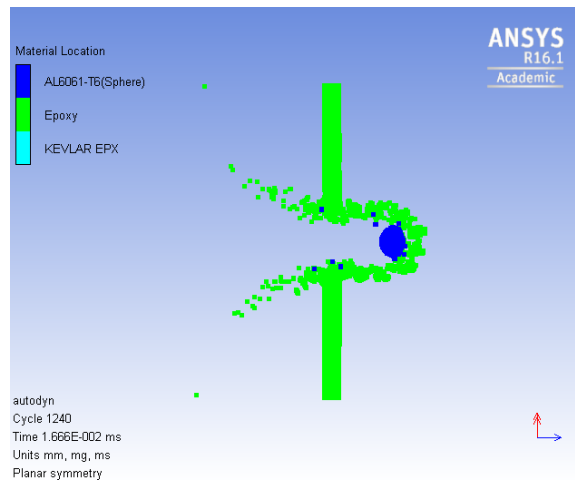
7km/sec



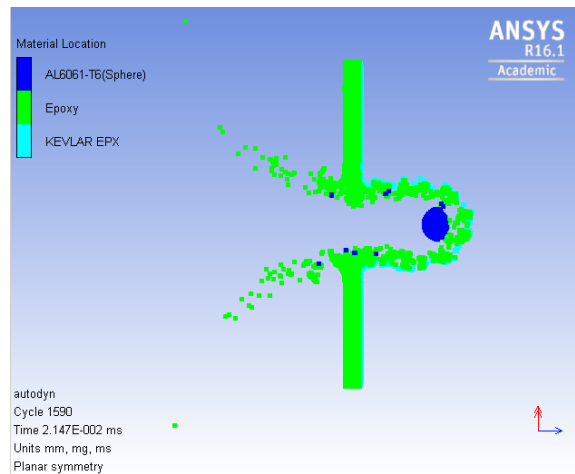
10km/sec

## II. Kevlar-Epoxy substrate

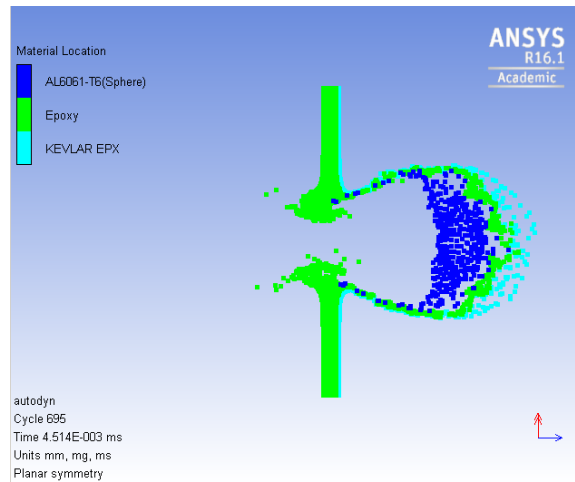
### 1. 2.58mm Coating



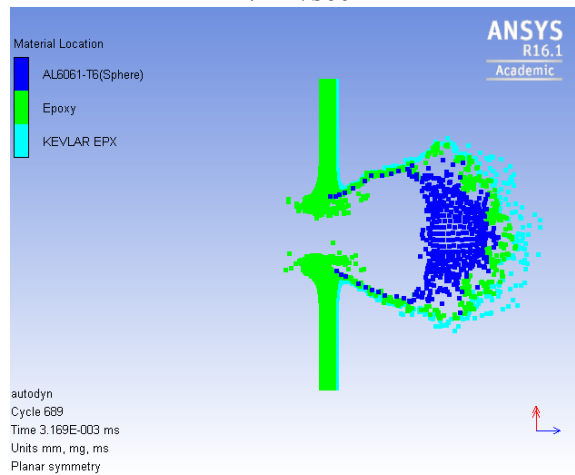
## 2. 2.26mm coating with 0.25mm Kevlar-Epoxy



1km/sec

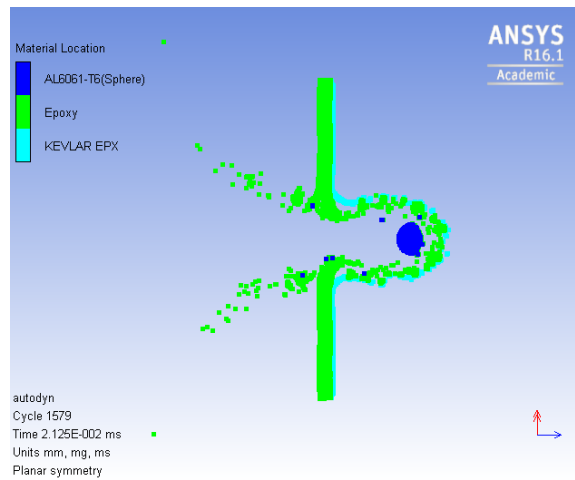


7km/sec

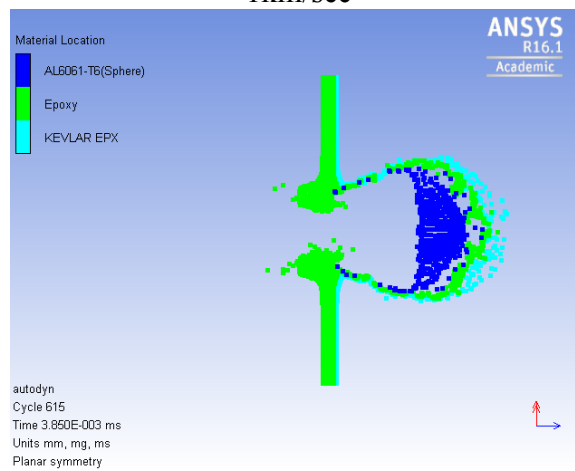


10km/sec

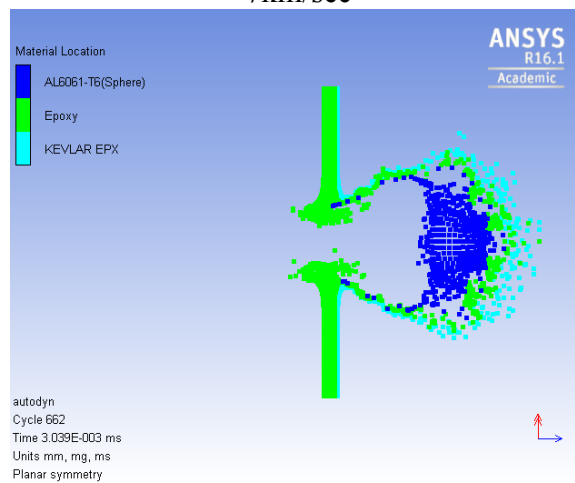
### 3. 1.94mm Coating with 0.50mm Kevlar-Epoxy



1km/sec

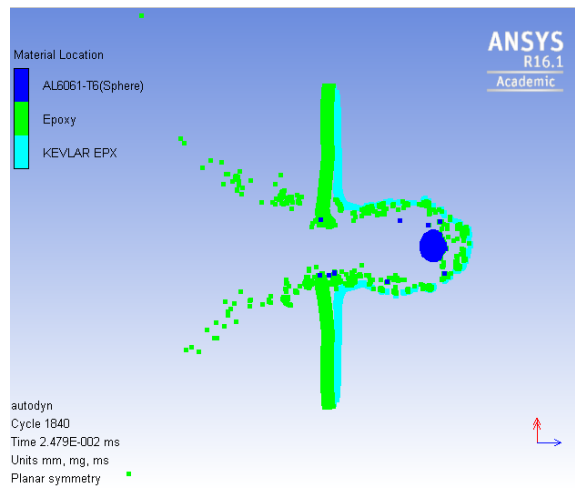


7km/sec

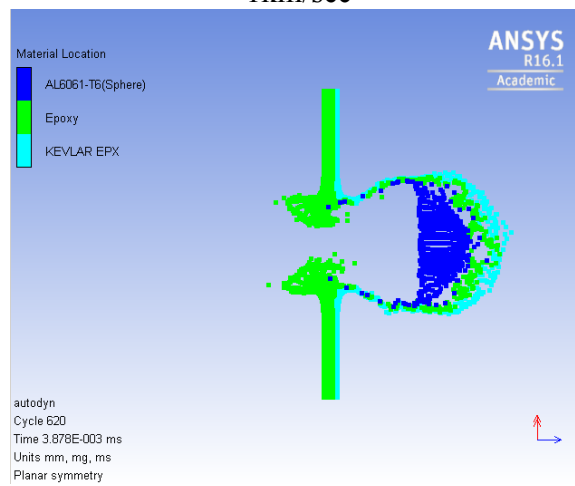


10km/sec

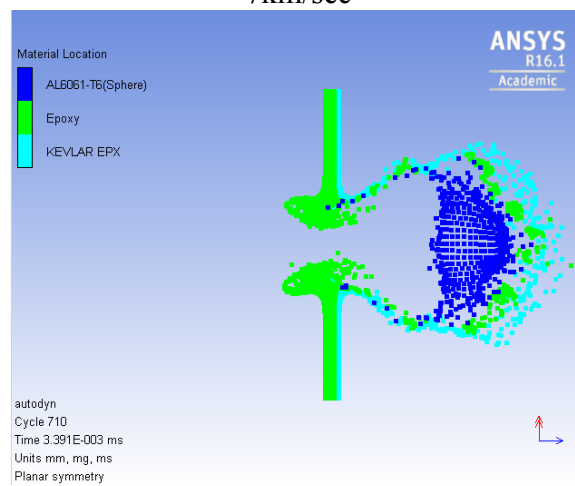
#### 4. 1.61mm coating with 0.75mm Kevlar-Epoxy



1km/sec

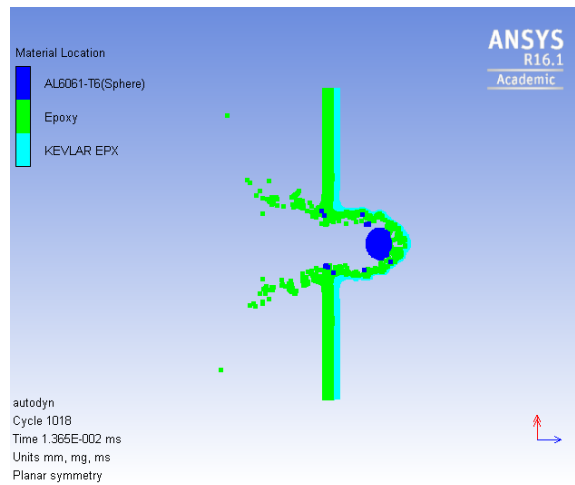


7km/sec

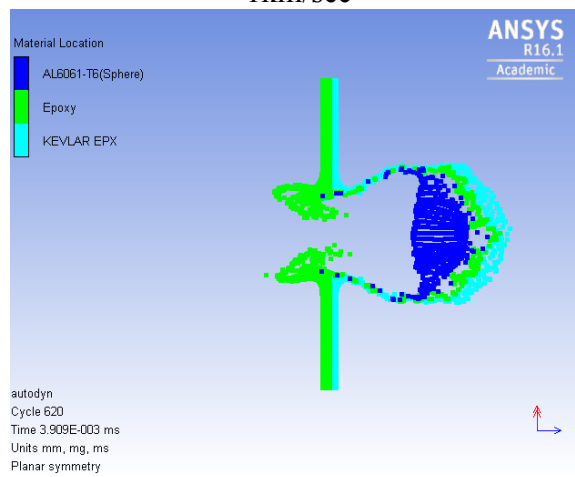


10km/sec

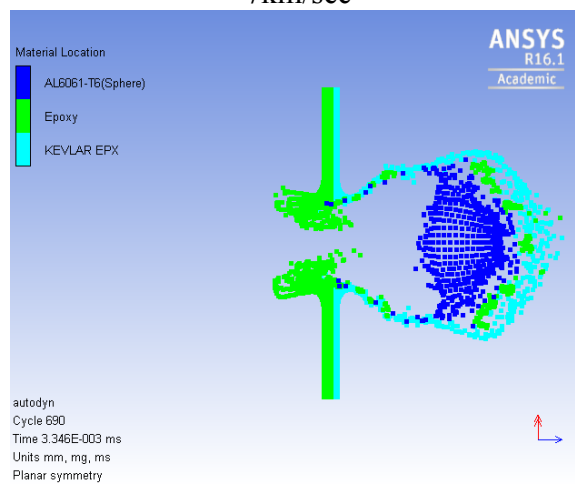
## 5. 1.29mm Coating with 1.00mm Kevlar-Epoxy



1km/sec



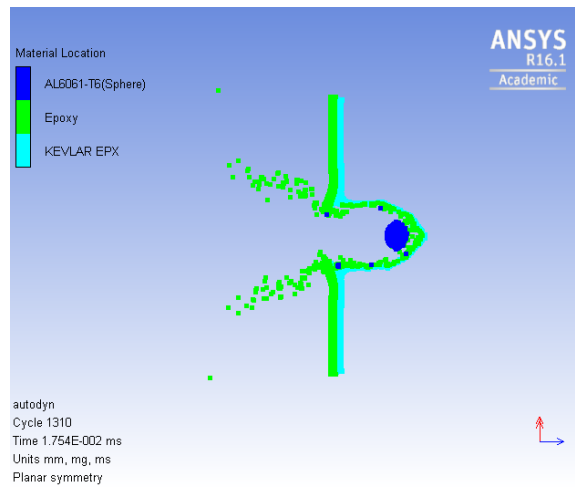
7km/sec



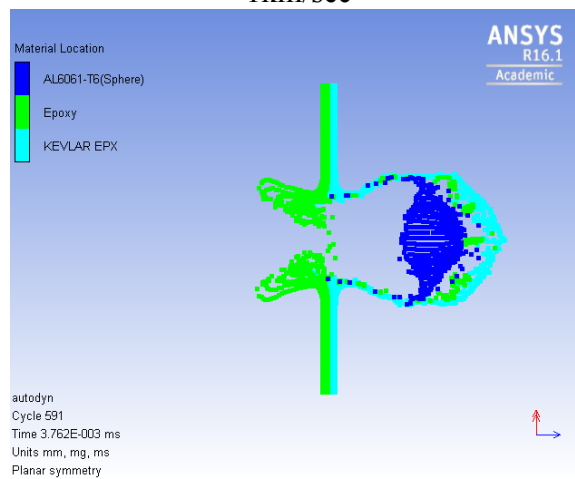
10km/sec



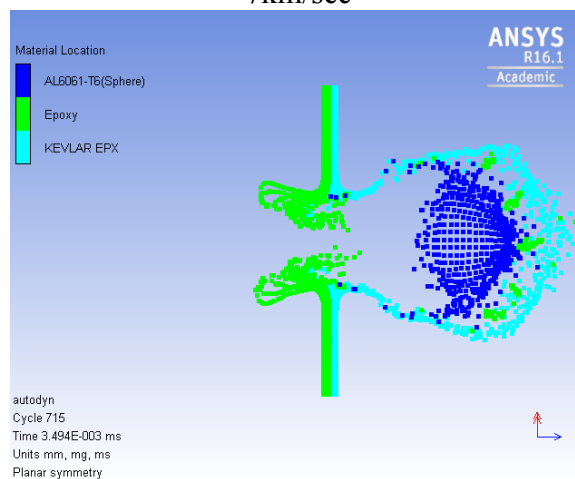
## 6. 0.97mm coating with 1.25mm Kevlar-Epoxy



1km/sec

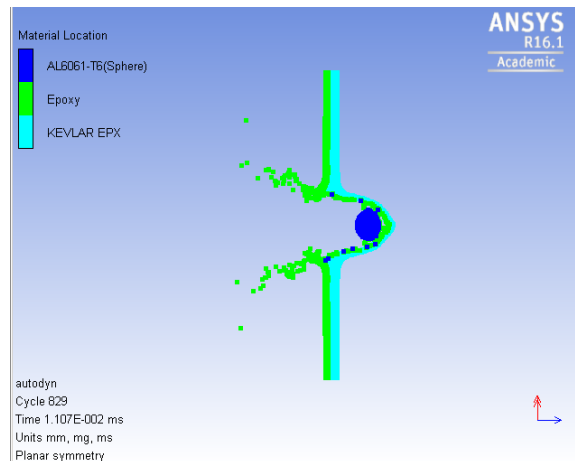


7km/sec

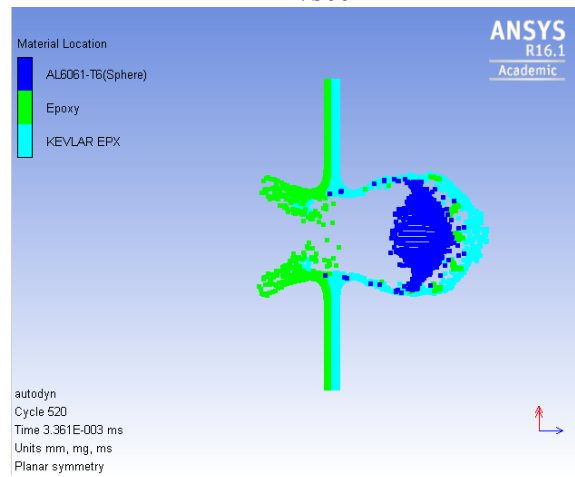


10km/sec

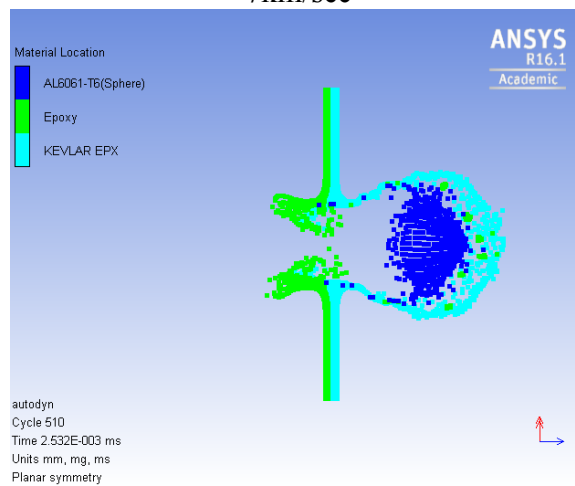
## 7. 0.65mm coating with 1.50mm Kevlar-Epoxy



1km/sec

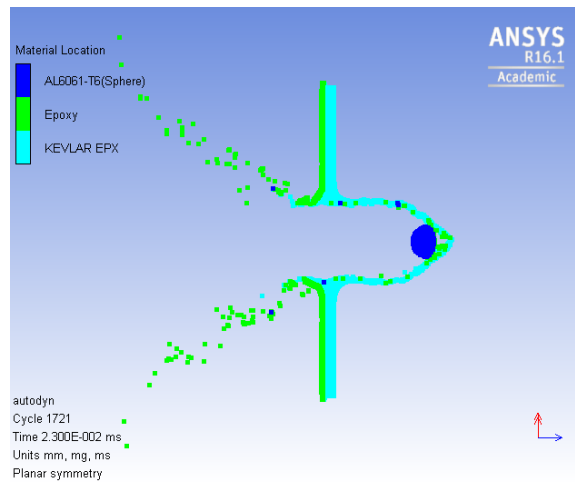


7km/sec

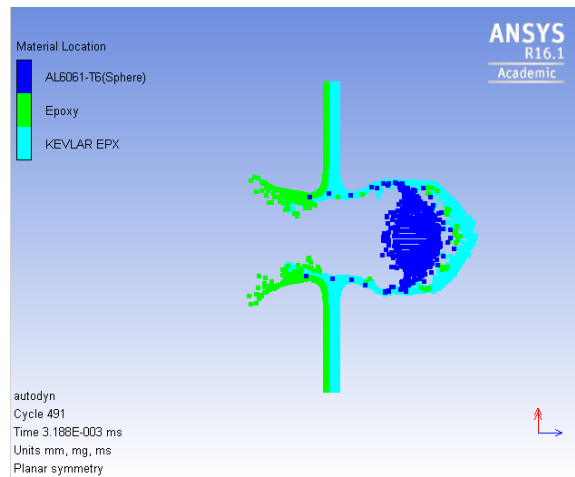


10km/sec

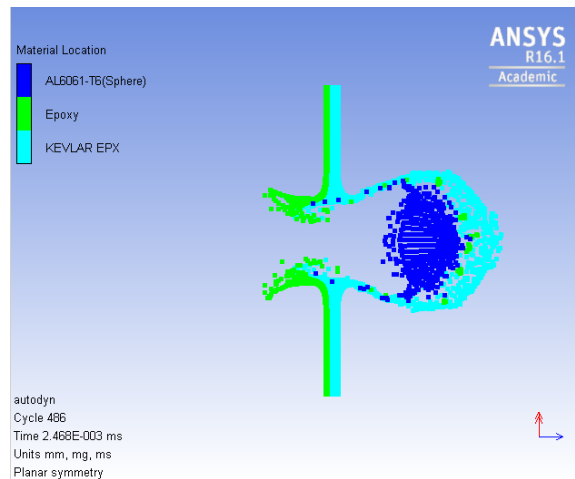
8. 0.32mm coating with 1.75mm Kevlar-Epoxy



1km/sec

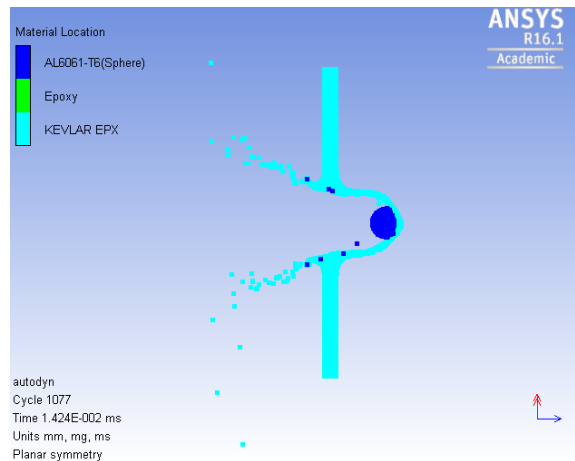


7km/sec

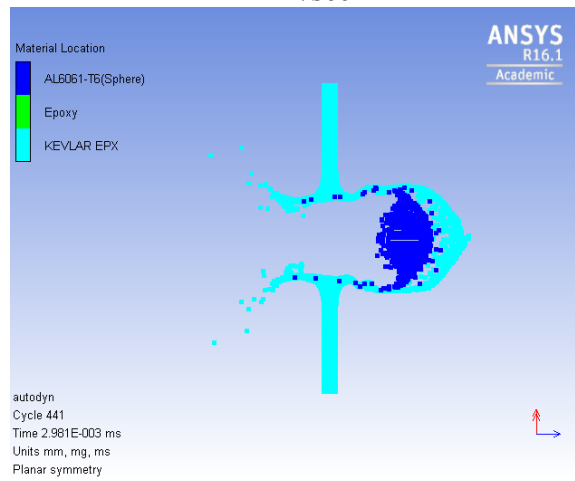


10km/sec

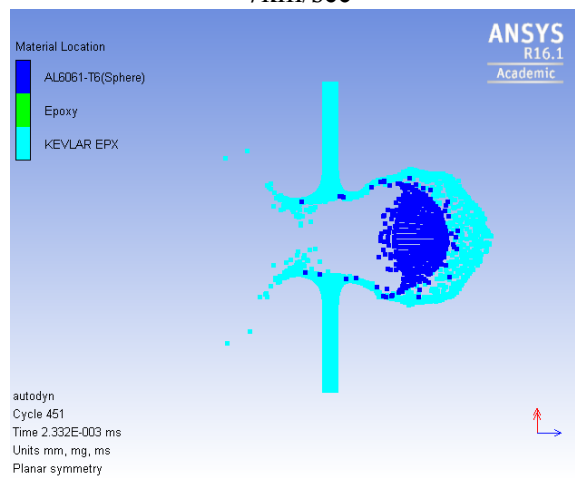
## 9. 2.00mm Kevlar-Epoxy



1km/sec



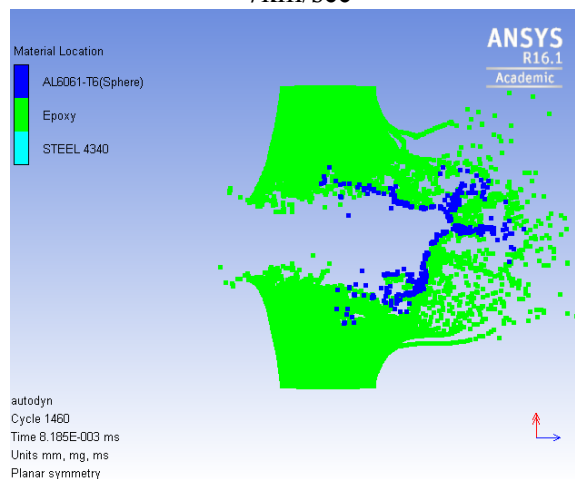
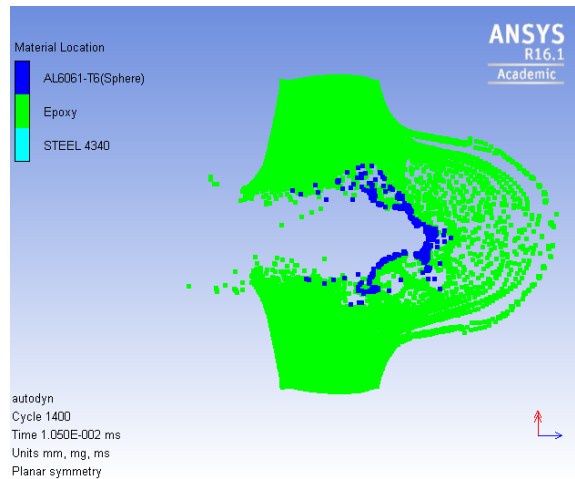
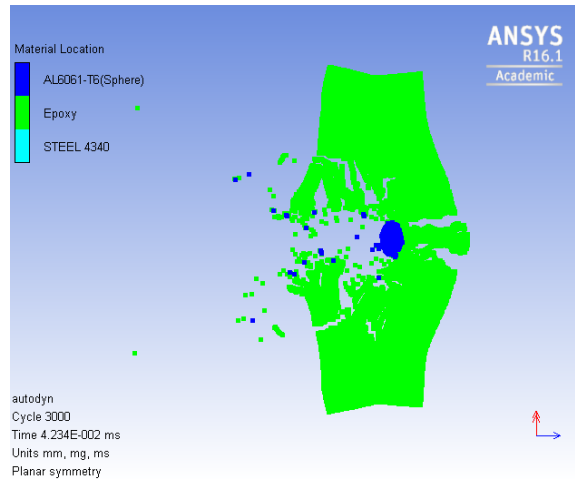
7km/sec



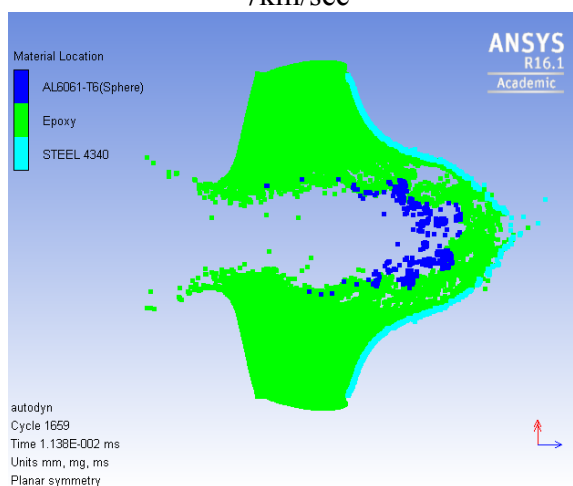
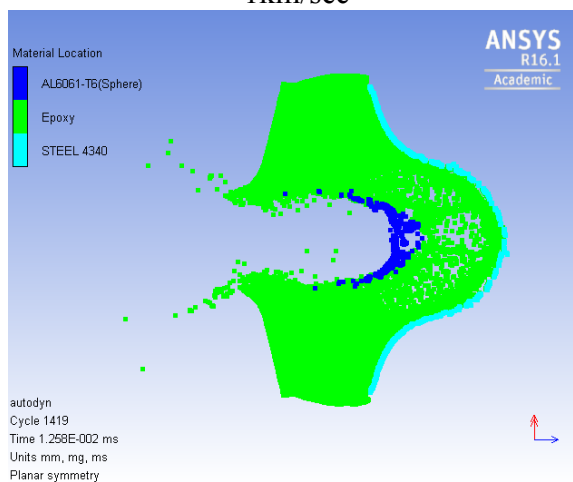
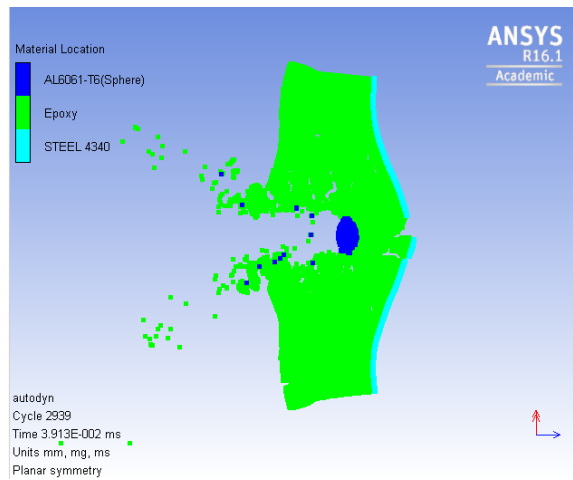
10km/sec

### III. Steel substrate

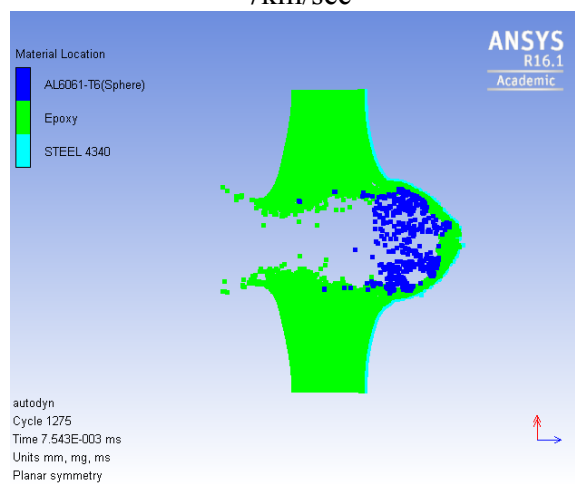
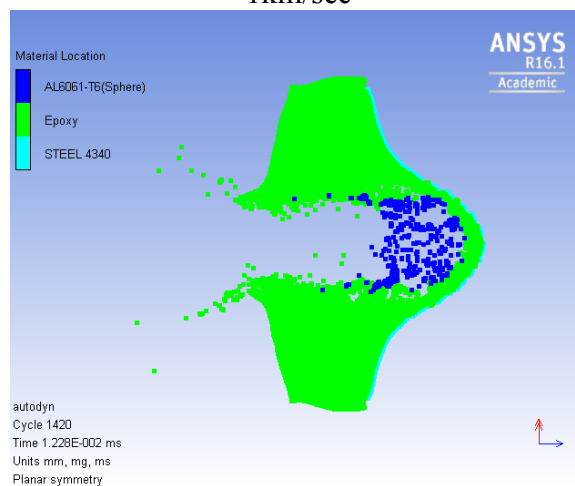
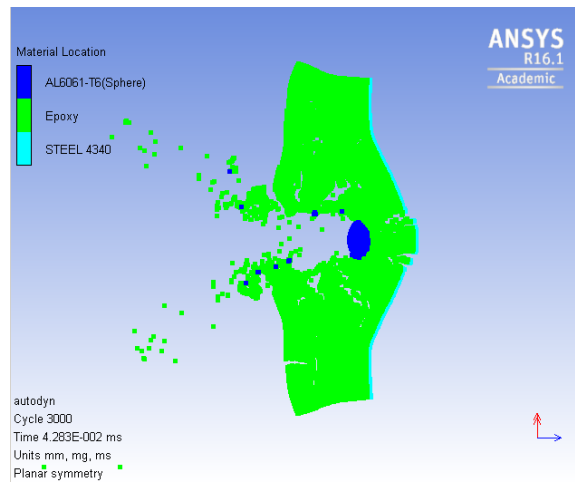
#### 1. 15.66mm coating



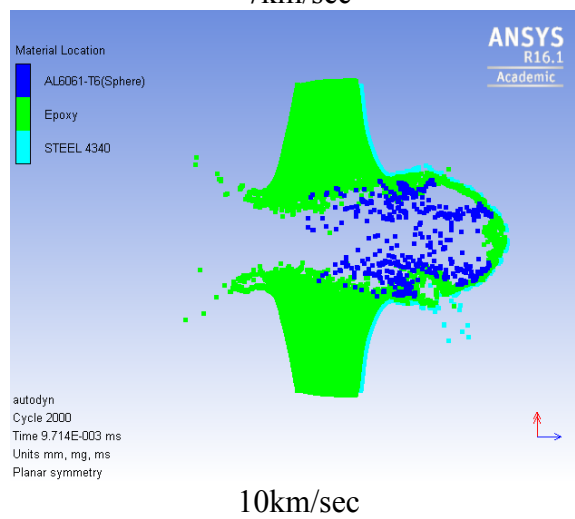
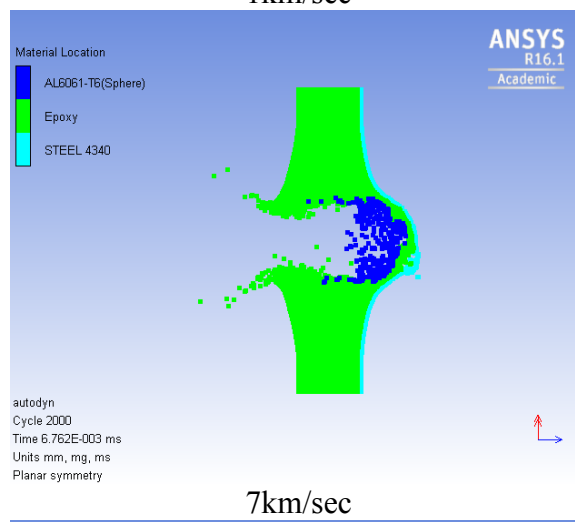
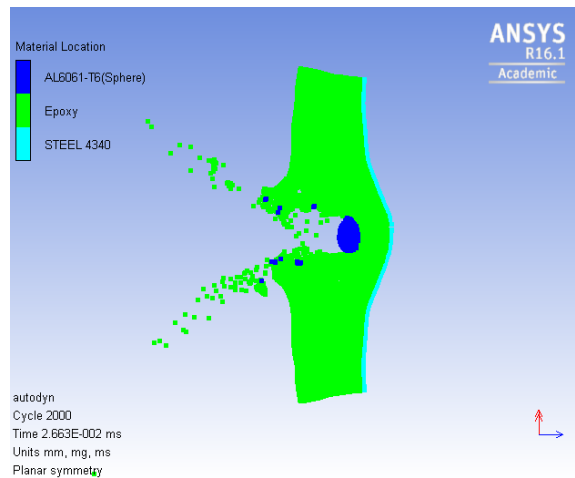
## 2. 13.7mm coating with 0.25mm Steel



### 3. 11.75mm coating with 0.50mm Steel

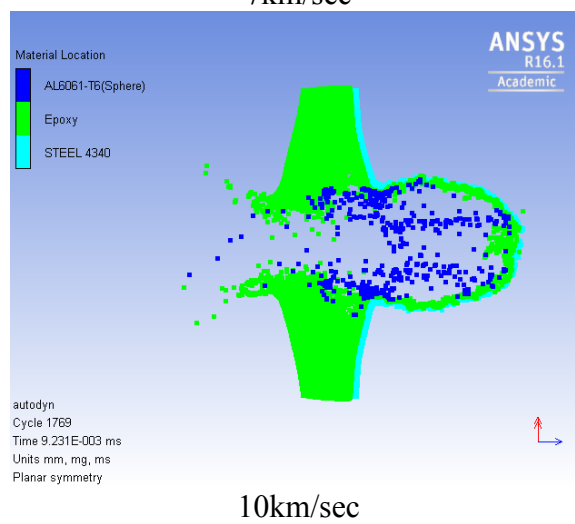
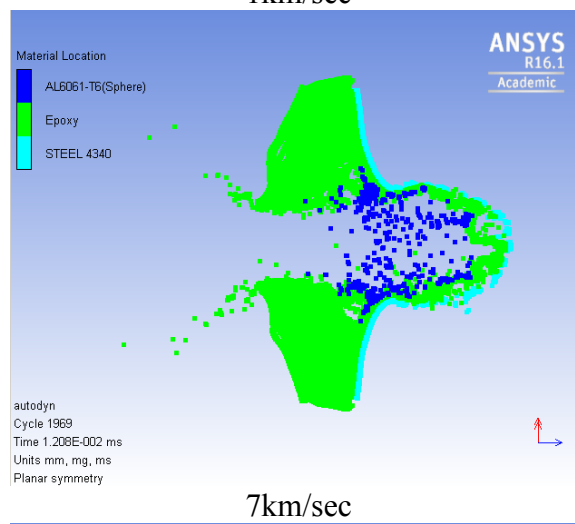
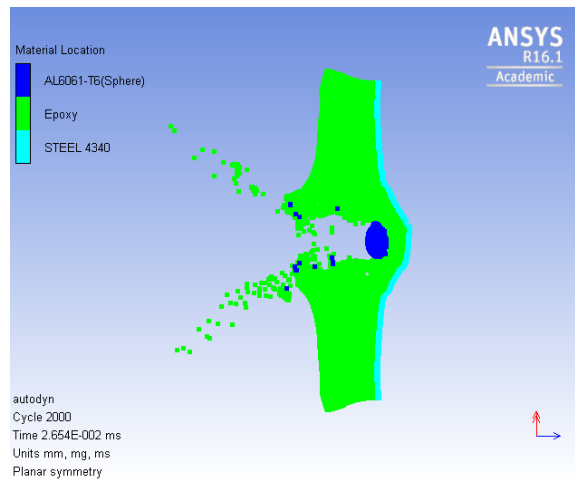


#### 4. 9.79mm coating with 0.75mm Steel

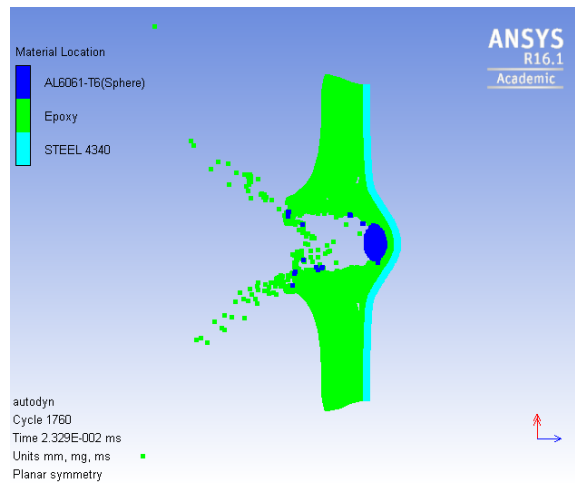




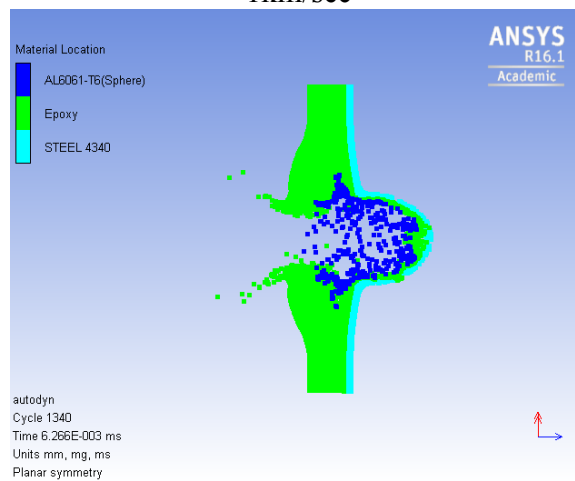
5. 7.83mm coating with 1.00mm Steel



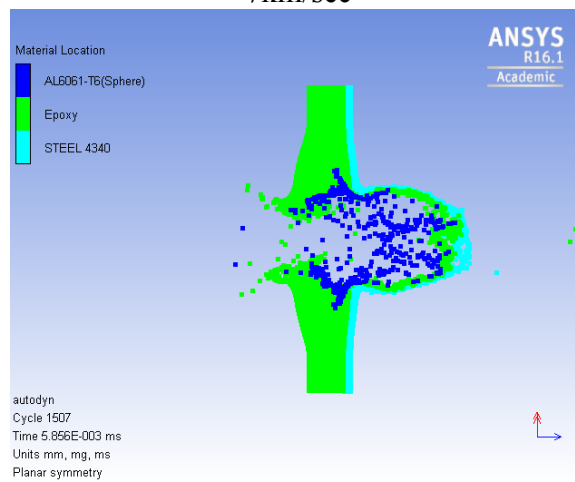
6. 5.87mm coating with 1.25mm Steel



1km/sec

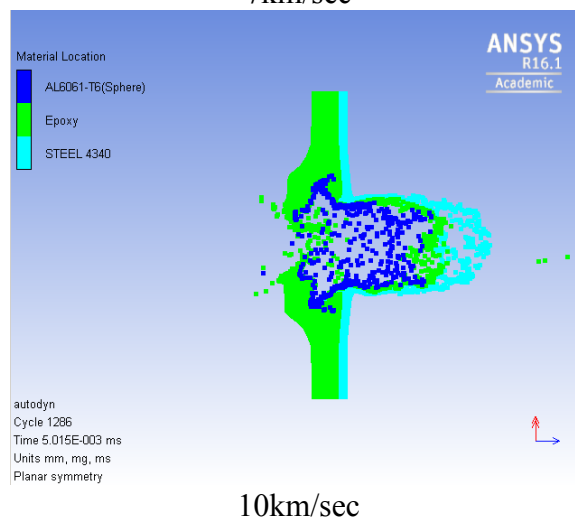
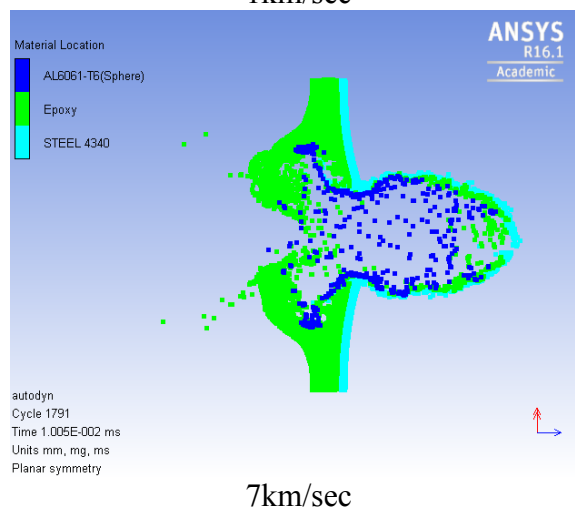
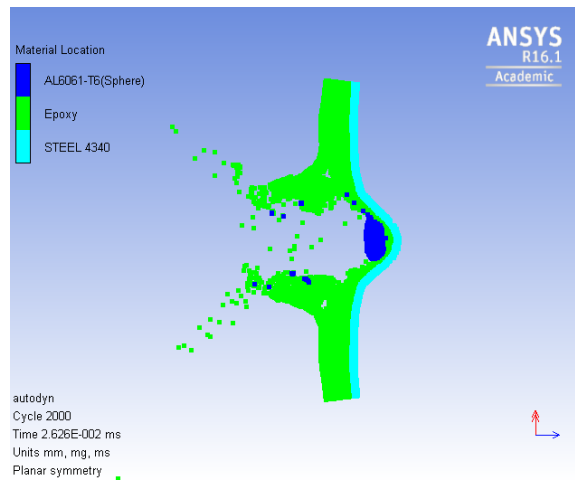


7km/sec

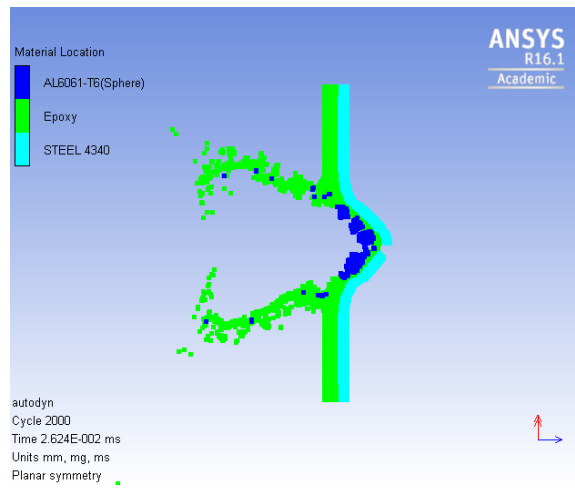


10km/sec

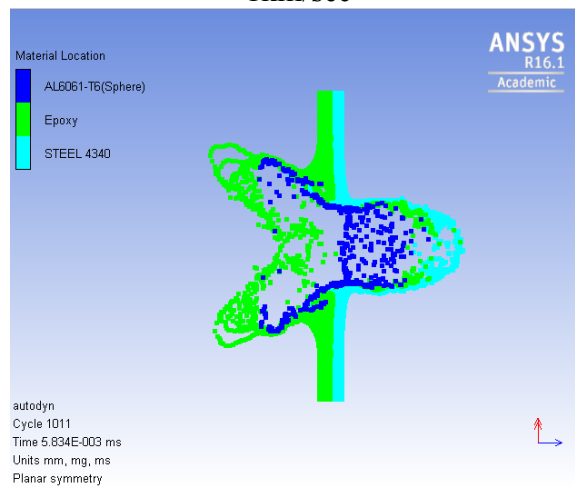
## 7. 3.92mm coating with 1.50mm Steel



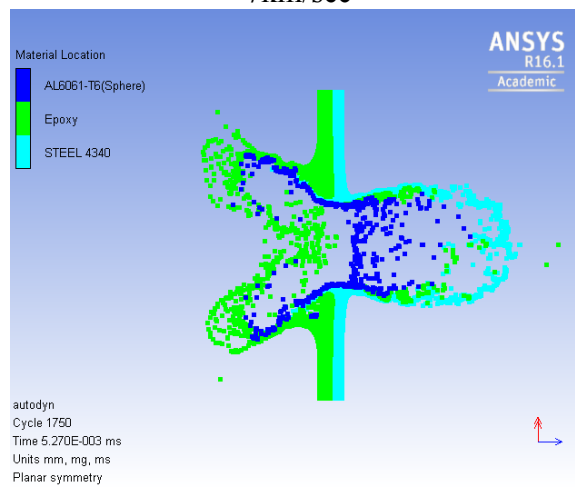
8. 1.96mm coating with 1.75mm Steel



1km/sec

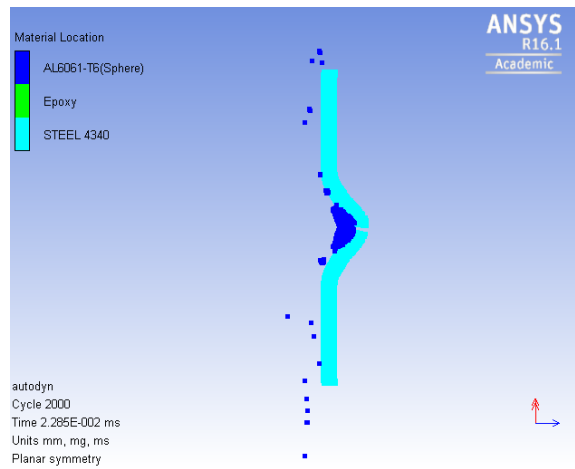


7km/sec

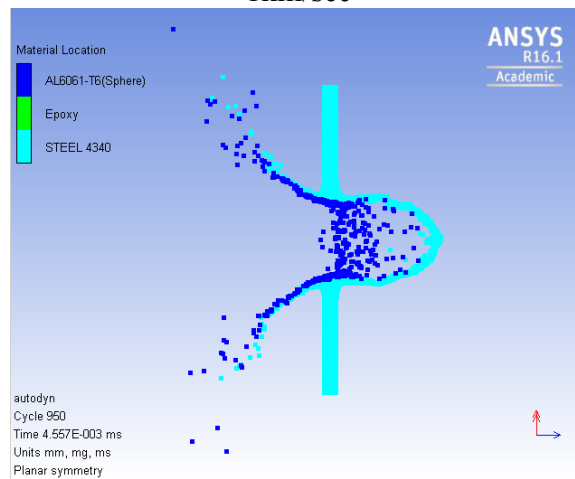


10km/sec

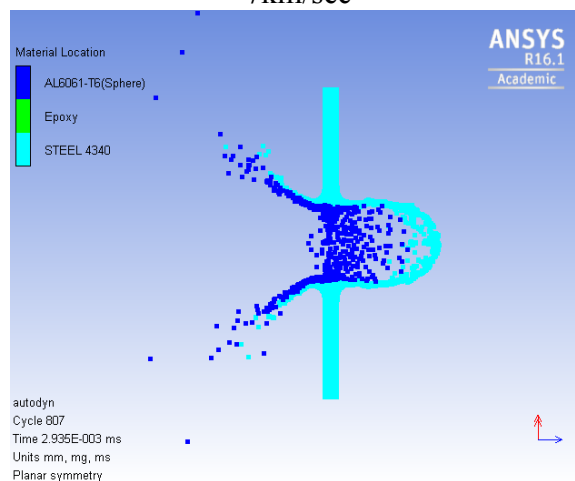
## 9. 2.00mm Steel



1km/sec



7km/sec



10km/sec

## VITA

Alharith Manasrah was born September 13, 1987, in Irbid, Jordan. Alharith received his Bachelor of Science in Civil Engineering in 2009. After obtaining his Bachelors at Jordan University of Science and Technology, he shortly began his Masters studies in the Civil Engineering department at the same university. Alharith received his masters in 2012. Later, He started working as QA/QC at Daewoo E&C. Afterwards, he started his Ph.D. Study at the University of Mississippi in 2013.